université PARIS-SACLAY

NNT : 2017SACLC065

CentraleSupélec

Analyse de la cinétique de transformation et des instabilités de déformation dans des aciers TRIP « Moyen Manganèse » de 3eme génération

Thèse de doctorat de l'Université Paris-Saclay
préparée à CentraleSupélec

École doctorale n°579 : Sciences Mécaniques et Energétiques, Matériaux et Géosciences (SMEMAG)
Spécialité de doctorat: Materials Science

Thèse présentée et soutenue à Gif-sur-Yvette, le 21 novembre 2017 par

Michael Callahan

Composition du jury :

Matthieu MAIZIERE Professeur, MINES ParisTech	Président du jury
Pascal JACQUES Professeur, Université Catholique de Louvain	Rapporteur
Véronique FAVIER Professeur, Arts et Métiers ParisTech	Rapporteur
Olivier HUBERT Professeur, ENS Cachan	Examinateur
Astrid PERLADE Ingénieure de Recherche, ArcelorMittal Global R&D	Examinateur
Jean-Hubert SCHMITT Professeur, CentraleSupélec	Directeur de thèse

Thèse de doctorat

université PARIS-SACLAY
ÉCOLE DOCTORALE
Sciences mécaniques et énergétiques, matériaux et géosciences (SMEMAG)

Titre : Analyse de la cinétique de transformation et des instabilités de déformation dans des aciers TRIP « Moyen Manganèse » de 3eme génération

Mots clés : bandes de Lüders, bandes de Portévin le-Châtelier, corrélation d'images, aimantation saturée, plasticité induite par la transformation (TRIP)

Abstract : Cette thèse caractérise un acier Moyen Mn à 0.2C-5Mn-2.5Al qui montre un écrouissage très fort au cours de la déformation plastique dû à l'effet TRIP. Pendant TRIP, l'austénite résiduelle paramagnétique se transforme en martensite ferromagnétique sous déformation plastique, ce qui conduit à un fort écrouissage. Le taux de cet écrouissage dépend des paramètres de fabrication et surtout la température de recuit intercritique. Ces aciers ont aussi des fois le tendance de se déformer de façon hétérogène par des bandes de Lüders ou PLC.

Dans cette thèse, une méthode de caractérisation de la cinétique de transformation de phase est développée sur la base des mesures de l'aimantation saturée de l'acier. La méthode magnétique est unique dans son implémentation in-situ sans aucun effet sur l'essai de traction. Une correction pour les effets de la contrainte appliquée sur l'aimantation est aussi introduite pour la première fois avec une base physique. Les résultats des mesures magnétiques ont été comparés contre des caractérisations des bandes de déformation pour montrer que la transformation de phase coïncide avec le passage des bandes de déformation. La sensibilité à la vitesse de déformation est analysée et une caractérisation de la présence et type de bande PLC est présentée en fonction de la cinétique de transformation de phase.

Title: Analysis of Transformation Kinetics and Strain Instabilities in 3rd Generation Medium Manganese TRIP Steels

Keywords: Lüders bands, Portévin le-Châtelier bands, digital image correlation, saturated magnetization, transformation-induced plasticity (TRIP)

Abstract: This thesis studies the mechanical behavior of a 0.2C-5Mn-2.5Al Medium Mn steel that exhibits a very high degree of work hardening due to transformation-induced plasticity (TRIP) during plastic deformation. During TRIP, paramagnetic retained austenite is transformed to ferromagnetic martensite with the application of plastic strain and generates a significant amount of work hardening. The rate of work hardening is seen to vary greatly depending on processing parameters—notably the intercritical annealing temperature. These steels also often deform heterogeneously through the propagation of Lüders or PLC strain bands.

This research develops a method to characterize the kinetics of the TRIP effect through measurements of the samples magnetic properties. The method is novel in that it is performed in-situ with no effect on the tensile test and is able to correct for the effects of the applied stress on the magnetic properties. The results of these experiments were compared to characterizations of the strain bands to demonstrate that TRIP coincides with the passage of a Lüders or PLC band. The strain rate sensitivity of the steels is analyzed and the presence and type of PLC bands are characterized with respect to the transformation kinetics.

Université Paris-Saclay
Espace Technologique / Immeuble Discovery
Route de l'Orme aux Merisiers RD 128 / 91190 Saint-Aubin, France

Logos, numéros d'accréditation et dénominations des écoles doctorales

n°581 : agriculture, alimentation, biologie, environnement et santé (ABIES)

n°127 : astronomie et astrophysique d'Ile-de-France (AAIF)

n°568 : signalisations et réseaux intégratifs en biologie (Biosigne)

n°582 : cancérologie : biologie - médecine - santé (CBMS)

n°574 : mathématiques Hadamard (EDMH)

n°572 : ondes et matières (EDOM)

n°570 : santé publique (EDSP)

Université Paris-Saclay
Espace Technologique / Immeuble Discovery
Route de l'Orme aux Merisiers RD 128 / 91190 Saint-Aubin, France

n°575 : electrical, optical, bio : physics and engineering (EOBE)

n°573 : interfaces : approches interdisciplinaires, fondements, applications et innovation (Interfaces)

n°569 : innovation thérapeutique : du fondamental à l'appliqué (ITFA)

n°571 : sciences chimiques : molécules, matériaux, instrumentation et biosystèmes (2MIB)

n°576 : particules hadrons énergie et noyau : instrumentation, image, cosmos et simulation (Pheniics)

n°564 : physique de l'Ile-de-France (PIF)

n°577 : structure et dynamique des systèmes vivants (SDSV)

Université Paris-Saclay
Espace Technologique / Immeuble Discovery
Route de l'Orme aux Merisiers RD 128 / 91190 Saint-Aubin, France

n°129 : sciences de l'environnement d'Ile-de-France (SEIF)

n°578 : sciences de l'homme et de la société (SHS)

n°579 : sciences mécaniques et énergétiques, matériaux et géosciences (SMEMAG)

n°580 : sciences et technologies de l'information et de la communication (STIC)

n°566 : sciences du sport, de la motricité et du mouvement humain (SSMMH)

n°567 : sciences du végétal : du gène à l'écosystème (SDV)

Logos et dénominations des établissements

Etablissement accrédité (de soutenance)

Université Paris-Saclay

Etablissement de préparation de la thèse, opérateur d'inscription

Université Paris-Sud

Université de Versailles-Saint-Quentin-en-Yvelines

Université d'Evry-Val-d'Essonne

Institut des sciences et industries du vivant et de l'environnement (AgroParisTech)

CentraleSupélec

CentraleSupélec

Ecole normale supérieure de Cachan

école
normale
supérieure
paris–saclay

Ecole Polytechnique

ÉCOLE
POLYTECHNIQUE
UNIVERSITÉ PARIS-SACLAY

Ecole nationale supérieure de techniques avancées

ENSTA
ParisTech
université
PARIS-SACLAY

Ecole nationale de la statistique et de l'administration économique

ENSAE
ParisTech
École nationale
de la statistique
et de l'administration
économique

HEC Paris

Université Paris-Saclay
Espace Technologique / Immeuble Discovery
Route de l'Orme aux Merisiers RD 128 / 91190 Saint-Aubin, France

HEC PARIS

Institut d'optique théorique et appliquée

INSTITUT d'OPTIQUE GRADUATE SCHOOL ParisTech

Télécom ParisTech

TELECOM ParisTech

Télécom SudParis

TELECOM SudParis

Université Paris-Saclay
Espace Technologique / Immeuble Discovery
Route de l'Orme aux Merisiers RD 128 / 91190 Saint-Aubin, France

Liste des spécialités

Voir sur ADUM ou bien sur

http://www.universite-paris-saclay.fr/fr/node/8208

- Accueil
- Doctorat
- Spécialités de doctorat

Université Paris-Saclay
Espace Technologique / Immeuble Discovery
Route de l'Orme aux Merisiers RD 128 / 91190 Saint-Aubin, France

Acknowledgements

I would first and foremost like to thank my advisor Jean-Hubert Schmitt for all of his advice, guidance, and especially friendship over the years we spent working together. So often our discussions of mechanics and dislocation dynamics and such would turn into conversations about life, family, or any number of things and it was an absolute pleasure to work together.

I would also like to thank my parents for their love and support, particularly during these last five years while I've been in France. I wouldn't have made it this far without them, and I'm eternally grateful for everything that they've done for me. I'd also like to thank my mom for proofreading my thesis, giving up lots of her free time to help me out. I love you, mom.

During the last year of my work while I was panicking trying to wrap up experiments, prepare conferences, write this dissertation, and prepare my defense, Laura Diaz Caselles was an enormous help in staying calm and focused. I thank her for the love and friendship she shows me, and for putting up with me when I was stressed.

Thank you to Olivier Hubert and François Hild at LMT ENS Cachan, who were both a great help in developing the experimental methods employed in this thesis and who became my friends in addition to being my colleagues.

I'd like to thank my colleagues at MSSMat, who made the three years I spent there so enjoyable. I've been able to form strong friendships there that I hope will continue for a long time.

Finally, I'd like to thank the members of the ANR project team with whom I worked on this research. Their insights and advice were invaluable to the success I had and I greatly appreciate the discussions we had.

This research was financed by the Association Nationale pour la Recherche, ANR project ANR 13-RMNP-0002 MedMnAl Steels and by the pole de competitivite Materialia.

I would like to dedicate this work to my parents, whose unwavering love and support was ever-present despite an ocean between us.

Contents

Context and Motivation **1**

1 Sommaire **5**

2 Literature Review **11**
2.1 Third Generation Advanced High Strength Steels 11
2.1.1 Microstructures 13
2.1.2 Mechanical Properties 18
2.2 Strain Localizations—Lüders and PLC Effects 20
2.2.1 Lüders Bands in Low-C Steels 20
2.2.2 Portevin-Le Châtelier Bands 23
2.3 Deformation Mechanisms in Steels 28
2.3.1 Dislocation Slip 31
2.3.2 Twinning-Induced Plasticity (TWIP) 32
2.3.3 Transformation-Induced Plasticity (TRIP) 35

3 Material Characterization **41**
3.1 Material and Fabrication Process 41
3.2 Macroscopic Mechanical Properties 42
3.3 Microstructure 47
3.4 Problem Statement and Objectives 55
3.4.1 Discussion of Initial Results 55
3.4.2 Objectives 57

4 Experimental Methodology **59**
4.1 DIC Characterization of Strain Bands 59
4.1.1 Strain Field Calculation by DIC 59
4.1.2 Finite Element-based DIC Algorithm 60
4.1.3 Regularization 61
4.1.4 DIC Parameterization 62
4.2 Magnetic Characterization 66
4.3 Characterization of Magnetic Properties 67
4.3.1 Macroscopic Characterization 67
4.3.2 Microscopic characterization 69
4.3.3 Example 1: Analysis of Anisotropy of TRIP by Saturated Magnetization 73

4.3.4 Example 2: Effects of Temperature and Triaxiality on TRIP Kinetics . . . 75
A note on ferritescopes . . . 79
4.4 Development of an *In-situ* Magnetic Testing Device . . . 79
4.4.1 Magnetic Measurement System . . . 81
4.5 Corrections to Retained Austenite Calculation . . . 85
4.5.1 Localization Correction . . . 86
4.5.2 Magnetoelastic Correction . . . 88
4.5.3 Measurement Precision Verification . . . 91
4.6 Experimental Procedure . . . 92
4.6.1 Strain Band Characterization by DIC . . . 92
4.6.2 Strain Rate Sensitivity . . . 94
4.7 Magnetic Experimental Procedure . . . 95
4.7.1 Intercritical Annealing Temperature Effect and Strain Localizations . . . 95
4.7.2 Strain Rate Effect and Strain Rate Sensitivity . . . 96

5 TRIP and Strain Instability Analysis **99**
5.1 Strain Band Characterization . . . 99
5.2 Sensitivity to Intercritical Annealing Temperature . . . 105
5.3 Effect of T_{IA} on Transformation-induced Plasticity . . . 106
5.4 Effect of Strain Rate on TRIP . . . 110
5.5 Strain Rate Sensitivity . . . 113

6 Discussion **125**
6.1 TRIP Kinetics when Deformation is Homogeneous . . . 125
6.2 Model of Macroscopic Mechanical Behavior . . . 130
6.2.1 Behavior Laws . . . 130
6.2.2 Determination of Model Parameters for T_{IA} =780°C . . . 132
6.3 Strain Localizations . . . 133
6.3.1 Lüders Bands . . . 136
6.3.2 Portevin-Le Châtelier Bands . . . 140
6.4 Strain Rate Effects on Tensile Behavior . . . 149
6.4.1 Effect of Strain Rate on TRIP . . . 149
6.5 Strain Rate Sensitivity . . . 154

Conclusions and Persectives **159**

Context and Motivation

Material selection in the design of mechanical components often leads an engineer to make compromises between mechanical resistance and component weight. Typically the specific elastic modulus and specific yield stress are used to choose a material, and then the component is dimensioned accordingly. This means that steel producers must seek to optimize the elastic modulus, yield stress, and density of their products in order to maintain competition against other materials such as aluminum, titanium, or fiber composites. Historically, while the elastic modulus and density can be varied only marginally as they are primarily defined the mass and atomic bond strength of iron, the yield stress can be easily changed from one alloy to another. As such, a precise understanding of the interactions between processing parameters, the resultant microstructure, and final mechanical behavior is necessary in order to both optimize the performance of existing steel alloys and to develop more advanced steels.

Significant progress in ferrous metallurgy has been made through the development of a first generation advanced high strength steels (dual-phase, TRIP, martensitic) with ferrite-based microstructures followed by a second generation (TWIP) with primarily austenitic microstructures. As with many fields, however, there remain significant improvements to be made particularly for the automotive industry.

Due to increasingly stringent emissions regulations, the automotive industry has made vehicle light-weighting one of its primary objectives in new product development. Lighter vehicle weight would evidently reduce fuel consumption and, in turn, CO2 emissions. As such, steels with a higher specific strength are needed. The recent development of a third generation of advanced high strength steels (AHSS) shows promise in attaining not only improved ductility and tensile strength, but also non-negligible reductions in density by the addition of aluminum to the alloy. These steels have complex multiphase microstructures composed of a mixture of ferrite, retained austenite, and martensite. In quenched and partitioned steels (Q&P), the martensite can be "partitioned" wherein carbon in the martensite diffuses into neighboring austenite and can lead to "soft" and "hard" families of martensite. In medium manganese steels, upon which this research will focus, ultra-fine-grained (UFG) microstructures are used to obtain retained austenite at room temperature which will then either transform to martensite, as in TRIP steel, or form twins, as in TWIP steel, when plastically deformed. These TRIP and TWIP effects provide significant work hardening and allow the steel to harden locally, delaying necking and improving ductility. Additionally, alloying medium manganese steels with several

weight percent of aluminum will reduce the density and the loss in strength that would normally accompany aluminum additions is compensated for by TRIP or TWIP. Medium manganese steels therefore offer opportunities to both increase tensile strength and decrease density and are an ideal candidate for use in automotive products.

The microstructures observed in medium manganese steels present a significant challenge in terms of their characterization. Not only does one need to consider the interactions of two or three phases, but significantly different plastic deformation mechanisms in each as well as evolving phase volume fractions due to martensite transformation during plasticity. With a UFG microstructure, mechanical characterization of individual phases is quite difficult. Behavior laws for each phase must thus be determined through a fit of the multiphase composite against macroscopic data rather than against data for each phase separately. Even once the behavior laws are identified and their parameters determined, the interactions between phases must be considered and the kinetics of the TRIP or TWIP effects characterized.

These challenges are not easily surmounted, but provide the opportunity to better understand the interaction of different phases in polycrystals and the effect of mechanical contrast between phases on macroscopic properties. It obliges the refinement of existing characterization techniques to enable the identification of single phase behaviors in multiphase materials, which is not easily achieved at the micron-scale as considered here. In fact, current progress in this area involves combined nanoindentation tests and crystal plasticity simulations to obtain phase behavior laws [1].

This thesis will focus on a medium manganese (Medium Mn) TRIP steel and will seek to achieve the following:

1. Identify and characterize the plastic deformation mechanisms present in each phase of each alloy and relate them to macroscopic behavior.
2. Understand the relationship between fabrication parameters and mechanical behavior, specifically regarding the degree of work hardening.
3. Provide a numerical tool for understanding the behavior of these steels regarding the strain instabilities than can be present.

The thesis will be structured as follows:

- A first chapter will present a bibliographic summary of the deformation mechanisms in steels, the state of the art in research on Medium Mn steels, and a description of Lüders and Portevin-Le Châtelier strain instabilities.
- Initial results of a microstructural and mechanical characterization of the steel are described and the questions motivating the core work of the thesis are presented.

- The methodology by which the TRIP effect and strain instabilities are analyzed are presented. Particular attention is given to the magnetic measurement method of the retained austenite fraction that was developed in this research.
- Results of the characterization of the TRIP effect via magnetic measurements, strain band characterizations using digital image correlation, and strain rate sensitivity measurements are presented with initial commentary.
- A discussion of the obtained results and the origin of the observed differences in TRIP kinetics and the characteristics of strain instabilities is presented.
- The primary conclusions of the work are given alongside perspectives for future work.

Chapter 1

Sommaire

L'imposition de limites de plus en plus strictes sur les émissions de CO2 par les véhicules automobiles nécessite une diminution importante de leur consommation d'essence. Du point du vue du fabricant automobile, cela peut se faire par des changements de conception du châssis et des matériaux utilisés. En fait, la performance du matériau est représentée par le ratio résistance mécanique — masse volumique. Ainsi, un matériau léger comme l'aluminium nécessitera une épaisseur importante pour atteindre la rigidité requise, ce qui aura tendance à augmenter le poids de la pièce finale. Par contre, l'accroissement de la résistance mécanique d'un acier permettra d'en réduire l'épaisseur, ce qui compense sa masse volumique relativement élevée. C'est dans cet objectif que l'industrie de l'acier développe une troisième génération d'aciers à très haute résistance (AHSS, pour Advanced High Strength Steels) dans le but d'améliorer les propriétés mécaniques tout en garantissant une facilité de mise en forme et de soudage. Cette thèse concerne l'un de ces aciers, ainsi que les liens entre sa microstructure et son comportement mécanique.

Le premier chapitre présente les aciers de troisième génération à partir d'une étude bibliographique qui servira de base pour la suite du manuscrit. Il décrit, en particulier, la microstructure et les comportements mécaniques typiques des aciers à moyenne teneur en manganèse (généralement entre 5 et 8% en poids), dit « Moyen Mn » La première partie de ce chapitre donne les bases des mécanismes de plasticité induite par la transformation (effet TRIP) et des phénomènes Portevin-Le Châtelier (PLC) et Lüders. Pour mieux comprendre ces phénomènes, la deuxième partie s'adresse plus particulièrement aux instabilités mécaniques de type PLC et Lüders, ainsi qu'à leurs origines microscopiques. Ces effets sont résumés pour des alliages d'aluminium et des aciers bas carbones et TWIP (plasticité induite par maclage). Finalement, les modes de déformation plastique observés dans les aciers sont décrits. Une attention particulière est portée à l'effet TRIP, à son effet sur le comportement mécanique et aux méthodes utilisées pour caractériser la cinétique de la transformation de phase pendant la déformation.

Le deuxième chapitre continue avec une étude d'un acier Fe-0,2C-5Mn-2,5Al qui est un acier TRIP « Moyen Mn TRIP » formé d'un mélange de ferrite et austénite résiduelle, avec éventuellement une faible proportion volumique de martensite thermique. Son but est de présenter une analyse microstructurale et mécanique afin

d'établir une relation entre la microstructure et le comportement mécanique, et leur dépendance en fonction des paramètres de fabrication. Dans cette étude, le paramètre de fabrication étudié est la température de recuit intercritique qui détermine les proportions des phases initiales et la stabilité de l'austénite résiduelle. Trois températures sont définies, 740, 760 et 780°C, pour un maintien constant de 2 minutes.

Les résultats expérimentaux montrent que, pour les recuits à 740 et 760°C, la déformation se passe de façon très hétérogène. Des instabilités mécaniques dues aux effets Lüders et PLC sont présentes en traction uniaxiale pendant toute la durée de l'essai. Par contre, pour un recuit à 780°C, la déformation est totalement homogène. Il est évident aussi que la température de recuit a un fort effet sur le comportement mécanique en termes d'allongement uniforme et de contrainte maximale. Une éprouvette recuite à 740°C par exemple, peut atteindre 30% d'allongement et 1100 MPa de contrainte maximale, quand une éprouvette recuite à 780°C présente plutôt un allongement de 15% et une contrainte maximale de 1500 MPa. Ces variations ont comme origine une différence de fraction volumique d'austénite résiduelle et de sa stabilité à température ambiante. Plus l'austénite est instable, plus sa transformation en martensite pendant la déformation est facilitée et plus l'écrouissage est rapide. Des expériences complémentaires montrent une apparente sensibilité négative à la vitesse de déformation. Cela est typique des alliages qui présentent un effet PLC, mais c'est également le cas en l'absence de PLC. Ce chapitre se conclut par plusieurs questions, auxquelles la thèse cherchera à répondre :

- Quel est l'effet de la température de recuit sur la cinétique de transformation martensitique ?
- Comment interagissent l'effet TRIP et les bandes de Lüders/PLC ?
- Comment s'explique la sensibilité négative à la vitesse de déformation ?

Le troisième chapitre détaille les méthodes expérimentales mises en œuvre pour répondre à ces questions. Des essais en traction uniaxiale avec corrélation d'images (DIC) sont réalisés pour caractériser les différentes bandes de déformation quand elles sont présentes. Le logiciel Correli TR3 est utilisé, qui régularise le champ de déformation calculé et qui assure ainsi que la solution est mécaniquement admissible.

La cinétique de transformation de phase pendant la déformation est caractérisée par une méthode magnétique. Ce choix permet une haute fréquence de mesure (ici, entre 2 Hz et 10 Hz) et donc des donnés continues et rapides par rapport, par exemple, aux méthodes par diffraction des rayons-X ou des électrons. Cette méthode est décrite en détail, avec une attention particulière à deux corrections par rapport à son utilisation habituelle.

- La première est une correction de l'effet de la contrainte appliquée sur l'éprouvette, qui a une influence marquée sur les propriétés magnétiques. Cette correction est assez simple : comme les résultats concernent uniquement à l'aimantation à

saturation, une correction linéaire est basée sur un coefficient de magnétostriction, ce qui lui confère un sens physique par rapport à d'autres méthodes de correction purement empiriques.

- La deuxième correction prend en compte le fait que les propriétés magnétiques de la microstructure sont hétérogènes, avec la ferrite et la martensite qui sont ferromagnétiques et l'austénite résiduelle qui est paramagnétique. Cette correction s'appuie sur un modèle du type Eshelby pour une inclusion sphérique dans un milieu équivalent homogène pour calculer la localisation du champ magnétique appliquée dans chacune des phases. Cette correction est une nouveauté dans la mesure où elle est appliquée à l'estimation de l'aimantation à saturation ; jusqu'à présente elle n'avait été faite que sur des mesures de susceptibilité magnétique.

Les quatrième et cinquième chapitres décrivent les résultats obtenus par ces deux méthodes, corrélation d'images et mesures magnétiques, et en présente une discussion. Les bandes de déformation sont caractérisées, avec des différences notables entre la première bande (bande de Lüders) et les bandes suivantes. La largeur de la bande et sa vitesse de propagation sont bien moins importantes pour la première bande que pour les autres bandes supposées de type PLC. De plus, la vitesse de déformation et l'incrément de déformation sont bien plus importants dans la première bande. Des graphiques spatio-temporels montre que la première bande – dans tous les cas où elle apparait – est très stable et se propage continument le long de l'éprouvette, alors que les bandes suivantes sont souvent plus perturbées, voire même aléatoires. Ceci confirme la nature et l'origine différentes de la bande initiale et des suivantes : une bande de Lüders à la limite d'élasticité suivie par des bandes de type PLC. Dans le cas du recuit intercritique à 740°C, les bandes PLC se propagent de façon plutôt continue alors qu'elles sont plus aléatoires dans les échantillons recuits à 760°C. Pour le recuit à 780°C aucune bande n'a été observée lors de la déformation des éprouvettes.

La section suivante du quatrième chapitre met en évidence une sensibilité notable du comportement mécanique à la température de recuit intercritique. Des éprouvettes provenant de deux lingots différents censées avoir subi les mêmes recuits à 740, 760 ou 780°C montrent finalement des comportements très différents pour une température de recuit donnée. Pour l'étude de ces aciers, il est donc critique de comparer des éprouvettes qui viennent d'un même lingot.

Les résultats de mesures magnétiques in situ pendant un essai de traction montrent l'effet de la température de recuit intercritique sur la cinétique de transformation de phase pendant la déformation. L'évolution de la fraction volumique d'austénite résiduelle est tracée en regard des courbes de traction pour prouver que, même considérant le fait que toutes les éprouvettes n'ont pas la même teneur initiale en austénite résiduelle, la transformation se produit d'autant plus rapidement que la température de recuit est élevée. De plus, le nombre de points de mesure

obtenus (quelques milliers par essai) permet de distinguer des paliers sur les courbes d'évolution de l'austénite correspondant au passage des bandes de Lüders ou PLC. Ceci ne serait pas possible avec d'autres méthodes basées sur la diffraction (sauf peut-être par diffraction X au synchrotron) et surtout pas dans une quinzaine de minutes par essai comme dans ce travail, vu que l'acquisition des données de diffraction est bien plus lente que l'acquisition des données magnétique. Ce résultat tend à prouver la coïncidence de l'effet TRIP et du passage des bandes de déformation et confirme l'utilité des mesures magnétiques pour doser la teneur en austénite résiduelle.

Comme le couplage entre la contrainte et l'aimantation est corrigée dans ce travail, il était possible de montrer que la transformation martensitique se déclenche uniquement après l'amorçage de la plasticité dans l'éprouvette. Des mesures de l'aimantation en fonction de la contrainte vraie ne montrent aucun changement avant la limite d'élasticité, suggérant que la transformation martensitique est plutôt induite par la déformation que par la contrainte, au moins en début d'essai. Ce résultat est unique car les méthodes classiques de mesure magnétique par ferritescope ne corrigent pas les couplages magnéto-mécaniques.

Pour analyser et comprendre l'origine de la sensibilité négative du comportement en traction à la vitesse de déformation, des essais ont été réalisés à des vitesses de déformation de 10^{-4}, 10^{-3} et 10^{-2} $s{-}1$. Des mesures magnétiques in situ one été également réalisées pendant ces essais pour quantifier l'effet de la vitesse de déformation sur la cinétique de transformation martensitique au cours de la déformation.

L'interprétation de ces données est compliquée par la présence des instabilités mécaniques en forme des bandes de déformation. Néanmoins à partir des cas dans lesquels la déformation se passe de façon homogène, il est possible de déduire que la cinétique de transformation martensitique est ralentie pour les vitesses de déformation élevées. Ceci pourrait être dû à l'échauffement adiabatique plus important quand la vitesse de déformation augmente. Des transitions entre différents types de comportement PLC apparaissent aussi en fonction de la vitesse de déformation. Ceci est surtout évident pour les échantillons recuits à 760°C où le PLC est du type C à 10^{-4} $s{-}1$, puis type B à 10^{-3} $s{-}1$ et disparait finalement à 10^{-2} $s{-}1$. Une carte est proposée dans la discussion qui indique le type de comportement PLC (s'il est présent) en fonction de la température de recuit et de la vitesse de déformation imposée.

La dernière partie expérimentale est consacrée à une quantification de la sensibilité à la vitesse de déformation par essais de traction avec des sauts de vitesse de déformation entre 10^{-4} et 10^{-2} $s{-}1$. La sensibilité « steady state » (c'est-à-dire, une fois que la courbe de traction se stabilise après le pique initiale au moment de l'accélération de vitesse de déformation) dépend fortement de la déformation à laquelle la mesure est faite. Les résultats sont très différents selon que la mesure est réalisée juste après le saut de vitesse (<0,5% déformation) ou après une déformation de 2% après le saut. Les mesures « continues » de l'évolution relative de contrainte

semblent être en accord avec les mesures prises à 2% déformation après le saut de vitesse confirmant donc la sensibilité négative à la vitesse de déformation.

Finalement, un modèle simple est proposé pour comprendre les comportements observés en termes de comportement mécanique des phases et de cinétique de transformation martensitique. Il s'agit d'une simple loi de mélange construite avec l'hypothèse « Iso-Work » pour laquelle il est supposé que le travail mécanique est identique dans chaque phase. Son application sur les cas où la déformation est homogène permet de déduire que les comportements des phases sont tels que la grosse majorité de l'écrouissage vient de l'effet TRIP par l'accroissement de la fraction volumique d'une phase martensitique très dure. Les courbes de traction expérimentales sont alors bien reproduites en utilisant une cinétique de transformation martensitique modélisée à partir de la relation d'Olson et Cohen identifiée à partir des données magnétiques expérimentales.

Le comportement des différents essais sont alors reproduits simplement en changeant les proportions des phases initiales. Ce modèle permet, par exemple, de montrer que l'origine de la bande le Lüders est très probablement dans la ferrite par comparaison avec la littérature en utilisant l'écrouissage estimée dans la ferrite par ce modèle au début de plasticité.

Les données magnétiques sont aussi utilisées pour décrire la cinétique de transformation martensitique dans le cadre du modèle de Ludwigson-Berger qui présente l'intérêt de ne dépendre que d'un seul paramètre ajustable. Dans ce cas, il est montré que la présence ou non de PLC est vraisemblablement liée à la cinétique de transformation martensitique. Cette approche permet de déduire l'existence d'une plage étroite de valeurs du paramètre k de Ludwigson-Berger dans laquelle se fait la transition entre un comportement hétérogène et une déformation homogène : pour les faibles valeurs de k, on n'observe pas de PLC, alors que le phénomène apparaît pour les valeurs plus importantes. Ce résultat est très intéressant pratiquement car il suggère que l'effet PLC pourrait être éliminé avec une composition permettant de contrôler l'instabilité de l'austénite.

Finalement, plusieurs conclusions générales sont déduites de ce travail :

- Des bandes de déformation ont pu être caractérisées expérimentalement en termes de déformation locale et de cinétique de transformation martensitique par mesure magnétique,
- Ces bandes de déformation coïncident avec la transformation martensitique locale,
- La cinétique de transformation martensitique au cours de la déformation est sensible à la température de recuit et à la vitesse de déformation,
- La sensibilité à la vitesse, apparemment négative, résulte d'une interaction complexe entre la cinétique de transformation martensitique, l'échauffement adiabatique, et l'existence éventuelle de bandes de déformation.

Des perspectives sont proposées afin d'identifier des chemins potentiels pour mieux comprendre et quantifier le comportement de ces matériaux en vue d'en optimiser la composition et le procédé de frabrication.

Chapter 2

Literature Review

2.1 Third Generation Advanced High Strength Steels

To provide higher strength, high formability materials for the automotive industry and remain competitive with other materials eg. aluminum for frame components, a third generation of AHSS is being actively researched. The desired properties include an ultimate tensile strength surpassing 1000 MPa and a tensile elongation of 30-40%. The sought properties of third generation AHSS relative to the first two generations is presented in Figure 2.1 [2]. These steels use far less alloy content than the second generation (TWIP) steels, and thus should be cheaper to manufacture and show improved weldability. High strength and high formability would enable automotive manufacturers to achieve further vehicle weight reductions through structural redesign using stronger materials, allowing component thicknesses to be reduced while maintaining rigidity.

Third generation AHSS typically contain 5-15 wt% Mn and up to 0.3-0.4 wt% C [3–5]. This is a stark difference from TWIP steels, which can contain more than 0.5 wt% C and more than 20 wt% Mn [6–8] and as such third generation steels are often referred to as Medium Mn steels. While 2^{nd} generation AHSS are primarily austenitic, 3^{rd} generation steels typically have multi-phase microstructures containing ferrite, retained austenite, and sometimes thermal martensite. The microstructure is generally finer and contains more retained austenite than the first generation of AHSS. It is possible to stabilize austenite at room temperature despite the lower Mn and C content by what has been termed an austenite reversion transformation (ART). The ART process typically consists of hot rolling at austenitizing temperature and quenching followed by cold rolling and an intercritical anneal in the ferrite + austenite domain to revert the quenched martensite to a mixture of ferrite and austenite. During the intercritical anneal martensite is reverted to an ultra-fine-grained (UFG) mixture of ferrite and austenite; this fine grain size allows the austenite to remain metastable at room temperature [9]. The intermediate cold rolling step included before the intercritical anneal will help to further refine the grain size. Figure 2.2 illustrates the ART process for fabricating Medium Mn steels.

While this thesis will deal primarily with Med Mn TRIP (Transformation-Induced

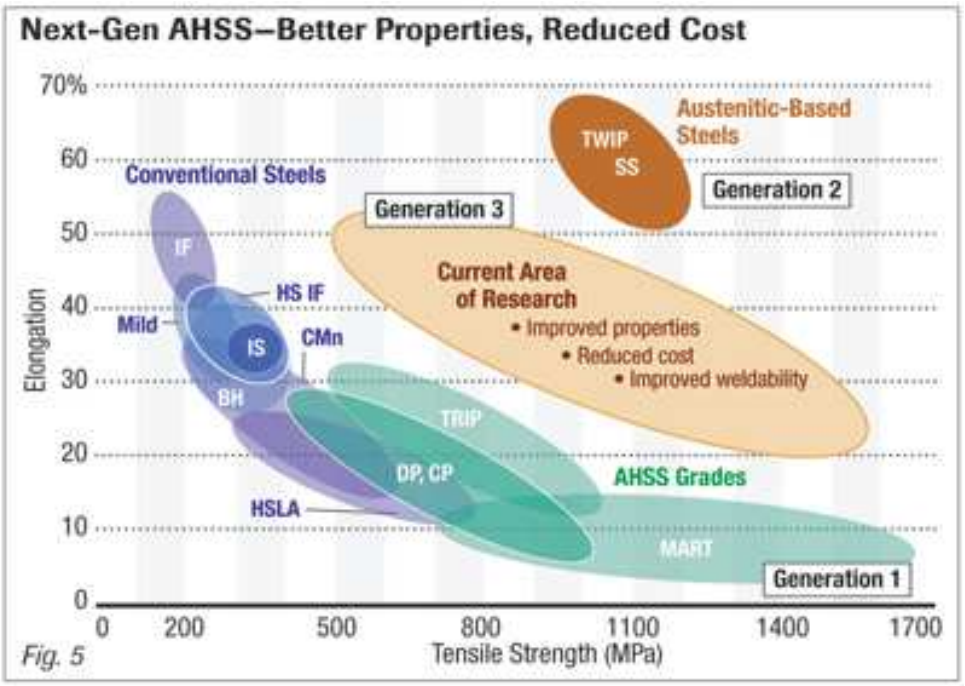

FIGURE 2.1: Different families of Advanced High-Strength Steels (AHSS) mapped with respect to the achievable elongation and tensile strengths for each. The third generation currently being developed provide a middle-ground between the first and second generations and provide several improvements due to the lower alloy concentration used [2].

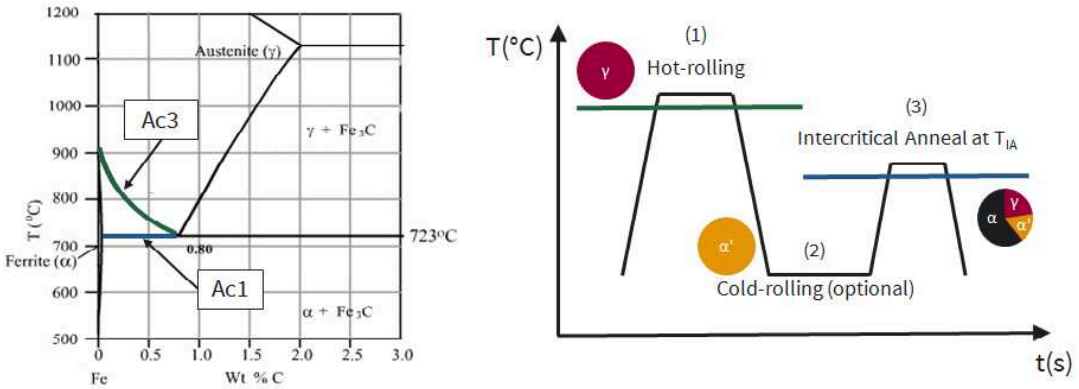

FIGURE 2.2: Medium Mn steels are fabricated by hot-rolling at austenitizing temperature above Ac3 followed by quenching. Cold-rolling in the next step creates a highly-deformed cold-rolled microstructure before annealing to refine the final microstructure. The anneal is carried out in the intercritical region between the Ac1 and Ac3 temperatures and allows ferrite and austenite to form from the previously martensitic microstructure.

Plasticity) steels, it is worth mentioning that there is another group of third generation AHSS called Quenched and Partitioned (Q&P) steels that fall into the same compositional ranges. These steels are also hot rolled at austenitizing temperature and quenched, but they are only quenched to 100-200°C (or otherwise below the martensite start temperature) to generate a partially martensitic microstructure and then reheated to 400-500°C for the partitioning step during which alloying elements, notably carbon, are partitioned from the martensite to the remaining austenite [10]. The alloy is then quenched to room temperature. This results in a steel that contains significant proportions of martensite with some metastable retained austenite. Tensile strengths upwards of 1500 MPa are not uncommon and tensile elongations are on the order of about 10% [11].

2.1.1 Microstructures

Much work has gone into the thermodynamics underlying the microstructural evolution of Medium Mn steels during processing. Here, an emphasis is placed on the result obtained rather than the process by which the different phases are formed. As mentioned previously, an ultra-fine-grained microstructure can be obtained by annealing a hot-rolled, quenched, and cold-rolled sheet that is thus comprised primarily of martensite and bainite. The duration and temperature of the anneal as well as the chemical composition will play critical roles in determining the final microstructure. Each of these will be examined here.

During intercritical annealing, small quantities of carbides such as pearlite that may exist within the microstructure dissolve and form austenite nuclei [12]. Increased annealing temperature or time will result in further dissolution of these carbides as well as higher retained austenite volume fractions. It also, however, results in more grain growth. This is not ideal given that the objective is to obtain a very fine austenite that remains metastable at room temperature. If too much grain growth occurs, the austenite will have partially transformed to martensite during cooling to room temperature. This has been well-illustrated by Li *et al.* in a cold-rolled Medium Mn TRIP steel, as can be seen in Figure 2.3 [13].

To avoid destabilization of the austenite via grain growth for very long anneals, the annealing temperature can be increased or decreased to control the nucleation of ferrite and austenite and thus their volume fractions. Gibbs *et al.* [14] showed that the retained austenite fraction increases with intercritical annealing temperature up until a certain peak after which the austenite destabilizes and large fractions of martensite are obtained. Figure 2.4 shows the results of their ThermoCalc model predictions compared to measured austenite volume fractions. The same drop-off in retained austenite volume fraction at room temperature also occurs if the annealing temperature is too high, as demonstrated by Li *et al.* as in Figure 2.3, so care must be taken to optimize the temperature and duration of the anneal to obtain the desired proportion of retained austenite. The sudden loss of stability could be related to the

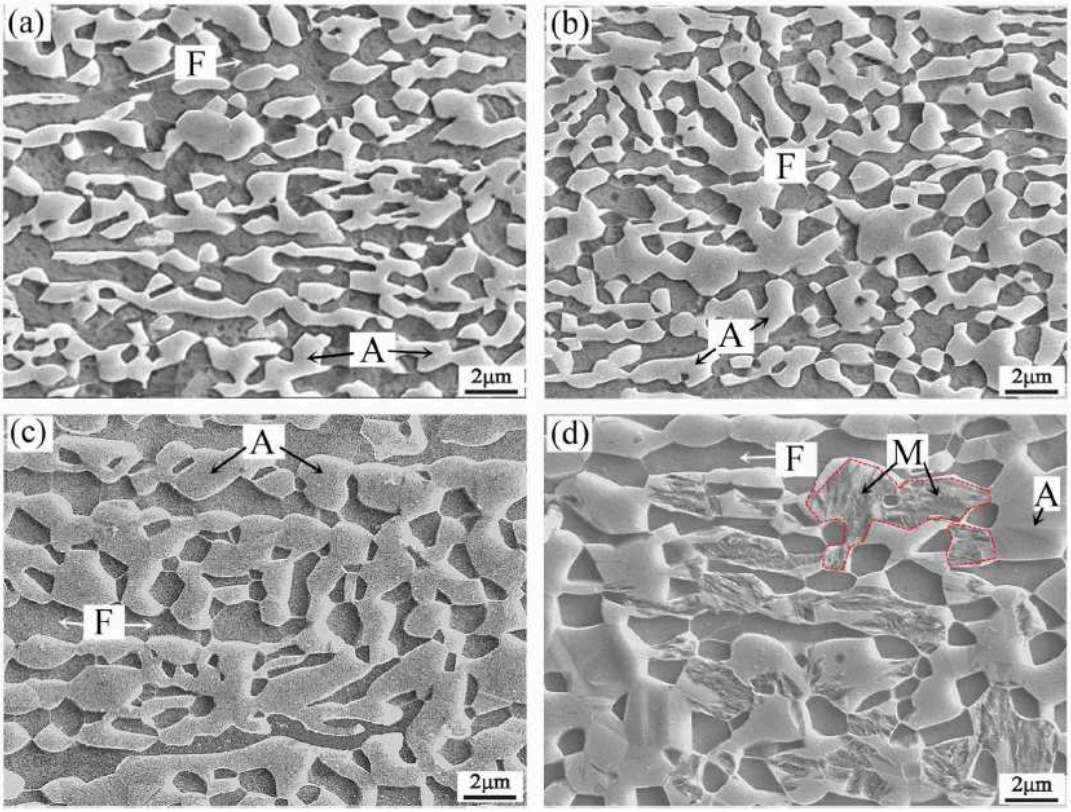

FIGURE 2.3: Microstructures observed in a 0.2C-1.6Al-6Mn Medium Mn steel for intercritical annealing at (a) 600°C (b) 630°C (c) 650°C and (d) 700°C [13]. With increasing annealing temperature, the austenite (A) grain size increases and after a certain point some martensite (M) is obtained at room temperature. Ferrite (F) is also present as a matrix phase [13].

composition of the austenite. It has been shown that the Mn concentration in austenite decreases with intercritical annealing temperature and that the C concentration shown a maximum at intermediate annealing temperatures, as shown in Figure 2.5, likely due to the increase in grain size for higher annealing temperatures. The peak in the retained austenite fraction could then be related to the peak in the stability of the austenite as induced by the combined effects of C and Mn.

The composition of the retained austenite is important in that it will alter not only the volume fraction of retained austenite after cooling, but also its stacking fault energy. It has been shown that the stacking fault energy is correlated to the active plastic deformation mechanisms in the steel [8, 15], though no direct link had been established between SFE and the active deformation mechanism. This is illustrated in Figure 2.6 in which the authors suggested that as the stacking fault energy (SFE) decreases, the deformation mode changes from dislocation slip to twinning induced plasticity (TWIP) to transformation induced plasticity (TRIP). Given that the SFE is heavily influenced by composition via substitutional defects in the crystal lattice, the concentrations of C and Mn in the austenite will play a critical role in determining which deformation modes are active for a given alloy.

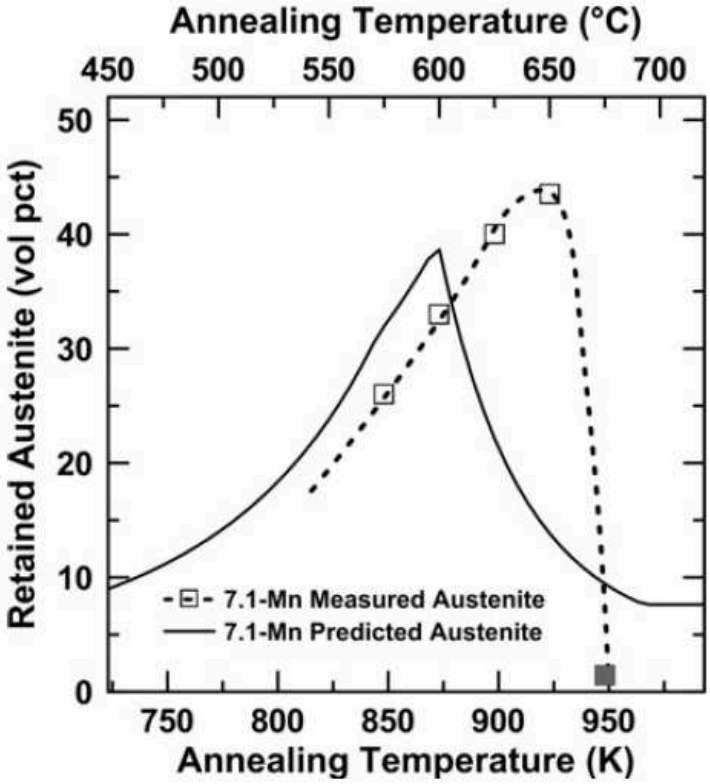

FIGURE 2.4: The retained austenite volume fraction obtained upon cooling to room temperature shows a peak for intermediate intercritical annealing temperatures in a 0.1C-7.1Mn steel. As the annealing temperature increases, the M_s temperature of the retained austenite increases above room temperature and allows some thermal martensite to form when cooled to room temperature [14].

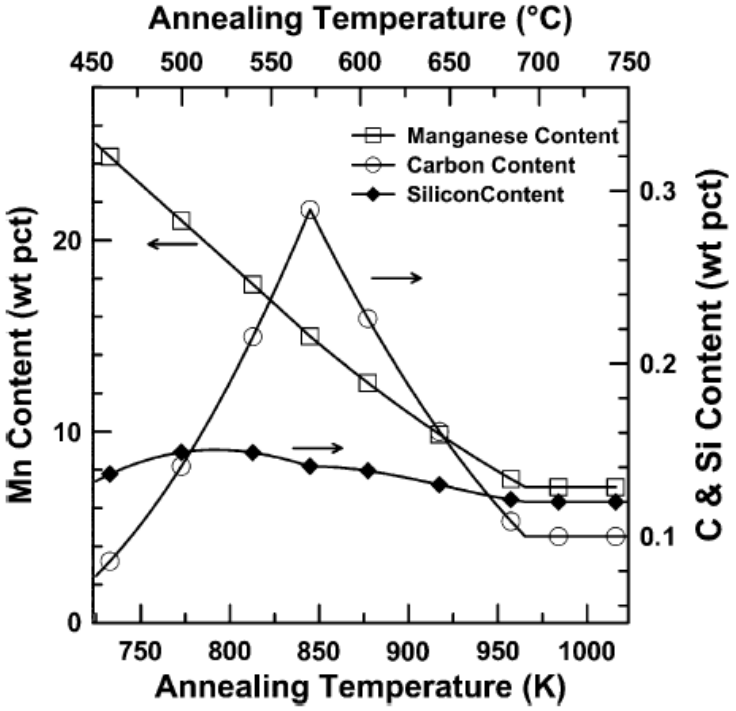

FIGURE 2.5: During intercritical annealing, the concentrations of stabilizing alloying elements in the retained austenite were modified. The Mn content decreased with increasing annealing temperature and the C concentration peaked at intermediate temperatures. The appearance of martensite in the initial microstructure in a 0.1C-7.1Mn steel steel roughly corresponds to the temperatures after the C concentration peak where both C and Mn concentrations are low [14].

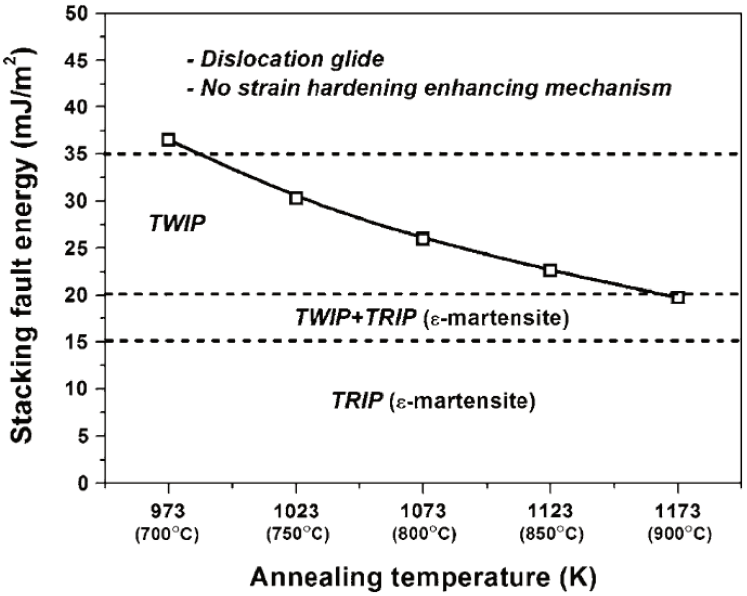

FIGURE 2.6: The active primary deformation mechanism in the retained austenite is related to the stacking fault energy (SFE) of the austenite. It is hypothesized that as the SFE decreases, the plastic deformation mechanism changes from dislocation slip to TWIP to TRIP. The SFE depends on the concentration of alloying elements and is thus controlled via the intercritical annealing temperature [15].

Some efforts have been made to produce "low density" steels by adding several weight percent of Al to a Medium Mn composition. The addition of aluminum can provide a density reduction of up to 10% via the substitution of Al atoms onto Fe lattice sites in significant proportion (for example, 5 wt% Al in pure Fe would give about 9.8 at% Al). While it does result in weight reductions, the addition of aluminum is also a ferrite stabilizer and will affect the final microstructure. It has been previously observed that the addition of enough aluminum will result in a microstructure that consists of large δ-ferrite bands with a UFG mixture of α-ferrite and austenite between the bands, as shown in Figure 2.7 [16]. This will also, obviously, have an effect on the mechanical properties of the steel.

The mechanical properties of the steel will directly depend on which deformation mechanisms are active at a given time—in particular the UTS and tensile elongation. For example, TWIP steels are known to exhibit very high tensile elongations due to the local hardening induced by twinning that delays the mechanical instability that leads to necking. In TRIP steels, the rate of strain-induced martensite transformation directly determines the hardening rate of the steel and its UTS. Martensite can also delay necking, though it is less effective than twinning as the martensite phase will not accommodate much plastic strain compared to ferrite or austenite.

Given the critical role that the intercritical anneal plays in the determination of the phase volume fractions in the final microstructure and their composition, it follows that the annealing time and temperature will also strongly influence the mechanical properties of the steel.

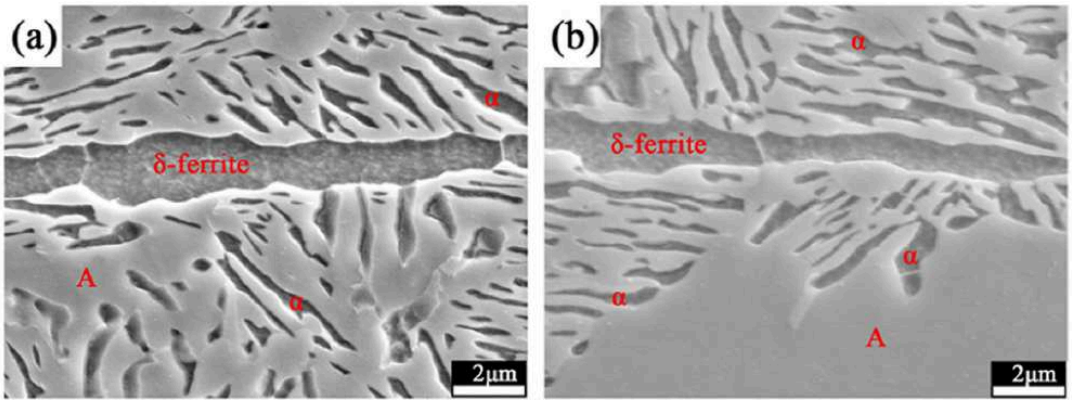

FIGURE 2.7: When higher concentrations of Al are added, it is possible for large δ-ferrite bands to form in the microstructure between regions of austenite (A) and ferrite (α) [16].

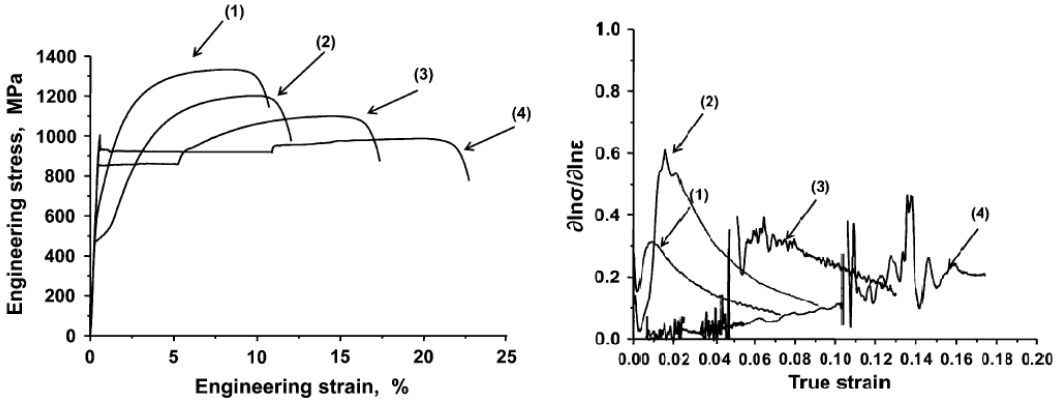

FIGURE 2.8: Changing the intercritical annealing temperature in a 0.05C-6.1Mn-1.5Si steel affected the stability of the retained austenite and thus the mechanical behavior. The stress-strain curves (left) and strain hardening curves (right) showed significant differences for intercritical annealing at (1) 700°C, (2) 680°C, (3) 660°C and (4) 640°C [17].

2.1.2 Mechanical Properties

Modifications to the annealing temperature and time will alter the stability of the retained austenite and thus heavily influence the mechanical properties of the steel. By changing the composition of the austenite, the deformation mechanism can be predetermined and its associated kinetics controlled. That is, by carefully optimizing the chemical composition and annealing parameters, one can make a steel that will plastically deform by a TRIP or TWIP with the desired transformation/twinning rate. It has been shown by [17, 18] that both the annealing temperature and the duration of the anneal have a significant impact on the resulting mechanical properties of the steel, as can be seen in Figures 2.8 and 2.9. This is a direct result of the partitioning of alloying elements between the ferrite and retained austenite and the associated modification of the stability of the austenite.

It is interesting to note, particularly in Figure 2.8, the enormous difference in

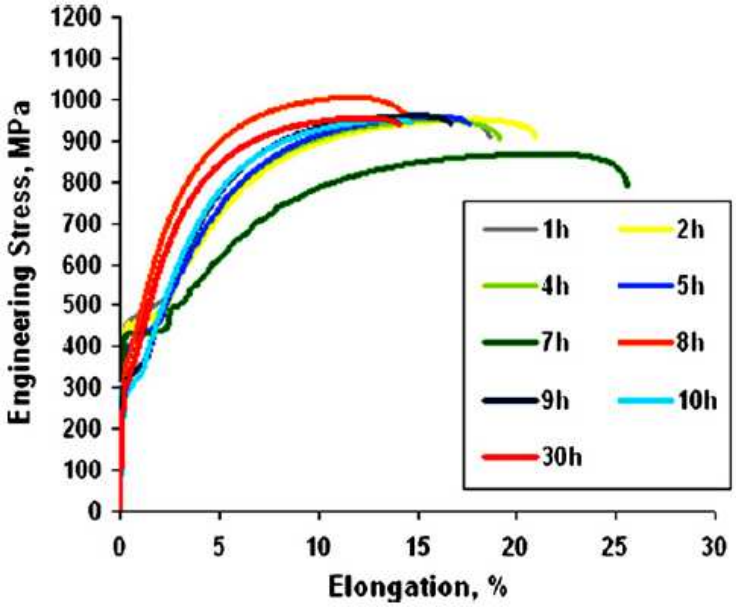

FIGURE 2.9: The annealing time also affected the mechanical response of a 0.09C-4.6Mn-3Si steel, as illustrated here for varying lengths of intercritical annealing at 670°C [18].

mechanical properties resulting from a change in annealing temperature of just a few degrees Celsius. The UTS in the 0.05C-6.1Mn-1.5Si steel studied by Lee *et al.* increased by 300 MPa and the elongation decreased by half just from a difference of 60°C in the intercritical annealing temperature. The work hardening rate also changed significantly from one temperature to another, with sharp increases in work hardening occurring at different levels of true strain. This is due to variations in the onset of TRIP due to varying retained austenite stability.

Also of interest are the long yield point elongation phenomena that are present in the two samples annealed at lower temperatures. The bands are the result of a form of static strain aging referred to as Piobert-Lüders bands (or often simply Lüders bands) and have been observed previously in ferritic steels [13, 19, 20]. When dislocation cores become pinned by interstitial C atoms, a barrier to dislocation slip is created wherein a certain stress is required to free the dislocation and allow plastic deformation to occur. This pinning results in an increase in yield strength, followed by a propagative macroscopic strain band that traverses the entire tensile specimen after which point the strain generally becomes homogeneous.

In the case of Lüders bands, the pinning occurs just once. However should the interstitial C be sufficiently mobile, they can "overtake" the mobile dislocations and pin them repeatedly, resulting in a series of strain bands than can either be stationary or propagative. This is referred to as dynamic strain aging or the Portevin Le-Châtelier (PLC) effect. It can occur in bcc phases (eg. ferrite) at temperatures above about 200°C, but in fcc phases (austenite) it can occur at room temperature [21]. This effect is frequently observed in Al alloys for example [22], and has been frequently observed in Medium Mn steels as well [17, 23, 24] as demonstrated in Figure 2.10.

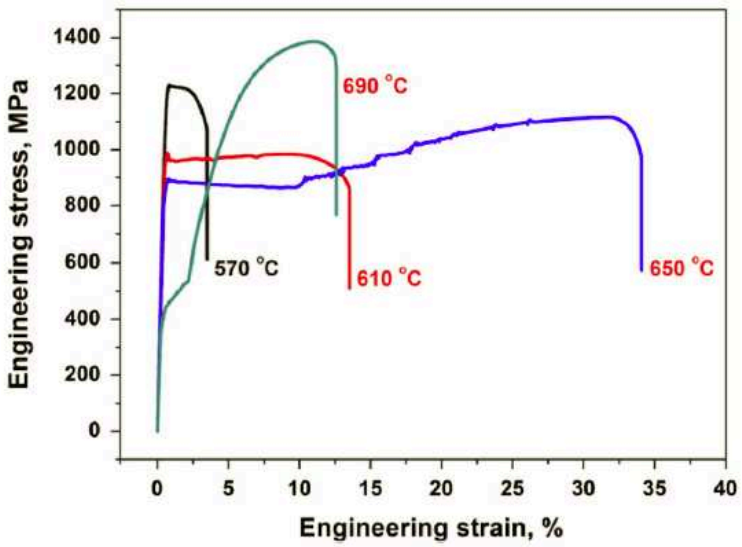

FIGURE 2.10: For a 0.17C-6.5Mn-1.1Al Medium Mn alloy, long Lüders plateaus and the PLC effect were observed for lower inter-critical annealing temperatures as in the samples annealed at 610°C and 650°C, though the cold rolled microstructure was not completely recovered in the sample annealed at 570◦C so it was much harder and more brittle than the others [24].

An understanding of these strain localizations is critical because the TRIP and TWIP phenomena are associated with plastic strain, so the presence of bands will alter the kinetics of TRIP and TWIP. Thus, if one seeks to optimize the mechanical properties of a Medium Mn steel, it is necessary to understand the Lüders and PLC phenomena in order to be able to quantify their influence on TRIP or TWIP.

It has recently been shown that even when Lüders plateaus are extremely long (about 10% strain), the Lüders strain can be greatly reduced by controlling the microstructure [25]. In the case of an UFG Medium Mn TRIP steel, an elongated lamellar microstructure seems to be desirable as it provides a grain-scale deformation that is more favorable than globular grains in terms of reducing the Lüders strain. This is illustrated in Figure 2.11 where the Lüders strain was reduced from about 10 % to 2-3% by the application of an additional heat treatment to modify the grain morphology. This same method was applied for several different samples annealed at different temperatures, shown in Figure 2.12, and the trend remained the same: lamellar grains resulted in a shorter Lüders plateau.

2.2 Strain Localizations—Lüders and PLC Effects

2.2.1 Lüders Bands in Low-C Steels

The Lüders phenomenon is well-known and often occurs in low carbon steels. It is a form of static strain aging wherein, as previously mentioned, interstitial carbon pins dislocations and increases the mechanical energy necessary to initiate plastic deformation. As shown in Figure 2.13a, the effect manifests itself in the form of a

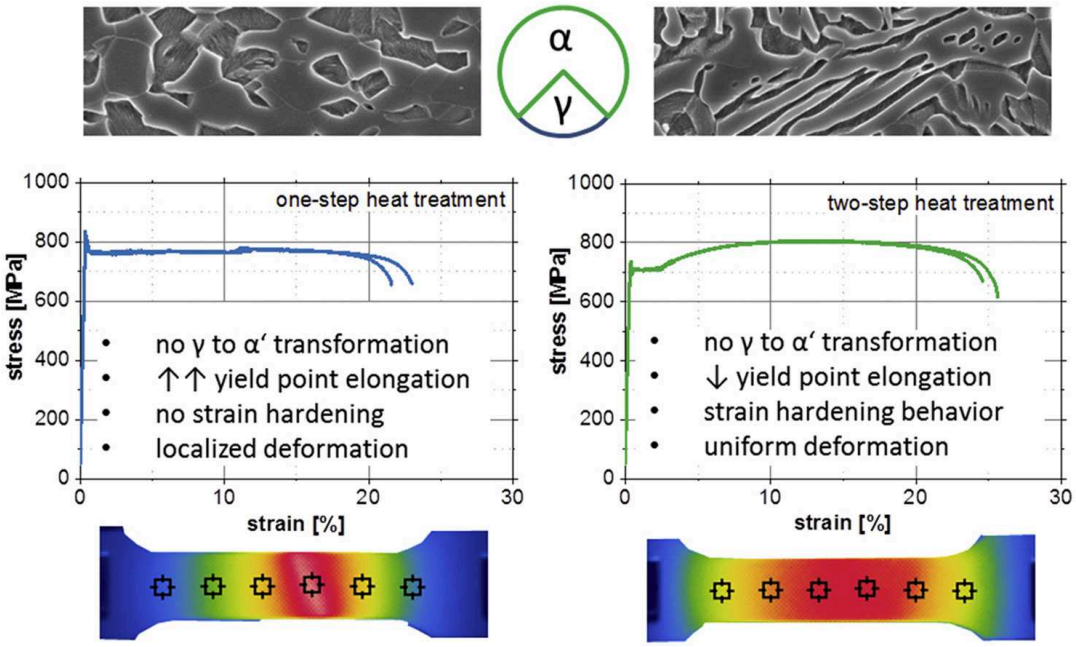

FIGURE 2.11: A two-step intercritical anneal was applied to a 0.1C-6.4Mn steel to greatly reduce the length of the Lüders plateau by forming a lamellar rather than globular microstructure [25].

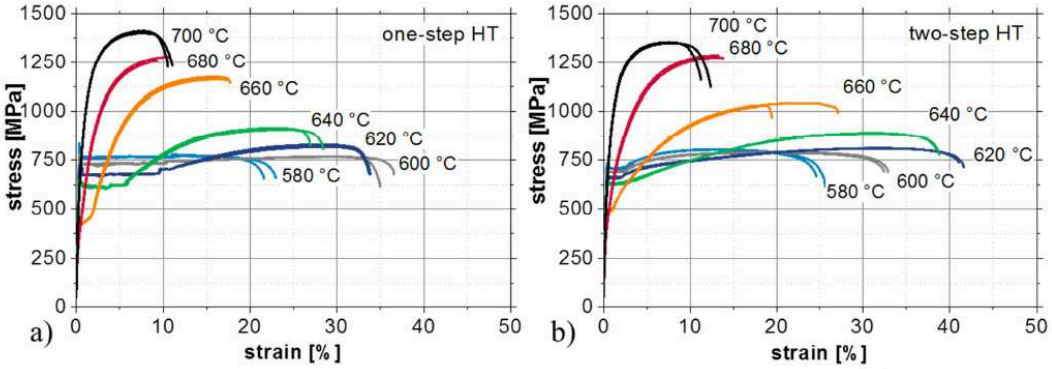

FIGURE 2.12: The two-step intercritical anneal, when applied to a 0.1C-6.4Mn Medium Mn TRIP steel, had a slight softening effect and either greatly shortened or eliminated the Lüders plateaus that existed in samples annealed only once at temperatures below 660°C [25].

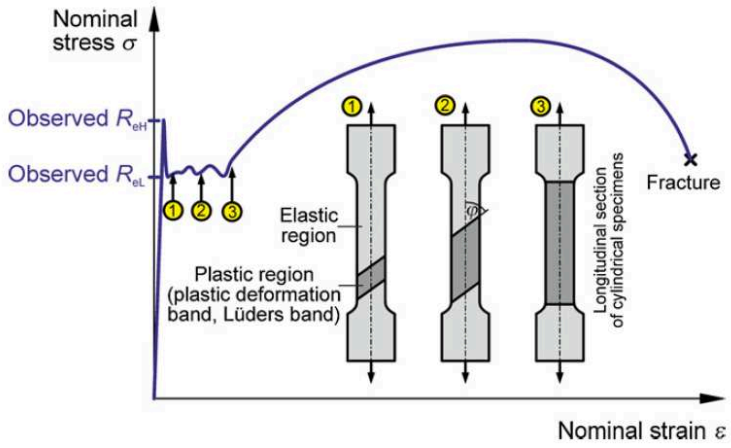

(A)

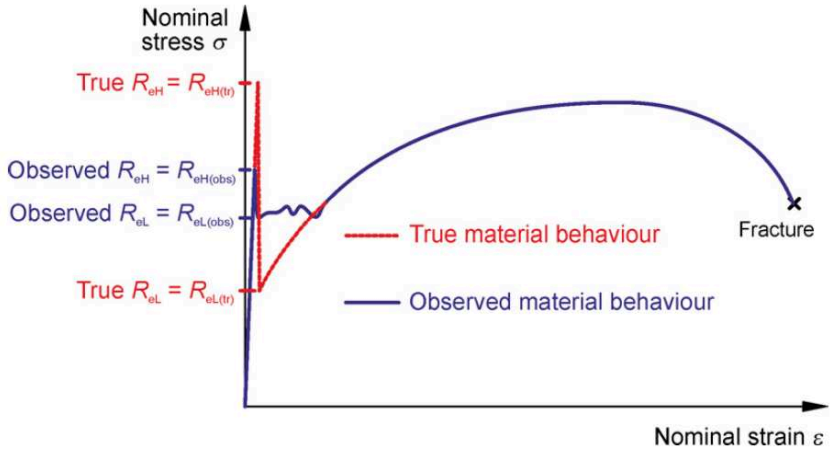

(B)

FIGURE 2.13: (A) The yield point elongation observed in some Medium Mn steels is due to the localization of strain in a Lüders band that propagates across the tensile length of the sample. (B) This behavior is the result of static strain aging that increases the yield stress and creates a plateau with a strain necessary to obtain the stress-strain state corresponding to the case where static strain aging does not occur [26].

macroscopic Lüders band that propagates across the sample at a constant stress. This results in a plateau in the tensile curve that can continue for several percent of plastic strain. The Lüders strain is hypothesized to correspond to the intersection of the observed mechanical behavior and the "true" tensile behavior of the material when yielding is continuous, as illustrated in Figure 2.13b by Schwab *et al.* [26]. The strain increment provided by the Lüders band depends on the mechanical behavior of each phase and notably this "true" yield stress of the material. The primary concern of end-users with respect to Lüders banding is the surface defects the band can create on a component. If the Lüders strain is reduced, these surface defects are easier to avoid and are less problematic in forming operations, so control of the Lüders strain is highly desirable.

It has been shown that the Lüders strain is correlated to the work hardening

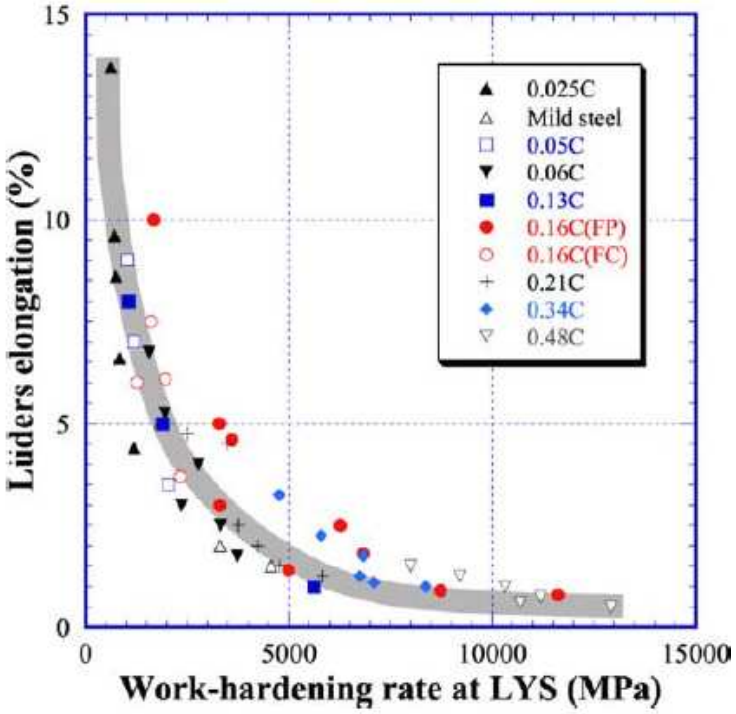

FIGURE 2.14: It was shown by [27] for C-Mn steels that, regardless of the carbon concentration (and thus availability of interstitial C to pin dislocations) the Lüders strain was directly related to the rate of work hardening at the lower yield stress.

rate at the lower yield point. Regardless of the carbon concentration, a low work hardening rate corresponds to a high Lüders strain, as seen in Figure 2.14 [27]. This is of interest in the current case because should the TRIP effect in a Medium Mn steel fail to provide enough work hardening, the Lüders plateau (if present) would be very long. Thus the Lüders strain should be linked to the stability of the retained austenite and to its transformation rate as well.

Evidently, since the underlying microscopic mechanism for Lüders bands is the impingement of dislocations by carbon atoms, the carbon concentration is of importance in determining the characteristics of the Lüders behavior. It is important, however, that the carbon be on interstitial sites and not tied up in carbides, so the Lüders effect is typically seen at lower levels of carbon. Johnson *et al.* [28] showed, as in Figure 2.15, that increasing concentrations of C resulted in lower Lüders strains based on experimental data from [27] and a model developed by [29].

2.2.2 Portevin-Le Châtelier Bands

While Lüders bands are most commonly seen in bcc alloys, there is another localization phenomenon that can occur in fcc alloys. The Portevin Le-Châtelier (PLC) effect (sometimes called dynamic strain aging) is, like the Lüders effect, the macroscopic manifestation of an interaction between dislocations and solute atoms [30]. PLC is referred to as a type of dynamic strain aging because, contrary to Lüders, the

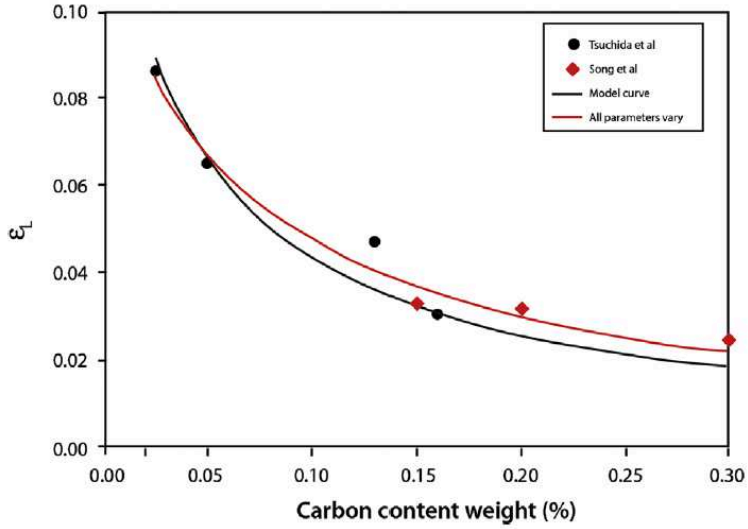

FIGURE 2.15: The carbon concentration in low C steels does modify the Lüders strain slightly as shown here by [28] where an increase of the concentration of C from 0.05 wt% to 0.16 wt% led to a 50% decrease in the Lüders strain. This decrease could be related to either solution strengthening of the ferrite or carbon being consumed by carbides rather than remaining in solid solution.

pinning effect occurs continuously throughout deformation. Dislocations become pinned and a certain mechanical energy is needed for them to unpin and become mobile again, at which time a sharp stress relaxation occurs as this stored energy is released. However, the now-mobile dislocations are soon re-pinned by solute atoms and the stress barrier must once again be overcome. Additionally, obstacles to dislocation motion can permit solutes to diffuse into dislocation cores and re-pin the dislocation, such as nanoprecipitates [31], or grain boundaries [32]. The unpinning and re-pinning occurs over a characteristic reloading time which depends on the defect type and strain rate, among other parameters. This continuous pinning-unpinning process leads to distinct serrations in the tensile curve as illustrated by Jiang *et al.* in Figure 2.16 [33].

Materials that undergo PLC often exhibit a negative strain rate sensitivity. That is, increasing the applied strain rate will decrease the UTS rather than increase it as in materials with a positive strain rate sensitivity. This is shown, for example, by Zavattieri [34] in the case of a high Mn austenitic TWIP steel. Figure 2.17 shows the mechanical response of this steel at three different crosshead displacement rates. Varying the crosshead speed will vary the strain rate in the sample, but because the displacement rate is maintained constant, the strain rate will decrease slightly over the course of the test (hence the use of crosshead speed rather than strain rate in Figure 2.17). It is quite clear that when the crosshead speed is increased, the maximum stress decreases by several percent. Increasing the applied strain rate will decrease the reloading time and accelerate the propagation speed of the band [30]. Bian *et al.* [35] showed that increases in the applied strain rate will also result in increases of the stress amplitude of pinning-unpinning cycles, as shown in Figure

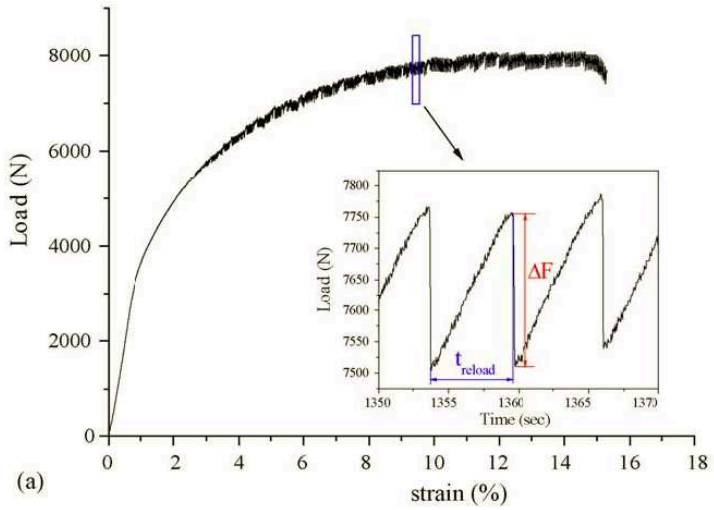

FIGURE 2.16: The serrations observed in the tensile curves of materials that exhibit PLC are directly related to the force required to unpin dislocations (ΔF) and the incubation time between pinning and unpinning (t_{reload}) [33].

2.18.

Higher deformation temperatures also influence PLC. Since the bands are the result of dislocation unpinning avalanches, the mobility of both dislocations and obstacles are important in determining the time between an unpinning event and the subsequent re-pinning. Dislocation motion is obviously aided by increases in temperature. Solute atoms can pin dislocations more effectively at higher deformation temperatures because their diffusivity within the parent lattice is increased. Previous experiments [22] have demonstrated this in an Al-Mg alloy, as shown in Figure 2.19, where deformation of a sample cooled in a mixture of ethanol and dry ice resulted in a complete loss of PLC. Additionally, Swaminathan *et al.* performed a temperature effect study on Hastelloy X, in which chromium carbide nanoprecipitates can form [31]. As illustrated in Figure 2.20, they showed that not only did increasing the deformation temperature result in the appearance of PLC, but further increases led to a change in the type of PLC band from propagative (type A) to a mixture of propagative and stationary bands (type A+B).

PLC bands are often characterized using digital image correlation (DIC). The parameters of interest are generally the band width, band propagation velocity, and strain rate in the band relative to the applied strain rate. It is important then, to understand the trends in these parameters in materials that exhibit PLC if one is to determine whether the bands in a different material are PLC bands or something else.

Shabadi *et al.* explored the effect of sample orientation relative to the rolling direction on PLC band parameters in an Al-Cu alloy [36]. As shown in Figure 2.21, they demonstrated that the band width increased slightly with increased strain, that the band velocity decreased with strain, and that the band angle relative to the load direction remained roughly constant. The sample orientation had a negligible effect

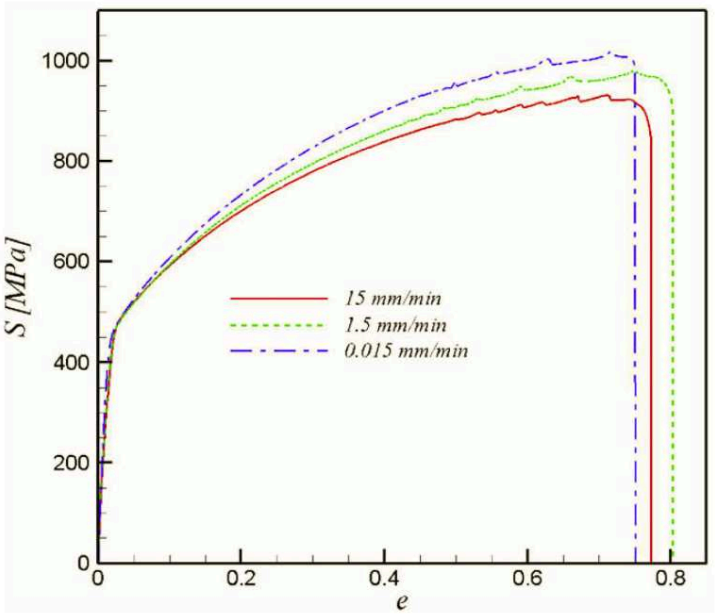

FIGURE 2.17: Materials susceptible to PLC often have a negative strain rate sensitivity (SRS) and will soften at higher strain rates as shown here for a 0.6C-17Mn austenitic TWIP steel [34].

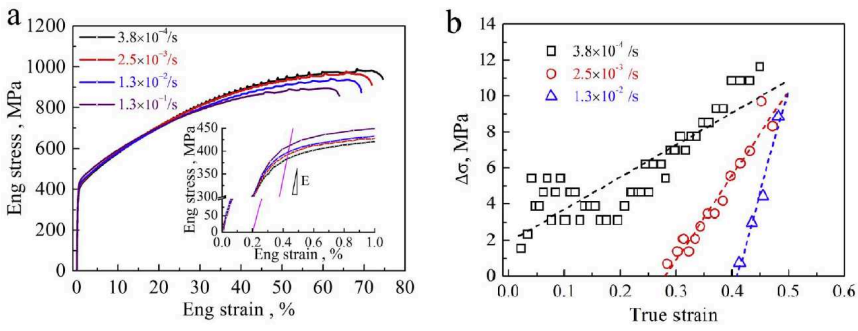

FIGURE 2.18: The applied strain rate can also affect the initiation strain for PLC and the stress intensity of the serrations observed in tensile curves as demonstrated here for a 0.6C-23Mn TWIP steel where $\Delta\sigma$ refers to the unpinning stress [35].

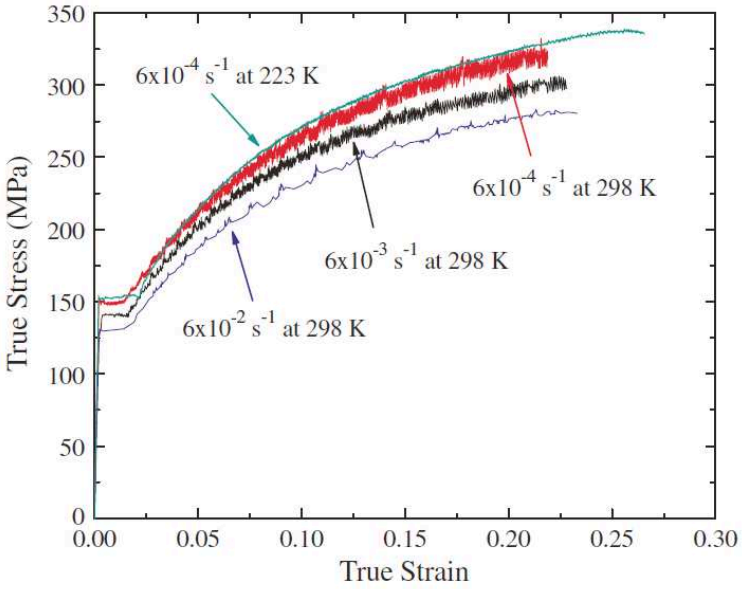

FIGURE 2.19: The presence of PLC is dependent on the deformation temperature, as shown here by [22] for an Al-Mg alloy where PLC disappears altogether when the sample is deformed at -75°C.

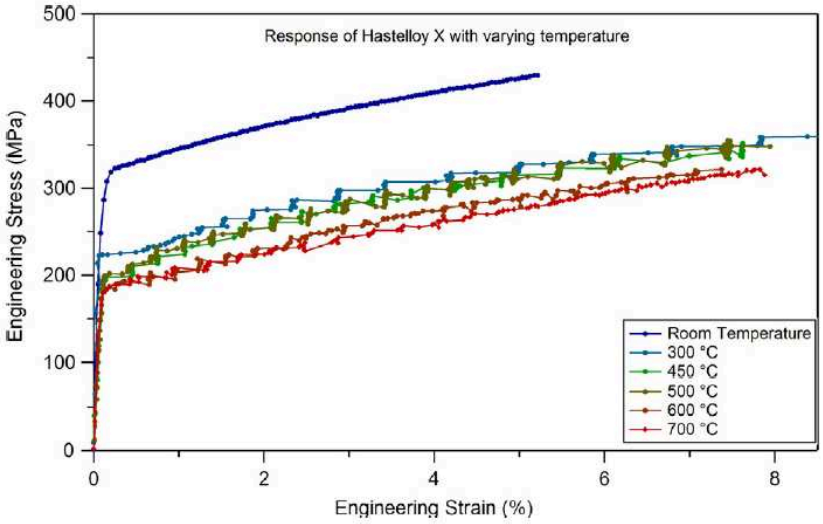

FIGURE 2.20: Increasing the deformation temperature can change the type of PLC observed. Swaminathan *et al.* [31] showed that no PLC was observed at room temperature in nickel-based Hastelloy X, but type-A propagative PLC appeared at 300°C and changed to a more random mixture of type-A and type-B as the temperature was increased to 700°C.

on these properties. Initially, the band propagation speed was relatively high, but rapidly decreased. The rate of decrease slowed down after the first few bands and continued roughly linearly throughout the rest of the experiments.

This trend in band velocity was confirmed by Bian *et al.* [35] for several different strain rates. Additionally, they showed that for a given sample geometry and material composition, this decrease in band speed does not depend on the applied displacement rate. That is, when the band speed ν_B is normalized by the crosshead speed ν_C, the ratio ν_B/ν_C as a function of strain produces the same result for tests at all crosshead speeds. Figure 2.22 suggests that the crosshead speed does not change the mechanism by which the band propagates, but simply accelerates its displacement.

The most commonly used and often easiest method of characterizing PLC is via the strain rate sensitivity parameter as calculated for tensile tests with strain rate jumps. Should the applied strain rate be increased from $\dot{\epsilon_1}$ to $\dot{\epsilon_2}$, the strain rate sensitivity can be calculated by

$$m_{ss} = \frac{\Delta log(\sigma)}{\Delta log(\dot{\epsilon})} \tag{2.1}$$

where $\Delta log(\sigma)$ is the stress difference between the steady state behavior at $\dot{\epsilon_2}$ and the extrapolated stress value at that strain level if the strain rate had remained at $\dot{\epsilon_1}$.

As previously shown, materials that undergo PLC very often have a negative strain rate sensitivity. Therefore, one would expect m_{ss} to be negative in these materials. It can be seen in Figure 2.23 that m_{ss} in an Al-Mg alloy is negative and remains constant with the progression of strain. However, if the testing temperature is altered, the strain rate sensitivity parameter can either decrease or increase and become positive. In the case of Picu *et al.*'s results in Figure 2.23, the sudden sign change in m when the temperature was increased to 50°C was explained by a change in the activation energy for PLC with increasing temperature [37].

2.3 Deformation Mechanisms in Steels

The prediction of mechanical properties for a given microstructure necessitates an understanding of the plastic deformation mechanisms that can be activated in a steel. Evidently, one must also be able to predict which mode is active, though this is quite complex and would likely be done using a correlation with the stacking fault energy of the retained austenite as the thermodynamic prediction of the activation of different mechanisms is a laborious undertaking. This section will provide an overview of the primary deformation mechanisms observed in the third generation of AHSS.

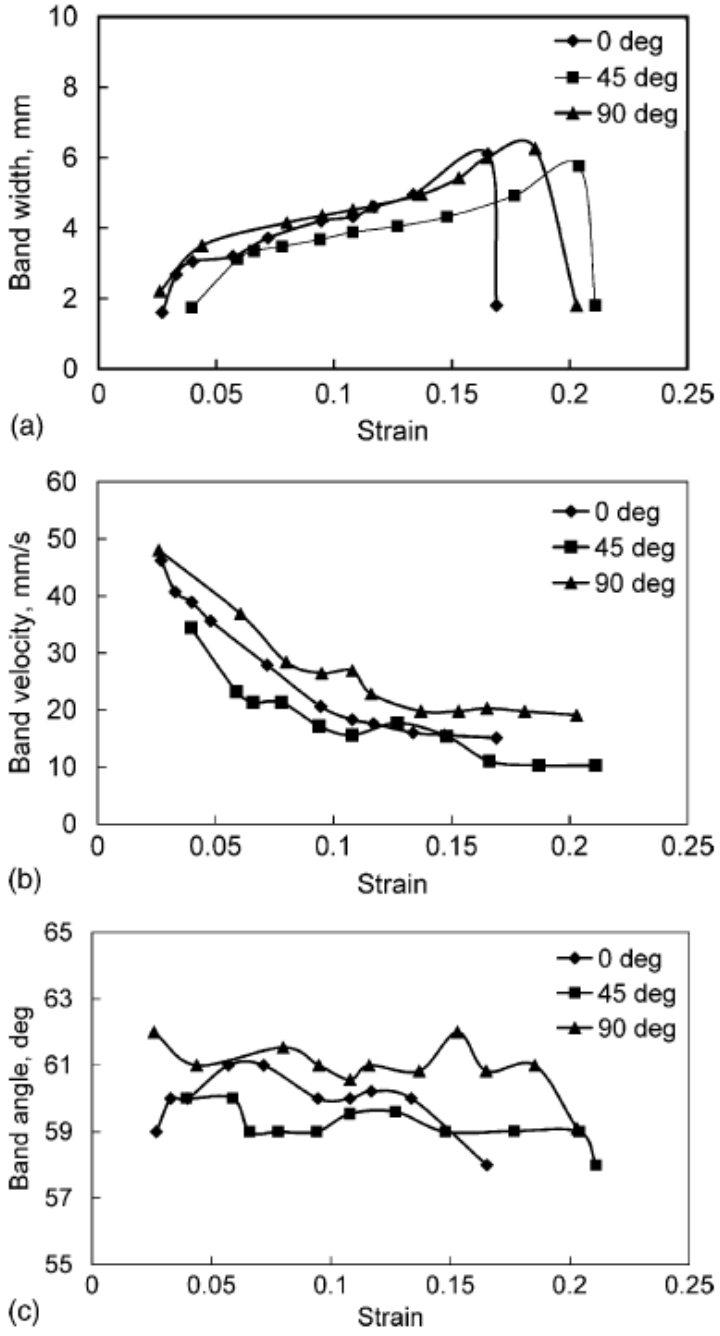

FIGURE 2.21: Variation of PLC band parameters in Al-Cu alloy AA2219. The parameters did not change significantly for different strain directions relative to the rolling direction. Band width was seen to increase with strain, propagation speed decreased with strain, and the band angle relative to the loading direction was more or less constant [36].

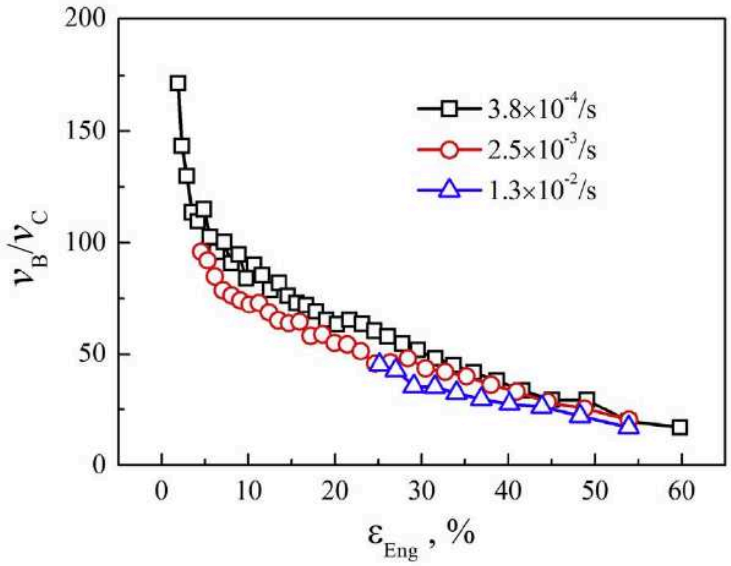

FIGURE 2.22: The propagation speed of PLC bands relative to the crosshead displacement speed was shown by Bian *et al.* in a 0.6C-23Mn TWIP steel[35] to initially decrease sharply, then converge to a linear decrease with increasing strain. This was true for three strain rates of three different orders of magnitude, suggesting that the strain rate affects only the velocity itself and not the velocity relative to the crosshead displacement.

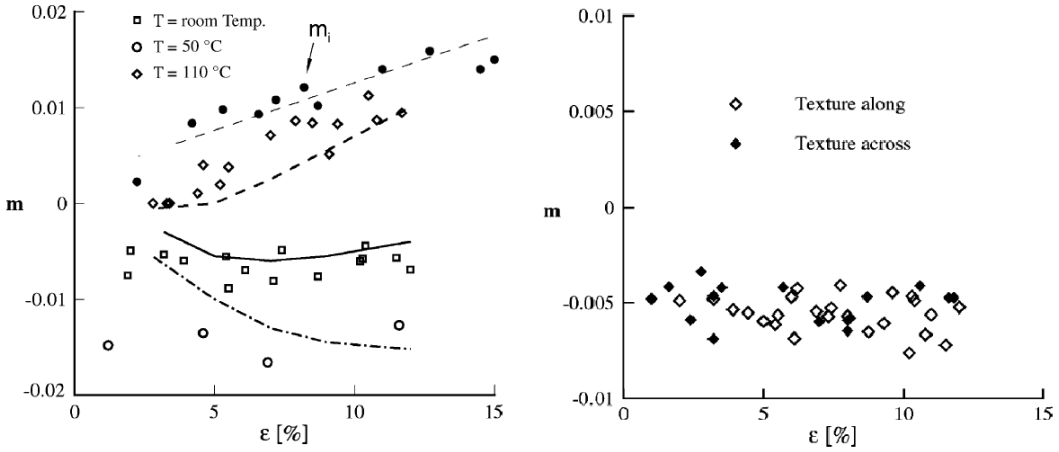

FIGURE 2.23: The SRS in an Al-Mg alloy was shown to be negative and constant with respect to strain in experiments performed by Picu *et al.* [37]. The deformation temperature, however, had an effect on the SRS with STS initially decreasing but then increasing as temperature was increased to 50°C and 110°C.

TABLE 2.1: Slip Systems in Iron

Phase	Plane	Direction	Total Slip Systems
austenite (fcc)	{111}	<110>	12
ferrite (bcc)	{110}	<111>	24
	{112}	<111>	

2.3.1 Dislocation Slip

If one were to strain a single-phase ferritic steel, plastic deformation would occur by dislocation slip. Pre-existing dislocations in the microstructure of the steel require an energy input to displace and will only become mobile once enough elastic mechanical work has been done. Upon yielding, dislocations begin to "slip" along certain crystalline slip systems in order to accommodate the deformation that is being induced by continued straining of the material. These slip systems are given in Table 2.1 for bcc and fcc systems (respectively, ferrite and austenite in steels). Which of these slip systems are activated depends on the resolved shear stress on that slip system. The resolved shear stress is calculated as

$$\tau = cos\psi \cdot cos\Theta \cdot \sigma \tag{2.2}$$

where ψ is the angle between the slip direction and the direction of the applied load, Θ is the angle between the slip plane normal and the direction of the applied load, and σ is the applied tensile stress. The factor $m = cos\psi \cdot cos\Theta$ is referred to as the Schmid factor and provides the ratio of the tensile stress that is resolved on a given slip system as a shear stress. The Schmid factor varies between 0 and 0.5. It can be related to the yield stress of a material by the relation

$$\tau_c = m_{max} \cdot \sigma_y \tag{2.3}$$

where m_{max} is the maximum Schmid factor among all slip systems for a given load geometry, σ_y is the observed yield stress, and τ_c is the critical resolved shear stress (CRSS) to initiate plasticity on that slip system. This is the shear stress needed to activate the slip system with the maximum Schmid factor, but as the applied stress increases other slip systems may also be activated.

On its own, dislocation slip provides no hardening. If there are no interactions between mobile dislocations, a material that deforms purely by dislocation slip could even be perfectly plastic with no hardening at all. However, dislocations can become pinned by inclusions and grain boundaries (which would affect the yield stress), or other dislocations (which would affect work hardening, especially as new dislocations are generated over the course of plasticity). The resulting restriction of dislocation motion increases the stress required to provide enough dislocation movement to accommodate the applied strain and will thus result in work hardening of the material. Slip on several adjacent parallel crystalline planes with increasing strain can result in the formation of slip bands which create observable

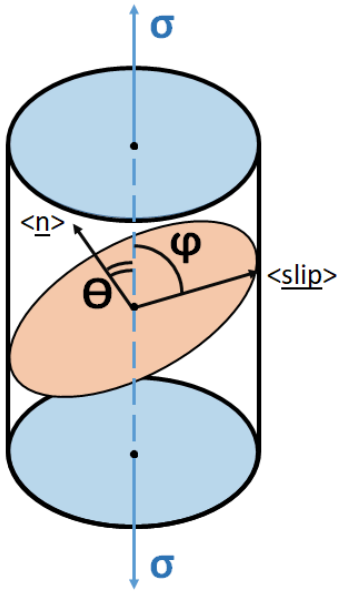

FIGURE 2.24: The shear stress on a given system depends on the angle between the slip plane normal and the load direction (θ) and the angle between the slip direction and the load direction (ψ).

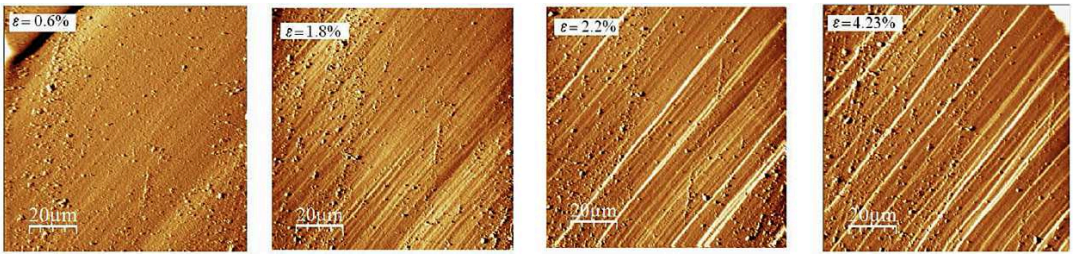

FIGURE 2.25: As strain increases in a grain, slip on neighboring planes can result in the formation of slip bands. Shown here by Kahloun *et al.* in ferrite, these bands are observable macroscopically and create surface roughness [38].

surface roughness in a grain, as shown in Figure 2.25 [38]. The separation of a dislocation into partial dislocations can lead to planar slip, as illustrated in Figure 2.26 by Wang *et al.* [39].

2.3.2 Twinning-Induced Plasticity (TWIP)

In fcc and hcp metals, it is possible to have a global shear displacement of several adjacent crystallographic planes simultaneously. A region with a distinctly different crystal orientation (but same crystal lattice) is created and is referred to as a twin. The generation of large number of twins is, then a means by which a grain can accommodate plastic deformation. In austenite, twinning occurs on the {111}<112> system [40].

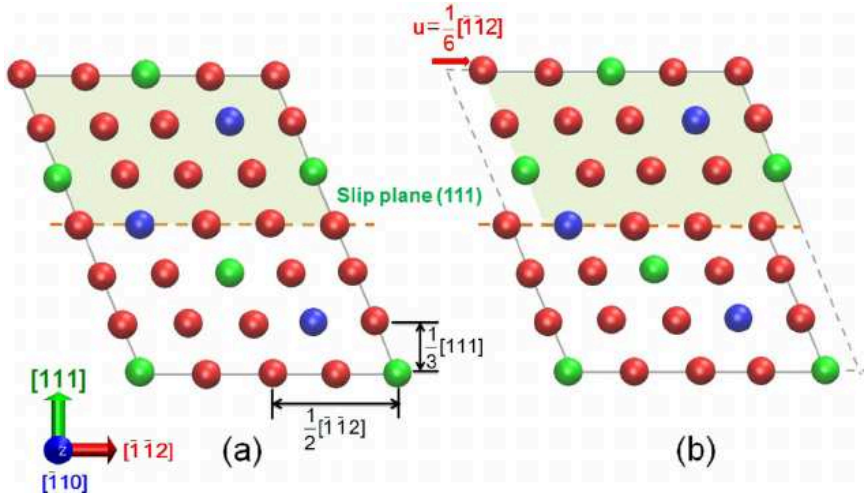

FIGURE 2.26: As shown by Wang *et al.* for $Ni_3Al_0.5Ta_0.5$, the dissociation of a dislocation into two partial dislocations can lead to planar slip [39].

Twinning can be modeled in the same way as dislocation slip by activating twinning when the resolved shear stress on the twinning system {111}<112> is sufficiently high. The activation of twinning does not preclude simultaneous dislocation slip, however. As shown in Figure 2.27, the both can occur in the same grain as long as the Schmid factors for each system are such that multiple systems can be activated. In the figure, TEM observations of hexagonal Mg are shown in which both slip traces and deformation twins can be observed to varying degrees in each grain. As one might infer from the image, the generation of twins also produces extra interfaces within a grain that could provide some strain hardening by a reduction in the mean free path for dislocation motion. This can lead to a dynamic Hall-Petch effect as described by Allain *et al.* [8]. Additionally, the sudden shear that occurs to accommodate the applied strain results in a stress relaxation that can in turn lead to the formation of strain bands as in PLC [15, 34, 35, 41].

Twinning results in a characteristic crystal orientation change locally and, as such, one would expect that the degree of twinning could be characterized by analyses of a sample's textural evolution with strain. In fact, TWIP steels do commonly show a texture concentration for <111>||TD (transverse direction) and <100>||TD. with a notable development of the {110}<112> Brass texture component [44–46]. An example of the texture development of a high-Mn TWIP steel for a strain increment of 20% is provided in Figure 2.28 [47]. In fact, it is uncertain whether the twin orientations themselves are responsible for these textural changes. Twin volume fraction saturates at relatively low values of only 0.15-0.20 within the austenite phase [48, 49] and it is thus unlikely that the twins themselves create a macroscopic texture change, but could be that the way twins affect dislocation slip leads to texture development along the <100>||TD fiber [47].

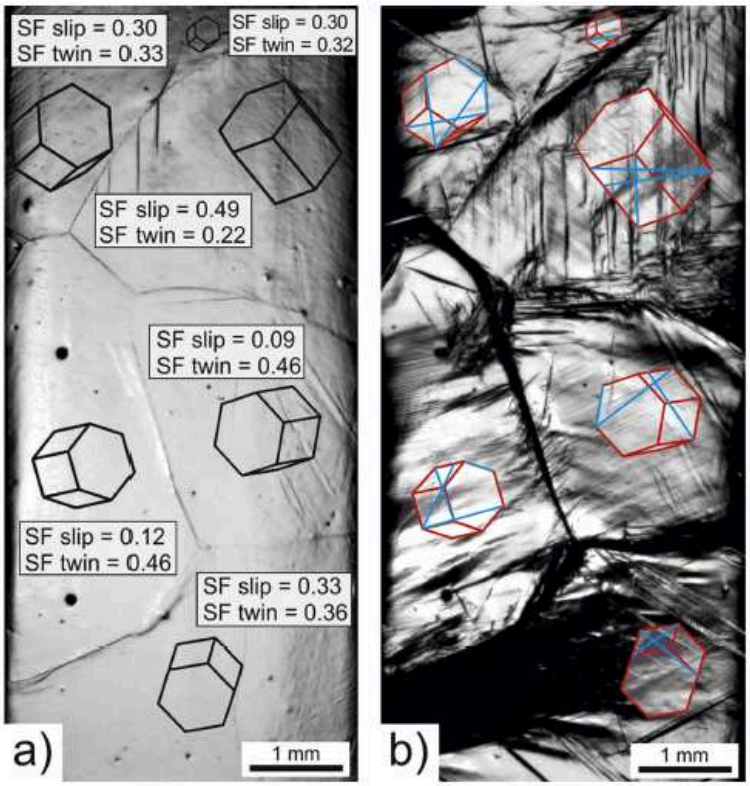

FIGURE 2.27: (left) TEM observations of various grains of hcp Mg with varying orientations denoted by the hexagonal prisms in each grain and (right) the presence of deformation twins in these same grains, with the twinning directions in each grain highlighted in blue [43].

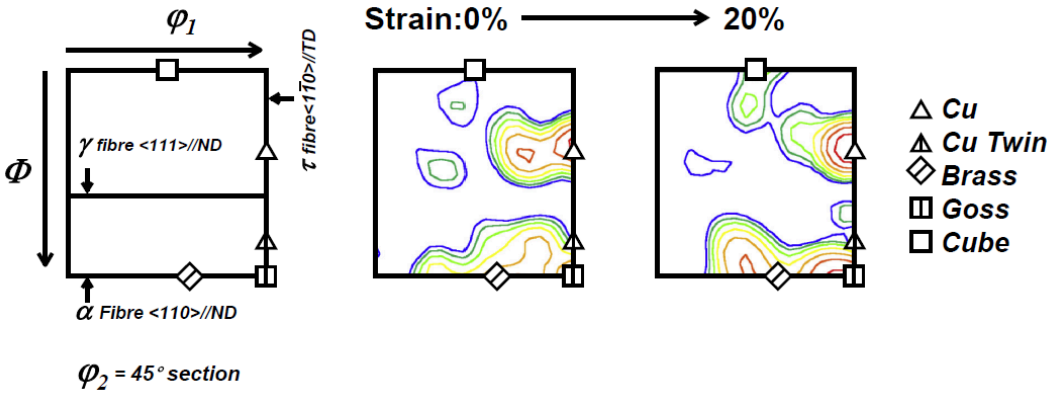

FIGURE 2.28: A 45° cross section of the texture of a high-Mn TWIP steel in Euler Space shows that the texture in TWIP steels is reinforced in the α-fiber and in the Cu component with increasing strain [47].

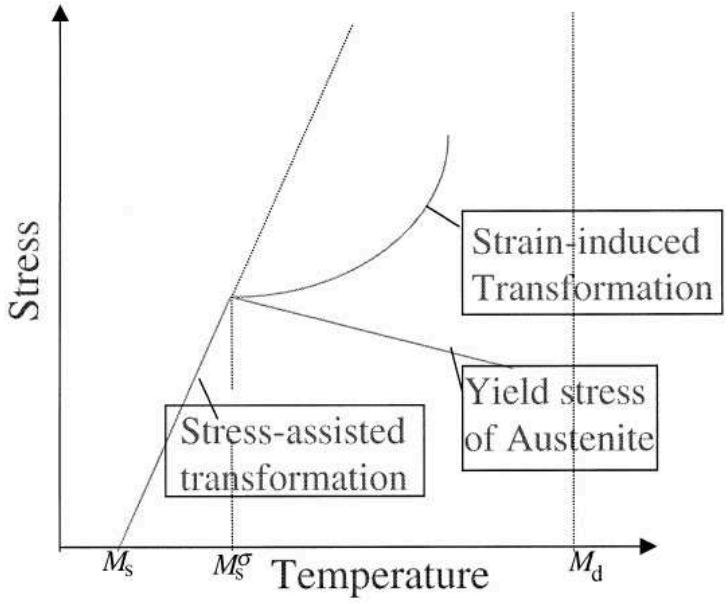

FIGURE 2.29: As illustrated by Cherkaoui *et al.* [50], TRIP can be either stress-assisted or strain-assisted depending on the deformation temperature relative to the M_s temperature of the retained austenite. Above the temperature M_d, the austenite is sufficiently stabilized that no transformation occurs and instead plasticity occurs through dislocation slip. The lines represent M_s^σ (stress-assisted transformation), the stress required for strain induced transformation, and the yield stress of the austenite as a function of temperature.

2.3.3 Transformation-Induced Plasticity (TRIP)

If a given grain of retained austenite is sufficiently thermodynamically unstable, the input of energy via mechanical work can cause the austenite to transform into martensite. This phase transformation is the namesake of TRIP steels.

One common way of characterizing the stability of the retained austenite phase is by the martensite start temperature, M_s, below which retained austenite will begin transforming to martensite without any external applied stress or strain. The amount of austenite that transforms is defined by both the temperature of the steel relative to M_s and the applied load. In Figure 2.29, the relationship between temperature, stress, and the types of possible phase transformation are mapped [50]. When the deformation temperature is between M_s and M_s^σ, it is possible for stress-assisted martensite transformation to occur during elastic straining. Above M_s^σ, the transformation becomes strain-assisted instead as plastic deformation creates martensite nucleation sites at the intersection of shear bands [51].

Olson and Cohen developed a model to describe the martensite transformation rate in TRIP steels that is commonly used as a quick characterization of austenite stability [51]. They described the kinetics of the nucleation of martensite via the generation of embryos at shear band intersections as a function of plastic strain in the austenite and the contribution of work energy ($\sigma \cdot \Delta\epsilon$) to the activation of the

transformation. They assumed that shear bands formed in the austenite at a constant rate with increasing strain and expressed the evolution of the volume fraction of shear bands as

$$f_{sb} = 1 - exp(-\alpha\epsilon) \tag{2.4}$$

where α is a constant that represents the rate of shear band formation. According to Olson and Cohen, this parameter increases with decreasing stacking fault energy and increases with strain rate. The number of shear bands is then related to the number of shear band intersections by

$$N_v^I = K\left(N_v^{sb}\right)^n \tag{2.5}$$

where N_v^{sb} and N_v^I are respectively the number of shear bands and number of shear band intersections with the subscript v indicating that the number is taken in the volume. K is a geometric constant related to the austenite grain size and n is a constant. The martensite transformation rate itself is described as

$$\frac{df_{\alpha'}}{1 - f_{\alpha'}} = \bar{v}_{\alpha'} \cdot dN_{\alpha',v} \tag{2.6}$$

which then permitted the martensite fraction to be calculated as

$$f_{\alpha'} = 1 - exp\big(-\beta[1 - exp(-\alpha\epsilon)]^n\big) \tag{2.7}$$

Thus the model relies on three parameters: α, β, and n. α is related to the rate of shear band generation, β is defined by the probability that a martensite nucleus will form at a shear band intersection, and the exponent n is a constant. These parameters are dependent on the testing temperature, and as such the dependence of each is described in Figure 2.30. It can be seen that both α and β increase with decreasing temperature. α is dependent mostly on the ability to form shear bands which in turn depends on the mobility of dislocations which decreases with temperature. β depends more on the stacking fault energy of the retained austenite. β will decrease with increasing temperature when tests are performed relatively close to the martensite start temperature, but will not change significantly as the temperature is decreased much further than about $-50°$C. Figure 2.30 (c) shows not the exponent n from Equation 2.7, but the "potency," as Olson and Cohen called it, of nucleation sites at shear band intersections. That is, the probability of a particular intersection forming a martensite nucleus. This probability is a function of the chemical driving force and, if the entropy change associated with the transformation is taken as a linear function of temperature, the temperature-dependent probability $n_v(T)$ can be expressed as a Gaussian distribution.

Olson and Cohen compared this model to experimental data from [52] for a 304 stainless austenitic steel deformed at varying temperatures. It was shown that the Olson-Cohen model is able to describe the transformation kinetics as well as the

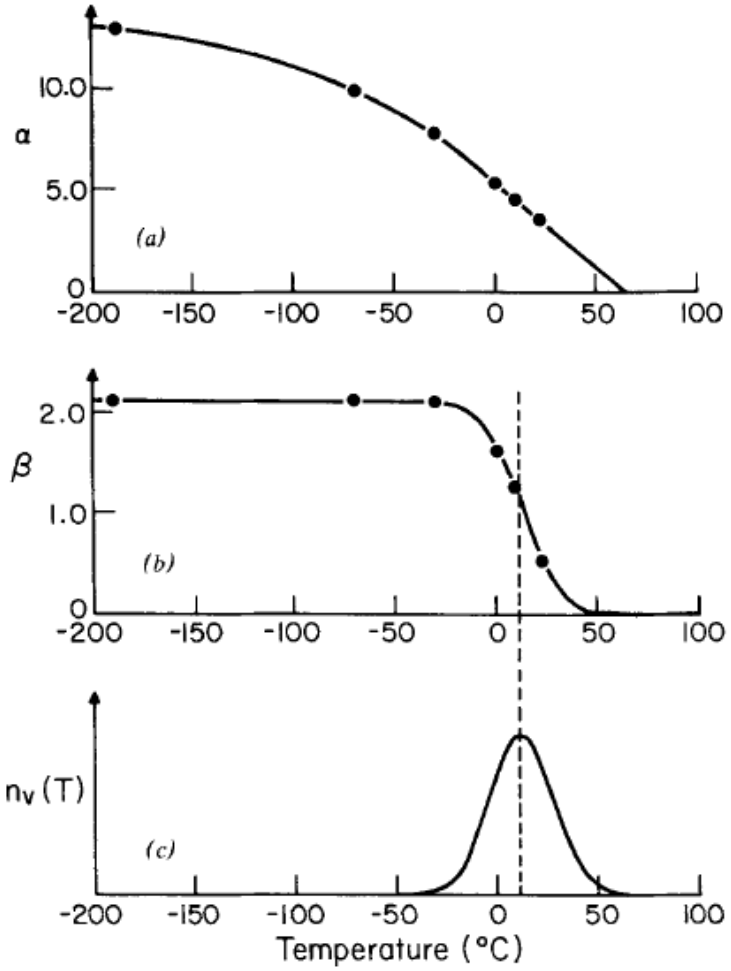

FIGURE 2.30: The parameters in the Olson-Cohen model are dependent on the deformation temperature of the sample. As the generation of shear bands (α) and probability of martensite nucleation (β) depend on dislocation mobility and SFE, respectively, their temperature dependence is evident. The driving force for transformation is described by $n_v(T)$ and takes the form of a Gaussian with respect to temperature [51].

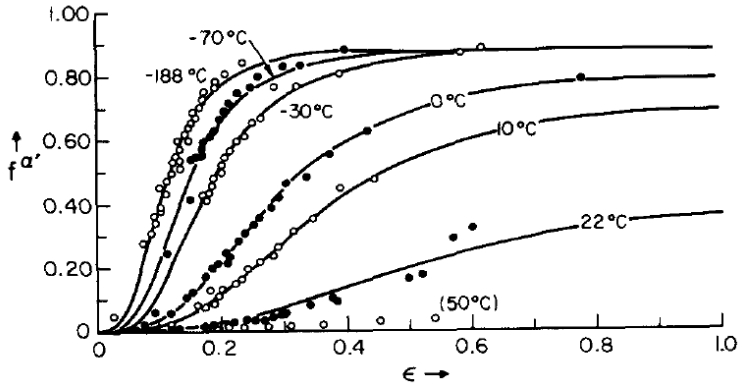

FIGURE 2.31: The Olson-Cohen model was able to accurately predict the changes in TRIP kinetics for tensile testing of a 304 stainless TRIP steel strained at different temperatures by Angel [52], making the model a common choice for characterizing TRIP from a macroscopic scale [51].

variation in kinetics as the testing temperature was changed. As the model is computationally simple to implement and given its rather accurate correlation to experimental data, this model has become common for describing TRIP kinetics from a macroscopic point of view.

The phase transformation results in the creation of a significant number of additional interfaces in the microstructure via either blocks or needle-like laths of martensite, as illustrated in Figure 2.32 that inhibit dislocation motion. The martensite phase itself can be very hard and brittle for higher carbon contents. The gradual addition of martensite to the microstructure will thus greatly increase the steel's UTS, but degrade its total elongation.

Spencer *et al.* performed an *in-situ* neutron diffraction study of the stress partitioning between the austenite and martensite phases in a 316L austenitic stainless steel [54]. The sample had been pre-strained to 15% at 77K to transform some of the austenite to martensite. The yield stress of the martensite was about 1000 MPa—nearly twice that of the retained austenite. Thus, a sudden burst of martensite transformation could result in a spike in the strain hardening rate in the sample. Proper optimization of the microstructure of a TRIP steel thus depends on the precise control of the retained austenite's stability and of the martensite transformation rate.

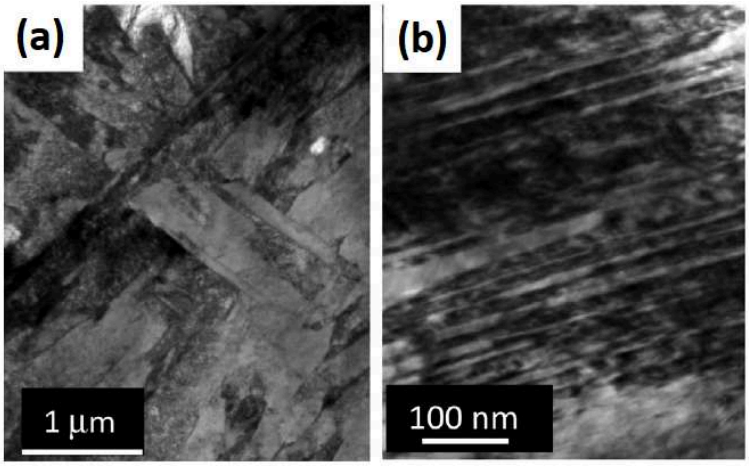

FIGURE 2.32: Cubic martensite in a 0.15C-1.4Mn-0.3Si steel took the form of either (a) blocks/plates or (b) laths/needles [53], meaning that the number of additional interfaces generated and thus the hardening capacity added by the martensite depends somewhat on its morphology.

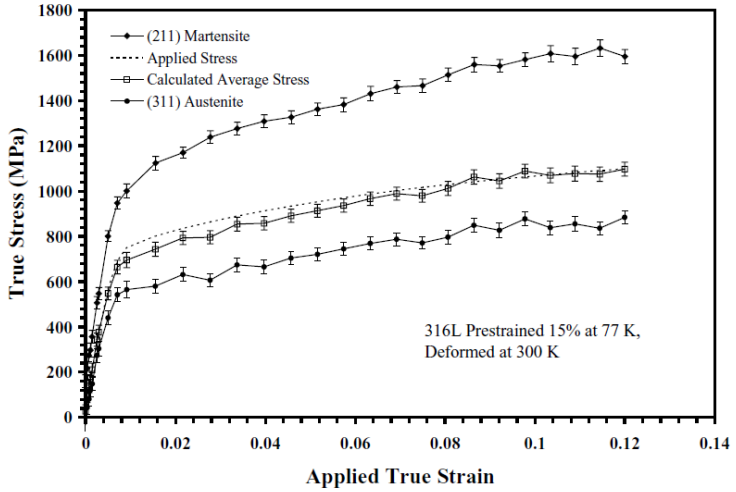

FIGURE 2.33: Neutron diffraction experiments by Spencer *et al.* [54] on a 316L austenitic stainless steel made it possible to determine the degree of stress partitioning between martensite and retained austenite in a pre-strained TRIP steel. Martensite has a much higher yield stress than austenite and thus acts as a strong elastic reinforcing phase.

Chapter 3

Material Characterization

3.1 Material and Fabrication Process

As described in Chapter 2, the fabrication process used to produce a Medium Mn steel has a significant impact on it's final properties. The intercritical annealing temperature, in particular, will directly influence the phase volume fractions of ferrite, retained austenite, and martensite as well as the stability of the retained austenite phase. Sheets of a Medium Mn steel with the composition provided in Table 3.1 were produced by ArcelorMittal for this study. The sheets were obtained from 60mm thick induction-cast ingots that had been roughed down to 30mm and hot rolled to 2.8mm in thickness at austenitizing temperature and then quenched and cold-rolled to a thickness of 1.25mm. After cold-rolling, they were intercritically annealed for 2 minutes at temperatures ranging from 740°C to 780°C in order to vary the microstructures generated and the stability of the retained austenite phase.

Tensile curves for each intercritical annealing temperature are presented in Figure 3.1. It can be clearly seen that the degree of work hardening changed drastically from one sample to another due to just a 10°C difference in annealing temperature. Increasing the annealing temperature led to a rapid decrease in total elongation and an increase in UTS due to changes in the initial retained austenite fraction and its stability in regards to the TRIP effect. When the austenite is unstable, a mechanically-induced transformation to martensite can occur rapidly during tensile testing and result in a very high degree of work hardening. This hardening comes from the high yield stress of the martensite relative to ferrite and austenite, which means that since the hardening in the ferrite and austenite remain unchanged, the true stress is increased but the work hardening rate remains the same

The initial microstructure is critical in understanding how a Medium Mn steel will behave mechanically. The phase volume fractions in the unstrained state must be known and some understanding of the degree of the thermodynamic stability

TABLE 3.1: TRIP Steel Composition

Alloy	C wt%	Mn wt%	Al wt%	Fe wt%
Med. Mn TRIP	0.2	5.0	2.5	bal.

of the retained austenite is needed. In order to study the effects of the initial microstructure on the mechanical response of Medium Mn TRIP steels, intercritical annealing temperatures of 740°C, 760°C, and 780°C were selected for the experiments performed during this thesis as they provided three distinctly different levels of work hardening in tension.

The objective of the study, then, was to identify how the plastic deformation mechanisms changed with respect to the initial microstructure and the retained austenite stability. Particular interest was given to the TRIP effect and its kinetics during unidirectional tension.

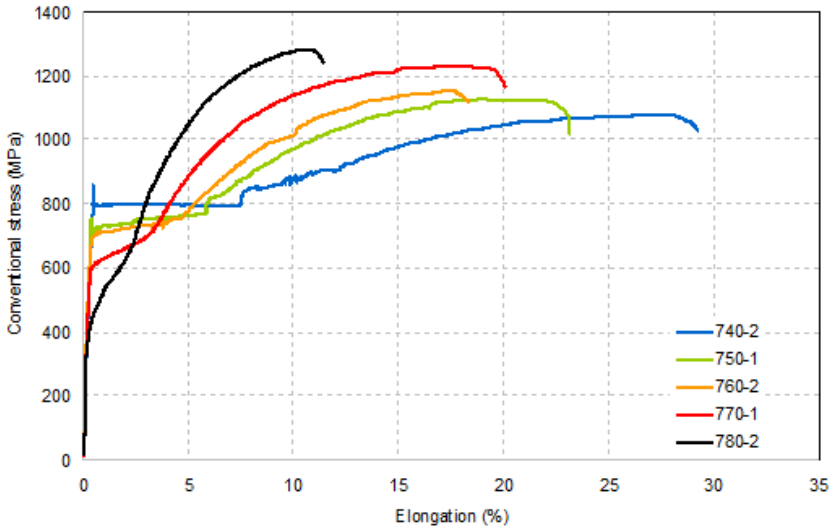

FIGURE 3.1: Tensile curves for a 0.2C-5Mn-2.5Al Medium Mn steel produced by ArcelorMittal with intercritical annealing temperatures ranging from 740°C to 780°C. For this research, temperatures of 740°C, 760°C, and 780°C were chosen for study.

TABLE 3.2: Compositions of Low-density Alloys

Alloy	C wt%	Mn wt%	Al wt%	Fe wt%	$T_{IA}(°C)$
LD-A	0.2	8.5	6	bal.	850
LD-B	0.3	6.5	6	bal.	850
LD-B	0.3	6.5	6	bal.	900

3.2 Macroscopic Mechanical Properties

Tensile tests were carried out on samples from each intercritical annealing temperature. Samples were cut in the rolling direction (RD), transverse direction (TD), and diagonal direction (45° from the RD) with a gauge length of 60mm, width of 10mm, and thickness of about 1.25mm. The sample geometry is shown in Figure 3.2 for a sample with an applied speckle pattern for DIC. The thickness varied slightly depending on where in the sheet the sample was cut and from which sheet. Initial

TABLE 3.3: Yield Stress as a Function of T_{IA}

$T_{IA}(^\circ C)$	$\sigma_0(MPa)$
740°C	750
760°C	675
780°C	500

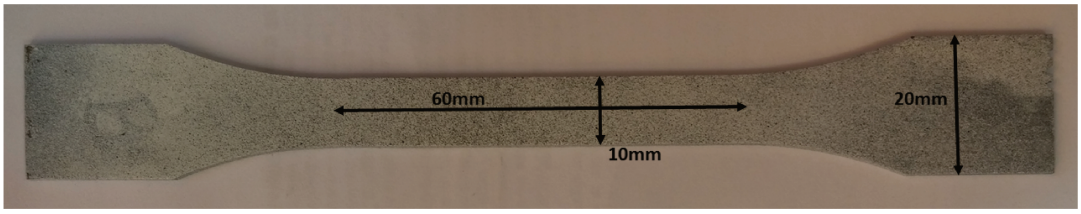

FIGURE 3.2: Sample geometry used for tensile testing.

tensile tests were conducted to assess the overall mechanical behavior for each intercritical annealing temperature, as shown in Figure 3.3. There was a significant difference in the degree of work hardening which manifested as an increase in UTS and decrease in total elongation with increasing intercritical annealing temperature.

Additionally, in the samples annealed at 740°C and 760°C, there was a very long yield point elongation followed by a series of "steps" in the rest of the tensile curves. The sample annealed at 780°C yielded in a continuous fashion and showed a sudden increase in work hardening rate at about 2.5% strain. The stark difference in work hardening capacity for each sample is hypothesized to be the result of varying retained austenite stabilities in each, and thus varying degrees of transformation-induced plasticity. There is a significant difference in yield strength as well when the samples that had Lüders plateau and those that didn't are compared. The average yield stresses for each intercritical annealing temperature are provided in Figure 3.3. The presence of a Lüders band, then, has a two-fold effect: a long yield point elongation and a significant increase in yield stress due to static strain aging.

The work hardening rate $\theta = {}^{d\sigma}/_{d\epsilon}$ was plotted as a function of the true strain for a sample from each intercritical annealing temperature. In Figure 3.4, some interesting trends in work hardening can be observed for samples strained at $5 \cdot 10^{-4}s^{-1}$. For the sample annealed at 780°C, an increase in work hardening rate was observed at about 525 MPa of applied true stress. The samples annealed at 740°C and 760°C showed some degree of work hardening as well, but it was discontinuous taking the form of a series of spikes in work hardening rate, as can be seen in Figure 3.4. These are important because it can be seen that the intensity of these spikes varies from one sample to another. If the stress sudden decrease in work hardening rate upon nucleation of a band is too large, it could bring the work hardening rate below the Considère criterion (${}^{\delta\sigma}/_{\delta\varepsilon} < \sigma_{true}$) and initiate necking much sooner than it would begin normally were the work hardening continuous.

Next, the anisotropy of tensile properties was evaluated by testing samples cut in the RD, TD, and diagonally at 45°. Samples were strained at $5 \cdot 10^{-4}s^{-1}$. For the

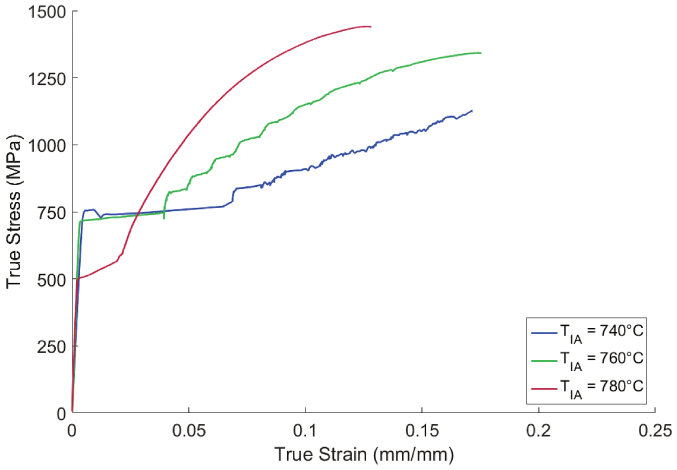

FIGURE 3.3: Comparison of the mechanical response in unidirectional tension for samples intercritically annealed at 740°C, 760°C, and 780°C. The samples were strained in the rolling direction with a strain rate of at $5{\cdot}10^{-4}$ s^{-1}. The rate of work hardening varied significantly between the three annealing temperatures due to changes in the stability of the retained austenite.

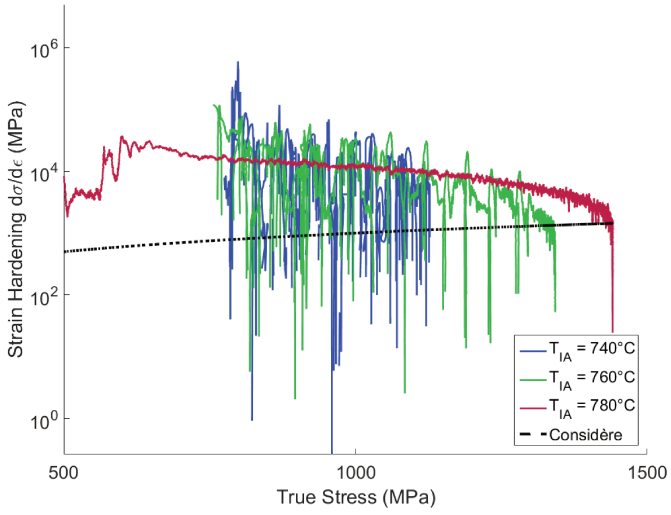

FIGURE 3.4: Comparison of the rate of work hardening for samples intercritically annealed at 740°C, 760°C, and 780°C. Samples were strained in unidirectional tension at 10^{-3} s^{-1}. In the curves for 740°C and 760°C, serrations can be observed in the work hardening curves that correspond to the presence of strain localizations.

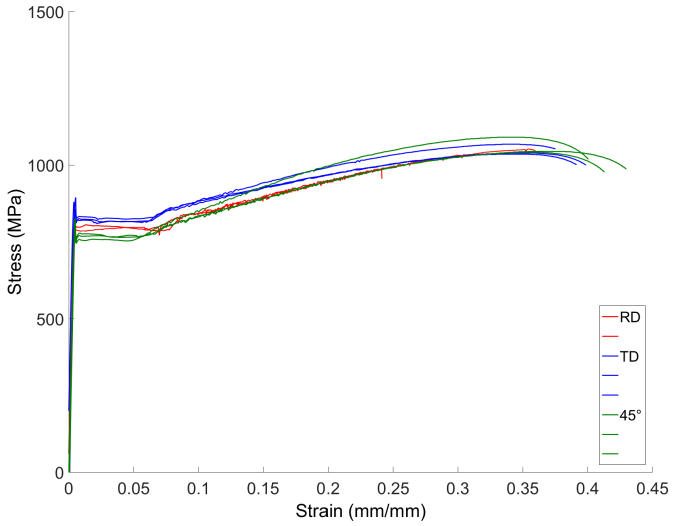

FIGURE 3.5: Tensile properties of samples annealed at 740°C strained in the rolling direction (RD), transverse direction (TD) and in the diagonal direction at 45°. A strain rate of $5 \cdot 10^{-4}$ s^{-1} was used.

samples annealed at 740°C, as can be seen in Figure 3.5, the loading direction did not have a significant effect on the tensile behavior. In the sample annealed at 760°C, the UTS attained was higher in the RD than in the TD or at 45°, as shown in Figure 3.6. Finally, in Figure 3.7 it can be seen that the loading direction had no significant impact on the tensile behavior of the samples. The slight difference between the RD and other directions in tension observed particularly in the sample annealed at 760°C is typical of a material with a cold-rolled texture and is not unexpected.

The appearance of steps or plateaus in the tensile curves for intercritical anneals at 740°C and 760°C suggests the presence of a dynamic strain aging effect such as the Portevin-Le Châtelier effect described in Chapter 2. Because materials exhibiting PLC typically have a negative strain rate sensitivity, tensile tests were conducted on samples from each intercritical annealing temperature at strain rates of $10^{-4}s^{-1}$, $10^{-3}s^{-1}$ and $10^{-2}s^{-1}$. If there is a negative strain rate sensitivity in the current case, then the UTS and overall degree of work hardening should decrease with increasing strain rate. Negative strain rate sensitivity is generally observed in fcc phases such as aluminum or iron austenite [35, 55] but ferrite does not show any strain rate sensitivity [56].

In samples annealed at 740°C, no truly significant effect on strain hardening was observed contrary to the hypothesis of negative strain rate sensitivity due to PLC. The three samples, shown in Figure 3.8, showed the same tensile behavior aside from a decreased total elongation in the sample strained at $10^{-2}s^{-1}$. This decrease in total elongation could however just be an effect of the strain localizations leading to early necking and not an effect of strain rate. There was also an increase in the length of the Lüders plateau with increasing strain rate, as seen in Figure 3.10a.

In the samples intercritically annealed at 760°C, the degree of work hardening

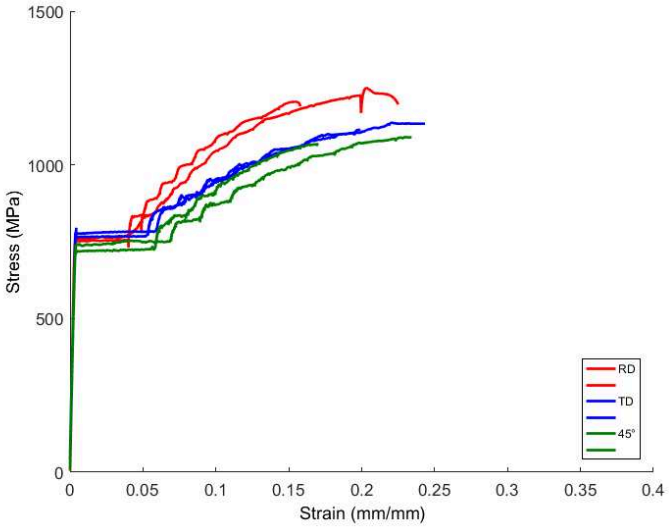

FIGURE 3.6: Tensile properties of samples annealed at 760°C strained in the rolling direction (RD), transverse direction (TD) and in the diagonal direction at 45°. A strain rate of $5 \cdot 10^{-4}$ s^{-1} was used.

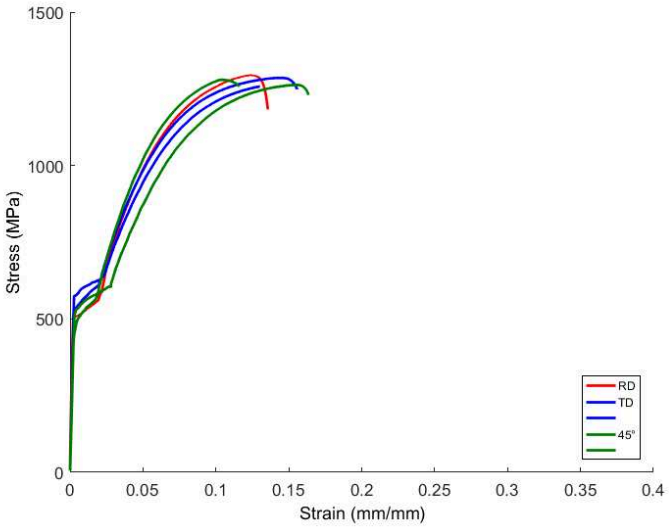

FIGURE 3.7: Tensile properties of samples annealed at 780°C strained in the rolling direction (RD), transverse direction (TD) and in the diagonal direction at 45°. A strain rate of $5 \cdot 10^{-4}$ s^{-1} was used.

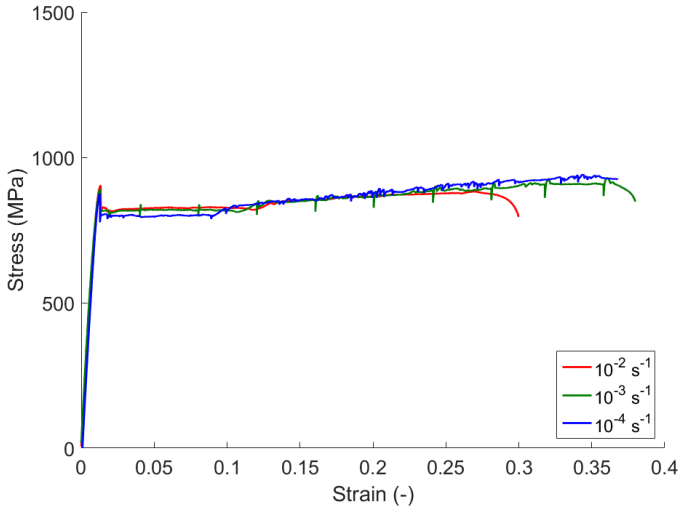

FIGURE 3.8: Variation in mechanical behavior of samples annealed at 740°C with varying strain rates. There was a decrease in total elongation for a strain rate of 10^{-2} s^{-1}, but no change in work hardening with respect to strain rate. The length of the Lüders plateau increased slightly as strain rate increased.

did not change significantly with strain rate, but the tensile test at $10^{-2}s^{-1}$ did show much more continuous work hardening, shown in Figure 3.9. It is possible that the strain instabilities are not present at higher strain rate, which would be in agreement with the observed effect of strain rate on materials exhibiting PLC. Regarding the Lüders band, the Lüders strain decreased at higher strain rates this time as illustrated in Figure 3.10b.

Finally, in the samples annealed at 780°C, there was an apparent negative strain rate sensitivity, as shown in Figure 3.11. While the trend appears to be clear for all three strain rates, it should be noted that the sample strained at $10^{-3}s^{-1}$ was periodically interrupted during testing which may have affected strain hardening. In the current case, the origin of the strain rate sensitivity (when and if it exists) is unclear due to the complex microstructure and the phase transformation that could possibly be retarded by adiabatic heating.

3.3 Microstructure

To understand the differences in mechanical properties for different T_{IA}, the corresponding microstructures of each need to be characterized. Samples were taken in the unstrained state and after straining until rupture and were cut such that the observed face is in the RD-TD plane. Samples were mechanically ground and polished down to a $1\,\mu m$ colloid and flash-etched by submersing the sample in a 2% Nital solution.

The microstructure is too fine to do any useful observations by optical microscopy,

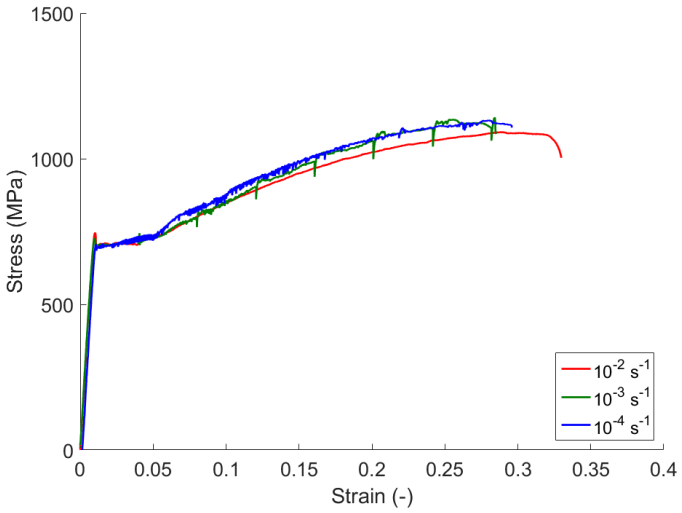

FIGURE 3.9: Variation in mechanical behavior of samples annealed at 760°C with varying strain rates. For a strain rate of 10^{-2} s^{-1}, the UTS decreased slightly and total elongation increased slightly. The length of the Lüders plateau increased as strain rate increased.

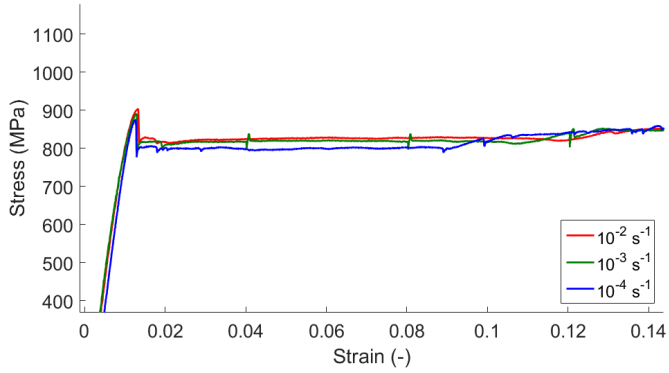

(A)

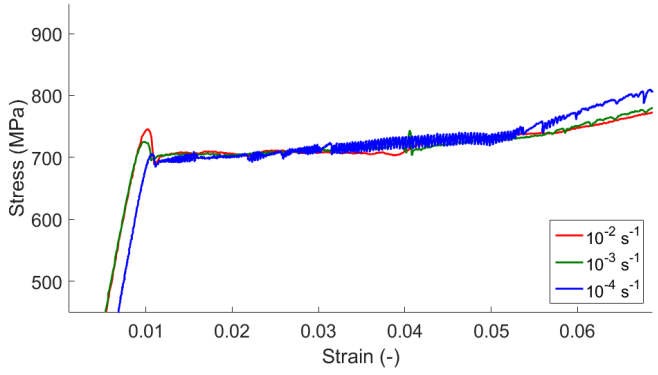

(B)

FIGURE 3.10: The strain rate had an influence on the Lüders strain, as can be seen here for the samples annealed at 740°C and 760°C.

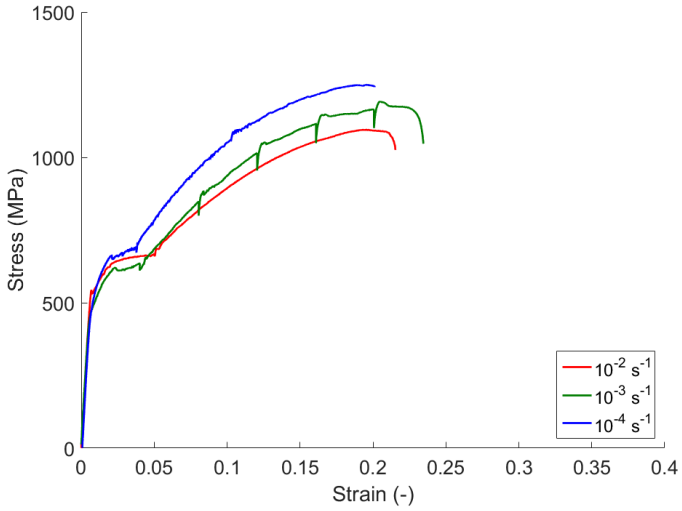

FIGURE 3.11: Tensile properties of samples annealed at 780°C strained in the rolling direction (RD), transverse direction (TD) and in the diagonal direction at 45°.

so samples were analyzed in a FEG-SEM at an accelerating voltage of $2\,\mathrm{kV}$, $30\,\mu\mathrm{m}$ diaphragm, and a working distance of about 4mm. The voltage used is much lower than the standard 15-25kV used for metallic samples, but in this case it enabled the fine microstructural features to be resolved clearly and in particular the fine martensite lamellae. The image for the sample annealed at 760°C in Figure 3.12b was acquired in a standard SEM (without FEG) with a 15kV voltage and a working distance of 8-9mm.

Sampled that were prepared for EBSD were prepared by either vibrational polishing or manual cloth polishing with a $0.01\,\mu\mathrm{m}$ colloidal silica solution. However, the retained austenite in these steels seems to be very sensitive to surface conditions and did not reliably diffract with any preparation method. As such, EBSD studies on these samples were unfortunately limited.

Initial characterizations of the microstructures in the unstrained state showed a few differences between samples from different intercritical annealing temperatures. The microstructures can be seen in Figure 3.12 in which ferrite grains are recessed with a very smooth surface and retained austenite is in relief with a rougher surface. The martensite in the sample annealed at 780°C is clearly distinguished by its characteristic lamellar morphology. The most clear difference was that samples annealed at 740°C and 760°C were composed of a mixture of ferrite and retained austenite, while samples annealed at 780°C contained a significant proportion of martensite. It can also be seen that, in all three samples, there are zones with a more banded structure of elongated grains. These are likely zones that have poorly recrystallized and the orientation of the bands is related to the orientation of the parent austenite grain from which they formed. The bands themselves are alternating layers of ferrite and austenite.

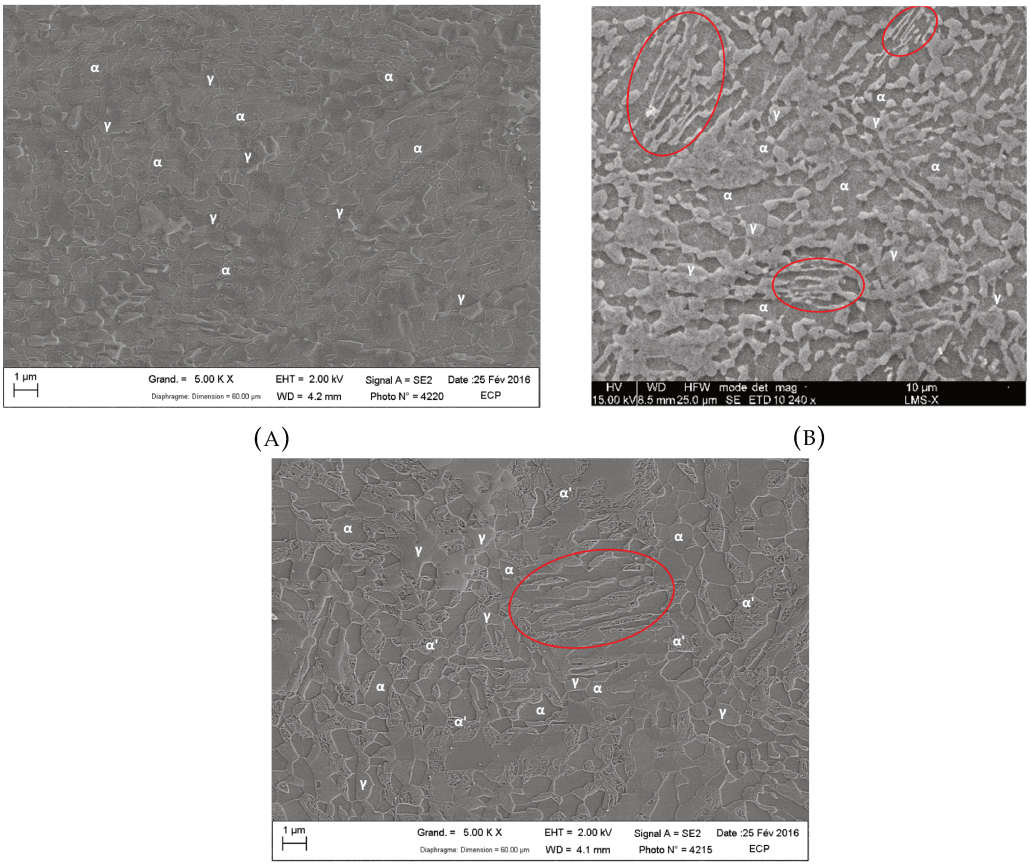

(A) (B)

(C)

FIGURE 3.12: Initial microstructures of Medium Mn TRIP samples annealed at 740°C (A), 760°C (B), and 780°C (C). The microstructures consisted of a UFG mixture of ferrite (α) and retained austenite (γ). The sample annealed at 780°C also had a significant volume fraction of martensite (α') in the unstrained state. The "banded" regions mentioned in the text are circled in red.

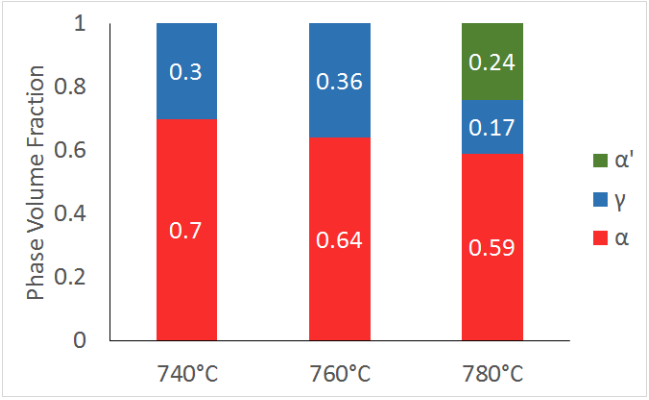

FIGURE 3.13: Initial phase volume fractions in the unstrained state after annealing and quenching as measured via XRD (α and γ) and as estimated from SEM images (α') as a function of the intercritical annealing temperature used.

X-ray Diffraction (XRD) was used to determine the initial austenite volume fraction for each intercritical annealing temperature. X-rays were produced with a Co-K_α source with an energy of 6.915 keV. As XRD is a surface measurement, the sample was oscillated in order to increase the volume of measurement (still at the surface) by scanning over a larger area. This provides better statistical sample size in terms of the number of grains analyzed. Spectra were obtained for several orientations of the sample relative to the incident beam. The inclination angle of the sample with respect to the incident beam, ψ, was varied from $0°$ to $70°$ with a step size of $5°$. The rotation of the sample around its normal to the sample surface, Φ, varied from $0°$ to $355°$ with a step of $5°$. These spectra were summed together in order to minimize texture effects on the relative peak intensities of the bcc and fcc phases, which can vary significantly depending on the orientation of the sample. The volume fraction of retained austenite was calculated using the method presented in [57] and the phase volume fractions for each annealing temperature are summarized in Figure 3.13. The volume fraction of martensite was estimated from SEM images for the sample annealed at 780°C. The volume fractions of austenite are accurate within a few percent as they are directly measured by XRD. The ferrite volume fraction is thus also accurate for annealing temperatures of 740°C and 760°C when no thermal martensite is present. The ferrite and martensite content for the anneal at 780°C are more variable, probably within 5-10%. The austenite fraction in this case is accurate, and there should be less ferrite so with an approximation of the ferrite volume fraction and the known austenite fraction, the martensite fraction is deduced.

When examining the samples after straining until rupture, the difference in the stability of the retained austenite was evident. In Figure 3.14, samples annealed at 740°C and 780°C are shown. It can be seen that for 740°C, there is still a non-trivial portion of retained austenite in the microstructure that has not yet transformed to martensite. The austenite in this case is more stable, which corresponds to the lower degree of work hardening observed for samples annealed at 740°C due to a lower

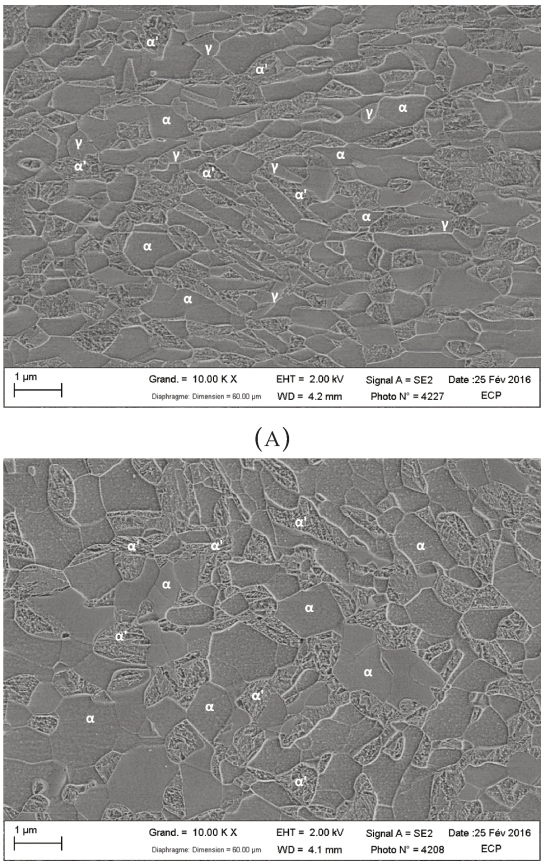

FIGURE 3.14: Microstructures of samples annealed at 740°C (A), and 780°C (B) after straining until rupture. The sample annealed at 740°C still contained a non-negligible quantity of retained austenite while the austenite in the sample annealed at 780°C had almost completely transformed to martensite.

amount of martensite transformation. The sample annealed at 780° showed nearly total transformation to martensite with only a few isolated blocks of retained austenite remaining in some grains. This could be because once the austenite has become sufficiently small due partial transformations, it is significantly stabilized and will not transform by the application of a mechanical load that is experimentally feasible. This idea will be revisited in Chapter 6.

The difference in the stability of the retained austenite is defined by its concentration in alloying elements, particularly Mn and C [58–60]. During the intercritical anneal when ferrite and austenite reform, C and Mn are partitioned into the austenite and Al into the ferrite. This stabilizes the austenite and permits it to exist at room temperature as a metastable phase. Energy-dispersive X-ray spectroscopy (EDS) was used in an FEI TITAN TEM operating at 200kV of accelerating voltage to map the partitioning of Mn between phases in a TEM foil taken from an unstrained sample annealed at 780°C. Figure 3.15 shows the results of these maps alongside an electron back-scatter diffraction (EBSD) map of the phases made using an FEI Helios nanolab SEM/FIB.

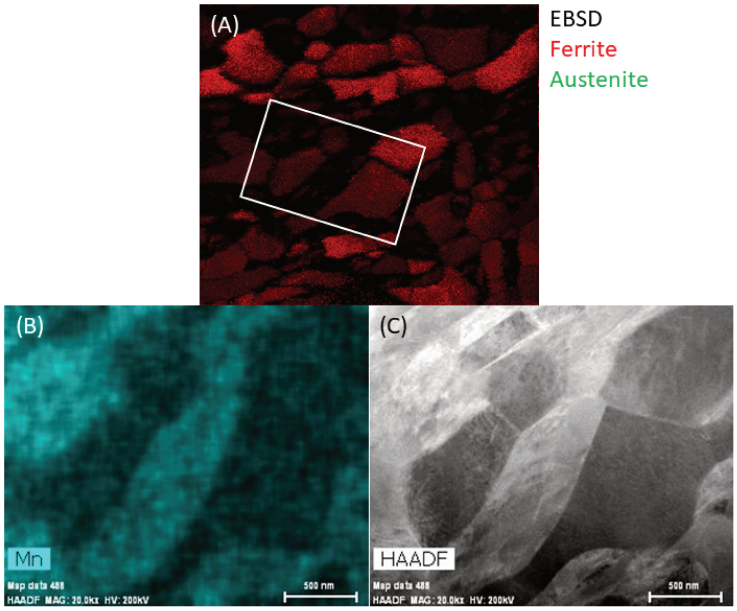

FIGURE 3.15: EBSD analyses of a TEM foil taken from a sample annealed at 780°C (A). The retained austenite did not diffract well enough to index, but as can be seen in (B) and (C)—which correspond to the area in the white box in (A)—the non-indexed zones contained a high concentration of Mn and were likely either austenite or martensite.

While the austenite did not diffract well enough to be indexed, the ferrite is rather well indexed (Fig 3.15 (A)) and can be used to identify the ferrite grains in EDS maps. It becomes clear then, that the grains identified by EBSD as ferrite are the same grains that show much lower concentrations of Mn in the EDS map in Fig 3.15 (B). The regions where the Mn concentration is high are non-indexed in EBSD, but must either be retained austenite or martensite because the martensitic transformation is instantaneous and the Mn cannot diffuse out of it during transformation. EDS could be useful to differentiate ferrite and martensite in EBSD maps (as EBSD cannot differentiate the two) by finding poorly-indexed ferrite grains with high concentrations of Mn.

Not only does the Mn concentration vary from one T_{IA} to another, but the distribution of Mn concentrations from grain to grain is also rather broad. EDS point measurements on a sample annealed at 740°C in the unstrained state showed that the Mn concentration can range from about 7.6wt% to 9.2wt%, as seen in Figure 3.16 while the Mn concentration in ferrite was around 3wt%. This dispersion in Mn content in the austenite makes a correlation between Mn concentration and T_{IA} difficult as a very large number of grains would be needed to see a statistically-valid difference between the average Mn concentrations from one T_{IA} to another. It should also be noted that a spheroidal pearlite inclusion was observed in some austenite grains and that, in one of the grains analyzed here, such an inclusion contained nearly 11wt% Mn— 2.5wt% more than the parent grain itself. The effect of such inclusions on the stability of the parent grain is unknown. Also interesting to note is that the

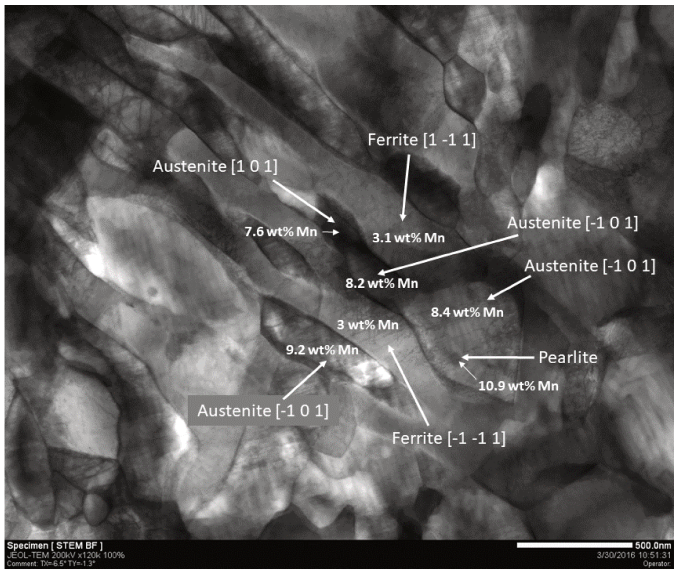

FIGURE 3.16: TEM image of a sample annealed at 740° in which EDS point measurements were made to determine the Mn content in several grains. Austenite grains contained between 7.6wt% and 9.2wt% Mn while ferrite contained only about 3wt%

grains analyzed here are in a "banded" region of the microstructure and all grains of each phase have similar orientations, very likely defined by the orientation of the parent grain from which they formed.

The martensite transformation does not only affect the austenitic phase. As can be seen in Figure 3.17, the transformation also results in the generation of dislocations in neighboring ferrite grains. In Fig. 3.17a, a ferrite grain in a sample annealed at 740°C is shown. It contains dislocations which are very linear (which is characteristic of screw dislocations in bcc metals), but which are rather few in number. However in a sample annealed at 780°C (Fig. 3.17b) the ferrite grains that are adjacent to martensite grains were very highly dislocated, with large numbers of dislocations near the grain boundary with neighboring martensite. Given that this martensite formed during cooling to room temperature and not during mechanical straining of the grain, one can assume that these dislocations are indeed generated by the transformation of the martensite.

The fact that the martensite transformation generates dislocations in nearby ferrite grains is significant when considering the overall work hardening of the material. It means that gradual transformation of austenite to martensite will harden the steel not only by the generation of a rigid phase, but by the increased hardening induced in the ferrite as well. Given the small grain size and thus inability to store large numbers of dislocations, it could even be problematic if too many dislocations are created in a ferrite grain making it unable to accommodate any useful degree of plastic deformation. The higher initial dislocation density in ferrite in samples with martensite in the initial microstructure could also be responsible for the lack of a Lüders plateau in samples annealed at 780°C. If enough mobile dislocations are

(A) (B)

FIGURE 3.17: TEM images of dislocations in ferrite grains in samples annealed at 740°C (A) and 780°C (B) in the unstrained state. There are dislocations in both samples, but in the one annealed at 780°C, there are far more dislocations in ferrite grains adjacent to martensite. These are likely due to the local deformation associated with the phase transformation.

available, it could be that yielding can occur continuously even if many dislocations are impinged upon by interstitial carbon.

3.4 Problem Statement and Objectives

3.4.1 Discussion of Initial Results

In this chapter, several interesting aspects of the mechanical behavior of Medium Mn TRIP steels and their micromechanical origins have been elucidated. This initial characterization is key to understand some of the primary characteristics of these steels and how they behave mechanically, and thus how they can be used industrially for fabrication purposes. A thorough understanding of the plastic deformation modes and work hardening capacity are critical for design of components and for planning forming operations and this first study lays the groundwork for a more in-depth analysis of these steels that will hopefully deepen the metallurgical community's understanding of the capabilities and limitations of this family of 3^{rd} generation AHSS.

The tensile behavior of these steels varied significantly for only slight changes of plus or minus 20∘C in the intercritical annealing temperature. This is rather typical of this family of steels and has been reported by several other groups [14, 17, 61]. It poses a significant challenge to steelmakers as extremely precise control of the annealing temperature and duration are needed to ensure reliable product quality.

This emphasizes the importance of understanding the effects of the annealing temperature on the steel and being able to predict the mechanical behavior based on processing parameters.

One notable characteristic of these steels is the presence of a long yield point elongation caused by the propagation of a Lüders band. This occurs in alloys with a low enough Al concentration that ferrite bands do not form and which are intercritically annealed within a certain range of temperatures that varies with alloy composition. In the current case, Lüders bands were observed for anneals at 740°C and 760°C, but not at 780°C. Lüders bands are problematic in that they result in a large amount of heterogeneous strain which is not desirable for forming operations.

In the same samples in which Lüders bands appeared, a series of strain instabilities were observed after the passage of the Lüders band, resulting in "steps" in the tensile curves. This was, as will be shown in Chapter 5 the result of additional strain bands in the sample. The presence of strain bands over the entire course of plasticity in these steels in interesting in that this sort of dynamic strain aging effect is often associated with a negative strain rate sensitivity and with deformation mechanisms which create a local and temporary softening. This occurs, for example, in Al-Mg alloys where solute atoms diffuse into dislocation cores and block dislocation motion [37, 62]. The resulting unpinning results in a drop in the applied force as the energy stored by dislocation pinning is released, then hardening continues normally. It also can occur in TWIP steels where the generation of a twin causes a local relaxation, followed by some hardening due to the reduction in the dislocation mean free path [15, 41]. The formation of these Portevin-Le Châtelier bands has not been confirmed to be a possible result of TRIP, but it has been suggested [54] that martensite transformation can localize in the form of a Lüders band.

The appearance of these bands in Medium Mn TRIP steels is common, but is poorly understood. Gibbs *et al.* [14] suggested that the serrations seen in work hardening curves are due to a variable martensite transformation rate resulting from the competition between the consumption and creation of martensite nucleation sites during plastic deformation. Lee *et al.* [63] attributed the serrations to dynamic strain aging (DSA) leading to the formation of Portevin Le-Châtelier (PLC) bands. Cai *et al.* [61] instead proposed that the stability of the austenite phase itself varied from one grain to another and thus could transform to martensite in bursts. It is important to understand what the origin of the PLC-type bands is in order to know which processing parameters need to be changed to eliminate it. At the very least, it is necessary to know how the localization of strain in bands affects the martensite transformation.

From the point of view of the steelmaker, it is important to be able to predict the mechanical behavior of a steel so that the composition and fabrication process can be optimized. It is particularly important to have an idea of the yield stress, UTS, and total elongation which are the parameters of interest for end users. To this end, a numerical tool to simulate the mechanical behavior of a Medium Mn steel would

be useful to be able to predict for a given composition and fabrication process what microstructure will be obtained and how it will perform under a mechanical load.

3.4.2 Objectives

With these observations in mind, the objectives of this thesis can be defined. As it seems that these steels plastically deform primarily by TRIP, it is necessary to understand how the kinetics of the martensite transformation are affected by the intercritical annealing temperature. It is also interesting to know whether the strain rate sensitivity that is observed in other studies but is not quite clear in the current case is truly present in these steels and what might be the cause. Finally, it is necessary to understand how the Lüders and PLC bands affect TRIP. The primary goals of this thesis can then be specified as:

- Understand how the intercritical annealing temperature affects the mechanical behavior of the steel, notably through the transformation kinetics during TRIP,
- Determine to what degree the observed strain instabilities are related to TRIP, characterize the type of instability and when they are or are not present, and
- Analyze the observed strain rate sensitivity of the steel and explain its origins.

This thesis will the concentrate on the kinetics of the austenite to martensite phase transformation in a 0.2C-5Mn-2.5Al Medium Mn TRIP steel. Particular attention is given to the characterization of Lüders and Portevin-Le Châtelier strain bands and the manner in which TRIP is affected by them. The strain rate sensitivity will be quantified at relatively slow strain rates compared to those used in industry (for reasons related to the mechanical testing equipment available and desire to observe strain instabilities that may disappear at higher strain rates). Finally, some numerical analyses of the kinetics of TRIP will be developed with the assumption that the microstructure is pre-determined. A thesis completed in parallel with this one [1] provides an in-depth analysis of the thermodynamics of microstructure formation during processing. The two data sets could then be combined into a more complete tool afterwards.

[1] Completed by Aurore Mestrallet at INP Grenoble entitled "Thermodynamique de nouvelles solutions d'aciers de 3éme génération á structure duplex"

Chapter 4

Experimental Methodology

4.1 DIC Characterization of Strain Bands

Analysis of the PLC bands observed in the Medium Mn TRIP alloy studied here was performed using digital image correlation (DIC). This chapter will first detail how the strain field is calculated using DIC and how the calculation parameters—element size and regularization length—were verified. A subsequent section will explain how the method was employed in the current case and how the strain bands were characterized.

4.1.1 Strain Field Calculation by DIC

Digital image correlation allows the experimenter to measure the displacement field and evaluate the strain field on the surface of a sample and its evolution during mechanical testing. A high-contrast, randomized pattern is applied to the surface of the sample, as in the example in Figure 4.1a, and images are recorded during deformation at regular intervals. Each pixel in an image registers a gray scale value, as illustrated in Figure 4.1b, and these gray scale values are used by the DIC algorithm to locate characteristic features on the sample surface and calculate their displacement from one image to another. The algorithm used in Correli T3R as explained hereafter is adapted from [64–66].

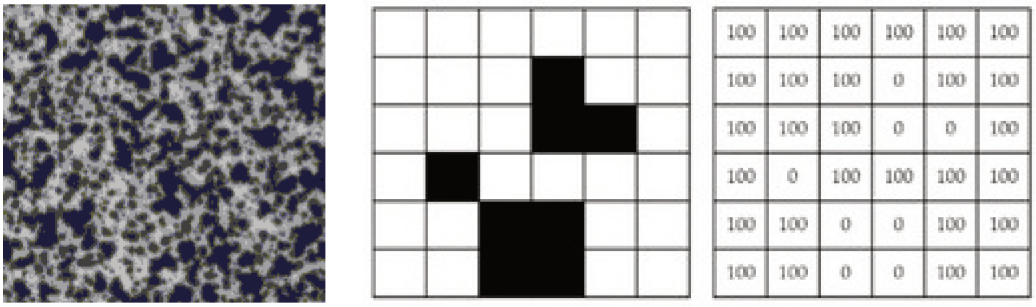

(A) (B)

FIGURE 4.1: A high-contrast, random speckle pattern (A) is painted on the sample's surface and is converted by the acquisition software into a matrix of gray scale values (B) that are used to measure displacement fields. The gray scale is depicted as simply black and white in the image.

4.1.2 Finite Element-based DIC Algorithm

While several methods of displacement fields through the correlation of gray scale images are possible [67], the current study will outline a finite element-based method. This method is used in the DIC software Correli T3R [68] that was used in the current study. Pixel displacements are calculated in the deformed image g with respect to a reference image f.

The displacement field $\vec{u}$ calculated in the deformed image g with respect to a reference image f satisfies gray level conservation

$$f(\vec{x}) = g(\vec{x} + \vec{u}(\vec{x})) \tag{4.1}$$

where $\vec{x}$ defines the location of each pixel. The displacement field $\vec{u}$ is optimized through the minimization of a correlation parameter (global residual field) η_c^2 over the whole region of interest (ROI) Ω

$$\eta_c^2 = \sum_{\Omega} \Phi^2(\vec{x}) \tag{4.2}$$

where Φ^2 is the local residual field

$$\Phi^2(\vec{x}) = [g(\vec{x} + \vec{u}(\vec{x})) - f(\vec{x})]^2 \tag{4.3}$$

However, Equation (4.3) cannot be minimized without additional information. The displacement vector is dependent on the gray scale values which may vary from one image to another not only due to displacement but also due to lighting fluctuations, acquisition noise or irregularities in the speckle pattern. This combined with the pre-existing fluctuations in gray scale values in the reference image makes the problem highly nonlinear. However Equation (4.3) can be solved through the use of

a Newton algorithm

$$\eta_c^2 = \sum_{\Omega} [g(\vec{x} + \vec{u}_i + d\vec{u}) - f(\vec{x})]^2 \tag{4.4}$$

where the displacement field $\vec{u}$ is decomposed into the displacement field from the preceding image $\vec{u}_i$ plus an incremental field $d\vec{u}$. If $d\vec{u}$ is small, Equation (4.4) can be rewritten as

$$\eta_c^2 = \sum_{\Omega} \left[g(\vec{x} + \vec{u}_i) + d\vec{u} \cdot \vec{\nabla} g(\vec{x} + \vec{u}_i) - f(\vec{x}) \right]^2 \tag{4.5}$$

It is worth noting that after the first iteration of Newton's scheme, $\vec{u}_i$ becomes the new evaluation about which corrections $d\vec{u}$ are updated.

The displacement field itself is a sum over each degree of freedom multiplied by a shape function $\vec{\psi}$

$$\vec{u} = \sum_{n} a_n \cdot \vec{\psi}_n(\vec{x}) \tag{4.6}$$

where a_n is the unknown associated with the displacement in the n^{th} degree of freedom. In the present case, 3-noded triangular elements are used (thus the T3 acronym in the DIC code) with linear interpolation functions.

With η_c now adapted for iterative minimization, the problem can be linearized in a typical finite element form as

$$\mathbf{M} \cdot d\vec{a} = \vec{b}^i \tag{4.7}$$

in which **M** is an allegory of the mass matrix in a finite element problem and $\vec{b}^i$ is the force vector. In the current case, **M** contains a dyadic product of image gradients and shape functions and $\vec{b}$ also contains the gray level residuals. **M** and $\vec{b}$ are respectively expressed as

$$\mathbf{M}_{nm} = \sum_{\Omega} \left(\vec{\psi}_n \cdot \vec{\nabla} f(\vec{x}) \right) \left(\vec{\psi}_m \cdot \vec{\nabla} f(\vec{x}) \right) \tag{4.8}$$

and

$$\vec{b}_n^{\,i} = \sum_{\Omega} \left(\vec{\psi}_n \cdot \vec{\nabla} f(\vec{x} + \vec{u}^i) \right) \left[f(\vec{x}) - g(\vec{x} + \vec{u}^i) \right] \tag{4.9}$$

4.1.3 Regularization

The fluctuations that exist in the gray scale images due to texture, lighting, and other effects may lead to calculated displacements that are not mechanically admissible. That is, we know that in elasticity the strain should be along the tensile axis with an accompanying reduction in cross section. Random localized spikes in the displacement also lack a physical sense and are likely computational errors. By applying a mechanical regularization scheme (i.e. the R acronym in the DIC code), these errors can be minimized and something closer to reality is obtained. In Correli T3R, this is achieved by the application of an elastic filter that helps the software to weed out mechanically inadmissible displacements. The regularization is applied over a

characteristic length that should be optimized and will be discussed in a subsequent section. The regularization is written for linear elastic equilibrium as

$$\mathbf{K} \cdot \vec{a} = \vec{f} \tag{4.10}$$

in which **K** is the stiffness matrix, $\vec{a}$ the nodal displacement vector, and $\vec{f}$ is the force vector. If $\vec{a}$ is not mechanically admissible it will result in residual forces

$$\vec{f}_r es = \mathbf{K} \cdot \vec{a} - \vec{f} \tag{4.11}$$

In the absence of body forces, no force should be applied on internal nodes. To account for this, a second minimization functional (i.e. the L2 norm of the equilibrium gap [69]) is introduced

$$\eta_m^2 = \vec{a}^\intercal \overline{\mathbf{K}}^\intercal \overline{\mathbf{K}} \vec{a} \tag{4.12}$$

for the interior nodes. The minimization of the weighted sum of both Equations (4.5) and (4.12) leads to a displacement field solution with a minimized effect of mechanically inadmissible displacements.

This is valid only for internal nodes, however. A final consideration must be made for the boundary nodes as well

$$\eta_b^2 = \vec{a}^\intercal \mathbf{L}^\intercal \mathbf{L} \vec{a} \tag{4.13}$$

where **L** acts on the boundaries [66].

The use of this regularization scheme helps ensure the physical sense of the measured displacement and strain fields. However, the regularization length over which local mechanical admissibility is enforced must be carefully optimized, particularly when strain localizations are present. The regularization tends to have a smoothing effect on strain fields and thus any real localizations will be affected just as the artifacts are [70].

4.1.4 DIC Parameterization

A proper parameterization of DIC is necessary to asses the quality of the result obtained. To that end, several calculations were performed in order to determine the effects of element size and regularization length on several output parameters of the DIC calculation. The width of the Lüders band, its propagation speed, and the total strain at the end of the Lüders plateau were selected to determine at what element size and regularization length the result converges. The calculation time was also assessed to optimize the calculation.

The data used were from a tensile test on a sample intercritically annealed at 740°C. The first 73 images were used, corresponding to the point at which the Lüders band initiated and propagated across most of the ROI. Element (mesh) sizes of 5,

10, 15, and 20px were used. The px/mm scale as determined from ImageJ using the measured width of the sample was 34.8px/mm. The element sizes were thus 0.13mm, 0.29mm, 0.43mm, and 0.57mm. A comparison of the meshes with 20px, 15px, and 10px element sizes is presented in Figure 4.2 to show the difference in resolution and its impact on the strain localizations. Each image in the figure is taken with a 5-element regularization length.

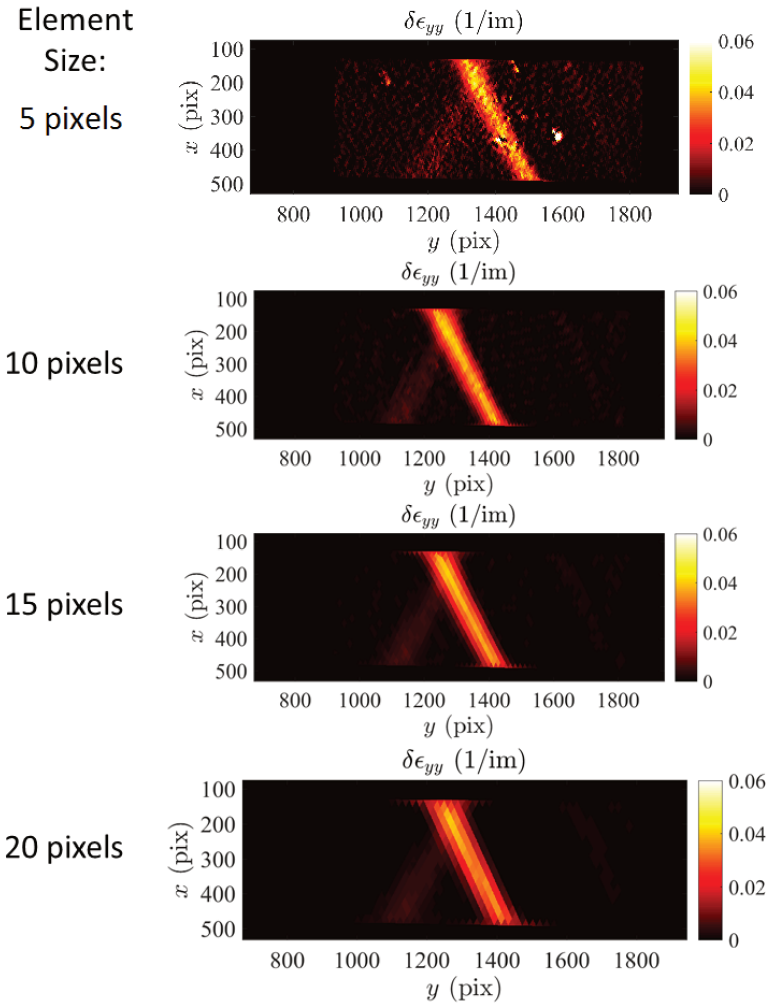

FIGURE 4.2: The element size of the mesh is an important factor in determining the width of the strain bands. If the mesh is too coarse, the band can appear wider than it really is and the maximum strain level can be diminished.

The band characteristics that would be later estimated over the course of complete tensile tests were measured for each pair of element size and regularization length only during elasticity and the passage of the Lüders band in one sample. The width of the Lüders band and its propagation velocity were characterized using ImageJ [71] in which the strain levels were re-encoded as gray levels. Images of the longitudinal strain field where the bands were clearly defined were selected and 8 line plots of the strain level were analyzed along the tensile direction in each image.

The resulting peaks in the line profiles were fitted with Gaussian functions. The full width mid height (FWMH) was used to calculate band width and the peak locations in each of the 8 profiles were used to calculate the band angle, as illustrated in Figure 4.3. Band width measurements are corrected for the displacement of the band during the 3s interval between images. The band velocity is calculated using the shift in position of the strain peaks from one image to another. Distances in pixels are converted to mm by using the known width of the sample to determine the px/mm scale.

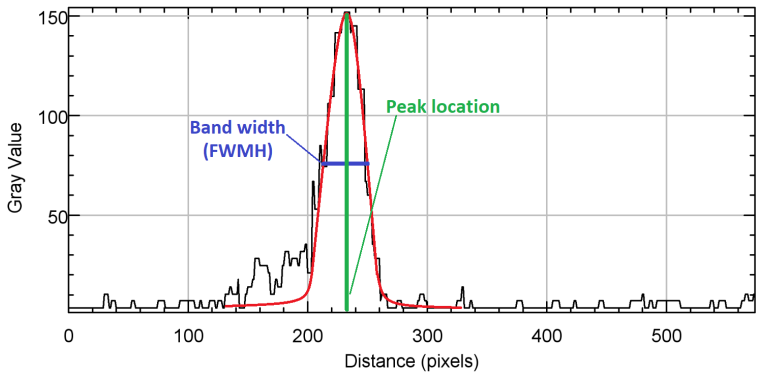

FIGURE 4.3: The band width and peak location were calculated by plotting line profiles and fitting the resulting peaks with Gaussian functions. The full width at mid height (FWMH) was used to represent the band width. The position of the peak was used for both the propagation velocity and the band angle. The strain level is re-encoded as gray level to be used by ImageJ.

The width of the Lüders band was reliant on both the regularization length and element size. The regularization length was particularly important because if it is too large, the band can be smoothed out and the width increased. At the same time, when the regularization length was too small, the strain field was too noisy for the band to be properly identified numerically. This was the case for the calculations made with a 10px mesh and 2-element (so 20px) regularization length and is illustrated in Figure 4.4 with a comparison between different regularization lengths for an element size of 10px. Because of this noise issue, the Lüders band width and propagation speed are not plotted for this case. For the calculation with a mesh size of 5px and regularization length of 25px, the peak associated with the Lüders band was composed of several small, sharp peaks that were able to be identified accurately but that did not provide a real measurement of the band width. It can be seen in Figure 4.5a that the Lüders band width seems to converge to a value around 0.3mm for all element sizes (aside from the erroneous value given at 5px element size and 25px regularization length, as mentioned).

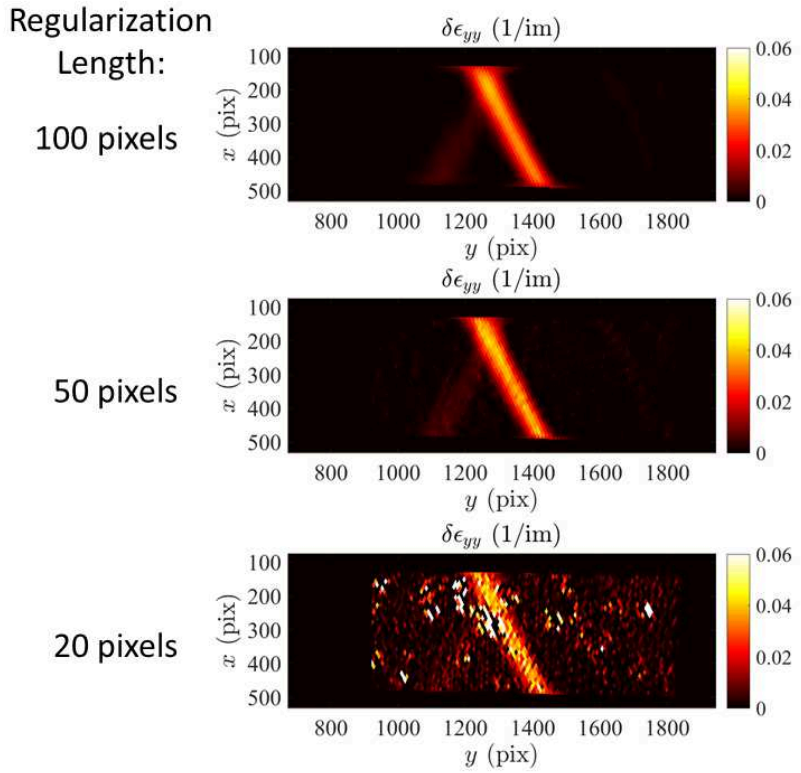

FIGURE 4.4: The regularization length used in the DIC calculation (here for an element size of 10px) is important in that it can reduce noise resulting from mechanically inadmissible strains, but it can also smooth out real localizations. Comparing the top 2 images, a large regularization length eliminates some minor noise that is visible with a shorter regularization length. However it also decreases the strain level in the band and widened it slightly. When the regularization length becomes too small however, noise can become problematic as seen in the bottom image.

The element size and regularization length did not have any significant influence on the band propagation speed or on the strain achieved with the passage of the Lüders band, as seen in Figures 4.5b and 4.5c. The band propagation speed was 0.21-0.22 mm/s in all cases in which the band location was identifiable (i.e. with acceptable levels of noise). The strain after the Lüders plateau showed a maximum at intermediate regularization lengths when the element size was larger (15 or 20px). It is uncertain if this is a real effect or simply a normal statistical dispersion. In any case, there was good agreement between the values obtained by DIC and those obtained with an extensometer (9.5-10%strain).

The calculation time was of interest purely from a practical point of view to avoid excessively long calculation times. The calculation for 73 images took approximately 1h in most cases. When the mesh size was 5px, the calculation time was quite long and a calculation with a 2-element regularization length was not attempted as it would likely have taken 8-10 hours. For smaller mesh sizes of 10 and 15px with a 2-element regularization length, the calculation time increased by about 100% and

200%, respectively. The regularization length did not seem to affect the calculation time for an element size of 20px, which was quite coarse and fairly manageable computationally.

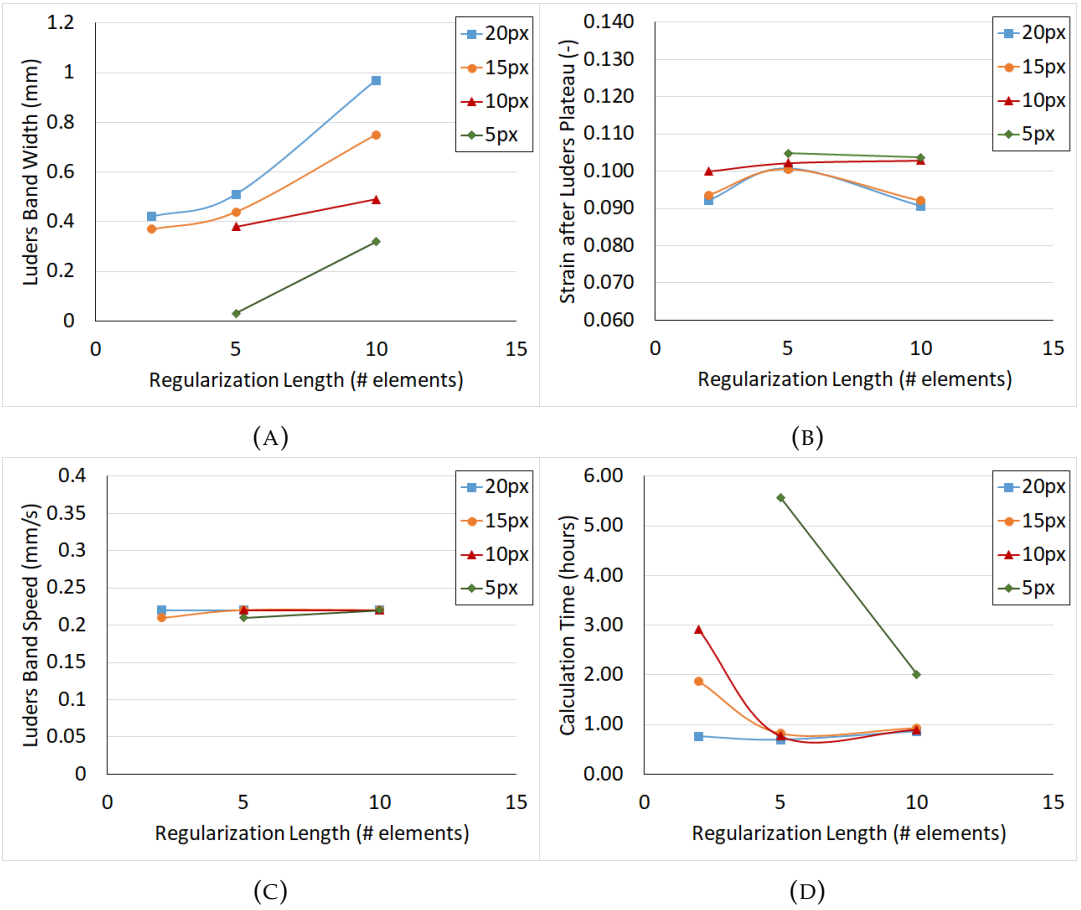

FIGURE 4.5: The calculation was performed at several regularization lengths and mesh sizes to determine the conditions for the convergence of (A) the band width, (B) the strain increment induced by the band, (C) the band propagation speed, and (D) the calculation time.

Based on these results, it was decided that for the complete DIC analyses for each sample and over the entirety of the tensile test (as described in the next section), an element size of 10px (0.29mm) and regularization length of 50px (1.45mm) would be used. This provided a good compromise between precision and calculation time and seemed an optimal choice.

4.2 Magnetic Characterization

An experimental methodology was developed that is able to describe the kinetics of the TRIP effect in steels by following the evolution of a sample's magnetic properties. The following sections seek to first describe the means by which magnetic materials are characterized and the microscopic origins of macroscopic magnetic properties. Next, the means of calculating the retained austenite fraction in a multiphase

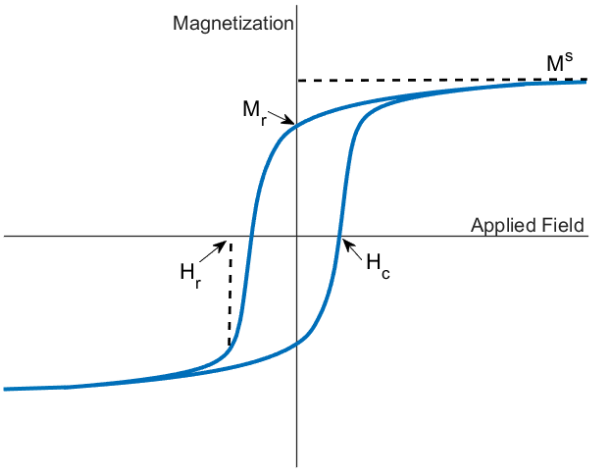

FIGURE 4.6: Schematic illustration of a magnetic hysteresis and the characteristic properties that can be extracted from it. In this work, the value of interest is the saturated magnetization, M^s.

Medium Mn TRIP steel using both magnetic susceptibility and saturation magnetization methods are developed and validated through comparison to other methods of dosing phase volume fractions. Corrections for the localization of the applied magnetic field within individual phases and for the Villari effect are subsequently developed. Finally, results of the *in-situ* generation of M-H hystereses during tensile testing are presented and used to explain the kinetics of the TRIP phenomenon in Medium Mn steels as it relates to the intercritical annealing temperature, strain instabilities, and macroscopic applied strain rate.

4.3 Characterization of Magnetic Properties

4.3.1 Macroscopic Characterization

When characterizing a magnetic material, the properties of interest are typically those related to the ease with which a material is able to be magnetized. Characterization methods are, then, based upon the application of magnetic H-fields of varying magnitude and measurement of the resulting induced B-field or magnetization, M. If one were to apply a cyclic H-field to a sample of ferromagnetic material, one obtains a hysteresis as in Figure 4.6 with several characteristic features that describe the magnetic state of the sample.

In a magnetic hysteresis such as the one shown in Figure 4.6, it can be seen that there is a minimum applied magnetic field that is necessary to induce a magnetization in the sample (after the "first" magnetization when starting from the origin). This value is referred to as the coercivity, H_c, of the material and is a means of quantifying the ease with which magnetic domains are able to reorient themselves in the direction of the applied field. The coercivity is the property that distinguishes

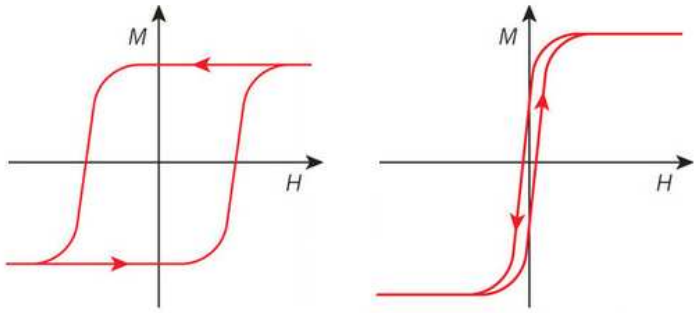

FIGURE 4.7: Schematic comparison of the magnetic hystereses of a magnetically hard material such as α' martensite (left) and a magnetically soft material such as iron ferrite (right). The field required to induce a magnetization in a hard material is significantly higher than in a soft material.

whether a given material is magnetically "hard" or "soft", meaning the amount of energy that needs to be applied in order to obtain a magnetic response from the material. A magnetically hard material will have a much higher coercivity than a magnetically soft material, as can been seen in Figure 4.7, and a hard material will consequently show higher losses represented by the integral of the hysteresis.

For a sufficiently high applied H-field, the magnetization in the sample becomes saturated. This saturation magnetization, M^s, is intrinsic to the material and is thus can be used to characterize the magnetic properties of a material. If the value of M^s is known for each independent phase in a dual-phase material, one could theoretically deduce the volume fractions of each phase by using the measured macroscopic value of M^s for the dual-phase system.

If the applied field is increased such that a strong magnetization is induced and then decreased back to zero, a remanent magnetization is created. That is, a portion of the induced magnetization will remain in the absence of an applied field due to, among other things, alignment of magnetic dipoles and rotation of magnetic domains in the microstructure. The existence of magnetic remanence shows that there is an effect of a material's magnetic history on its actual magnetic state. If one wishes to remove this remanent magnetization to study the case in which there is no magnetic history, one must apply a magnetic field that is of opposite sign to the field used to induce the magnetization in the first place and that is of a magnitude equal to the coercivity of remanence, H_r. The coercivity of remanence is the field in the opposite direction of the magnetization that needs to be applied to negate an existing remanent magnetization and demagnetize the material. Practically speaking, it is difficult to apply an H-field of exactly the value of H_r. As such, the demagnetization of a material is typically achieved by cycling the applied field between positive and negative values with a progressively decreasing amplitude. In this way, most of the remanent magnetization is negated with each cycle and eventually the material arrives at a state with a magnetic remanence very close to zero.

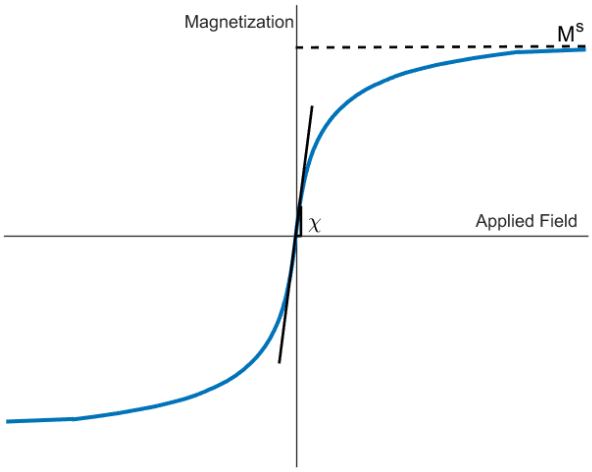

FIGURE 4.8: Schematic representation of the data obtainable via anhysteretic magnetic measurements. The primary interest in this case is χ, which is the magnetic susceptibility of the material and is an intrinsic material property.

This demagnetization procedure is useful in that it permits one to study the magnetic response of a material over a broad range of applied magnetic fields without the need to account for the magnetic load history of the sample. By demagnetizing the sample and then applying a constant H-field, one obtains the induced magnetization for that field magnitude without any remanent effects. This can be performed over a series of values of H to generate a so-called "anhysteretic" curve, as shown in Figure 4.8. Such data is of interest because the magnetic behavior near the origin in an anhysteretic curve is linear and its slope is the initial magnetic susceptibility, which is a physical parameter defining the magnetic response of the material.

The properties defined in this section would permit the experimenter to characterize a magnetic material, but analysis of the properties measured necessitates a certain level of understanding of the microstructural origins of these properties. This is especially important in the current study because the objective is to study the microstructural evolution of a Medium Mn TRIP steel through analysis of its magnetic properties, making a high level of precision essential to the study. In order to obtain such precision, the effects of texture, deformation, and applied load need to be understood.

4.3.2 Microscopic characterization

In magnetic materials, there exists a magnetic microstructure composed of magnetic domains with individual magnetization directions. Figure 4.9 provides the example of magnetic domains in a grain of cohenite in an iron meteorite. Here, the sample

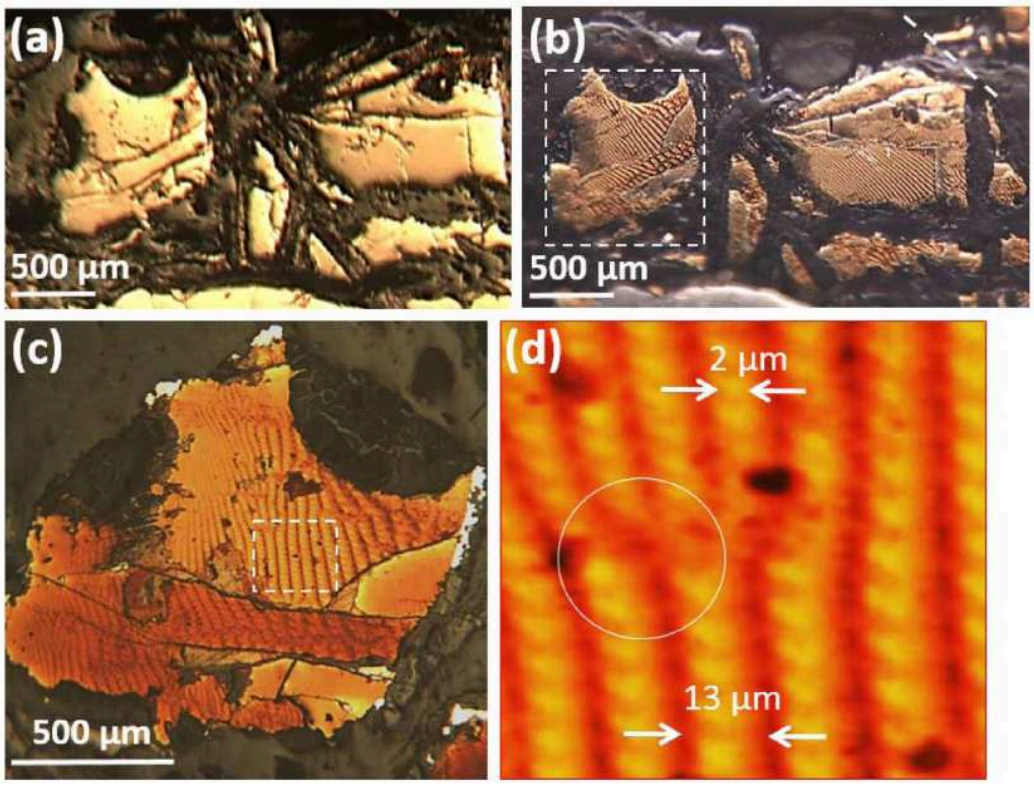

FIGURE 4.9: Sample of an iron meteorite containing magnetic cohenite. The application of a ferrofluid to the surface of the sample creates magnetic constrast that allows magnetic domains to be observed, as illustrated in (c) and (d) here by Reznik [72]

is polished and coated with a ferrofluid to provide magnetic constrast in optical microscopy, revealing the columns of ellipsoidal magnetic domains [72]. The magnetization of a domain is usually aligned with one of the "easy" magnetization directions within the parent grain. In fact, in a single crystal of a magnetic material, there exist families of crystalline directions in which magnetization is more easily induced [73]. For example in bcc iron, the <100> and <111> directions are more easily magnetized, as can be seen in Figure 4.10 [74] where ξ represents the angle between the applied field H and the <100> direction of an iron monocrystal.

A particularly important point illustrated by Figure 4.10 is the minimal variation in the value of M^s. The saturated magnetization in the easy and hard magnetization directions differ by no more than $5{\cdot}10^{-6}$ for an applied field of $4{\cdot}10^6$ A/m, clearly demonstrating that crystal orientation does not affect M^s. This is important from an experimental point of view as it eliminates what would otherwise be a cumbersome analysis of textural effects on the measurement.

There is, however, a coupling of magnetic and mechanical behaviors that will have a significant effect on the measured magnetic properties. When a material in magnetized, an elastic strain is induced in the magnetization direction. This is referred to as magnetostriction. The magnetostrictive strain, ϵ^μ, is sensitive to the

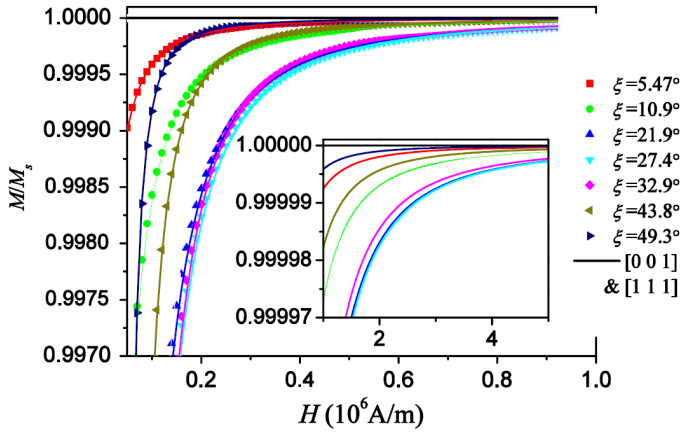

FIGURE 4.10: Zhang [74] showed that the magnetization of a sample depends on the angle between the magnetization direction and the easy magnetization direction in a single crystal, represented by ξ. The effect on saturated magnetization, however, is negligible (see inset).

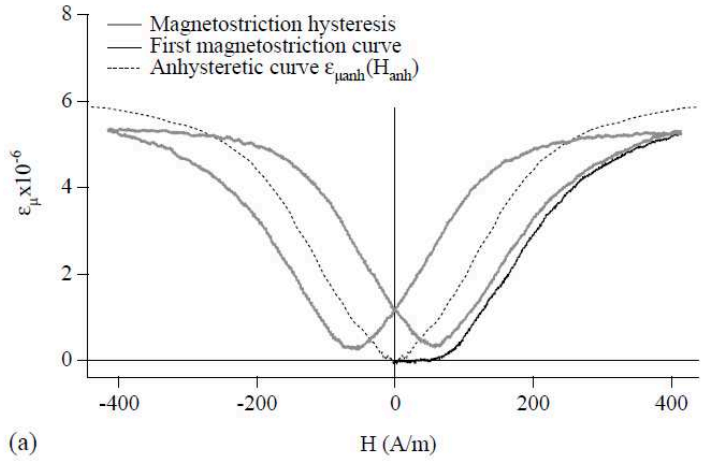

FIGURE 4.11: Hysteretic and anhysteretic representations of the magnetostriction strain as a function of the applied field [75].

sample texture due to varying magnetic hardness relative to the magnetization directions. The evolution of the magnetistrictive strain during cyclic or anhysteretic magnetic fields is shown in Figure 4.11. The magnitude of ϵ^{μ} depends on the average angle between the easy magnetization direction and the direction of the applied field. It is therefore important to take the sample orientation and texture into account when measuring magnetoelastic strains.

Daniel *et al.* have shown [76] that if one assumes that ϵ^{μ} is isochoric, the magnetostrictive strain tensor in a cubic lattice can be expressed in the crystalline reference

frame as

$$\boldsymbol{\epsilon^{\mu}} = \begin{bmatrix} \lambda_{100}(\gamma_1^2 - \frac{1}{3}) & \lambda_{111}\gamma_1\gamma_2 & \lambda_{111}\gamma_1\gamma_3 \\ \lambda_{111}\gamma_1\gamma_2 & \lambda_{100}(\gamma_2^2 - \frac{1}{3}) & \lambda_{111}\gamma_2\gamma_3 \\ \lambda_{111}\gamma_1\gamma_3 & \lambda_{111}\gamma_2\gamma_3 & \lambda_{100}(\gamma_3^2 - \frac{1}{3}) \end{bmatrix} \tag{4.14}$$

where λ_{xyz} is the magnetostrictive constant in the direction $[xyz]$ in the crystalline reference frame and γ_n are the magnetization directions 1, 2, or 3 in the sample reference frame. The magnetostrictive constant λ is defined as the magnetostrictive strain along a given direction of the crystal lattice when the crystal is magnetized to saturation along that direction.

This formulation of the magnetostriction is true for a monocrystal, but if one considers a polycrystal with isotropically-oriented magnetic domains, this microscopic magnetostriction can be translated to a macroscopic effect. When no magnetic field is applied to the sample, the magnetization directions in each domain remain isotropic and the induced magnetostrictions cancel each other out. However, if a field is applied, the domains will attempt to align themselves with the direction of the applied field. The distribution of magnetization directions in domains is thus no longer isotropic and a net magnetization is obtained. This magnetization results in a magnetostriction that is concentrated in the magnetization direction and thus a strain that is measurable at the macroscopic scale is obtained.

The existence of this magneto-mechanical coupling also means that an applied stress will have an effect on the magnetic properties of the loaded sample. For example, it has been shown on several occasions that a compressive stress of only a few dozen MPa can considerably decrease the susceptibility of a magnetic material, whereas tensile stresses have the opposite effect. However this magnetoelastic effect—also referred to as the Villari effect [77]—will reverse itself (Villari reversal) at sufficiently high magnitudes of the applied field. Such behavior is illustrated in Figure 4.12 where anhysteretic data for a ferritic material are given at 0 and $\pm$55 MPa. Looking at, for example, the curve for -55 MPa it can been seen that while the magnetization is initially lower than at 0 MPa, it surpasses the magnetization at 0 MPa at an applied field of about 1500 A/m. This stress effect is attributed to the deformation of the crystal lattice and resulting changes in the magnetocrystalline energy of the domains. The applied stress forces a reorientation of the magnetic domains within a given grain and consequently changes the net magnetization.

With a basic understanding of how magnetic materials are characterized and how microstructure and mechanical loads can affect magnetic properties, it is now possible to look at some examples of how magnetic measurements have been previously applied to steels.

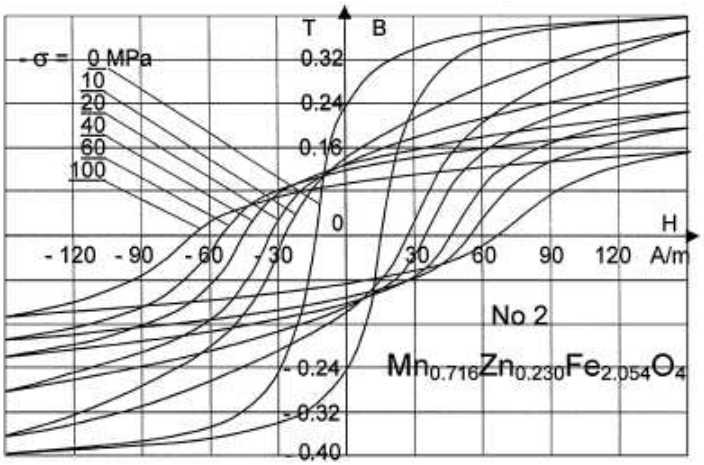

FIGURE 4.12: The Villari effect [78] is defined by a change in magnetic properties due to an applied stress. Note that at a certain field level, the sign change of the effect reverses. This is referred to as Villari reversal. The effect on the value of M^s is significant, even for a small applied load. As such, this effect needs to be corrected for *in-situ* application of magnetic measurements.

4.3.3 Example 1: Analysis of Anisotropy of TRIP by Saturated Magnetization

The most commonly employed use of saturated magnetization measurements in the characterization of the austenite to martensite transformation rate in TRIP steels. Compared to XRD or EBSD, magnetic methods provide a simpler means of obtaining several retained austenite measurements over the course of a mechanical test. It is also more convenient in terms of equipment availability than, say, synchrotron or neutron diffraction experiments. One such study performed by Beese and Mohr [79] will now be presented in which directional magnetic measurements were made on a tensile sample *in-situ* to determine the degree of anisotropy of the martensite transformation in an austenitic stainless TRIP steel.

Flat specimens of a 301LN austenitic stainless steel with the composition provided in Table 4.1 containing retained austenite and approximately 20% thermal martensite were studied in unidirectional tension. Samples were taken in the rolling direction, transverse direction, and on the diagonal at 45° from the rolling direction of the sheet. The samples were strained in tension and a ferritescope was used to measure the saturated magnetization at several points during testing. As can be seen in Figure 4.13, the work hardening rate when strained in the rolling direction was lower than in the transverse or diagonal directions. It was hypothesized that this could be to do anisotropy in the martensite transformation rate. EBSD texture measurements were also performed to determine the texture evolutions before and after straining.

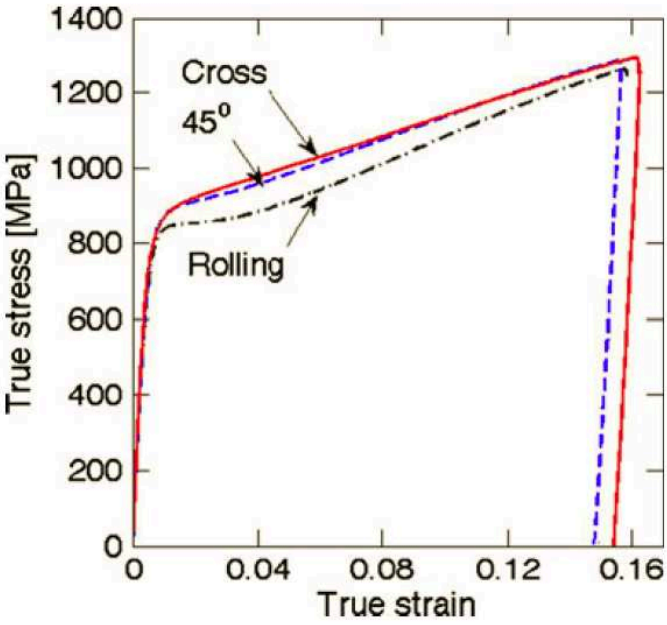

FIGURE 4.13: Variations in strain hardening rate with tensile direction relative to the rolling direction of the sheet. Beese and Mohr suggested that this was due to anisotropy in the martensite transformation rate with respect to the tensile direction. [79]

TABLE 4.1: Austenitic Stainless Steel 301LN Composition (wt%)

C	Cr	Ni	N	Fe
0.025%	17.5%	6.5%	0.15%	*bal.*

It was observed in this study that the applied load had a significant effect on the ferritescope measurements, so the authors periodically unloaded the sample to obtain more reliable measurements. Figure 4.14 illustrates the data obtained and their variation during the loading and unloading cycles.

This use of loading and unloading cycles made it possible to minimize the effects of the Villari effect, thus improving the accuracy of the measurements. The authors noted that while unloading will remove the macroscopic load, there will be a residual stress at the grain scale that remains due to the martensite transformation. To confirm that the calibration parameters used remained valid given the existence of these residual stresses, neutron diffraction experiments were performed to determine the lattice strains in the martensite in the unloaded state. The ferritescope data was extrapolated to obtain the ferritescope reading that would correspond to a zero residual stress state under the hypothesis that the magnetoelastic effect is linearly correlated to stress. It was found that the error of 4-8% induced by residual stresses in the martensite was able to be accounted for in the calibration through the extrapolation of the macroscopic ferritescope data.

With the ferritescope measurements validated, tensile tests were performed on

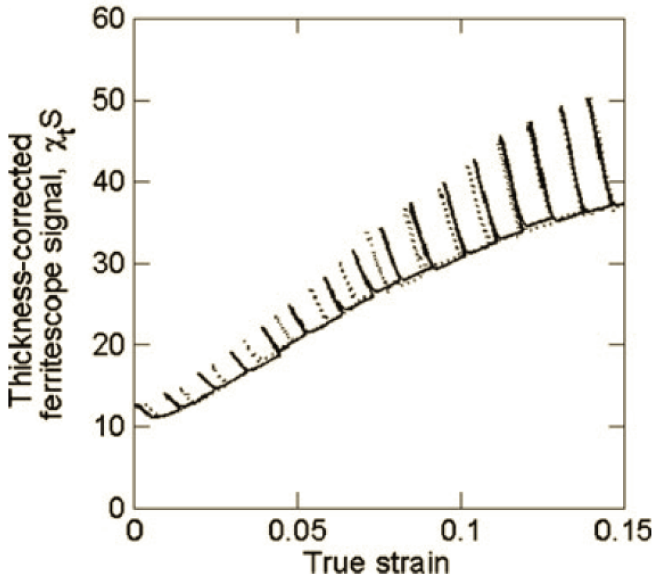

FIGURE 4.14: Ferritescope signal obtained *in-situ* over the course of a tensile test. Periodic unload/reload cycles show a very strong effect of the applied stress on the saturated magnetization due to the Villari effect [79].

samples taken in the rolling, transverse, and diagonal directions of the sheet. Ferritescope measurements were taken throughout with the periodic unloads and, as can be seen in Figure 4.15, the kinetics of the martensite transformation did not vary significantly for different loading directions. This, combined with EBSD texture measurements performed on the same samples, would suggest that the variations in hardening rate observed in Figure 4.13 are due to the initial texture rather than differences in the rate of martensite transformation.

4.3.4 Example 2: Effects of Temperature and Triaxiality on TRIP Kinetics

A study was performed by Kim *et al.* [80] in which the martensite transformation rate in a TRIP 780 steel was characterized as a function of deformation temperature and stress triaxiality. Martensite volume fractions were measured using an MSAT30 ferritescope with a field strength of 300 kA/m. The composition of the steel studied is provided in Table 4.2 and the test types and associated triaxialities are given in Table 4.3. Tests were performed at 25°C, 60°C, and 100°C with the exception of the shear test which was only performed at 25°C.

TABLE 4.2: TRIP 780 Composition (wt%)

C	Mn	Al	Cr	Si	Ni	P	S	Fe
0.15%	2.1%	1.5%	0.12%	0.06%	$< 0.01\%$	0.015%	0.003%	*bal.*

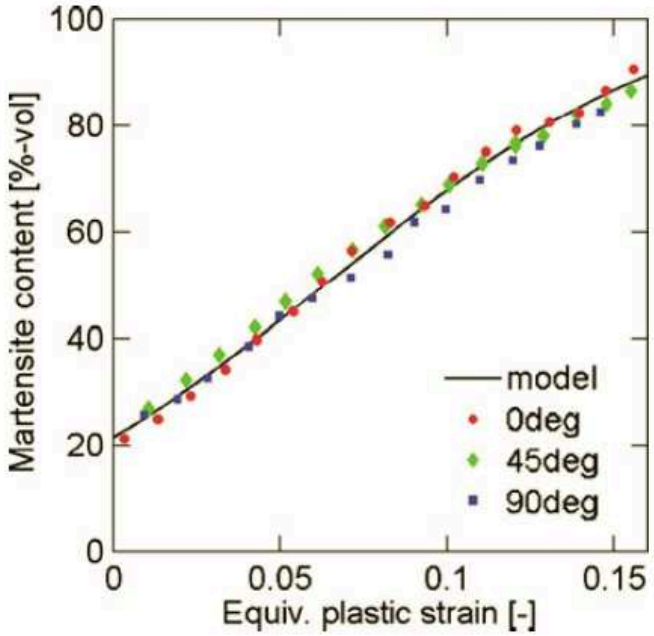

FIGURE 4.15: Beese and Mohr demonstrated that the TRIP effect was not dependent on the tensile direction relative to the loading direction and concluded that the observed differences in strain hardening were likely due to the initial texture in the sheet [79].

TABLE 4.3: Stress Triaxialities by Test Type

Uniax. Tension	Biaxial Tension	Plane Strain	Shear	Uniax. Compression
$\frac{1}{3}$	$\frac{2}{3}$	0.58	0	$-\frac{1}{3}$

Strain rates of $10^{-3}s^{-1}$ were used for all tests. Biaxial tests were performed using the hydraulic bulge methodology, shear tests using simple shear for sheet metals, and compression on flat samples using an anti-buckling jig. In cases where extensometers could not be used to measure strain (biaxial, shear) DIC was used. No strain measurement was made for the plane strain samples because the tensile length was too small and the furnace window did not permit the use of digital image correlation (DIC).

Kim *et al.* showed that as the deformation temperature increased, the martensite transformation rate decreased significantly. Figure 4.16a shows that this trend occurred for all triaxialities and that there was a significant effect of the stress triaxiality on the transformation rate. While in this case the trend was not clear, a previous study by Beese and Mohr [79] showed that the transformation rate varied linearly with stress triaxiality.

Beese and Mohr [79] had proposed an empirical model to predict the martensite fraction as a function of strain, triaxiality, and the Lode parameter. Beese and Mohr's

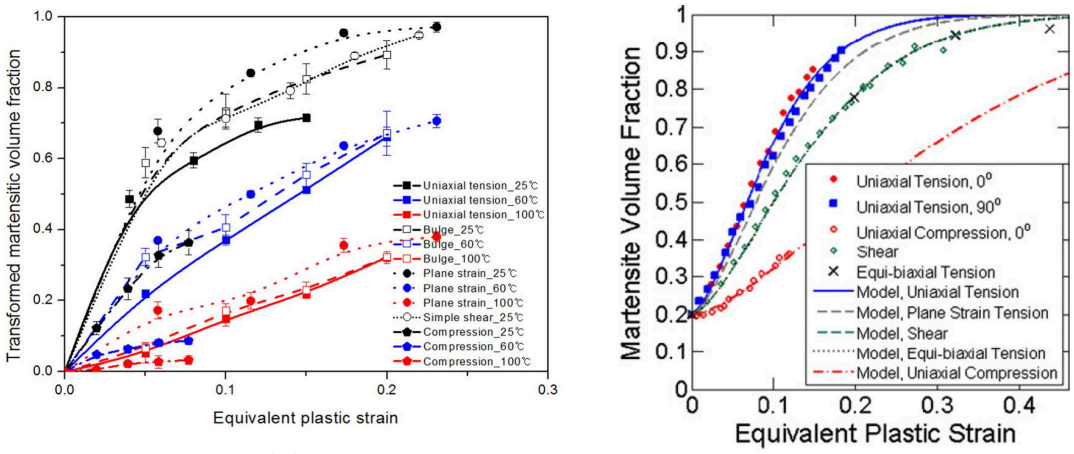

(A) (B)

FIGURE 4.16: Kim *et al.* experimentally illustrated the differences in TRIP kinetics for different stress triaxialities and deformation temperatures (A) and developed a model that was able to reproduce these results fairly well (B) by adding temperature effects into a model previously proposed by Beese and Mohr [80].

model is given by:

$$\dot{f}_{\alpha'} = (f_{\alpha',max} - f_{\alpha'})nD(D\bar{\epsilon})^{n-1}\bar{\epsilon} \tag{4.15}$$

where $\bar{\epsilon}$ is the Von Mises equivalent strain, $f_{\alpha'}$ and $\dot{f}_{\alpha'}$ are the martensite fraction and it's time derivative, and n and D are material parameters. The parameter D is determined by

$$D = D(\eta, \theta) = (D_0 + a_\theta \theta + a_\eta \eta) \tag{4.16}$$

where θ and η are respectively the Lode parameter and stress triaxiality and a_θ, a_η and D_0 are material parameters. Kim *et al.* modified this model by redefining D as a product of an adjusted version of Beese and Mohr's $D_1(\eta, \theta)$ times Kim *et al.*'s newly-defined $D_2(T)$:

$$D = D_1(\eta, \theta) \cdot D_2(T) \tag{4.17}$$

where

$$D_1(\eta, \theta) = (D_0 + a_\theta \theta^a + a_\eta \eta^b) \tag{4.18}$$

and

$$D_2(T) = A + B \cdot exp(-\frac{T - 25}{C}) \tag{4.19}$$

The exponents a and b in Equation 4.18 have been added by Kim *et al.* to account for the nonlinearity of the relationships between $\dot{f}_{\alpha'}$ and θ and η that they observed. The parameters A, B, and C in Equation 4.19 are model parameters.

The comparison of their model to experimental data is shown in Figure 4.17.

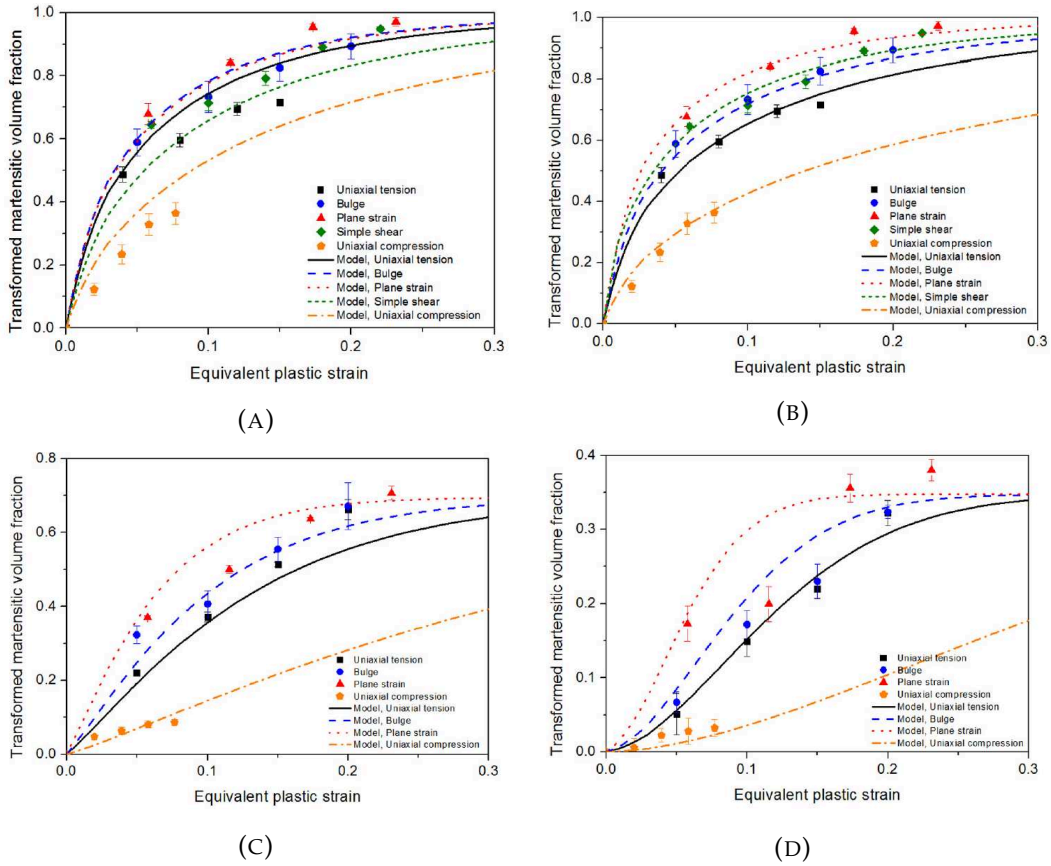

FIGURE 4.17: The model developed by Beese and Mohr tended to overestimate the transformed martensite fraction as observed by Kim *et al.* (A), but the addition of temperature effects improved the model fit for experiments performed at 25°C (B), 60°C (C), and 100°C (D) [80].

Figure 4.17a shows the comparison of Kim *et al.*'s room temperature data to the unmodified model proposed by Beese and Mohr. Figures 4.17b, 4.17c, and 4.17d show the comparison of the temperature sensitive model to experimental data at 25°C, 60°C, and 100°C respectively. The model accurately reproduces the trends observed in the experimental data for both deformation temperature and stress triaxiality, albeit with 7 calibrated model or material parameters. Nonetheless, the study clearly demonstrates that both stress triaxiality and deformation temperature play a critical role in determining the martensite transformation rate in TRIP steels by using magnetic saturation measurements to calculate retained austenite volume fractions in deformed samples.

A note on ferritescopes

Ferritescopes are a common tool for making measurements of the saturated magnetization of a sample during mechanical testing. They use a magnetic probe to measure variations in the induced magnetic field when the probe is place on the surface of a sample. The ferritescope outputs a "ferrite number" that is related to the magnetic phase content of the sample. The ferritescope reading needs to be calibrated for the thickness of the sample and a proportionality constant needs to be determined using several samples with different martensite volume fractions. This leads to a measurement of the ferromagnetic phase fraction that strongly depends on empirical fits and calibrations and thus the measurement obtained via ferritescopes loses some of its physical sense. This problem is compounded by the fact that ferritescope manufacturers, to the author's knowledge, do not provide a method of accounting for the effect of an applied load on the measurement.

For this reason, the current work forgoes the use of a commercial ferritescope and opts for a homebrew solution. While more physically cumbersome than a ferritescope probe, it allows the experimenter to directly access the physical properties of the sample and be more certain of how the ferromagnetic volume fraction is calculated.

4.4 Development of an *In-situ* Magnetic Testing Device

The results presented in Chapter 3 showed that in Medium Mn TRIP steels, the intercritical annealing temperature used had a drastic effect on the stability of the retained austenite present in the steel. In order to understand the relationship between the intercritical annealing temperature and the amount of work hardening obtainable, it is necessary to quantify the amount of retained austenite that transforms to martensite for a given strain increment. That is, a description of the phase transformation kinetics as a function of strain is needed for each intercritical annealing temperature. A number of methods (such as XRD, EBSD, thermal diffusivity, etc. [81]) would be suitable if this were the only goal, but the presence of strain localizations complicates the issue.

It was observed previously that the presence of strain bands during tensile testing of samples annealed at 740°C and 760°C led to steps or plateaus in the tensile curves. Additionally, Lüders plateaus of up to 7-8% were observed in these samples. It would be interesting, then, to understand how the TRIP effect is manifested when

the strain is localized in bands in this way. However while the Lüders bands are visible on the surface of the sample, the subsequent PLC type bands are not. An *in-situ* method of measuring the retained austenite volume fraction is thus needed to characterize the interaction between the bands and the phase transformation. Further reducing the number of appropriate retained austenite measurement methods is the fact that these bands propagate relatively quickly, providing a burst of induced strain over several seconds of tension. Any *in-situ* retained austenite measurement must then be able to be performed very rapidly (in terms of time per measurement) and at a high sampling rate (in terms of the number of measurements made per unit time). Given these constraints, the decision was made to use a magnetic measurement system.

To truly capture the microstructural evolution over the course of a tensile test *in-situ*, the best option is to use the saturated magnetization to determine the retained austenite volume fraction. Using this metric would permit rapid, high frequency measurements of the retained austenite volume fraction by rapidly cycling the applied magnetic field. However, it was decided that the magnetic results should be compared to previous XRD measurements to ensure that the system developed here enables accurate retained austenite fraction measurements. Then, the system needed to be adapted for *in-situ* use; that is, in the presence of an applied load. It was demonstrated in Section 4.3.3 that the Villari effect results in a very strong influence of the applied stress on the magnetization measurement. A correction for this magnetoelastic effect was thus developed based on [77, 82].

Another consideration was that, due to the presence of multiple phases with very different magnetic properties, the local applied magnetic field would vary from one phase to another. In steels, there are both magnetically hard or soft phases–such martensite and ferrite, respectively–meaning that stronger applied fields are needed to obtain the saturation magnetization if magnetically hard phases are present. Additionally, other phases show a negligible magnetic response. Austenite and pearlite would be examples of negligibly magnetic phases that can be present in steels. Austenite in particular is a paramagnetic phase. This means that the magnetic dipoles resulting from the presence of free electrons in fcc iron can be aligned through the application of a magnetic field but do not interact with neighboring dipoles, resulting in a very weak magnetization. Because of this lack of dipole interaction, once the applied field is removed austenite reverts to a zero-magnetization state. While it does technically magnetize, the magnetization obtainable in austenite for a given applied field are dwarfed by the magnetization in ferrite or austenite for the same field. This stark difference in magnetic properties results in demagnetizing effects at the phase boundaries [83]. A correction was thus developed that would take into account the local applied field in each phase, rather than just the macroscopic "average" applied field.

The localization correction had previously been developed by Daniel and Hubert

[76] in a model and is used here as a correction to experimental data. The magnetoelastic correction is based on the work of Hubert and Lazreg [77] but is novel in its implementation *in-situ* during tensile experiments. This is, to the author's knowledge, the first use of *in-situ* magnetic measurements that do not affect the tensile test or require its interruption and for which the stress effect is corrected. Moreover, it is the only existing method (aside from synchrotron) that can measure the retained austenite volume fraction *in-situ* without a need to pause the experiment. The two corrections employed here provided a significant improvement in measurement accuracy and an advancement in the way that magnetic measurements of retained austenite fractions are performed. The system developed will be described in the subsequent sections.

4.4.1 Magnetic Measurement System

A measurement system was developed based on the work of Bormio-Nunes and Hubert [84] in order to perform *in-situ* measurements of the retained austenite volume fraction during tensile testing. The device is capable of producing both anhysteretic (see Figure 4.8) and hysteretic (see Figure 4.6) data. As such, it was possible to first use the magnetic susceptibility obtained via anhysteretic data to verify the precision of the method using a physical material property. The major downside to anhysteretic measurements, however, is that they take a long time to perform. With the system developed here, a single anhysteretic curve takes 30-40 minutes to record, hence the preference for saturated magnetization which takes only a fraction of a second per cycle.

The setup consists of a primary coil placed around a tensile sample that creates a magnetic field in the sample. A schematic of the setup is provided in Figure 4.18. The applied field is cycled through the application of a triangular current waveform. This current is then integrated over the length of the coil to obtain the applied field. The applied field is enclosed by two high-permeability ferrimagnetic yokes used to contain the magnetic field and concentrate it in the sample. The induced magnetic flux in the sample is then measured as a voltage using a pick-up coil wound around the sample surface. The pick-up coil measures the average flux in the portion of the sample around which the driving coil is placed. In the current setup, this corresponds to a measurement over 37mm of the 60mm active tensile length of the sample.

Because the driving coil encloses the sample, strain measurements must be performed with a strain gauge if the local strain is desired. Here, the plastic strain in tensile experiments is instead calculated using the displacement of the crosshead and the assumption that the tensile machine is rigid.

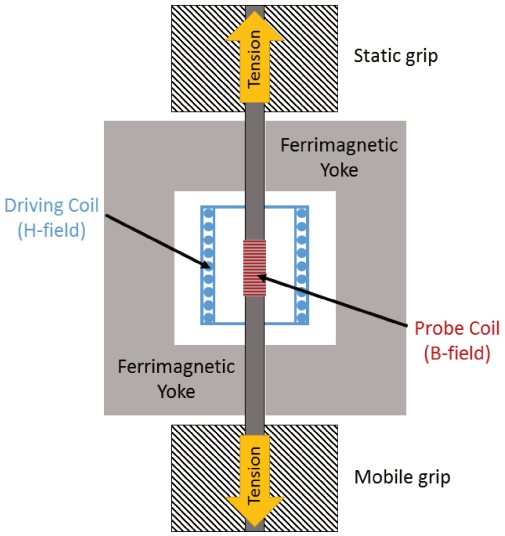

FIGURE 4.18: Schematic of the magnetic measurement system. A primary coil (H-field) placed around the tensile sample induced a magnetic H field in the sample, and the current thereby induced in the sample is measured by the probe coil (B-field) and converted to magnetization, M. The coils are enclosed in two ferrimagnetic yokes to contain the magnetic field.

The measurement is performed at low frequency (on the order of 1 to 10Hz) in order to ensure that no eddy currents are present and that the penetration depth of the measurement is sufficient to include the whole thickness of the sample. While the setup used is applied to flat tensile samples, it could easily be adapted to other geometries for either uniaxial or biaxial tests [85]. The sizes of the coils can be made larger or smaller as needed (as long as one is careful to note the number of loops in the coil as that will be needed for magnetostatic calculations and to calibrate the applied field using, for example, a Hall effect H-coil). The primary consideration when changing sample geometries is that of the measurement depth, or "skin depth", e, which is related to the frequency in the driving coil by

$$e = \frac{1}{\sqrt[2]{\pi f \sigma \mu}} \tag{4.20}$$

where σ is the electrical conductivity of the sample, μ its magnetic permeability, and f is the frequency of the cyclic applied field. In the current case, this provides an estimation of the skin depth of 8mm which is several times greater than the thickness of the sample and ensures that the measure is volumetric. For this particular sample geometry, the frequency could be increased to 200-300Hz while still maintaining a volumetric measurement. It should be noted that this would affect the measurement in other ways, however, such as increasing the noise in the signal. The fact that the measurement is a bulk measurement over the entire volume inside the driving coil provides a significant advantage over other common austenite fraction measurement methods such as XRD or EBSD in that the volume analyzed is several orders of magnitude larger. XRD and EBSD both provide surface measurements over an

area of several μm^2 to several mm^2. This magnetic measurement is made over a volume of approximately $450 mm^3$, providing an excellent statistical representation of the microstructure particularly in the current case when the average grain size is less than $1 \mu m$.

The applied field and induced magnetization are averaged over the microstructure in the portion of the sample contained within the driving coil and can be written as

$$\vec{H} = f_\alpha \vec{H}_\alpha + f_{\alpha'} \vec{H}_{\alpha'} + f_\gamma \vec{H}_\gamma \tag{4.21}$$

$$\vec{M} = f_\alpha \vec{M}_\alpha + f_{\alpha'} \vec{M}_{\alpha'} + f_\gamma \vec{M}_\gamma \tag{4.22}$$

where $f_n, \vec{H}_n$, and $\vec{M}_n$ are respecitvely the volume fraction, applied field, and induced magnetization in the phase n. For the purposes of the current study (and as is often done when performing magnetic characterizations of TRIP alloys) the ferrite and martensite are treated as a single ferromagnetic phase which will be referred to from here on using the subscript α. The assumption, then, is that ferrite and martensite have the same magnetic properties. In reality there is a difference between the two—ferrite is a magnetically soft phase whereas martensite is magnetically hard. Carbon content also has an effect on the magnetic properties of iron. While it is entirely possible the distinction could be made between the two phases through the use of an additional property like the coercivity or remanent magnetization, it would require a significant time investment and is thus viewed as a future perspective for the moment. In the current work both phases are assumed identical which will lead to a slight but acceptably small over-estimation of the retained austenite content. Simplifying Equations 4.21 and 4.22 as such leads to

$$\vec{H} = f_\alpha \vec{H}_\alpha + f_\gamma \vec{H}_\gamma \tag{4.23}$$

$$\vec{M} = f_\alpha \vec{M}_\alpha + f_\gamma \vec{M}_\gamma \tag{4.24}$$

where the subscript α now represents the combined behavior of ferrite and martensite. Essentially, the phases in the sample are divided into two group: ferromagnetic phases and non-magnetic phases. This includes then, the hypothesis that austenite is non-magnetic. This is a strong hypothesis because austenite's magnetic response is minimal compared to that of ferrite or martensite and as such it will have a negligible contribution to the macroscopic magnetic response of the sample. If the magnetization in the austenite is then assumed to be 0,

$$\vec{M} = f_\alpha \vec{M}_\alpha \tag{4.25}$$

from which one obtains the magnetization ratio that is typically used when making magnetic measurements of the retained austenite volume fraction:

$$f_\alpha = \frac{\vec{M}}{\vec{M}_\alpha} \tag{4.26}$$

where $\vec{M}$ is the measured average induced magnetization in the sample and $\vec{M}_\alpha$ is the induced magnetization in the ferromagnetic phase only. This ratio can be related to the magnetic susceptibility, χ, by recognizing that $\chi = \vec{M}/\vec{H}$ to obtain

$$f_\alpha = \frac{\chi}{\chi_\alpha} \cdot \frac{H}{H_\alpha} \tag{4.27}$$

and if one then assumes that the applied field is the same in all phases (as is commonly done) one obtains a simple ratio of susceptibilities

$$f_\alpha = \frac{\chi}{\chi_\alpha} \tag{4.28}$$

where χ_α is the susceptibility of an purely ferromagnetic sample.

The formulations for the retained austenite volume fraction proposed in Equations 4.26 and 4.28 were then compared to XRD measurements. A tensile sample that had been intercritically annealed at 780°C was strained and periodically unloaded to perform both hysteretic (to obtain M^s) and anhysteretic (for χ) measurements at several levels of plastic strain. The change of magnetic behavior with the progression of plastic strain is shown in Figure 4.19 where both anhysteretic curves and hysteretic cycles are shown for several levels of plastic strain[1]. The retained austenite volume fraction was calculated using equations 4.26 and 4.28 and compared to previous XRD experiments on the same alloy for four different strain levels. The comparison is presented in Figure 4.20. It can be seen in the figure that while the overall agreement between magnetic measurements and XRD measurements is good, there is a large discrepancy between the two methods over the first 1-2% of strain: the moment of the test where the largest volumes of retained austenite are present. This discrepancy then can be said to be due to the demagnetizing effect at the phase boundary between the ferromagnetic and non-magnetic phases as previously discussed. To improve the accuracy of the measurement when large volume fractions of austenite are present, a localization operation was performed to take into account the heterogeneity of the applied field at the grain scale.

[1]Note that the coercivity of the sample increases as the phase transformation progresses. This is due to the generation of magnetically hard martensite and hints at the future possibility to distinguish between the ferrite and martensite via magnetic measurements.

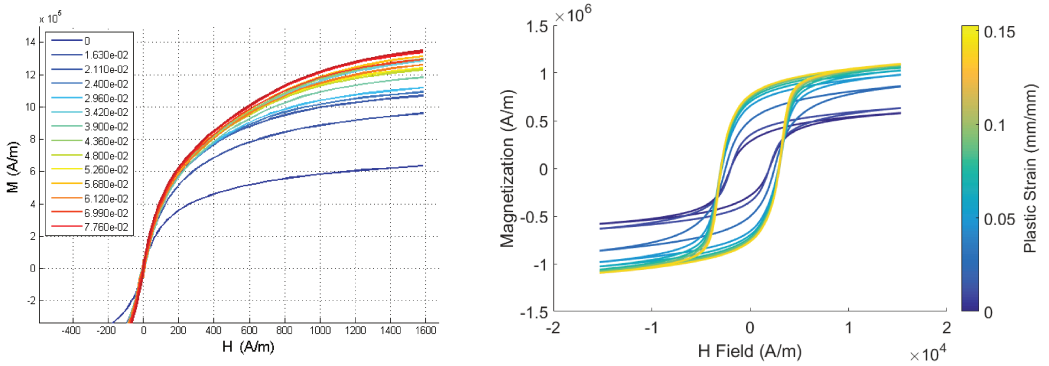

(A) (B)

FIGURE 4.19: Comparison of anhysteretic curves (A) and hystereses (B) obtained as a function of plastic strain in a sample annealed at 780°C. The saturated magnetization M^s and magnetis susceptibility χ both increased with plastic strain due to the transformation of paramagnetic austenite to ferromagnetic martensite.

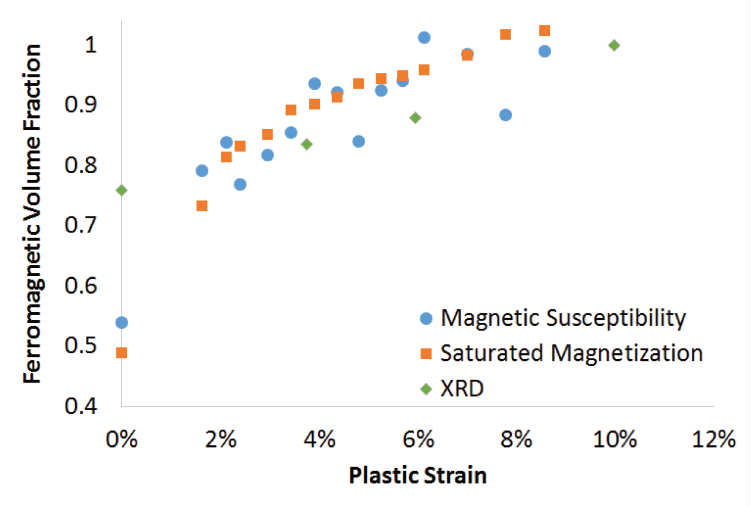

FIGURE 4.20: The magnetic measurements based on M^s and χ were in good agreement except for the initial point where large fraction of retained austenite were present. This underlines the need to correct for the grain-scale demagnetizing effect that occurs at phase boundaries and results in an over-estimation of the austenite fraction.

4.5 Corrections to Retained Austenite Calculation

The data provided in Figure 4.20 make it obvious that a correction for the grain-scale demagnetizing effect at phase boundaries is needed. Such a correction would greatly improve the accuracy of the measurement when large volume fractions of retained austenite are present. Additionally, a correction for the effect of stress on the magnetic properties via the Villari effect is needed for this system to be usable *in-situ*. This section will describe the corrections made for these two effects and will borrow from published work [86].

4.5.1 Localization Correction

In mechanics a commonly employed method of localizing the macroscopic stresses and strains into each phase is the application of the localization model developed by Eshelby [87] which considers a spherical particle embedded in an infinite homogeneous equivalent medium. This same model can be applied to any material property to obtain a localization of that property in each phase.

If a given phase i is treated as a spherical particle embedded in a homogeneous matrix and that the particle's magnetic behavior follows a linear constitutive law (since the demagnetizing field is small enough to remain in a linear regime), the magnetization in the particle can be expressed as

$$\vec{M}_i = \chi_i \vec{H}_i \tag{4.29}$$

then the solution to the Eshelby problem will give

$$\vec{H}_i - \vec{H}^\infty = \frac{1}{3 + 2\chi^\infty}(\vec{M}^\infty - \vec{M}_i) \tag{4.30}$$

where $\vec{H}^\infty$ and $\vec{M}^\infty$ denote the macroscopic (average) magnetic field and magnetization and χ^∞ is the macroscopic susceptibility defined as $\chi^\infty = M^\infty/H^\infty$. Applying Equation (4.30) to the current problem without an applied stress, the field along the magnetization axis in the ferromagnetic phase α becomes

$$H_\alpha = H + \frac{1}{3 + 2\chi}(M - M_\alpha) \tag{4.31}$$

with $\chi = M/H$. With the magnetic susceptibility of the ferromagnetic phase defined as $\chi_\alpha = M_\alpha/H_\alpha$, it follows

$$\frac{H}{H_\alpha} = \frac{3 + 2\chi + \chi_\alpha}{3 + 3\chi} \tag{4.32}$$

where the volume fraction of the ferromagnetic phase is defined as

$$f_\alpha = \frac{M}{M_\alpha} \tag{4.33}$$

It should be noted that this definition differs from the classical one given in Equation (4.26) since saturation is not achieved. This relationship is most appropriate for low magnetic field levels where the magnetic behavior can be considered as linear. Equation (4.33) is transformed by introducing the corresponding magnetic fields and susceptibilities

$$f_\alpha = \frac{\chi H}{\chi_\alpha H_\alpha} \tag{4.34}$$

Finally, by combining Equations (4.32) and (4.34), f_α reads

$$f_\alpha = \frac{\chi(3 + 2\chi + \chi_\alpha)}{\chi_\alpha(3 + 3\chi)} \tag{4.35}$$

However, this expression is only valid considering the initial susceptibility (or linear behavior). By recognizing that $\chi = \frac{1}{3}A_s\mu_0 M^{s2}$ and $\chi_\alpha = \frac{1}{3}A_s\mu_0 M_\alpha^{s2}$ and considering $\chi \gg 1$, the volume fraction of ferromagnetic phase is expressed as

$$f_\alpha \approx \left(\frac{M^s}{M_\alpha^s}\right)^2 \tag{4.36}$$

The volume fraction of ferromagnetic phase thus obtained provides a second estimation of $f_{\alpha+\alpha'}$ with the hypothesis that the ferromagnetic areas do not interact. It is unlikely that no interaction occurs between individual grains in the ferromagnetic phase in reality, but a compromise between expressions (4.26) and (4.36) can be made through the use of a ratio parameter, κ, leading to

$$f_{\alpha+\alpha'} = \frac{M^s}{M_\alpha^s} + \kappa \cdot \left[\left(\frac{M^s}{M_\alpha^s}\right)^2 - \frac{M^s}{M_\alpha^s}\right] \tag{4.37}$$

where κ is a mixing parameter identified using an unstrained sample with a known ferromagnetic volume fraction.

When Equation 4.37 is used with $\kappa = 2/3$, the calculation of the retained austenite volume fraction is greatly improved compared to the non-localized data presented in Figure 4.20. The localized data are presented in Figure 4.21 alongside the same XRD data for comparison. It should be noted that because ferrite and martensite do not quite have the same magnetic properties as is assumed here [77], the initial retained austenite fraction in this case is overestimated. This is due to the presence of thermal martensite in the initial microstructure which is more weakly magnetic than ferrite.

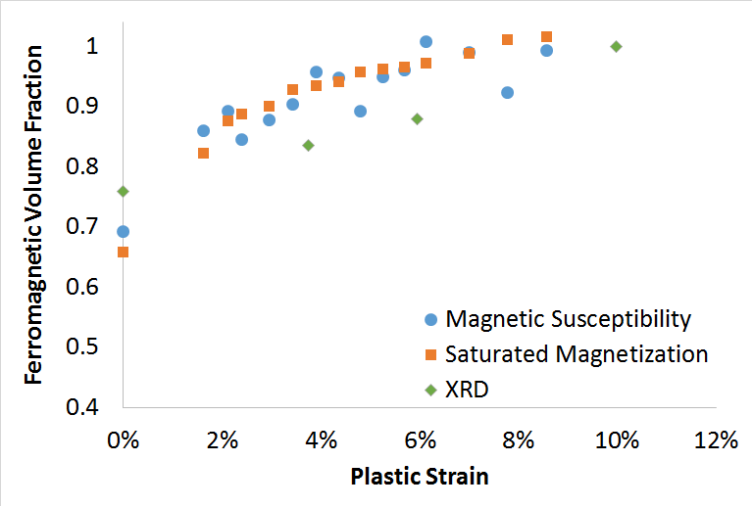

FIGURE 4.21: The application of the localization correction results in a significant improvement in the calculated retained austenite fraction when large proportions of austenite are present compared to the case without the correction in Figure 4.20.

4.5.2 Magnetoelastic Correction

If measurements of the sample magnetization are to be made *in-situ*, then the effect of the applied stress on the magnetic properties must be taken into account since it has been shown that even modest loads can have a non-negligible impact on magnetization [88]. This can be clearly seen in Figure 4.22 where magnetization data obtained during unloading of a sample annealed at 760°C is shown. The magnetization changes drastically with the applied stress even though during unloading the microstructure remains constant, illustrating rather definitively the significance of the Villari effect and its impact on the saturated magnetization.

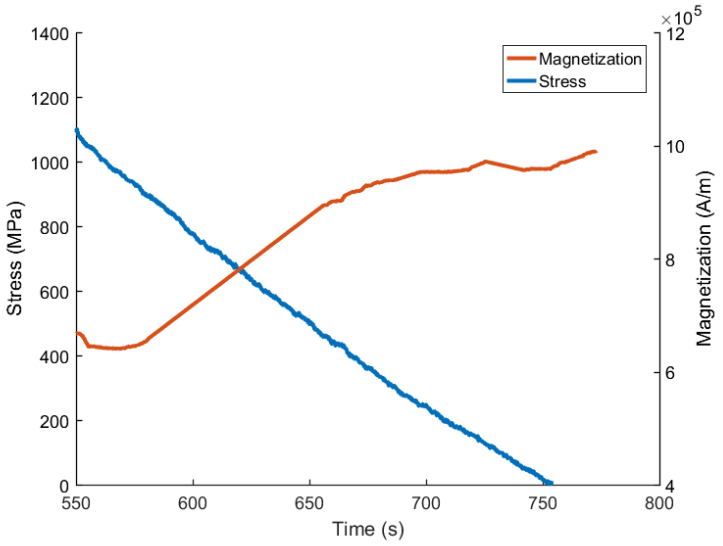

FIGURE 4.22: *In-situ* magnetization measurements of a sample annealed at 760°C during unloading after straining until a point just before necking. During unloading, the microstructure does not change (i.e. no TRIP occurs), yet the magnetization increases. This is a result of the Villari effect. The magneto-mechanical coupling demonstrated herein must be corrected if measurements are to be made under an applied stress.

A model has been recently developed which was used to predict the magneto-mechanical coupling in dual phase steels for stresses up to approximately 600MPa by relating kinematic hardening to magneto-elastic effects occurring within each phase at the grain scale [77]. A correction of the Villari effect that derives from the same approach is proposed.

The multidomain modeling used was first introduced by Lazreg and Hubert [82]. It is able to model the magnetization and the magnetostrictive strain of an isotropic polycrystalline ferromagnetic material submitted to a uniaxial applied stress. Two scales are involved: the domain scale (at which 6 domains are considered) and the grain scale at which an equivalent polycrystalline medium is assumed. The macroscopic and crystallographic frames of reference are coincident (i.e. $(\vec{x},\vec{y},\vec{z})$=([100],[010],[001])).

In the simplified description proposed here, rotation of the magnetization is not considered. The stress tensor $\boldsymbol{\sigma}$ and magnetic field $\vec{H}$ are assumed homogeneous. The free energy of a domain ϕ then becomes simply a sum of the magnetostatic (Zeeman) and magnetoelastic energies written as

$$W_\phi = -\mu_0 \vec{H} \cdot \vec{M}_\phi - \boldsymbol{\sigma} : \boldsymbol{\epsilon}^\mu_\phi \tag{4.38}$$

where μ_0 is the magnetic permeability of vacuum, $\vec{M}_\phi$ the magnetization vector inside a domain that satisfies $|\vec{M}_\phi| = M^s_\alpha$, and $\boldsymbol{\epsilon}^\mu_\phi$ the magnetostrictive strain tensor (see details in Ref. [82]). The volume fraction of a domain f_ϕ is calculated from Boltzmann statistics

$$f_\phi = \frac{exp(-A_s\, W_\phi)}{\sum_\phi exp(-A_s\, W_\phi)} \tag{4.39}$$

where A_s is a fitted parameter proportional to the magnetic initial susceptibility χ^0 without an applied stress ($A_s = \frac{3\chi^0}{\mu_0\, M_\alpha^{s2}}$). The magnetization of the single crystal is obtained from an averaging operation

$$\vec{M} = \sum_\phi f_\phi \vec{M}_\phi \tag{4.40}$$

when the magnetic field and uniaxial stress σ are applied along $\vec{x}$. After a few calculations and a second order Taylor expansion of the exponential, one obtains

$$M = \vec{M} \cdot \vec{x} = \chi_0 H (1 + \frac{6\chi_0}{\mu_0\, M_\alpha^{s2}} \lambda\sigma) \tag{4.41}$$

where λ is a global magnetostriction constant. This relationship permits a new definition of the initial susceptibility in which it is linearly related to the magnitude of stress as

$$\chi^0_\sigma = M/H = \chi^0 (1 + \frac{6\chi^0}{\mu_0 . M_\alpha^{s2}} \lambda\sigma) \tag{4.42}$$

This equation applies for the initial susceptibility but is assumed to be applicable for the secant susceptibility at any magnetic field level and especially at the magnetic field level where the experimental saturation of magnetization is measured. A linear correction of stress effect is then obtained

$$\chi_\sigma = \chi (1 + \eta\sigma) \tag{4.43}$$

where η is a constant that can be identified using experiments where some variation of magnetization with stress is observed (see Figure 4.22) without phase change. The constant η is typically on the order of -10^{-5} MPa^{-1}. This relationship between susceptibility and stress applies to the magnetization level as well, so a stress sensitive

magnetization "saturation" is defined as

$$M_\sigma^s = f_{\alpha+\alpha'}\chi_\sigma H = f_{\alpha+\alpha'}M_\alpha^s(1+\eta\sigma) = M^s(1+\eta\sigma) \tag{4.44}$$

Equation (4.26) is thus modified to become

$$f_{\alpha+\alpha'} = \frac{M_\sigma^s}{(1+\eta\sigma)M_\alpha^s} \tag{4.45}$$

which provides a correction to the ferromagnetic volume fraction $f_{\alpha+\alpha'}$ for a magnetic saturation value M^s obtained with applied stress σ.

The effect of the stress correction is shown in Figure 4.23 for a sample annealed at 780°C. This linear correction of the M^s value improves the accuracy of retained austenite measurements at high stress where differences of up to 0.05 in $f_{\alpha+\alpha'}$ were observed between calculations using M^s and M_σ^s. It also makes it possible to determine whether or not stress-induced martensite transformation occurs.

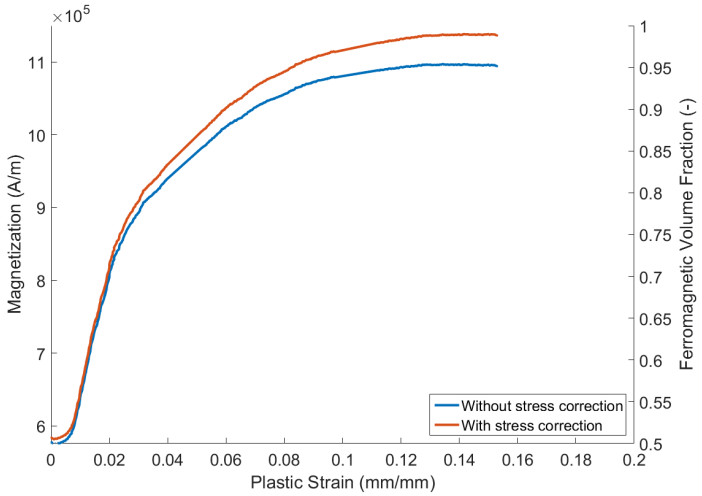

FIGURE 4.23: Magnetization and volume fraction of ferromagnetic phases (ferrite + martensite) for $T_{IA} = 780$°C as functions of plastic strain as calculated from *in-situ* data with and without the stress correction developed in this study. High levels of stress reduce the measured magnetization and result in several percent difference in calculated volume fractions.

If this stress correction is included in the previous localization correction, Equation 4.37 becomes

$$f_{\alpha+\alpha'} = \frac{M_\sigma^s}{(1+\eta\sigma)M_\alpha^s}\left[1+\kappa\left(\frac{M^s}{(1+\eta\sigma)M_\alpha^s}-1\right)\right] \tag{4.46}$$

As previously mentioned, the κ parameter is identified via a magnetic measurement on a sample (in the unstrained state) with a known volume fraction of ferromagnetic material and was determined to be $\frac{2}{3}$ in the current case.

4.5.3 Measurement Precision Verification

One of the intended uses of this measurement system is to analyze the interaction between strain bands and the martensite transformation. However one may note that the strain hardening in the samples annealed at 740°C is very low, so the passage of a strain band should result in only a small portion of austenite that transforms to martensite. As such, the magnetic measurements need to be able to detect changes of only a few percent of ferromagnetic phase.

To confirm whether the system is capable of such precision, samples annealed at 740°C and 760°C were strained into the Lüders plateau and stopped when the Lüders bands had propagated towards the center of the tensile length. A single-loop probe coil was placed on the sample and hysteretic magnetic measurements were made at several positions along the tensile length of the sample. At each position, 40 hystereses were obtained by cycling the field at 10Hz. This provided some statistical information on the standard error of M^s. Figure 4.24 shows the results of this experiment.

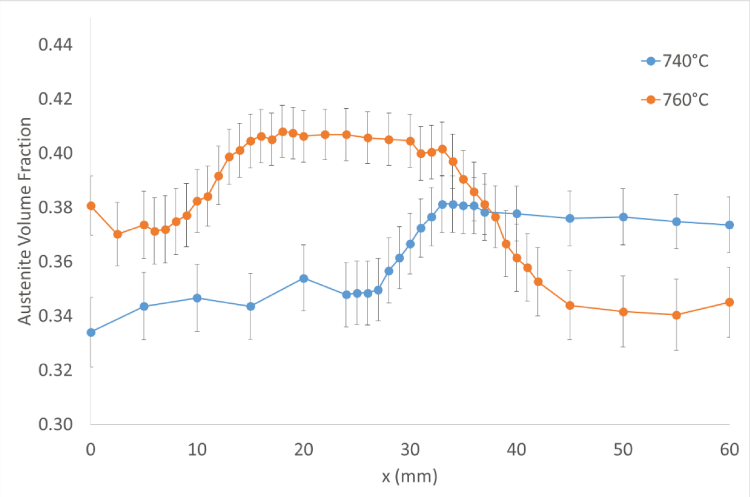

FIGURE 4.24: Determination of retained austenite content in samples annealed at 740°C and 760° that were strained into the Lüders plateau. The sudden change in austenite fraction at the L uders front is easily observed and the standard error for 40 obtained cycles was about ±1%.

A few things can be observed here. First, the locations of the Lüders bands are clearly visible in the austenite volume fraction measurements. The sample annealed at 740°C shows a clear transition of the austenite volume fraction from 34% up to 38% going from left to right. The Lüders band initiated on the left side of the sample and propagated towards the right, transforming austenite to martensite as it passed. In the sample annealed at 760°C, Lüders bands nucleated at both ends of the sample and propagated towards the center, leaving a region of higher austenite content in the middle of the sample. Interestingly, the Lüders band did not transform the same amount of austenite on both sides of the sample annealed at 760°C. This could be

simply because the strain increment in both Lüders bands were not identical, or that the cross section of the sample varied slightly from one side of the sample to the other.

The error bars represent the standard error of the measurement calculated by

$$SE = \frac{\sigma}{\sqrt[2]{n}} \tag{4.47}$$

where σ is the standard deviation of the measurements and n is the number of measurements performed (here, 40). It can be seen then, that the retained austenite volume fraction calculated from M^s using the methods defined in this chapter provides a measurement error of roughly $\pm 1\%$. This is quite good and shows that the measurements obtained using hysteretic data are reliable and repeatable.

4.6 Experimental Procedure

4.6.1 Strain Band Characterization by DIC

In order to characterize the strain bands present in the steel studied, tensile dog bone specimens were cut along the rolling direction from 1.25mm thick sheet. The specimens had an active gauge length 60mm long and 10mm wide. Unidirectional tensile tests were performed using an Instron extensometer with a 12.5mm initial length to confirm DIC measurements as previously demonstrated. The samples were strained until rupture using an Instron 4430 electromechanical tensile testing machine with a strain rate in the sample of $5 \cdot 10^{-4}\text{s}^{-1}$.

Images for DIC analyses were obtained by painting the polished sample surface with a black and white speckle pattern and taking pictures every 3s during testing. A single Canon 60D camera with a 105mm macro objective lens was used to acquire the images with an exposure time of $\frac{1}{320}s^{-1}$, ISO grade of 800, and an aperture f-stop of f/9. Two halogen lamps were used to illuminate the specimen surface. The images recorded were 3465×5202px in definition with 16bit encoding and were cropped to remove excess empty space and converted to .tif format for registration purposes. Correlation of the images was done using 3-node triangular elements and regularization using RT3-DIC [66]. A 10 pixel element size and regularization length of 50 pixels were used for the calculations. Pixel sizes varied between 0.025 and 0.05mm from one test to another and this scale was determined using the measured width of the sample. The displacement fields in photo n were calculated with respect to the reference image using the results from photo $n-1$ to initialize the calculation. The strain rate fields are computed from the (Lagrangian) velocity fields.

Analyses of the strain bands were performed by using profiles as outlined in the previous section in Figure 4.3. Images of the strain increment fields were taken from periods during which bands were present. On each image, 8 profiles were plotted along the tensile length at 20px intervals using ImageJ [71] as shown in Figure 4.25.

The angle of the band was calculated using the positions of the peak in each line profile from a single image. The distance between the peaks in the transverse direction of the sample is known and the lateral shift in peak position is measured, allowing the calculation of the band angle via a simple arctangent calculation. Band speed is calculated using the change in position of a single peak in successive images and the known duration between images. The band speed was calculated for bands which travelled in the same direction for at least 3 images by fitting the position of the band as a function of time with a linear function. This requires the assumption that the band propagation speed is constant, which has been shown to be true in TWIP steels by Zavattieri *et al.* [34]. The width of the band was calculated using the full width at mid height (FWMH) of the band and is corrected for the distance that the band travelled during the time between images (via the calculated propagation speed). It should be noted that the width is calculated along the tensile direction and not along the normal of the band itself. The primary interest of the measurement, however, is to determine whether there is a difference in band width between the Lüders and PLC-type bands to confirm that they are indeed two separate phenomena, so this methodology is preferred in the current case to avoid adding the measurement error of the band angle to the error in the width measurements.

The measurement error for each characteristic was calculated as a simple statistical standard error by

$$e = \frac{\sigma(m)}{\sqrt{n}} \tag{4.48}$$

where σ is the standard deviation of the measurements and n is the number of measurements made. In the case of the band width or band angle, n is the number of line profiles used. In the case of the band propagation speed, n is the number of images used to calculate the propagation speed. Because the error in propagation speed affects the measurement of the width via the correction for band displacement between images, the reported error for width measurements includes the error in band speed.

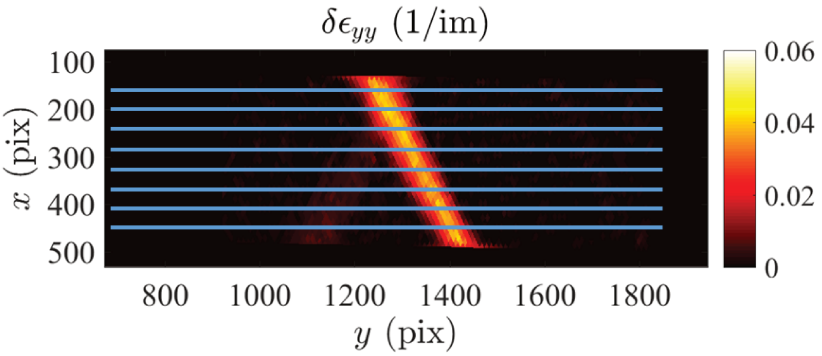

FIGURE 4.25: ImageJ was used to plot 8 line profiles along the tensile length in order to characterize strain bands' width, propagation speed, and angle with respect to the loading direction.

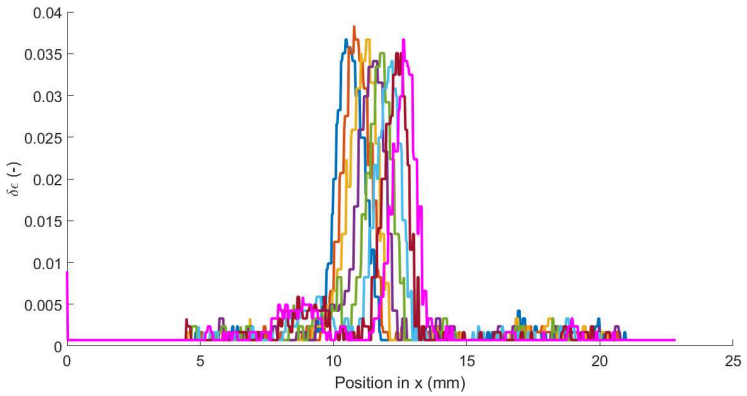

FIGURE 4.26: The line profiles measured by ImageJ for a given image are post-treated in Matlab and scaled to distances in mm. The center of the peak is used as its location for calculating propagation speed and band angle. The FWMH is used to calculate the width of the band.

4.6.2 Strain Rate Sensitivity

Additional experiments were carried out in which strain rate jumps were performed intermittently during tensile testing. The base strain rate was $10^{-4}s^{-1}$ and strain rate jumps to $10^{-2}s^{-1}$ were performed until a relative displacement of 2mm was achieved, at which point the strain rate decelerated back to $10^{-4}s^{-1}$ for another 2mm of displacement.

During these experiments, DIC images were captured using a pco.1200 high speed camera. 780×500px images were captured at 5 frames per second. This high speed was necessary in order to minimize the strain step between images at high strain rate (and thus facilitate convergence of the DIC calculation), however it is much more than is necessary for the slow strain rate. As such, DIC calculations were performed by taking every fifth image for the periods at slow strain rate and every image during periods of high strain rate. As such, for a strain rate of $10^{-4}s^{-1}$ a 1s interval between images was used and for a strain rate of $10^{-2}s^{-1}$, a 0.2s interval was used.

The images were analyzed in the same manner as explained in the previous section. Line profiles were plotted over each images and the fitted peaks were used to characterize the strain bands.

In this case, the interest is to observe how the strain bands are affected by the sudden change in strain rate. The applied strain as measured macroscopically must be accommodated within the band. When the strain rate jump occurs, it could be that the band widens to strain a larger volume of material. It could also simply increase in strain increment while maintaining the same width. The response to this question is critical to understanding the manner in which the strain rate jumps affect TRIP and could provide some insight into the micromechanical mechanism responsible for the PLC-type bands observed.

4.7 Magnetic Experimental Procedure

Three goals were defined for the use of the *in-situ* magnetic measurement system:

- Quantify the differences in TRIP kinetics for different intercritical annealing temperatures
- Determine how the presence of strain localizations affects TRIP
- Characterize the effect of strain rate on TRIP

This was achieved through two experimental campaigns. The first sought to use saturated magnetization measurements to compare TRIP kinetics for different intercritical annealing temperatures. These results were compared to DIC analyses of the strain bands sometimes present in order to determine how the strain bands and TRIP could interact. A second set of experiments was conducted to study the effect of strain rate on TRIP and any effects of the microstructural evolution on strain rate sensitivity. These were, once again, coupled with DIC experiments.

In both sets of experiments, a current is induced in the driving coil and an induced voltage is read by the probe coil. The applied field is calculated by

$$H = I \cdot \frac{N}{L_{eq}} \tag{4.49}$$

where I is the applied current, N is the number of loops in the driving coil (81), and L_{eq} is the length of the driving coil (37mm). From H, the induced B-field can be calculated by

$$B = V \cdot \frac{1}{n \cdot A \cdot 10^{-6}} - \mu_0 H \left(\frac{A_0}{A} - 1 \right) \tag{4.50}$$

where V is the voltage in the probe coil, n is the number of loops in the probe coil (50), A is the instantaneous area of the sample (approximated by $\frac{A_0}{1+\epsilon}$, and μ_0 is the permittivity of vacuum. Finally the B-field can be transformed to magnetization by

$$M = \frac{B}{\mu_0} - H \tag{4.51}$$

after which the retained austenite volume fraction is calculated using the methods outlined in Section 4.5.

4.7.1 Intercritical Annealing Temperature Effect and Strain Localizations

The saturated magnetization method for measuring the retained austenite volume fraction was implemented for *in-situ* tensile testing of flat tensile samples intercritically annealed at temperatures of $T_{IA} = 740°C$, 760°C, and 780°C. The objective was to explore how the intercritical annealing temperature affects the martensite transformation rate and to observe any effects of strain localizations. At the same time, the experiments would serve as a proof of concept for this newly-developed *in-situ*

experimental method, demonstrating that high-frequency determination of the retained austenite volume fraction is possible. This would open up the possibility of *in-situ* mechanical tests at strain rates more representative of those used in industrial forming operations.

Flat tensile specimens with an active tensile length of 60mm, width of 10mm, and thickness of 1.25mm were strain using a crosshead displacement speed of 1.8mm/min ($\dot{\epsilon} = 5 \cdot 10^{-4} s^{-1}$). Tensile tests were interrupted and unloaded when necking was observed so that anyhsteretic data could be obtained both before and after tensile testing. This was done to confirm that the initial and final points obtained with M^s were coherent with those obtained with χ. The sensor probes were directly wound on the sample surface and consisted of 50 loops.

The current in the driving coil was cycled at a frequency of 2Hz with a current probe sensitivity of 100 A/V. 500 points per period (so 1000 per cycle) were saved. Due to memory buffer limitations in the data acquisition card used, 400 cycles were saved per data file. As such, several files were needed per test which resulted in occasional periods of about 30s during which no data was recorded. At a frequency of 2Hz, this results in about 13% of "downtime" during which no measurements are made. The resulting data are more than satisfactory for fitting the phase transformation kinetics despite these measurement gaps.

4.7.2 Strain Rate Effect and Strain Rate Sensitivity

The same method was also employed to study the effect of strain rate on the kinetics of TRIP. Strain rates of $10^{-4} s^{-1}$, $10^{-3} s^{-1}$, and $10^{-2} s^{-1}$ were chosen. The frequency at which the applied H-field was cycled was 10Hz this time in order to assure that enough data points were obtained for the tests at $10^{-2} s^{-1}$. A current probe sensitivity of 50A/V was used and 1000 points per period were recorded. This was done because each hysteresis would be taken over a larger increment of strain—particularly in the sample strained at $10^{-2} s^{-1}$—and as such a more well-defined hysteresis was desired to avoid problems with the larger strain increment.

The samples strained at $10^{-4} s^{-1}$ and $10^{-2} s^{-1}$ were performed as before. For the slow strain rate, gaps in the data were permissible and for the fastest strain rate the test was completed in one data file. If the previous method was used for the test at $10^{-3} s^{-1}$, however, a much higher portion of the experiment would have been conducted while no data was being acquired. As such, the tension was paused (and stress maintained) during the approximately 30-40 seconds during which each data file was saved and the next one created.

Additional tests were performed for each intercritical annealing temperature wherein strain rate jumps from $\dot{\epsilon} = 10^{-4} s^{-1}$ to $\dot{\epsilon} = 10^{-2} s^{-1}$ were performed. In this case, once the Lüders band (when present) completely traversed the sample and an additional 0.5mm of crosshead displacement was attained, a strain rate jump was initiated. The jump was set to continue for 2mm of displacement (3-4% strain) after which the strain rate would decelerate to $10^{-4} s^{-1}$. The test continued at $10^{-4} s^{-1}$ for another

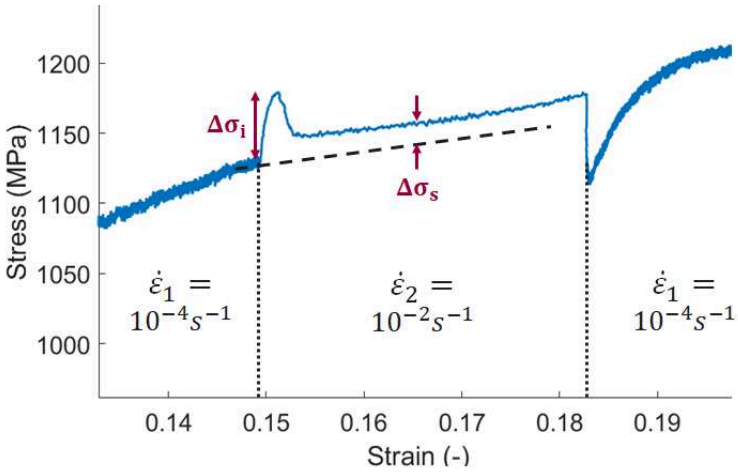

FIGURE 4.27: Illustration of the instantaneous and stabilized stress changes that are used in calculating the strain rate sensitivity. The instantaneous stress change $\delta\sigma_i$ is calculated at the stress peak and the stabilized stress change $\delta\sigma_s$ is calculated by extrapolating the slower strain rate behavior and subtracting it from the stress measured experimentally at high strain rate.

2mm of displacement, at which point another strain rate jump was performed. The two strain rate were alternated as such until rupture.

The instantaneous strain rate sensitivity was calculated using the instantaneous stress change that occurred upon accelerating, $\delta\sigma_i$. For the stabilized strain rate sensitivity, the stress change $\delta\sigma_s$ was calculated at three different points: the middle of the high rate domain as well as 0.2% and 0.5% strain after the acceleration. This was done to compare the three and determine which point is best for calculating $\delta\sigma_s$. The strain rate jump and associated stress changes are illustrated in Figure 4.27. The instantaneous strain rate sensitivity was calculated by

$$m_i = \frac{log(\delta\sigma_i)}{log(\frac{\dot{\epsilon}_1}{\dot{\epsilon}_2})} \tag{4.52}$$

and the stabilized strain rate sensitivity is

$$m_s = \frac{log(\delta\sigma_s)}{log(\frac{\dot{\epsilon}_1}{\dot{\epsilon}_2})} \tag{4.53}$$

where $\delta\sigma_s$ is calculated by taking a linear regression of the 200-300 points before the strain rate jump and extrapolating them to get an approximation of the stress that would have been obtained had the strain rate jump not been performed.

The advantage to performing magnetic measurements of the retained austenite fraction during tensile tests with strain rate jumps lies in the potential correlation between the austenite fraction and the strain rate sensitivity. It is sometimes hypothesized that the negative strain rate sensitivity in Med Mn TRIP alloys comes from a solute effect in the austenite wherein dislocations are pinned by C-Mn clusters. If

this is true, one would suspect that the strain rate sensitivity would be more negative when more austenite is present. Not only that, but the trend should be the same for all intercritical annealing temperatures, as the PLC effect in that case would be determined only by the austenite fraction and not its stability.

Chapter 5

TRIP and Strain Instability Analysis

The preceding chapters outlined the experimental methodology that was employed to analyze the strain localizations in a 0.2C-5Mn-2.5Al Medium Mn TRIP steel as well as the kinetics of the martensite transformation during TRIP. This chapter will begin by presenting the results of these experiments as they relate to the stability of the retained austenite as modified by the intercritical annealing temperature T_{IA} and its effect on the work hardening. This is accomplished using magnetic measurements of the retained austenite volume fraction to characterize the microstructural evolution. Next, a DIC characterization is presented to differentiate the initial band that creates a yield point elongation and the other bands that follow, as well as magnetization analyses to characterize their interaction with TRIP. Finally, the results of studies on the strain rate effect on TRIP and the strain rate sensitivity of the steel are provided. This chapter seeks to compile experimental results with the intention of using the subsequent chapter to discuss them in depth.

5.1 Strain Band Characterization

While the first strain band and subsequent bands observed in tensile curves for samples annealed at 740°C and 760°C appear to be distinctly different, it was not a certainty that they were the result of two independent phenomena. The perceived difference could, for example, simply be an effect of the onset of plasticity.

By analyzing images of the calculated strain increment in the longitudinal direction as previously outlined in Chapter 4, it was possible to show that the width of the first band is significantly different from that of the subsequent bands. Table 5.1 shows the band width, band angle, and band propagation velocity for the Lüders bands in samples annealed at 740°C and 760°C as well as the average of the PLC-type bands in the sample annealed at 740°C. The PLC bands in the sample annealed at 760°C were too random to obtain statistically reliable values because the passage of the band occurred over only 2-3 images in most cases. Thus, the PLC bands from this sample are excluded from Table 5.1.

TABLE 5.1: DIC strain band characterization

		Velocity (mm/s)	Band Width (mm)	Inclination $\theta(^\circ)$
740°C	Lüders	0.381 ± 0.008	0.605 ± 0.033	66.4 ± 0.496
	PLC	0.583 ± 0.084	0.770 ± 0.042	69.8 ± 0.605
760°C	Lüders	0.623 ± 0.003	0.246 ± 0.044	69.3 ± 0.800

The magnitude of the strain in each band was characterized by the maximum value of a line profile across the sample in images in which a band was present. The strain amplitude as a function of time is plotted in Figure 5.2 for the samples annealed at 740°C and 760°C. There is a clear distinction between the initial bands, which had maximum strain increments in the longitudinal direction of approximately 0.03 to 0.035, and the subsequent PLC-type bands which had a more or less constant strain amplitude of about 0.015. This supports the assertion that the two types of bands are the result of different phenomena.

As can be seen in Figure 5.3, the velocity of the PLC-type bands decreased roughly linearly with total strain while the strain rate in the band remained constant. The propagation velocity is related to the macroscopic displacement rate. In the current case, a constant crosshead displacement speed of 1.8mm/s was used to provide a strain rate of $5 \cdot 10^{-4} s^{-1}$, but because the sample elongates during tensile testing the macroscopic strain rate decreases slightly over the course of the experiment. As a point of reference, the expected actual strain rate at 30% strain is $3.8 \cdot 10^{-4} s^{-1}$– slightly higher than the roughly $3 \cdot 10^{-4} s^{-1}$ shown in Figure 5.3. When considering the strain rate in the band as measured by DIC, the strain rate was approximately constant at 0.005–0.006s^{-1}. Note however, that the strain rate and propagation speed in the Lüders band differed significantly from those of the PLC-type bands. The propagation speed of the Lüders band was 0.4mm/s while that of the first PLC-type band was nearly 1mm/s. The strain rate in the bands showed the opposite trend, with a strain rate of about 0.01s^{-1} in the Lüders band before the strain rate decreased to 0.005–0.006s^{-1} in each subsequent band as mentioned previously.

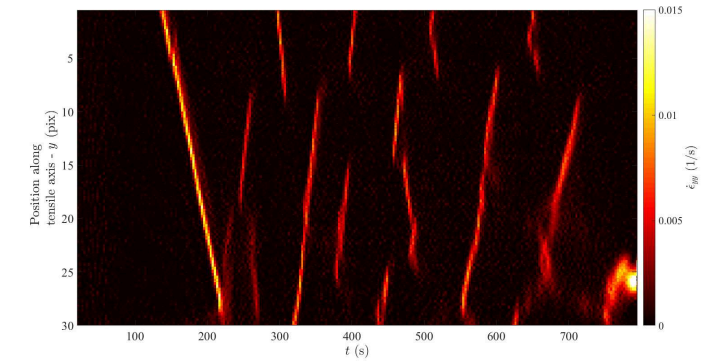

(A)

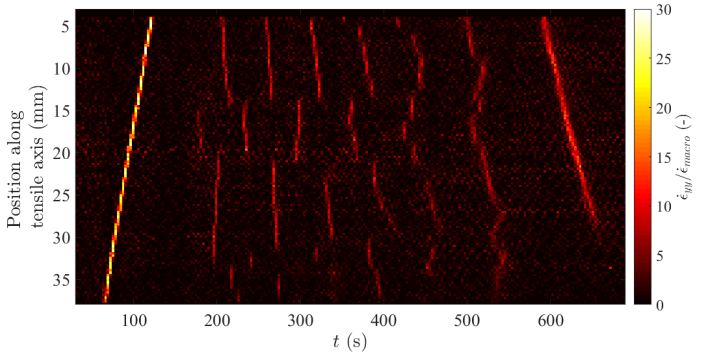

(B)

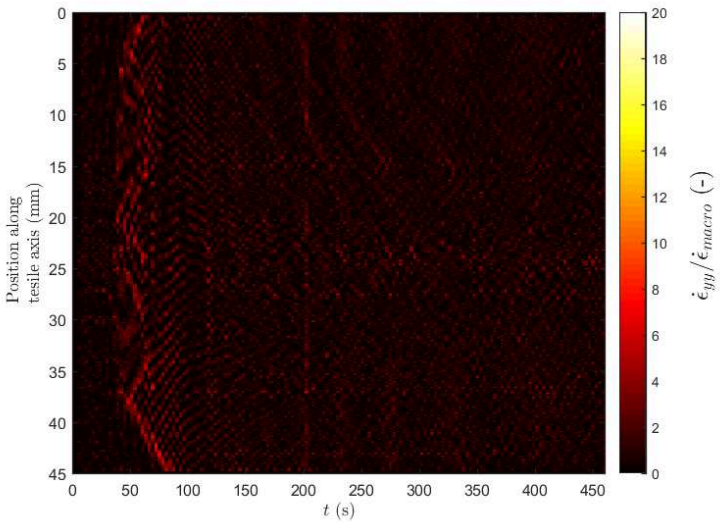

(C)

FIGURE 5.1: Spatiotemporal DIC measurements of the strain rate as measured by DIC normalized by the applied macroscopic strain rate of $5 \cdot 10^{-4} s^{-1}$ for intercritical annealing at (a) 740°C, (b) 760°C, and (c) 780°C. The vertical axis represents the position along the tensile direction and the color bar represents the ratio of the strain rates in the tensile direction. Clear strain bands are observed in (a) and (b), but not in (c).

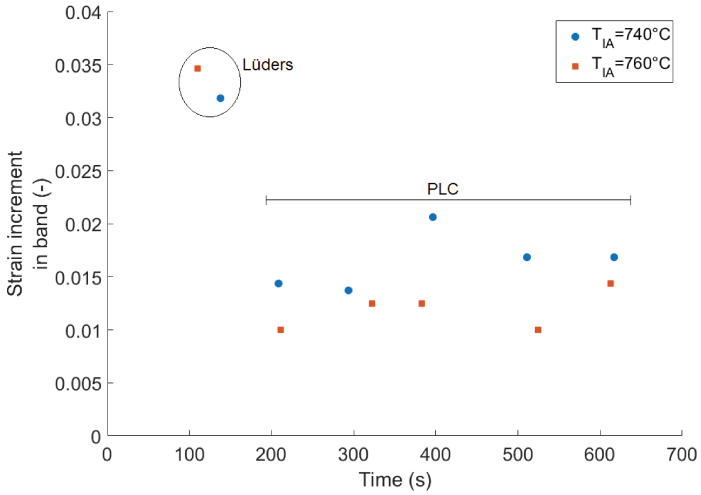

FIGURE 5.2: Plot of the longitudinal strain increment in each band as a function of time for samples annealed at 740°C and 760°C. The stark difference in magnitude between the first band and those that follow suggests two different underlying mechanisms. It is proposed that there is an initial Lüders band followed by PLC-type bands.

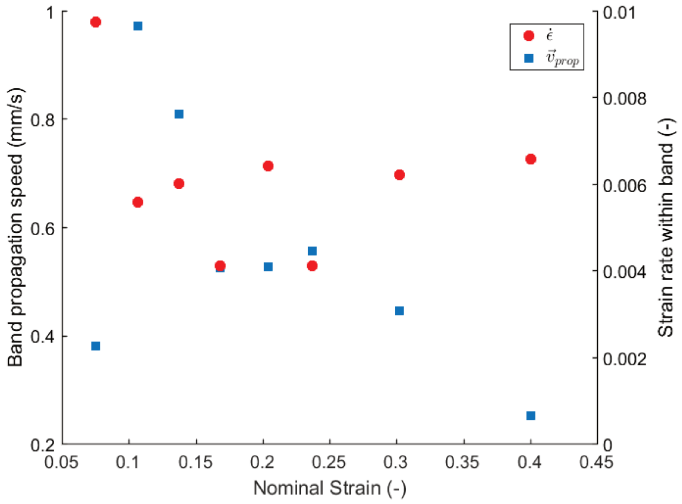

FIGURE 5.3: Calculated band propagation velocities and the strain rate within each band plotted as a function of the nominal strain for the sample annealed at 740°C. The velocities of the PLC-type bands decrease roughly linearly with strain while the strain rate in the band remains more or less constant for bands occurring after the Lüders band.

By plotting strain profiles along the tensile length of each sample from the total strain fields, it is possible to assess the homogeneity of the strain increment created by the passage of a strain band. In Figure 5.4, for example, the Lüders band propagated from right to left (towards $x = 0mm$) inducing a very uniform total strain after the passage of the band. Each subsequent band (now propagating from left to right each time) provided a roughly equivalent strain increment to the first PLC band. As

the experiment progressed, a strain concentration corresponding to necking developed around $x = 8 - 15mm$ roughly.

In the sample annealed at 760°C (Fig. 5.5) which showed a more random PLC behavior, the same strain profile characterization did not provide as clear of a result as the sample annealed at 740°C. The Lüders band is clearly visible, but after that there are not distinct bands until the very end of the test where a propagative band formed and lead to necking. Looking at a few individual profiles the profiles take the same general form with each passage, but no obvious bands are observed.

Finally, the sample annealed at 780°C deformed homogeneously throughout the tensile test as can be seen in Figure 5.6. There was no observed Lüders band at yielding even though significant strain hardening did not occur until after about 2% of total strain. It is quite interesting that no bands were detected by DIC because there were some very slight "bumps" in the tensile curve as measured from extensometer data that resemble the steps corresponding to PLC-type bands, as shown in Figure 5.7

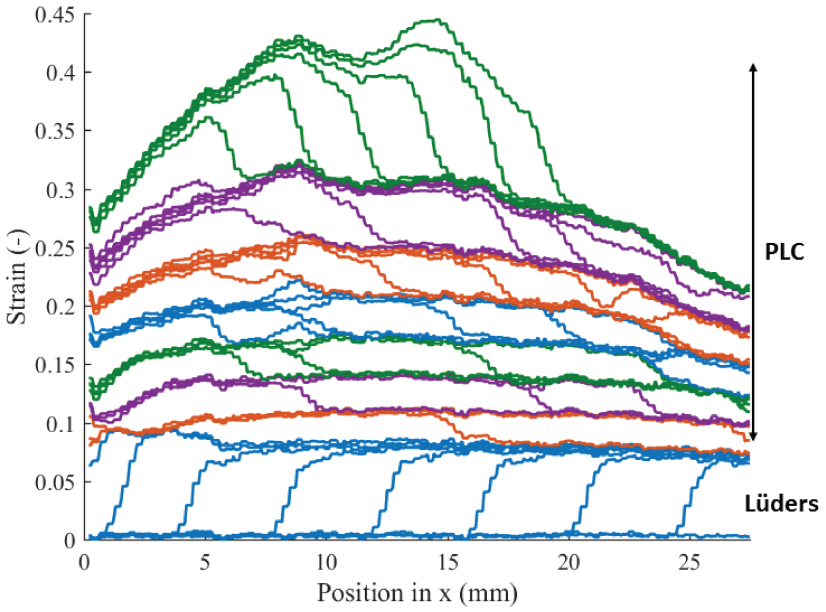

FIGURE 5.4: Profiles along the tensile length of a sample annealed at 740°C as measured by DIC. An initial Lüders band propagates from right to left, followed by a series of PLC-type bands that propagated in the opposite direction. While there was a concentration of the strain in the region between 5 and 15mm, each band provided a roughly equivalent strain increment across the length of the sample.

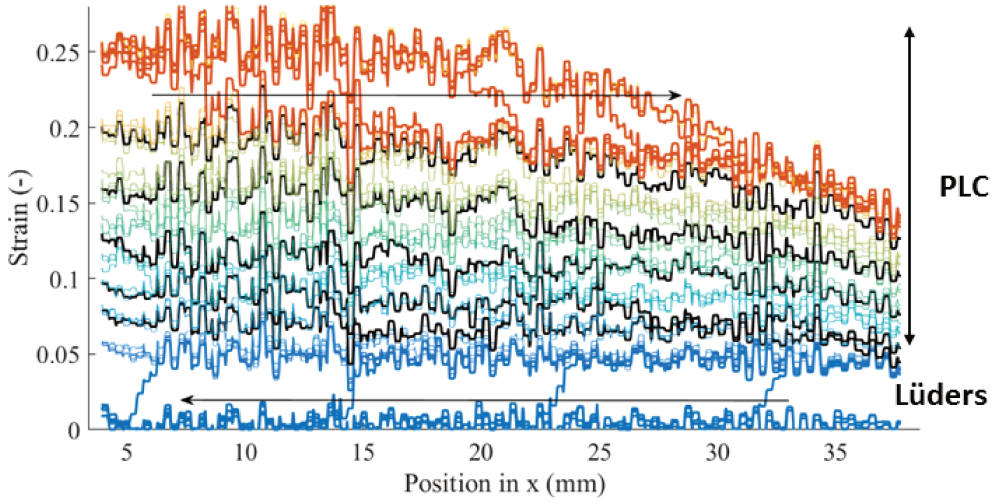

FIGURE 5.5: Strain profiles along the tensile length of a sample annealed at 760°C as measured by DIC. In this case, no bands were observed. In this case, an initial Lüders band is observed but afterwards no propagative bands can be seen until just before rupture.

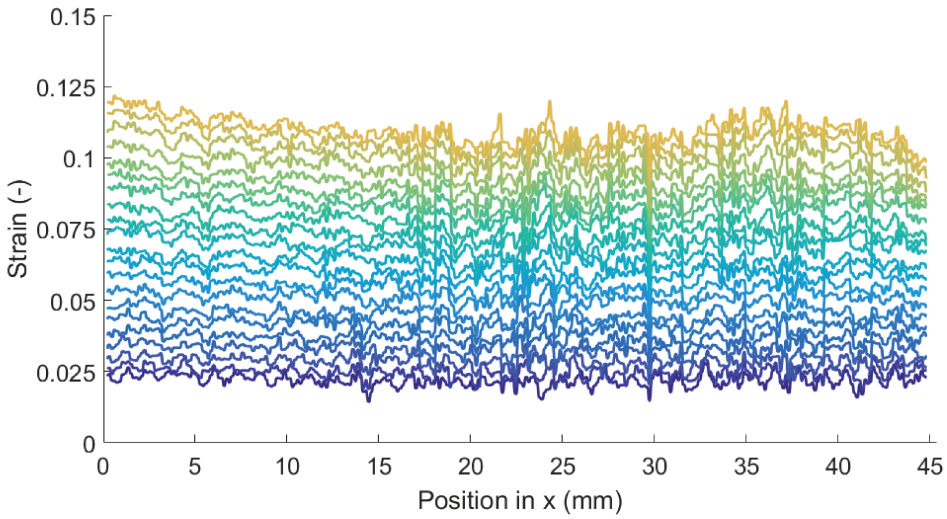

FIGURE 5.6: Strain profiles along the tensile length of a sample annealed at 780°C as measured by DIC. In this case, no bands were observed. Instead a gradual, homogeneous increase in strain was recorded with only minor concentrations at the extremities of the measurement zone.

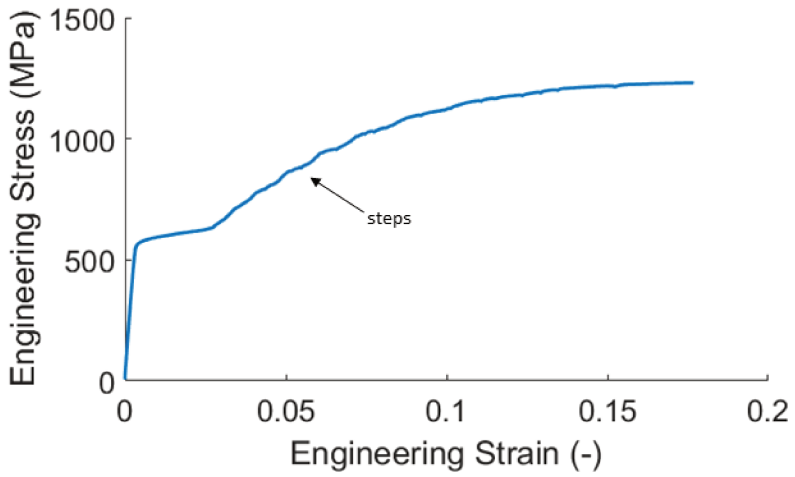

FIGURE 5.7: Tensile data with strain measured via extensometer for the sample annealed at 780°C used for DIC experiments. The beginning of plasticity where work hardening is very low showed no Lüders band in DIC results, nor did the rest of the experiment despite the pseudo "steps" in the tensile curve during the period where work hardening was significant.

5.2 Sensitivity to Intercritical Annealing Temperature

The third generation of AHSS are notoriously sensitive to the intercritical annealing temperature employed, and the 0.2C-5Mn-2.5Al Medium Mn TRIP steel studied here is no exception. It was observed that the tensile properties of samples obtained for identical annealing temperatures (in terms of furnace settings) but different ingots were significantly different. In Figure 5.8, tensile results of the initial mechanical characterization are presented alongside those from a later set of tests on samples from a second ingot (marked with a "-b" in the figure). Particularly interesting are the changes in the yield stress and the presence (or not) of strain localizations. In the sample from the second ingot annealed at 780°C for example, there were what appeared to be steps possibly due to PLC bands and the initial retained austenite content was about 40 vol% compared to only 17 vol% for the previous ingot as measured by XRD.

It was seen that the intercritical annealing temperature affects the work hardening capacity and the degree to which the PLC-type bands are either propagative or random. Because the steel was so sensitive to the annealing temperature, there were observed differences in band character between samples from different plates annealed at the same temperature. Figure 5.9 shows the spatiotemporal plots for two different samples annealed at 740°C but from two different plates. In the first, the bands are clearly propagative and continuous with each band completing its passage along the tensile length before the next band nucleates. In the second, the Lüders band was continuous but after that the PLC-type bands were a bit more perturbed even if they remained largely propagative. In this case it is more difficult to

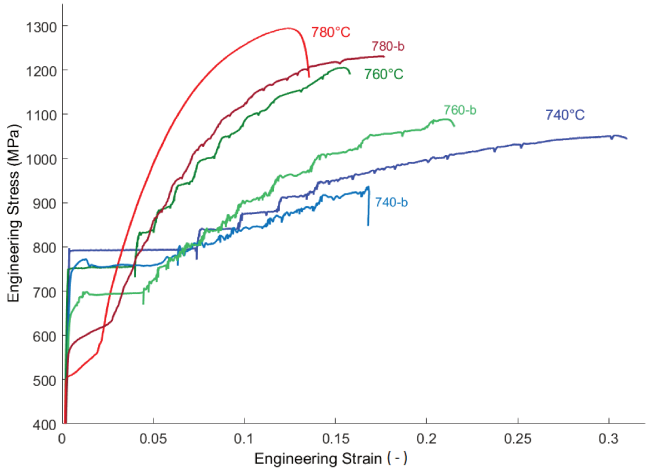

FIGURE 5.8: Tensile tests on samples that were processed at the same intercritical annealing temperature but from two different ingots showed significant variability in mechanical properties. Notably, the 780-b sample showed what appear to be some strain localizations while the preceding 780 sample did not.

see whether multiple bands can exist at the same time or if the entire sample must undergo a given strain increment before a "new" strain band can nucleate.

The notable difference between samples annealed at the same temperature but from different batches is critically important when attempting to analyze the sensitivity of the steel to other parameters like strain rate. The samples being compared should come from the same batch in order to eliminate some of the variability that can exist between samples from two different batches.

5.3 Effect of T_{IA} on Transformation-induced Plasticity

The magnetic measurement system allowed the retained austenite volume fraction to be calculated from *in-situ* measurements of the sample's saturated magnetization. This measurement is made in the portion of the sample contained within the 37mm long primary coil and is a volumetric measurement. The fact that the magnetic measurement volume has a length of 37mm and the tensile length of the sample geometry used is 60mm, the fluctuations of the saturated magnetization that occurred during the passage of a strain band were able to be observed as the same sort of steps that were seen in tensile data using an extensometer with a gauge length of 12.5mm, as can be seen in Figure 5.10.

The stark difference in work hardening from one T_{IA} to another was the result of drastically different rates of transformation during TRIP. Only the sample annealed at 780°C showed complete transformation of austenite to martensite. The sample annealed at 740°C showed very little hardening and very little phase transformation while the sample annealed at 760°C was between the other two in both total work hardening and transformation rate of austenite to martensite.

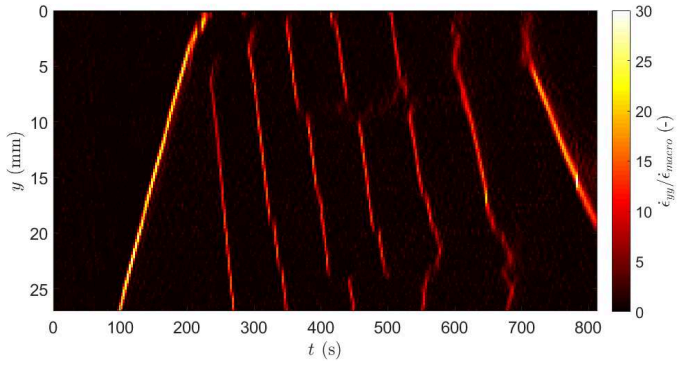

(A)

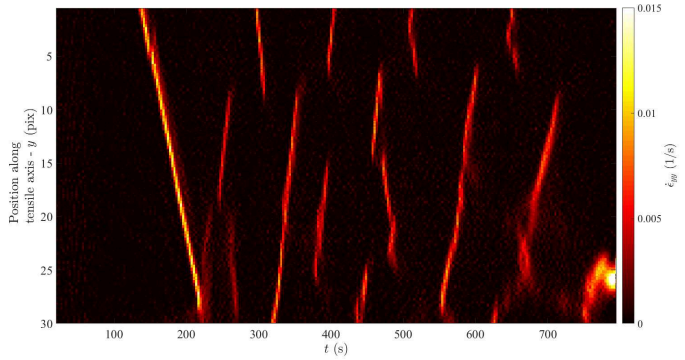

(B)

FIGURE 5.9: Spatiotemporal DIC measurements of (a) nominal longitudinal strain and (b) longitudinal strain rate measurements for annealing at 740°C. The horizontal axis is the time in seconds, the vertical axis represents the position along the tensile direction, and the color bar represents either the total strain in the tensile direction or the strain rate (1/s) in the tensile direction. The data in (a) is taken from the 740-b sample while that in (b) is from 740, demonstrating again the difference observable between two batches.

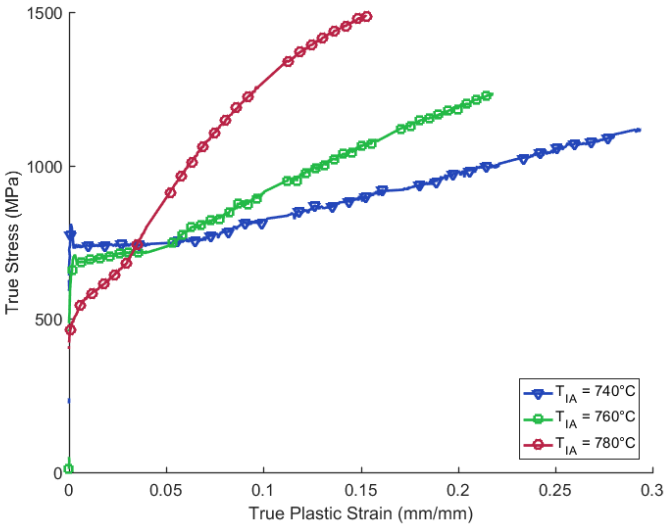

(A)

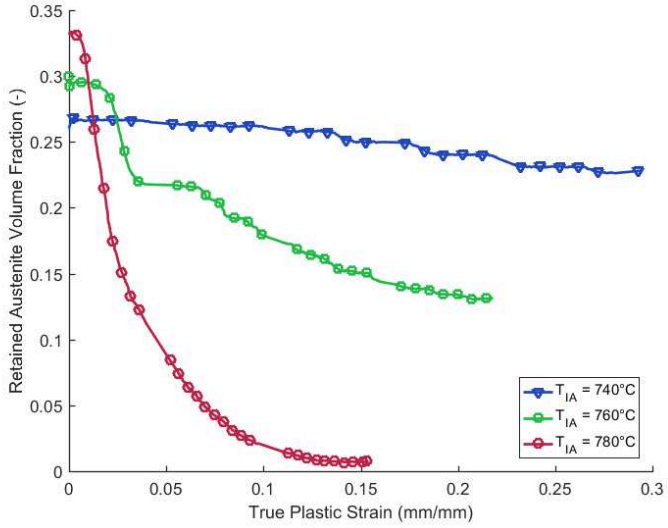

(B)

FIGURE 5.10: Plots of (a) true stress and (b) retained austenite volume fraction vs. true plastic strain for each intercritical annealing temperature. The same steps previously observed in tensile data are again seen in the retained austenite volume fraction, suggesting that the TRIP effect coincides with the passage of strain bands. Both plots share identical strain axes.

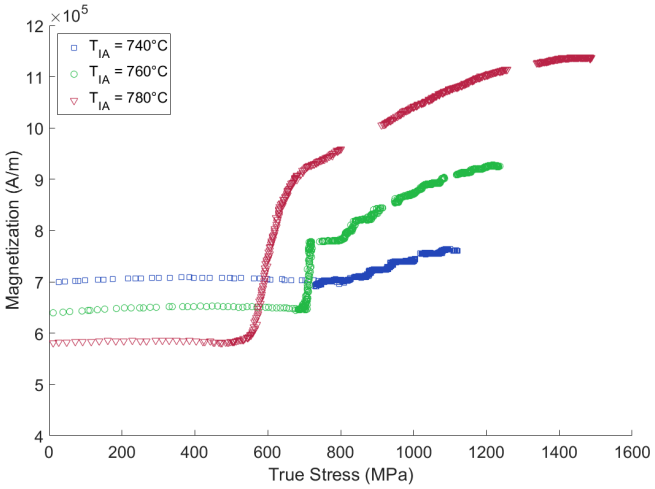

FIGURE 5.11: Sample magnetization (with stress correction) plotted as a function of true stress shows that during elasticity, the magnetization remained constant meaning that there is no stress-induced transformation before yielding.

Because the magnetic measurements made here correct for the effect of stress on the magnetization, it was possible to determine whether or not any stress-induced transformation occurred during elasticity. Figure 5.11 shows the saturated magnetization of the sample as a function of the applied true stress for each intercritical annealing temperature. It can be seen that the saturated magnetization in each sample remained constant until the yield stress was attained. After yielding, the martensite transformation occurred readily in the samples annealed at 780°C and 760°C while the sample annealed at 740°C showed very little transformation even after yielding. Because the magnetization did not change during elasticity, it can be concluded that no stress-induced transformation occurred.

The evolutions of the austenite volume fraction as calculated from magnetization measurements on each sample were used to fit the parameters of an Olson-Cohen model [51]

$$f_{\alpha+\alpha'} = 1 - exp(-\beta(1 - exp(-\alpha\epsilon^p)^n) \tag{5.1}$$

where the α parameter is related to both the number of shear bands and the stacking fault energy of the austenite, β accounts for the probability of a martensite nucleus to form, which is in turn defined by the driving force for the phase transformation. The exponent n is usually considered a material constant, and in the current case is fixed at 2 because the nominal composition of the steel does not change. Perhaps surprisingly, the model can be fit to the measured austenite volume fraction change fairly well even when strain localizations are present as can be seen in Figure 5.12. This provides a set of effective Olson-Cohen parameters, given in Table 5.2, that are valid in a macroscopic sense for a given microstructure and austenite stability. Estimations of the martensite start temperature, M_S, obtained from ThermoCalc are also provided in Table 5.2.

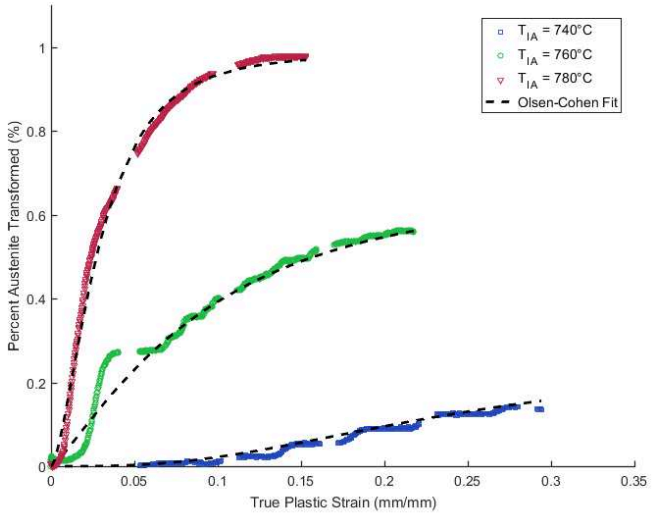

FIGURE 5.12: Experimental transformation rates of retained austenite in alloys annealed at 740°C, 760°C, 780°C (symbols), fit with a standard Olsen-Cohen model (dashed lines).

TABLE 5.2: Macroscopic Olson-Cohen Parameters

$T_{IA}(^{\circ}C)$	α	β	n	$M_S(^{\circ}C)$
740	6	0.3	2	-7.5
760	15	1.2	2	26
780	18	1.9	2	58

5.4 Effect of Strain Rate on TRIP

Because materials exhibiting PLC typically have a negative strain rate sensitivity [35, 89], tensile tests were conducted at several strain rates to observe whether this is the case for these steels. Strain rates of $10^{-4}s^{-1}$, $10^{-3}s^{-1}$, and $10^{-2}s^{-1}$ were used on samples from each intercritical annealing temperature and with *in-situ* magnetic measurements showed some interesting results. The data is not easily interpreted, however, as the presence of strain bands modifies the true strain rate seen by the material through the localization of the strain in a much smaller volume than if plasticity occurred homogeneously. As such, trends in behavior with respect to strain rate need to be considered with the knowledge that the presence of strain localizations can increase the strain rate by 20 to 30 times the imposed value, as demonstrated previously in Section 5.1.

In samples annealed at 740°C, the strain hardening in tension was identical for all three strain rates, as seen in Figure 5.13. The true stress–true strain curves overlapped perfectly, with the only difference being a decrease in total elongation for the sample strained at $10^{-2}s^{-1}$. This finding is reflected in the transformation kinetics as measured via the saturated magnetization and normalized by the initial retained

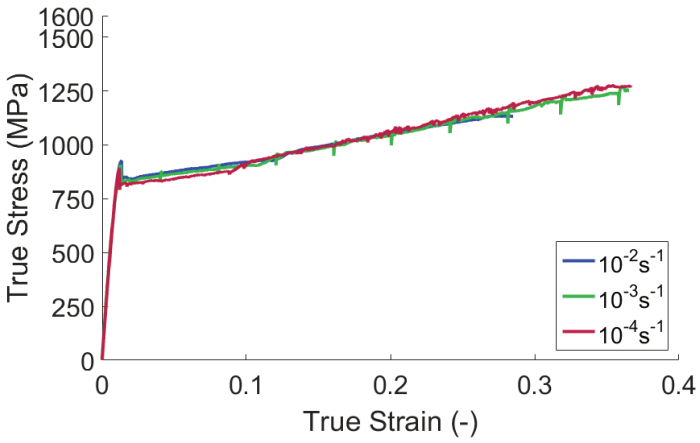

(A)

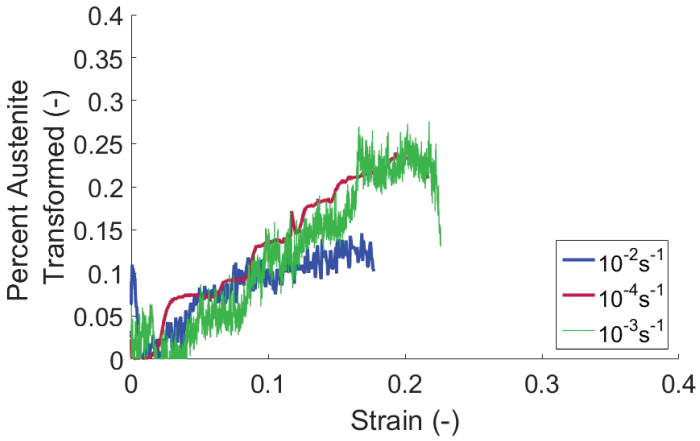

(B)

FIGURE 5.13: Tensile data (a) and the percent of the initial retained austenite fraction that has transformed (b) as calculated from magnetic measurements for strain rates of $10^{-4}s^{-1}$, $10^{-3}s^{-1}$, and $10^{-2}s^{-1}$ for an intercritical anneal at 740°C. No major effect was observed aside from perhaps a slight decrease in transformation rate at $10^{-2}s^{-1}$.

austenite content to provide a percentage of the initial austenite content that has transformed at a given point during the experiment. The transformation kinetics for samples strained at $10^{-4}s^{-1}$ and $10^{-3}s^{-1}$ were identical, while the sample strained at $10^{-2}s^{-1}$ showed very little transformation after the passage of the Lúders plateau. All three samples seemingly deformed via PLC bands.

The samples annealed at 760°C showed an interesting trend in tensile behavior with increasing strain rate. While the overall mechanical behavior did not change significantly, the plastic deformation mechanism did change. In Figure 5.14, the TRIP kinetics showed an increasing transformation rate for increasing strain rate despite the fact that the tensile curves overlap nearly perfectly. In Figure 5.15 (which is a zoom of Figure 5.14), it can be seen that at $10^{-4}s^{-1}$ the tensile curve showed distinct serrations that are typical of randomized PLC reminiscent of PLC in solution strengthened aluminum alloys. At $10^{-3}s^{-1}$, serrations are present between the

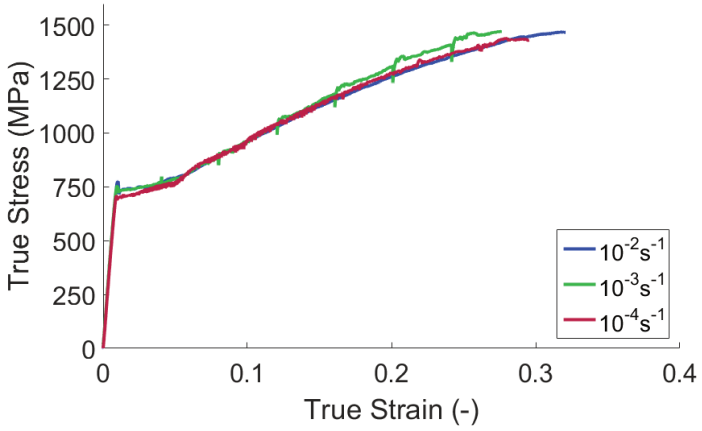

(A)

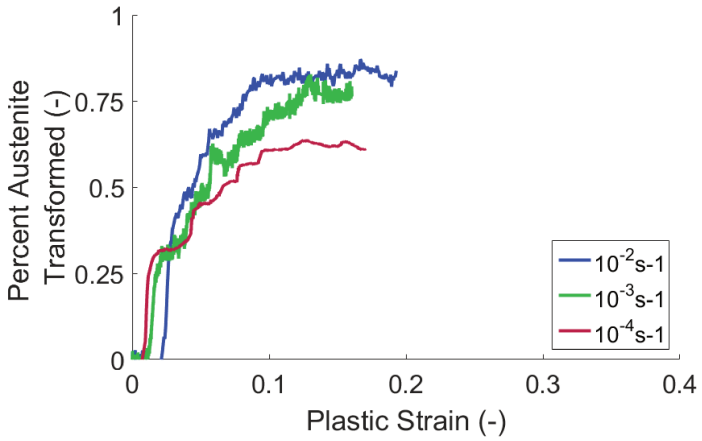

(B)

FIGURE 5.14: Tensile data (a) and the percent of the initial retained austenite fraction that has transformed (b) as calculated from magnetic measurements for strain rates of $10^{-4}s^{-1}$, $10^{-3}s^{-1}$, and $10^{-2}s^{-1}$ for an intercritical anneal at 760°C. In this case, the transformation rate increased with increasing strain rate.

unloading cycles, but their amplitude is diminished. This suggests perhaps that this strain rate is nearing a transition zone where PLC might disappear. Finally at $10^{-2}s^{-1}$, little to no discontinuities appear in the tensile curve suggesting that there is no longer any localization of the strain at this strain rate.

The sample annealed at 780°C showed an interesting trend in that the work hardening decreased progressively with increasing strain rate, indicating a negative strain rate sensitivity. The trend in TRIP kinetics is less obvious, showing an increase in transformation rate from $10^{-4}s^{-1}$ to $10^{-3}s^{-1}$ followed by a decrease in transformation rate when the strain rate is further increased to $10^{-2}s^{-1}$. The behavior is perhaps modified at $10^{-3}s^{-1}$ due to the need to pause the tensile test in order to save magnetic data. The resulting stress relaxations and stress "overshoot" upon reloading could affect TRIP and thus the degree of work hardening.

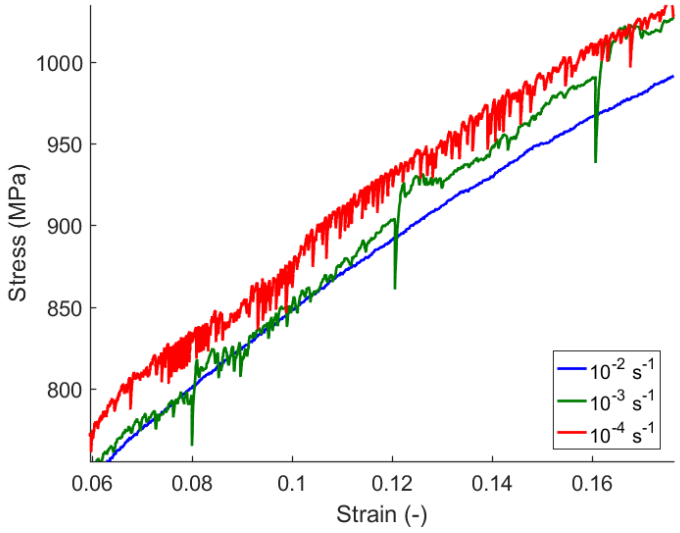

FIGURE 5.15: The samples annealed at 760°C and strained at $10^{-4}s^{-1}$, $10^{-3}s^{-1}$, and $10^{-2}s^{-1}$ showed that the type of PLC observed changes with the strain rate. At the slowest strain rate, serrations in the stress strain curve suggest random PLC while at $10^{-3}s^{-1}$ the serration amplitude is diminished. At $10^{-2}s^{-1}$, no noticeable PLC was observed.

5.5 Strain Rate Sensitivity

The strain rate sensitivity of steels can be measuring using strain rate jump tests in which the strain rate is suddenly increased. Tensile tests during which the strain rate was alternated between $10^{-4}s^{-1}$ and $10^{-2}s^{-1}$ were performed with *in-situ* magnetic measurements to determine the strain rate sensitivity of the steel as a function of both strain and retained austenite fraction. This was done to determine whether the negative strain rate sensitivity originated from a solute effect in the austenite (and, if so, the SRS should go towards 0 as the austenite fraction decreased) or from the phase transformation itself (in which case the SRS could either remain constant until the transformation is completed or could decrease progressively with austenite content).

One of the primary goals of these experiments was to compare them against other experiments with DIC in which strain rate jumps were performed. These experiments have been performed for anneals at 740°C and 760°C, but a complete analysis is not yet finished. Initial results are inconclusive–in a sample annealed at 740°C no PLC bands were observed during the period at high strain rate.

In a sample annealed at 740°C submitted to strain rate jumps, it was observed that the work hardening was significantly higher than at constant strain rates of either $10^{-4}s^{-1}$ or $10^{-2}s^{-1}$, as seen in Figure 5.17. This corresponded to a series of sharp increases in the ferromagnetic volume fraction at the moment of the strain rate acceleration, indicating a burst of transformation that surpassed the transformation rates of either sample strained at a constant strain rate. This is shown in Figure 5.18

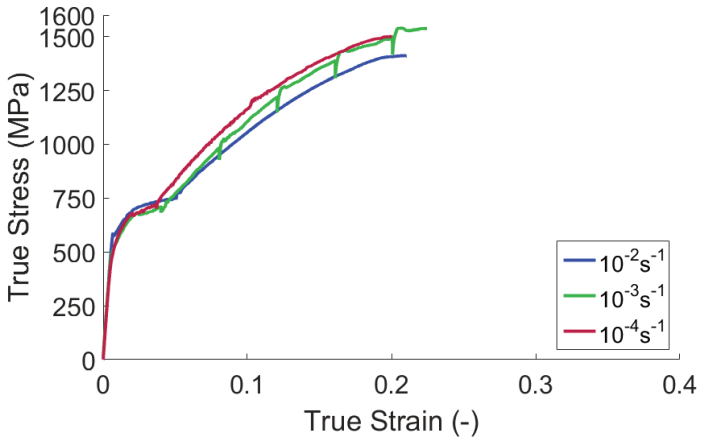

(A)

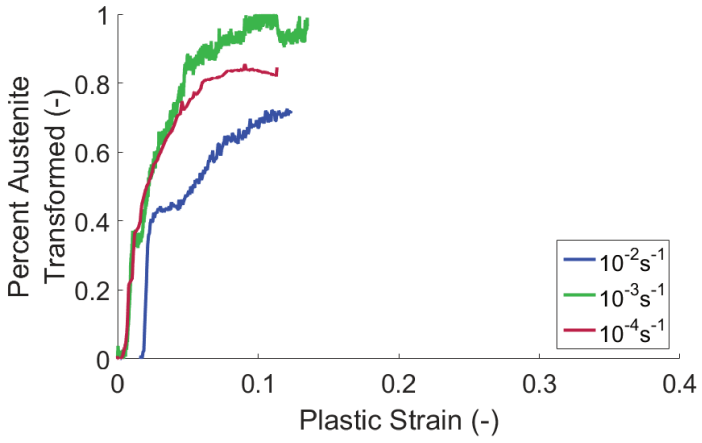

(B)

FIGURE 5.16: Tensile data (a) and the percent of the initial retained austenite fraction that has transformed (b) as calculated from magnetic measurements for strain rates of $10^{-4}s^{-1}$, $10^{-3}s^{-1}$, and $10^{-2}s^{-1}$ for an intercritical anneal at 780°C. Here, the transformation rate first increased and then decreased for increases of strain rate to $10^{-3}s^{-1}$ and $10^{-2}s^{-1}$, respectively.

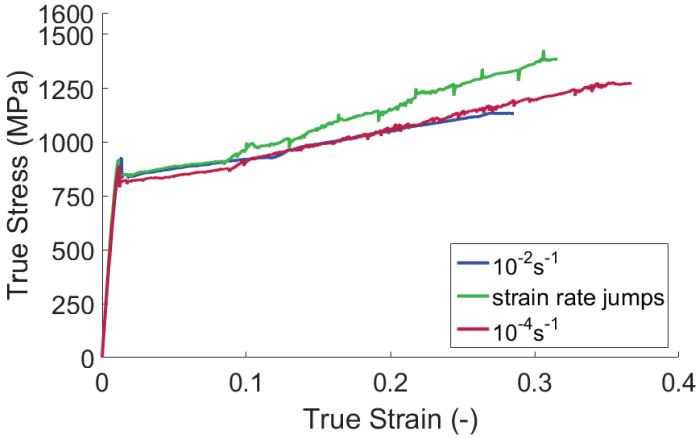

(A)

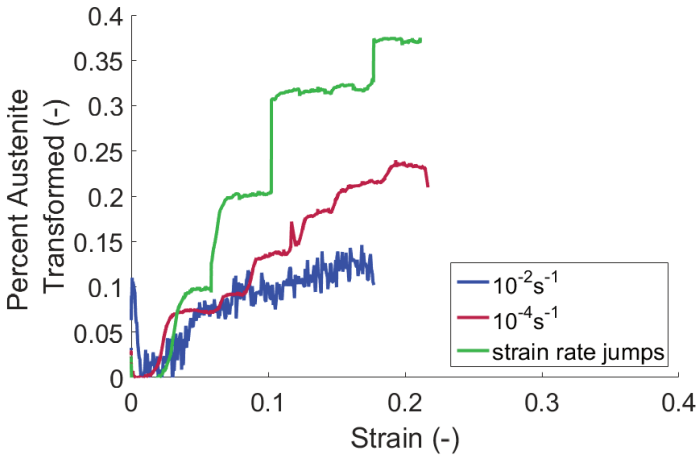

(B)

FIGURE 5.17: Tensile (a) and magnetic (b) results of strain rate jump tests on a sample annealed at 740°C. Jumps were performed between $10^{-4}s^{-1}$ and $10^{-2}s^{-1}$ and results are presented alongside the results for the corresponding continuous strain rates. The work hardening when jumps were performed was much higher due to higher transformation rates

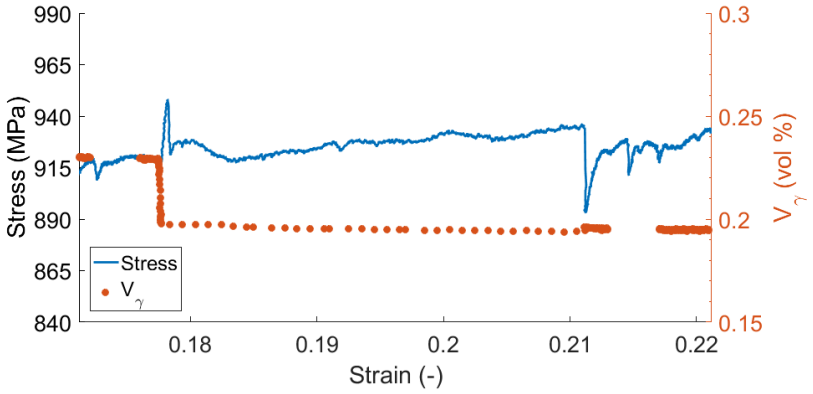

FIGURE 5.18: Example of a strain rate jump in a sample annealed at 740°C with *in-situ* magnetic measurements of the retained austenite volume fraction. When the strain rate is accelerated, a burst of martensite transformation occurs. No transformation occurs thereafter until the strain rate is decelerated and plasticity continues.

The sample strained at 760°C showed a similar trend, shown in Figure 5.19, with a much higher work hardening rate when strain rate jumps were performed than in the cases with a constant strain rate. The transformation rate curves showed that there were the same bursts of transformation associated with the strain rate jumps, however this time they seemed to coincide with the deceleration rather than acceleration as seen in samples annealed at 740°C or 780°C. An illustration of this behavior is provided in Figure 5.20. While the transformation rate in the sample that underwent strain rate jumps is between that of the two constant strain rates, the work hardening in the tensile curves suggest that it is in fact higher than either of the two other samples. This discrepancy could be due to the fact that only one sample was used at each temperature.

The sample annealed at 780°C exhibited decreased work hardening as the strain rate was increased from $10^{-4}s^{-1}$ to $10^{-2}s^{-1}$, as seen in Figure 5.21. The sample upon which strain rate jumps were performed seemed to show the same behavior as the sample strained at a constant strain rate of $10^{-4}s^{-1}$, though the transformation rate was higher when strain rate jumps were performed than without jumps. In this case, as is shown in Figure 5.22, a burst of martensite transformation is observed when the strain rate is accelerated much like the sample annealed at 740°C. The transformation rate at $10^{-2}s^{-1}$ was much lower than at $10^{-4}s^{-1}$. This could be once again a statistical effect of the small sample size, or it could indicate an effect of adiabatic heating due to higher strain rate and consequent stabilization of the retained austenite.

When analyzing the strain rate sensitivity, two different sensitivities were measured: the instantaneous sensitivity, m_i, and the steady state sensitivity, m_{ss}. The calculation of these terms was explained previously in Chapter 4. Both descriptions of the SRS were plotted as a function of strain and of the retained austenite volume fraction (for samples upon which magnetic measurements were made).

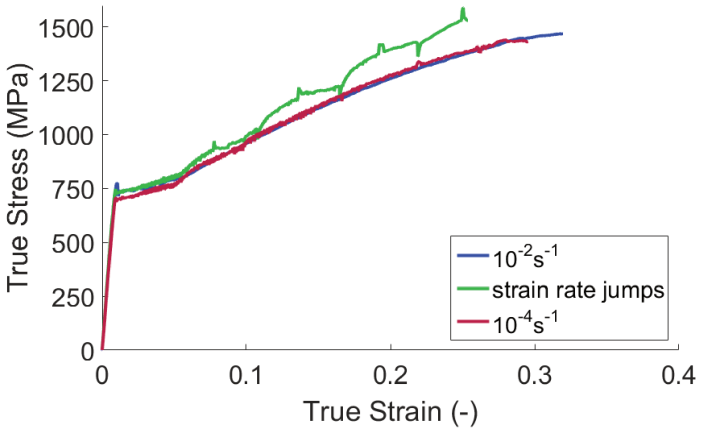

(A)

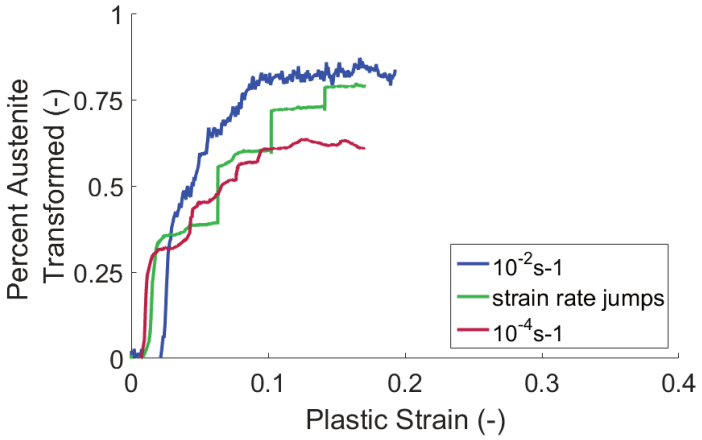

(B)

FIGURE 5.19: Tensile (a) and magnetic (b) results of strain rate jump tests on a sample annealed at 760°C. In this case, the work hardening is again higher but the transformation rate seems to jump between those of tests at $10^{-4}s^{-1}$ and $10^{-2}s^{-1}$.

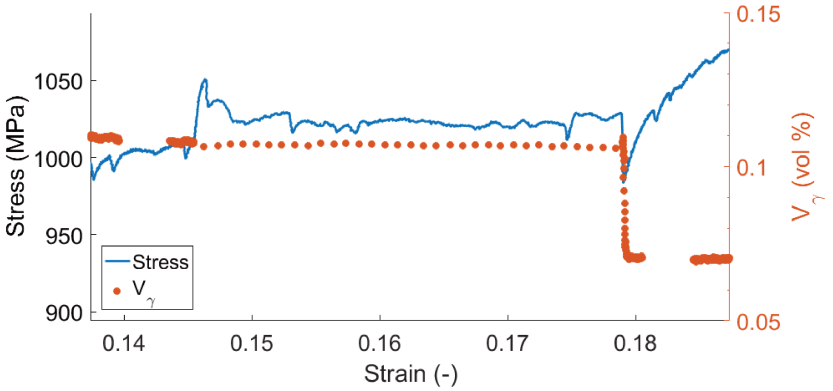

FIGURE 5.20: Example of a strain rate jump in a sample annealed at 760°C with *in-situ* magnetic measurements. This time, no transformation occurs during the higher strain rate period until the strain rate is decelerated, at which time a burst of transformation occurs.

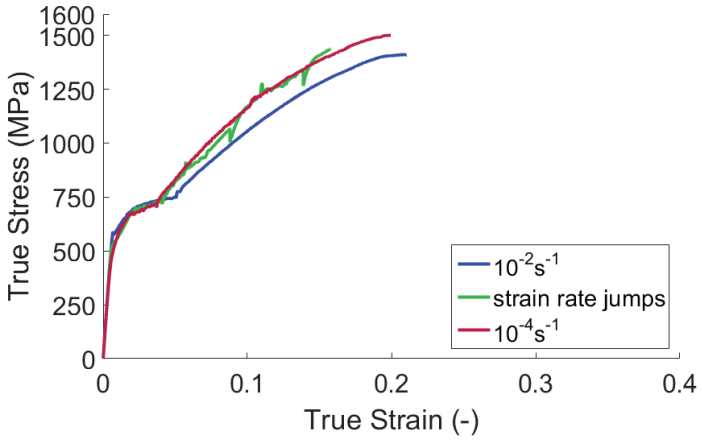

(A)

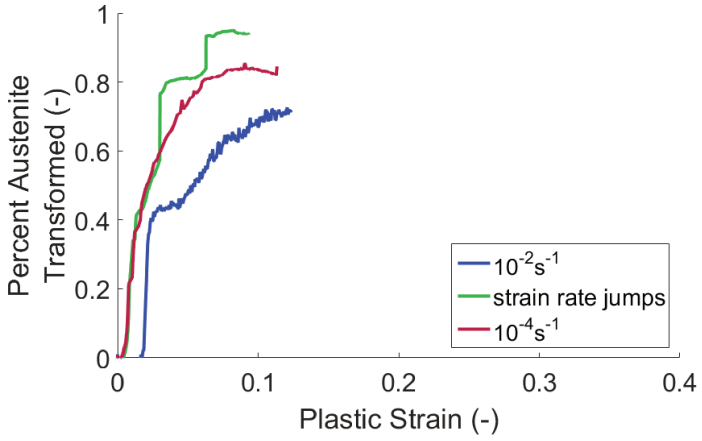

(B)

FIGURE 5.21: Tensile (a) and magnetic (b) results of strain rate jump tests on a sample annealed at 780°C. The work hardening achieved in this case is identical to that obtained at $10^{-4}s^{-1}$, but the transformation rate was slightly higher than in either of the two constant rate experiments.

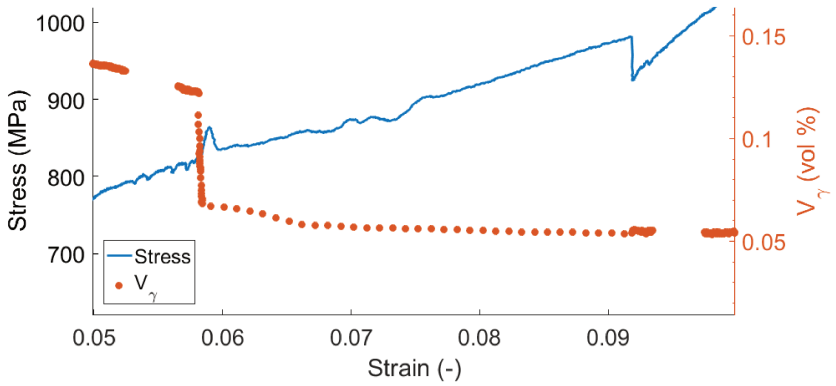

FIGURE 5.22: Example of a strain rate jump in a sample annealed at 780°C with magnetic measurements of the retained austenite volume fraction. As in the sample annealed at 740°C, the burst of transformation occurs at the time of acceleration of the strain rate.

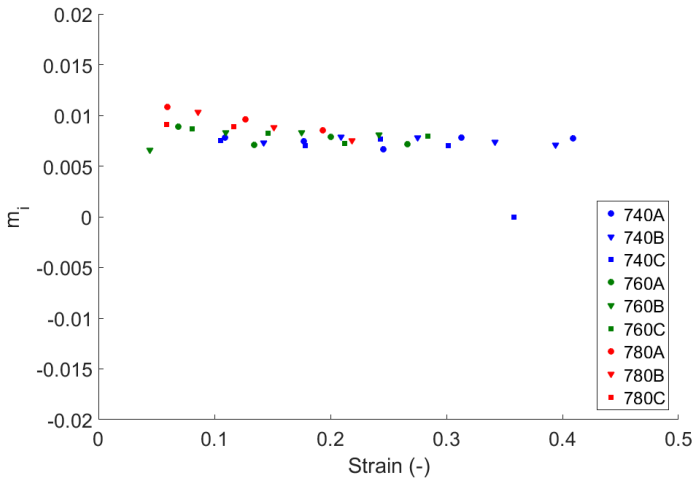

FIGURE 5.23: Instantaneous strain rate sensitivity for strain rate jumps from $10^{-4}s^{-1}$ to $10^{-2}s^{-1}$. The SRS was constant and positive for all samples. A, B, and C in the legend entries denote individual samples.

The instantaneous sensitivity, as can be seen in Figure 5.23, was positive and constant over the course of the tensile tests for all intercritical annealing temperatures. This is a typical result and was expected. However, there was perhaps a slight decrease of m_i with strain in samples annealed at 780°C. More data would be needed to determine if this effect is real or simply a statistical anomaly.

It was observed that the steady state SRS, m_{ss}, shows different trends depending on the point at which m_{ss} is evaluated. If m_{ss} is calculated 0.002mm/mm after the stress peak at the moment of acceleration, it can be seen in Figure 5.24a that $m_{ss}^{0.002}$ is constant and slightly positive. However if it is evaluated 0.005mm/mm after the peak or in the middle of the period of higher strain rate deformation (about 0.02mm/mm after the stress peak), the trends are different. In Figure 5.25a, $m_{ss}^{0.005}$ is still more or less constant with greater dispersion and is centered around 0. When m_{ss} is calculated at the middle of the high strain rate period, m_{ss}^{mid} was initially negative but gradually tended towards 0 as strain increased. The fact that three different trends can be obtained depending just on the point at which m_{ss} is calculated demonstrates the need to check the calculation with a more global view than just calculating a ratio at a single point.

When m_{ss} is considered as a function of the retained austenite volume fraction rather than the macroscopic strain, the observed trends become more complicated. It should be noted, however, that the small number of points obtained means that these trends should be taken in a qualitative sense rather than quantitative as more data is needed for the result to have a statistical meaning.

For $m_{ss}^{0.002}$, the values remained positive and for samples annealed at 760°C and 780°C an increasing trend was observed for decreased austenite volume fraction. The sample annealed at 740°C showed the opposite trend, with $m_{ss}^{0.002}$ decreasing with decreased retained austenite fractions.

For $m_{ss}^{0.005}$, it seems that the SRS is negative for small austenite fractions and becomes positive linearly as the austenite fraction increases. This is the opposite of what was expected for either possibility for the mechanism underlying the negative SRS observed in this steel because it would imply that the austenite has a positive SRS and that perhaps martensite has a negative SRS..

Finally for m_{ss}^{mid}, a similar trend to the one seen for $m_{ss}^{0.005}$ is observed, but shifted down to lower values. m_{ss}^{mid} is negative for low austenite volume fractions and increases somewhat linearly to 0 as the austenite volume fraction is increased. For T_{IA} values of 740°C and 760°C, m_{ss}^{mid} increased towards 0 as the retained austenite fraction decreased. For a T_{IA} of 780°C, m_{ss}^{mid} decreased very slightly as the austenite fraction was decreased. These trends seem to imply an effect of the composition or grain size of the retained austenite on the SRS as these are the primary characteristics that change with T_{IA}. While the increase in SRS seems more or less linear with decreasing retained austenite fraction, the slopes are not the same for each annealing temperature, which implies perhaps a difference due to the initial phase volume fractions or some other microstructural parameter. If there was not an additional effect, there should be no difference in the behavior from one annealing temperature to another.

Because the location of the calculated m_{ss} had such a significant impact on the trends observed for varying strain levels or retained austenite volume fractions, a "continuous" SRS estimation was made using tensile curves for samples strained at constant strain rates of $10^{-4}s^{-1}$ and $10^{-2}s^{-1}$. This is done to determine approximately what value of m is expected and thus determine which measurement point for m_{ss} is most appropriate. The two curves were projected onto a common strain axis and the difference in stress between the two used to calculate m_{cont} as

$$m_{cont} = \frac{ln(\Delta\sigma)}{ln(\dot{\varepsilon}_2/\dot{\varepsilon}_1)} \tag{5.2}$$

This ratio m_{cont} is plotted for each T_{IA} in Figure 5.27. Interestingly, once the Lüders band was completed, the SRS estimation was negative for all samples with an annealing temperature of 780°C giving the most negative result. In the samples annealed at 760°C and 780°C, m_{cont} began to increase slowly after a certain point. This is perhaps related to the near-completion of the martensite transformation. The sample annealed at 740°C did not show this effect and it did not approach 100% transformation of the retained austenite to martensite. The values of m_{cont} thus obtained seem to suggest that m_{ss}^{mid} is the best method for assessing the strain rate sensitivity as it is the one that gave distinctly negative values of the SRS as for m_{cont}.

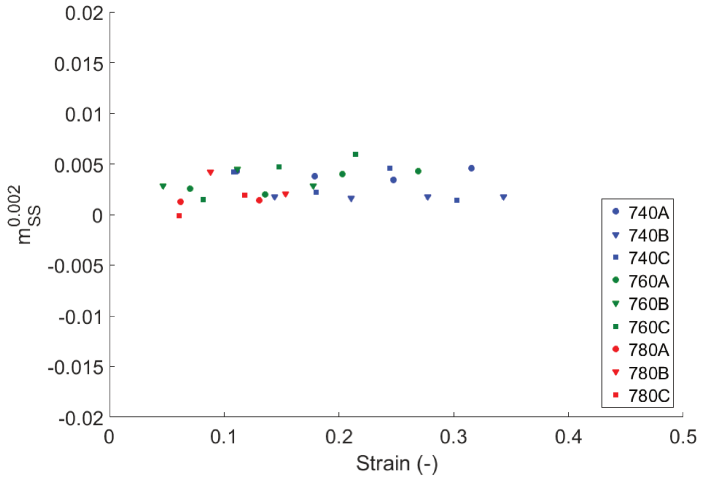

(A)

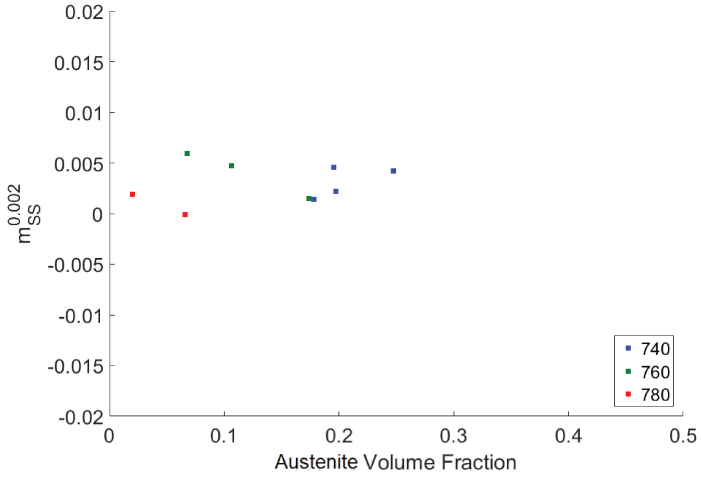

(B)

FIGURE 5.24: (a) When the steady state SRS is evaluated at 0.002 strain after the strain rate jump, m is positive and more or less constant as a function of strain. (b) When plotted against the austenite volume fraction, there is no notable trend in m.

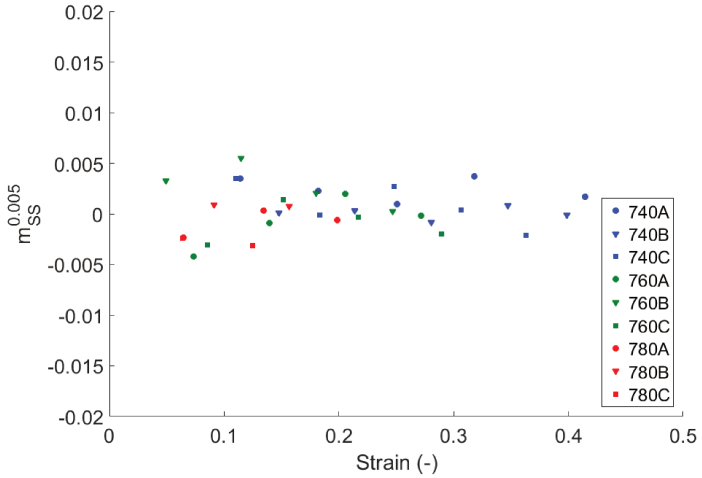

(A)

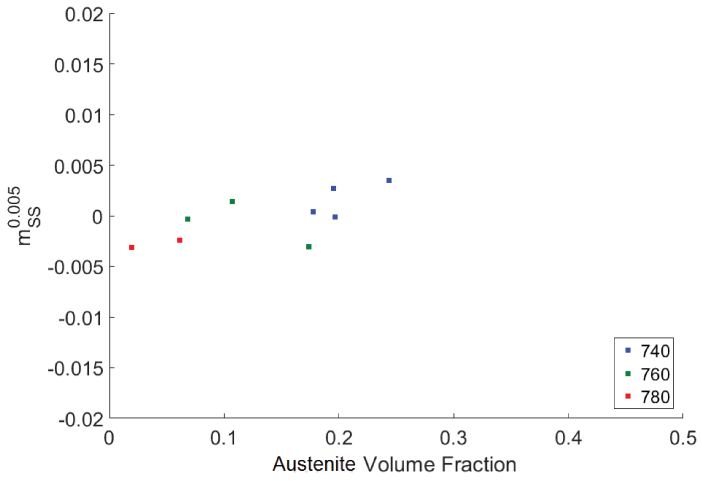

(B)

FIGURE 5.25: (a) When m_{ss} is evaluated at 0.005 strain after the strain rate jump, it is now seemingly constant and centered around 0. (b) When plotted as a function of the austenite volume fraction, there is perhaps an increasing trend in m_{ss} in which it begins positive at high V_γ and becomes more negative as TRIP occurs.

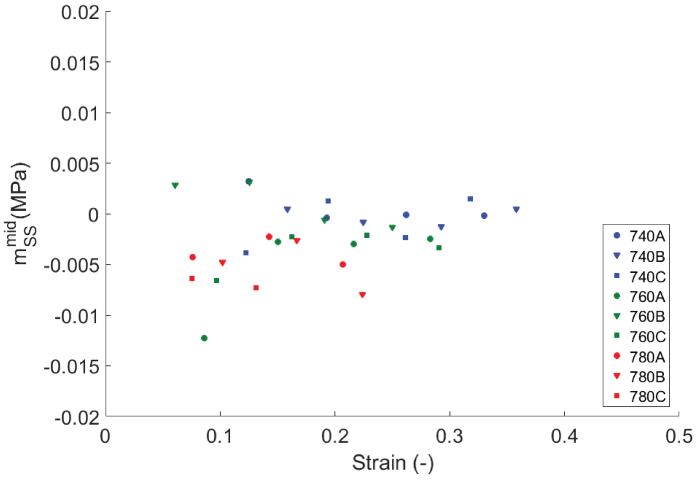

(A)

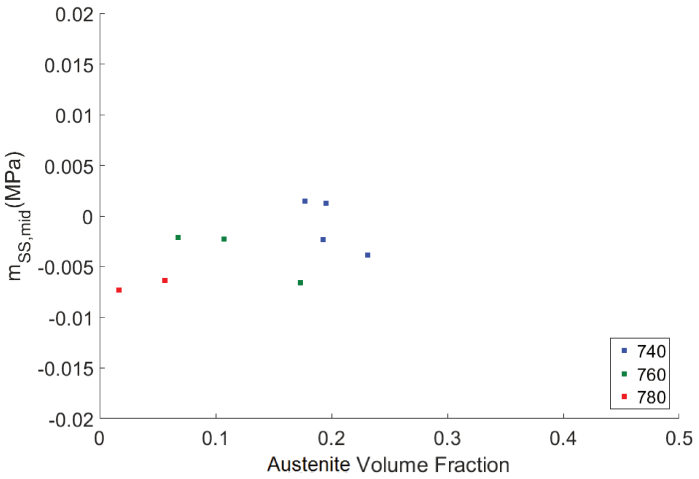

(B)

FIGURE 5.26: (a) When m_{ss} is calculated at the midpoint of the jump (about 2% strain after the jump), it is negative at low strains and seemingly becomes more positive as strain progresses. (b) when plotted versus the austenite fraction, m decreases with decreasing V_γ. However, if a single T_{IA} is considered, m_{ss} becomes more positive as TRIP progresses.

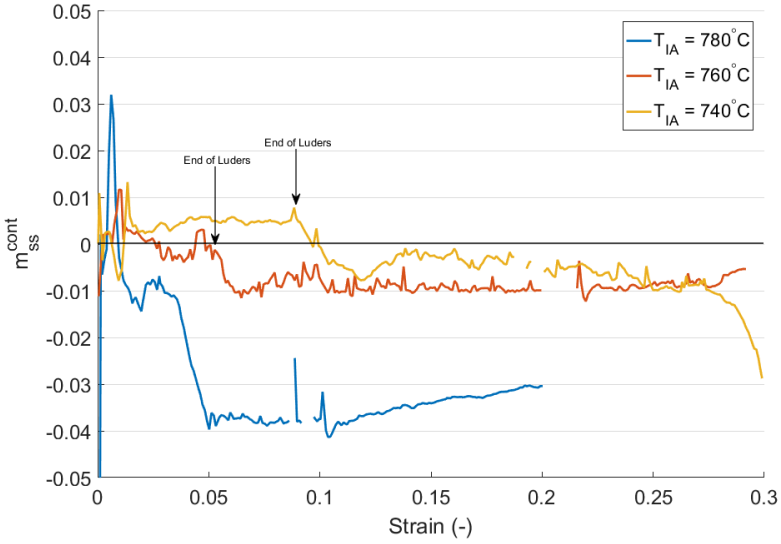

FIGURE 5.27: Strain rate sensitivity as calculated using tensile data with continuous strain rates of $10^{-4}s^{-1}$ and $10^{-2}s^{-1}$ for each intercritical annealing temperature. The approximate strain corresponding to the end of the Lüders plateau is indicated in relevant samples. The SRS is seemingly constant and negative in all cases, with perhaps a slight increasing trend towards the end of the test in samples annealed at 760°C and 780°C.

Chapter 6

Discussion

This chapter will seek to analyze in detail the results presented in the previous chapter. First, the results obtained in samples showing homogeneous deformation are considered. Next, a model will be described which will be used as a tool for interpreting the results obtained experimentally and which is parametrized using data for samples which were annealed at 780°C. This model will then be applied to examine the strain instabilities, changes in TRIP kinetics with both T_{IA} and $\dot{\epsilon}$, and the strain rate sensitivity. The Lüders strain is analyzed and is correlated with the degree of work hardening. Particular attention is paid to the presence or not of strain instabilities and the relation of their presence to the kinetics of TRIP.

6.1 TRIP Kinetics when Deformation is Homogeneous

In order to determine the conditions for the appearance of strain instabilities, the case when the strain is homogeneous must first be understood. This section will analyze the samples annealed at 780°C and determine how the transformation kinetics change during TRIP with strain rate. The strain rate sensitivity will be analyzed and compared to microstructural information obtained via the magnetic properties of the samples.

The Olson-Cohen model, as presented in Chapter 2, uses three parameters to describe the transformation kinetics in TRIP steels. The parameter α is defined by the probability of a nucleation site to form a martensite nucleus, and is as such dependent on the stability of the retained austenite. A second parameter β is related to the rate of generation of nucleation sites at the intersection of shear bands and is thus a function of the mechanical properties of the retained austenite. Finally the parameter n is based on composition and is fixed at 2 for all samples which has been shown to be an appropriate value for multiphase TRIP steels [90]. The Olson-Cohen model could, as suggested in Chapter 5, provide some insight into the changes in kinetics for different intercritical annealing temperatures. Figure 6.1 provides Olson-Cohen fits for samples annealed at 780°C submitted to tensile deformation at $10^{-4}s^{-1}$, $10^{-3}s^{-1}$, and $10^{-2}s^{-1}$. The corresponding parameters of the Olson-Cohen model are provided in Table 6.1. Because in these samples there is some initial thermal martensite from the quench, the transformation is considered

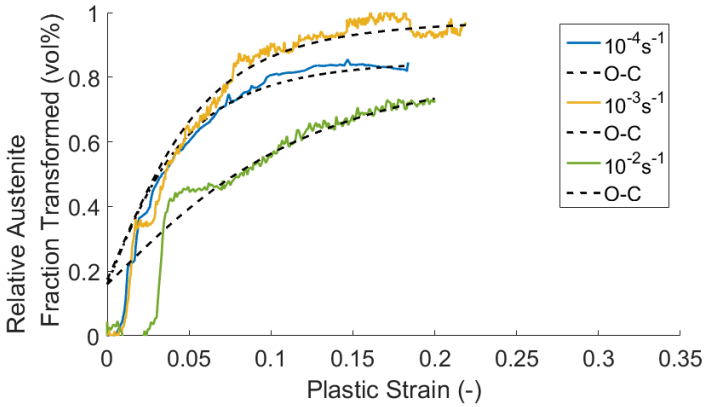

FIGURE 6.1: Transformation kinetics in samples annealed at 780°C and strained at imposed strain rates of $10^{-4}s^{-1}$, $10^{-3}s^{-1}$, and $10^{-2}s^{-1}$. The curves were fitted with the Olson-Cohen model, using the parameters provided in Table 6.1.

TABLE 6.1: Olson-Cohen Parameters for $T_{IA} = 780°C$

$T_{IA}(°C)$	$\dot{\epsilon}(s^{-1})$	α	β	n	ϵ_{pre}
	10^{-4}	18	1.9	2	0.02
780	10^{-3}	10	3.9	2	0.025
	10^{-2}	7.2	1.9	2	0.05

to be partially complete. During the formation of thermal martensite, it is likely that a large number of dislocations were created in the austenite, increasing the number of nucleation sites available for transformation. To account for this, a pre-strain factor was added to the Olson-Cohen model such that the amount of transformed austenite present in the initial microstructure predicted by the model was about the same level as predicted in Chapter 3 (roughly 20 vol%). This parameter is given as ϵ_{pre} in Table 6.1 and the new formulation of the Olson-Cohen model is

$$f_{\alpha'} = 1 - exp\big(- \beta[1 - exp(-\alpha(\epsilon + \epsilon_{pre})]^n\big) \tag{6.1}$$

It should be noted that for the sample strained at $10^{-3}s^{-1}$ (for all T_{IA}) it was necessary to pause the tensile test at regular intervals so that magnetic data could be saved to disk and the acquisition restarted. This resulted in stress relaxation during these pauses and slight overshoots of the flow stress upon reloading as was seen in Figure 5.14b. This resulted in increased work hardening and a higher rate of transformation, perhaps due to the additional mechanical energy input during yielding when reloading the sample. The samples at $10^{-3}s^{-1}$ will then not be included when analyzing trends in Olson-Cohen parameters as the resulting behavior is not the same as the other samples.

The parameters in Table 6.1 show that when the strain rate is changed from $10^{-4}s^{-1}$ to $10^{-2}s^{-1}$, β remains the same but α decreases by more than half. If the hypotheses made by Olson and Cohen [51] are correct, then this would indicate that martensite nucleation sites were generated at the same rate, but that the probability

of the formation of a martensite nucleus decreased with strain rate.

The kinetics of the martensite transformation are typically not strain-rate sensitive [91], so it is unlikely that the change in the Olson-Cohen parameters would be directly due to the increased strain rate. However, TRIP is temperature sensitive and the adiabatic heat generated at higher strain rates could reduce the transformation rate. In the samples annealed at 780°C, the transformation kinetics for a strain rate of $10^{-3}s^{-1}$ are difficult to interpret as previously mentioned. However, the transformation rate slows significantly when the strain rate is increased from $10^{-4}s^{-1}$ to $10^{-2}s^{-1}$.

The idea that the TRIP kinetics are slowed because of adiabatic heating is fairly well supported in the literature. It has previously been shown that increasing the strain rate can increase the temperature of the sample to such a level that the kinetics of the martensite transformation are affected [92–95]. This was demonstrated by Choi *et al.* for example, as shown in Figure 6.2 [95].

As can be seen in Figure 6.3, simulations including a small change in sample temperature showed a significant effect on the work hardening rate in a 304 austenitic stainless TRIP steel when the sample temperature increases via adiabatic heating. This observation is confirmed by the experimental results of Choi *et al.* on a duplex stainless TRIP steel [95]. They reported that the loss of work hardening was due to reduced TRIP from a combination of adiabatic heat and changes in strain partitioning between ferrite and austenite with strain rate. Figure 6.2 shows that an increase in strain rate from $10^{-3}s^{-1}$ to $10^{-2}s^{-1}$ resulted in an increase in sample temperature from 44°C to 99°C and the complete disappearance of the TRIP effect due to austenite stabilization at higher temperature.

These results seem to support the idea that the macroscopic strain rate sensitivity observed in the samples annealed at 780°C is due to a reduction in the work hardening rate provided by TRIP.

Assuming then, that the reduction in transformation rate is indeed due to an increase in sample temperature due to adiabatic heating and a consequent stabilization of the retained austenite, the parameters of the Olson-Cohen model can be explained. While the rate of generation of nucleation sites does not vary significantly with strain rate, the stabilization of austenite via adiabatic heat reduces the probability of transformation on an existing nucleation site. Revisiting the variations in model parameters with testing temperature as defined by Olson and Cohen [51]– which were previously presented in Chapter 2 and are now reused in Figure 6.4–the invariance of β is logical because the M_s temperature of the samples annealed at 780°C is about 58°C, so it is probable that ambient temperature falls in the flat region to the left of the curve for β. Additionally, if adiabatic heating were to increase the temperature, Olson and Cohen suggest that α should decrease. These expectations are perfectly in line with the parameter values obtained, so it seems that the assertion that adiabatic heat is responsible for the negative strain rate sensitivity in samples annealed at 780°C is well-founded.

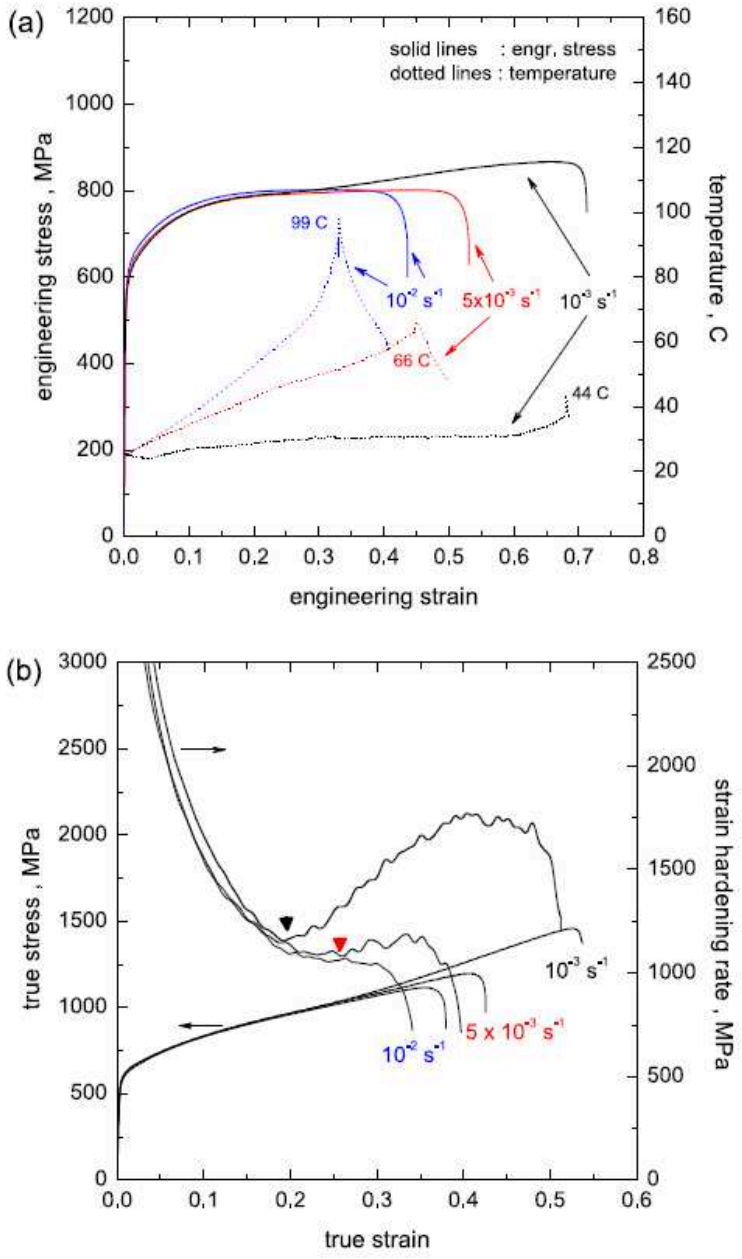

FIGURE 6.2: Experiments by Choi *et al.* [95] showed that the temperature increase due to adiabatic heating at high strain rates has a significant effect on the work hardening capacity of a duplex stainless TRIP steel.

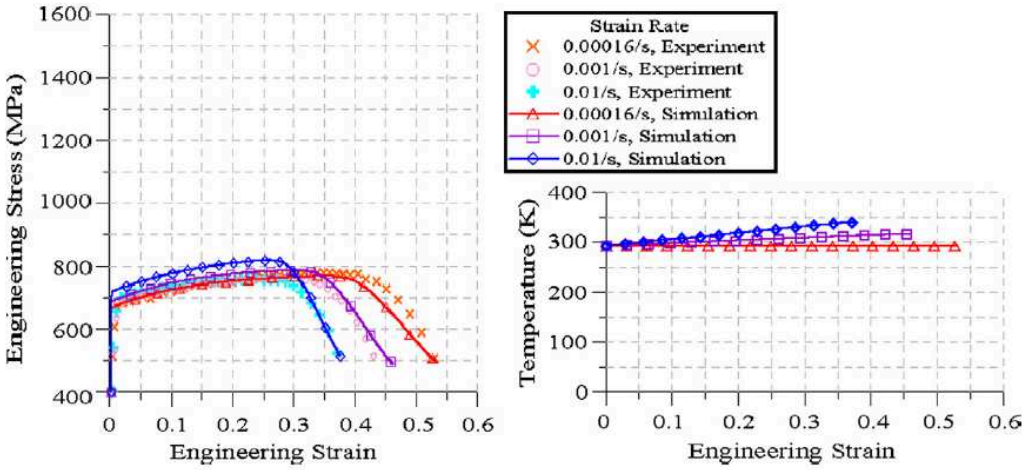

FIGURE 6.3: Simulations performed by Yoo *et al.* [93] showed that the slight increase in sample temperature with increasing strain rate has a significant effect on the kinetics of TRIP through a reduction of the uniform elongation when no transformation occurs to delay necking.

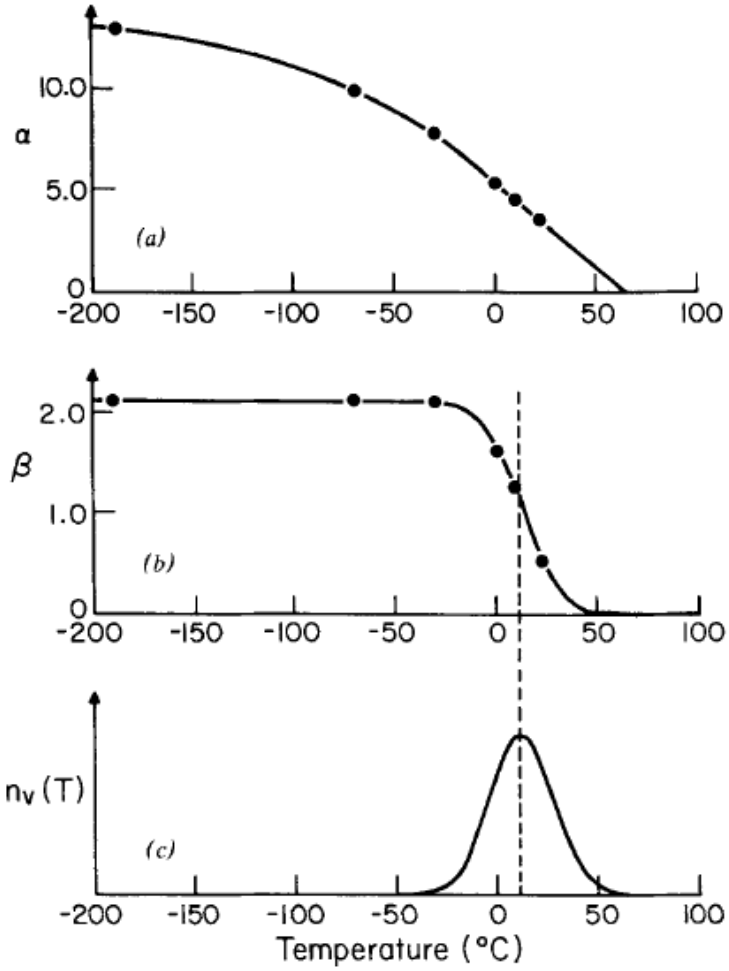

FIGURE 6.4: Trends in the parameters of the Olson-Cohen model with respect to deformation temperature support the hypothesis that adiabatic heat is responsible for the negative SRS observed in samples annealed at 780°C

.

In order to better understand the observed mechanical behavior of these steels with respect to the martensite transformation rate during TRIP in each, a simple model was constructed and calibrated using the data from samples annealed at 780°C as a baseline.

6.2 Model of Macroscopic Mechanical Behavior

The results obtained in this study provide an almost purely macroscopic description of the mechanical behavior of the steel. However, to understand the effects of microstructure, intercritical annealing temperature, retained austenite stability, and strain rate on the kinetics of TRIP or on the presence of Lüders or PLC bands, some knowledge of the micromechanical behavior of each phase is needed.

The physically-based models often used by metallurgists with hardening laws based on dislocation interactions are often poorly adapted for the sub-micrometric grain sizes seen in the UFG Medium Mn steel studied here. As such, a simple numerical model based on Voce hardening laws was developed to use not as a predictive tool, but as a means of understanding some of the trends observed in the mechanical behavior of this steel. This section will describe the model and the determination of its parameters.

6.2.1 Behavior Laws

In this steel, the vast majority of the work hardening comes from the martensite transformation. This was observed in the previous chapter, for example, in samples annealed at 780°C or 740°C. The stark difference in transformation rate led to drastically different amounts of work hardening. If, then, it is assumed that TRIP is the primary contributor to work hardening, a simple mechanical model with little hardening in the ferrite and austenite phases can be used. This assumption is reasonable, as it has been demonstrated previously that dynamic recovery of dislocations by absorption into grain boundaries severely limits work hardening when the grain size is very small [96]. The ferrite, austenite, and martensite phases were thus modeled with Voce laws such that the elasto-plastic transition was relatively rapid and hardening in the ferrite and austenite were low:

$$\sigma_i = \sigma_y + \sigma_s(1 - e^{-m\epsilon}) \tag{6.2}$$

where σ_y is the yield stress of the phase i, σ_s is the saturation value of the stress used for work hardening, and m is a strain hardening exponent. The values of these parameters could then be used, for example, to modify the relative strengths of each phase and observe the effect on the phase transformation. The yield stress σ_y was

calculated using the phase compositions as determined by ThermoCalc using the expression

$$\sigma_{y,\alpha} = 52 + 33C_{Mn} \tag{6.3}$$

for the ferrite [97],

$$\sigma_{y,\gamma} = 228 + 187C_c - 2C_{Mn} \tag{6.4}$$

for the austenite [98], and

$$\sigma_{y,\alpha'} = 800\sqrt[3]{C_c} + 33C_{Mn} \tag{6.5}$$

for the martensite [99]. As such, the behavior of the composite of all the phases is then determined by the chemical composition of each phase and the TRIP effect. The determination of the parameters σ_i and m_i will be described in Section 6.2.2. The macroscopic behavior is obtained using a mixture rule with the iso-work hypothesis. Iso-work assumes that the mechanical work performed by each phase in equivalent (rather than the stress or the strain in each phase) and has been shown to be effective in modeling multi-phase steels [97, 100]:

$$\Sigma dE = \sigma_\alpha d\epsilon_\alpha = \sigma_\gamma d\epsilon_\gamma = \sigma_{\alpha'} d\epsilon_{\alpha'} \tag{6.6}$$

where σ_i and $d\epsilon_i$ are the stresses and strain increments in each phase and Σ and E are the macroscopic stress and strain. The transformation kinetics were implemented using the Olson-Cohen model described in the previous section.

This model then relies on the Olson-Cohen parameters α and β, the saturated stresses in each phase i, $\sigma_{s,i}$ and exponents m_i from the Voce hardening laws, the phase volume fractions, and their chemical compositions. The Olson-Cohen parameters were obtained by fitting experimental data for each intercritical annealing temperature and strain rate. The Voce parameters σ_s and m were adjusted for each phase to fit experimental tensile results. The volume fractions used are obtained via magnetization measurements and, in the case of thermal martensite, estimations made considering SEM images and XRD measurements as well. The initial volume fractions of each phase used for each temperature are presented in Table 6.2.

The martensite volume fraction, when thermal martensite is present, is estimated based on ThermoCalc estimations made by ArcelorMittal and magnetic measurements of the ferromagnetic volume fraction. The ThermoCalc estimations suggest that at T_{IA}, the retained austenite fraction increases with annealing temperature but after a certain point it destabilizes. As such, the sample annealed at 780°C should have less ferrite than a sample annealed at 760°C. The measured retained austenite volume fraction is then used to estimate the ferrite and martensite volume fractions.

TABLE 6.2: Initial Phase Volume Fractions Used in Model

$T_{IA}(°C)$	$\dot{\epsilon}(s^{-1})$	α	γ	α'
	10^{-4}	0.68	0.32	0.00
740	10^{-3}	0.70	0.30	0.00
	10^{-2}	0.70	0.30	0.00
	10^{-4}	0.72	0.28	0.00
760	10^{-3}	0.70	0.30	0.00
	10^{-2}	0.67	0.33	0.00
	10^{-4}	0.59	0.21	0.20
780	10^{-3}	0.59	0.21	0.20
	10^{-2}	0.63	0.17	0.20

TABLE 6.3: Values of M_s and C_{Mn} for Each T_{IA}

$T_{IA}(°C)$	$M_s(°C)$	$C_{Mn,\alpha}$	$C_{Mn,\gamma}$
740°C	-7.5	0.0310	0.0829
760°C	26	0.0315	0.0775
780°C	58	0.0319	0.0727

The chemical composition of the phases affects the mechanical behavior and retained austenite stability. While the Olson-Cohen model does not directly use composition as an input (though the parameters can vary with respect to SFE, which is composition dependent), the effect of composition on the yield stress of each phase will have an effect in that the austenite will be more or less hard and thus make a smaller or larger contribution to mechanical work as defined in Equation 6.6. If the austenite is softer, it will undergo more strain and transform more rapidly through an accelerated generation of nucleation sites whereas the opposite is true if the austenite is very hard. The same ThermoCalc results that provided estimations of the M_s temperature of each alloy were used to obtain an accurate estimation of the manganese concentration in the ferrite and austenite for each intercritical annealing temperature. These are presented in Table 6.3 .

6.2.2 Determination of Model Parameters for T_{IA} =780°C

The results of experiments in which *in-situ* magnetic measurements were made were fitted with an Olson-Cohen model with the parameters provided in Table 6.1. However concerning the Voce model, it was observed by modifying the yield stress and saturation stress of the austenite that the martensite transformation rate is quite insensitive to changes in the austenite's behavior law. Increasing or decreasing the yield stress significantly did not change the transformation kinetics much due to the already rapid transformation as measured for this annealing temperature. Thus, a first approximation of the Olson-Cohen parameters can be made without any consideration of the mechanical behavior of the retained austenite and then fine-tuned as the macroscopic mechanical behavior is fitted to tensile data.

TABLE 6.4: Voce Parameters for $T_{IA} = 780°C$

	σ_y (MPa)	σ_s (MPa)	m (-)
Ferrite	135.0	250	10
Austenite	303.5	500	10
Martensite	931.0	5000	20

Once the Olson-Cohen parameters had been determined, the properties of the Voce laws were fitted against tensile data. In this way, one can assure that the model reproduces the same mechanical behavior and TRIP kinetics as observed experimentally. The only parameters left to be fit then, since the yield stresses are determined using Equations 6.3-6.5, are the saturation stresses $\sigma_{s,i}$ and the exponents m_i. The experiments performed at strain rates of $10^{-4}s^{-1}$ and $10^{-2}s^{-1}$ on samples annealed at 780°C were used as a baseline to determine these hardening parameters. The volume fractions of each phase are defined in Table 6.2.

Figure 6.5 shows the comparison of the model and the experimental data for samples annealed at 780°C and strained at $10^{-4}s^{-1}$ and $10^{-2}s^{-1}$ while the parameters of the Voce law for each phase are summarized in Table 6.4. The behavior of each phase for both strain rates is provided in Figure 6.6. Notably, the yield stress of the austenite is about 170 MPa higher than that of the ferrite. This seems counter to the idea that when austenite is softer than ferrite, TRIP can begin immediately and the work hardening is high enough to yield continuously. It is possible to fit the data with the austenite at lower stress (eg. 100 MPa works), but there is no physical reasoning (to the best of the author's knowledge) to justify such a change that warrants ignoring Equation 6.4.

It was seen that the level of work hardening observed in tensile experiments was not obtainable purely from the progressive addition of martensite via TRIP (with martensite and ferrite taken as perfectly plastic). As such, a small degree of work hardening was permitted in the ferrite and austenite, but small enough that the TRIP effect is still responsible for the gross majority of hardening. The martensite was also allowed to harden, but the parameters were defined such that it hardened very rapidly to simulate a predominantly elastic deformation. From the calibration process on samples annealed at 780°C it can be seen already that a simple change in transformation kinetics (and use of measured initial phase volume fractions) allows the model to fit the data for strain rates of $10^{-4}s^{-1}$ (A) and $10^{-2}s^{-1}$ quite well, as was shown in Figure 6.5.

6.3 Strain Localizations

In Chapter 5 the characteristics of the strain bands observed in samples annealed at 740°C and 760°C were quantified. The band widths, propagation velocities, strain increment within the band, and strain rates in the bands seemed to indicate that the first band that occurs at yielding is different from the subsequent bands. The

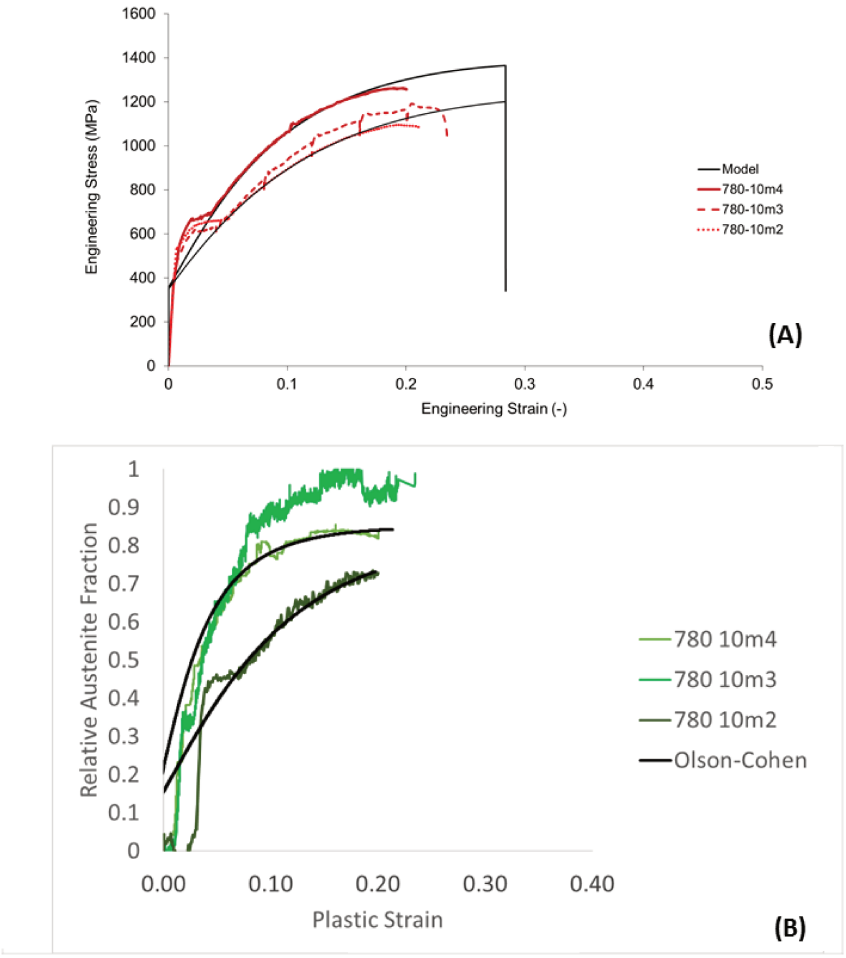

FIGURE 6.5: Comparison of the model to experimental data for a sample annealed at 780°C and strained at $10^{-4}s^{-1}$ and $10^{-2}s^{-1}$ (A) with the Olson-Cohen data fitted to magnetic measurement data (B).

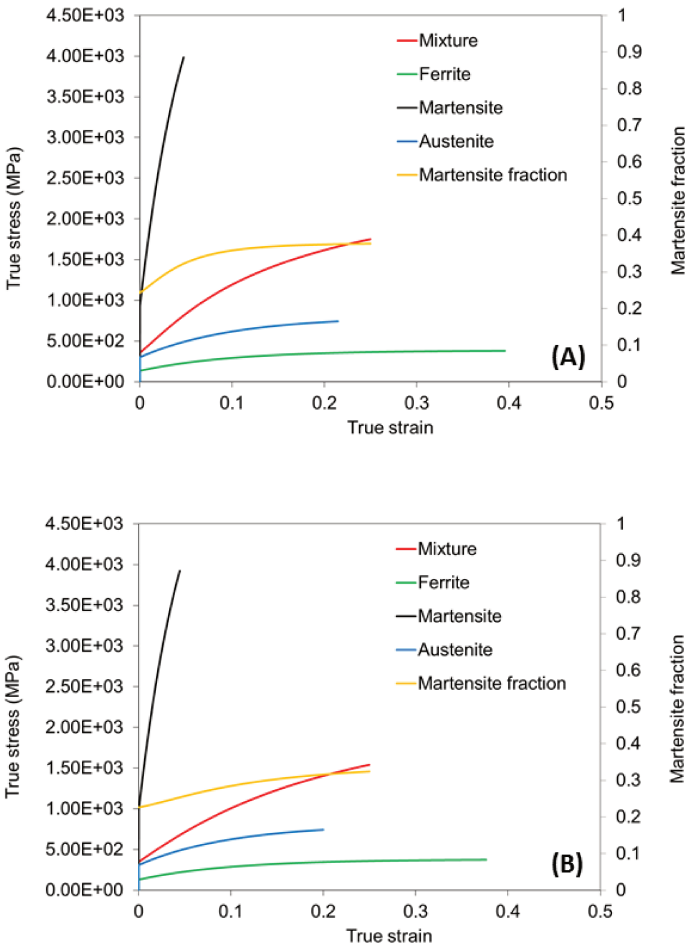

FIGURE 6.6: Mechanical behavior of each phase as predicted by the model for samples annealed at 780°C and strained at $10^{-4}s^{-1}$ (A) and $10^{-2}s^{-1}$ (B).

width of the first band was significantly smaller than those of the subsequent bands, the propagation velocity was distinctly different, and—for the sample annealed at 740°C—the strain increment and strain rate in the bands changed significantly between the first band and the following ones. It seems clear then, that the first band and the subsequent bands are the result of two different phenomena: an initial Lüders band at yielding followed by a PLC-type behavior during plasticity. This section will provide an analysis of both types of bands and the variations in band character that occur for different T_{IA} or strain rate.

6.3.1 Lüders Bands

The presence of Lüders bands was observed in all samples annealed at 740°C and 760°C, while those annealed at 780°C did not have any form of yield point elongation. This was shown with DIC spatiotemporal graphs in the previous chapter where the strain increment between images is plotted. The presence or not of strain bands has yet to be explained in the literature. Some have suggested that it is a true Lüders band that propagates through the ferrite matrix due to either a Cottrel dislocation-pinning effect [23, 101] or a grain size effect where dislocations are absorbed into grain boundaries and which can be overcome through the formation of a bimodal grain size [96]. This section will seek to analyze the Lüders bands through the use of both experimental data and the model developed in the previous section.

In the samples annealed at 740°C and 760°C, the observed Lüders bands differed in the magnitude of the Lüders strain and showed some variation with strain rate. Interestingly, the Lüders strain increased with strain rate in the sample annealed at 740°C, but decreased with strain rate for samples annealed at 760°C, as can be seen in Figure 6.7.

In materials exhibiting the Lüders phenomenon, the Lüders strain has previously been shown to increase with increasing strain rate in mild steel [102], so the result for intercritical annealing at 740°C is expected. The decrease in Lüders strain with increasing strain rate for samples annealed at 760°C, however, suggests an effect of TRIP on the Lüders band. It has been shown previously that TRIP can decrease the Lüders strain by increasing the work hardening rate at the lower yield stress [103], which seems to be the case here. In the previous chapter it was shown that in samples annealed at 760°C there is a burst of martensite transformation as the Lüders band passes, which could result in high local hardening and affect the Lüders strain.

Considering the sample annealed at 780°C, the presence of thermal martensite in the initial microstructure could result in sufficient hardening to avoid the appearance of the Lüders band, in particular because the thermal transformation is homogeneous rather than localized in a specific area.

A study by Tsuchida *et al.* [27] compiled data for various steels with yield point elongations and was able to correlate the work hardening rate at the lower yield

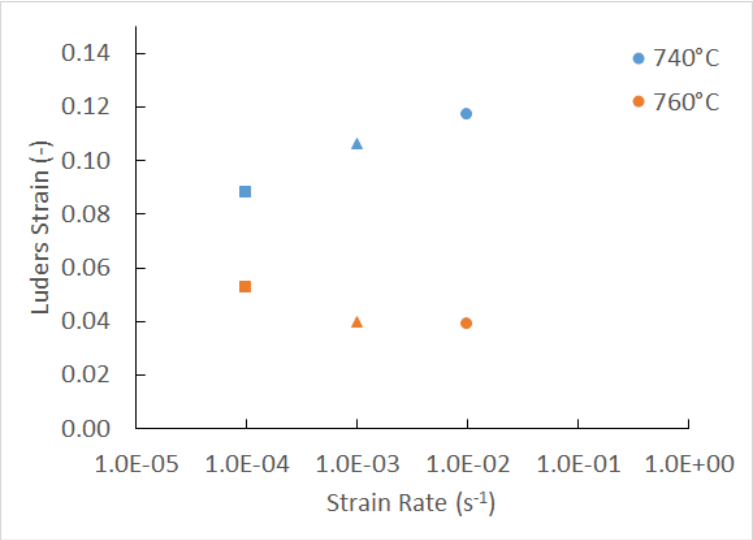

FIGURE 6.7: Observed Lüders strain plotted as a function of the applied strain rate for samples annealed at 740°C and 760°C. The Lüders strain increased with increasing strain rate for samples annealed at 740°C, but decreased for 760°C.

stress to the Lüders strain. They used a Holloman law to fit tensile data and calculate the work hardening rate at the lower yield stress by

$$\frac{d\sigma}{d\varepsilon} = Kn\left(\frac{\sigma_{LYS}}{K}\right)^{\frac{n-1}{n}} \tag{6.7}$$

where σ_{LYS} is the true stress at the lower yield stress and K and n are the parameters of the Holloman law. This methodology was applied to the steels studied here and added to Tsuchida's compilation of results in Figure 6.8. As can be seen in the figure, the current results do not quite fit with Tsuchida's analysis. However, the work hardening rate measured is that of the macroscopic sample.

Lüders bands often occur in ferritic steels, so perhaps the work hardening rate needed here is that of the ferrite. If the ferrite is softer than the retained austenite, then the initiation of yielding in ferrite could take the form of a Lüders band that passes through the other phases without significantly straining them beyond what is necessary to accommodate the strain the the ferrite, as suggested by Gibbs *et al.* [104]. An estimation of the work hardening rate in the ferrite was made by multiplying the calculated work hardening by the ratio of the stress in the ferrite to the macroscopic stress at yielding (which maintains the Iso-Work assumption used in the model). The model estimated this ratio to be about 0.251 for annealing at 740°C and 0.223 for annealing at 760°C. The data from the current study then shifts to the left and superimposes with Tsuchida's data, as seen in Figure 6.9. This suggests, then that the Lüders bands observed in Medium Mn steels could indeed be due to static strain aging in the ferrite.

If the Voce parameters for T_{IA} =780°C are now used as a starting point for the parameters at 760°C and strained at $10^{-2}s^{-1}$, the model can be tested in a case with

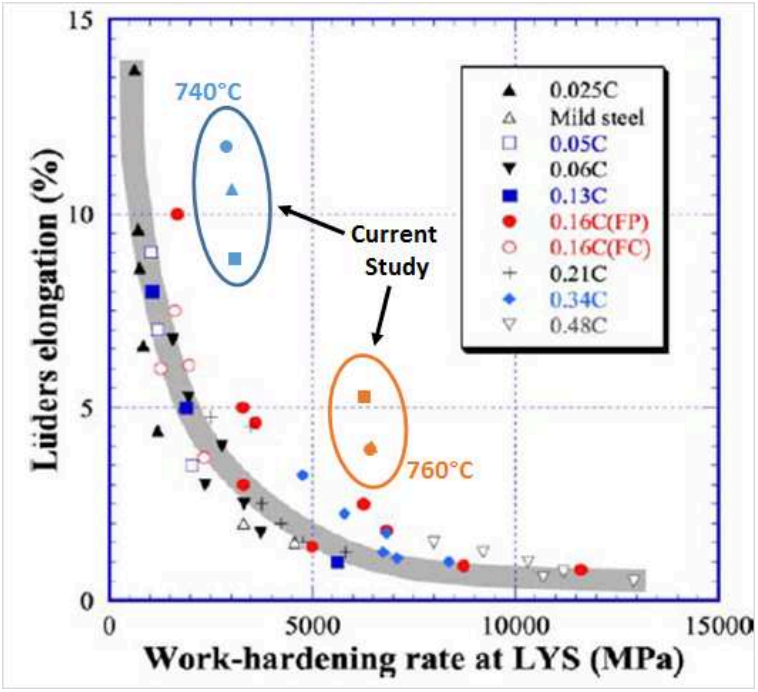

FIGURE 6.8: The Lüders strains and work hardening rates at the LYS for the Medium Mn TRIP steel studied here were superimposed on Figure 6 from [27] in which similar results are compiled for various different steels with Lüders bands.

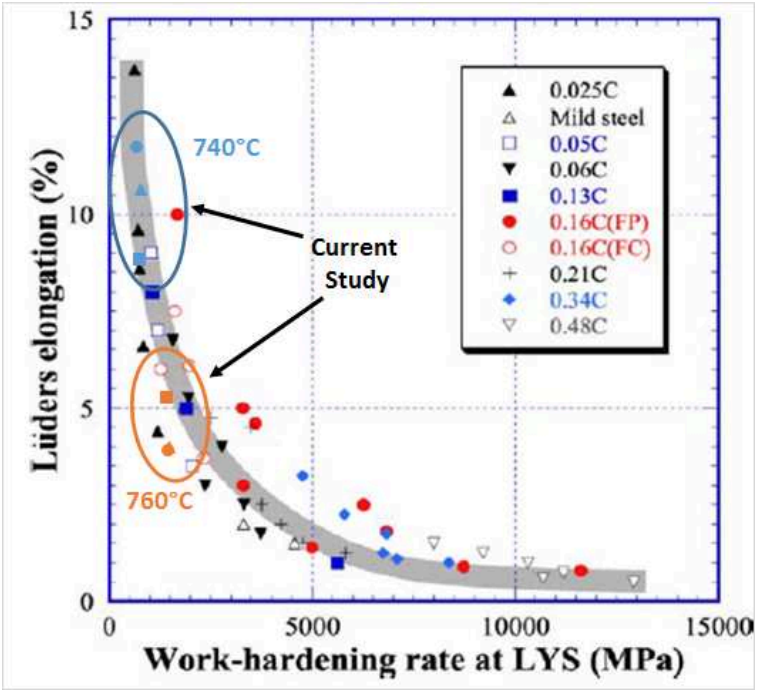

FIGURE 6.9: If the work hardening rate calculated for the current samples is multiplied by the ratio of the stress in the ferrite to the macroscopic stress at yielding, the results are in perfect agreement with those of Tsuchida *et al.*

TABLE 6.5: Olson-Cohen Parameters

$T_{IA}(^\circ C)$	$\dot{\epsilon}(s^{-1})$	α	β	n
	10^{-4}	6	0.3	2
740	10^{-3}	6	0.3	2
	10^{-2}	8	0.15	2
	10^{-4}	15	1.2	2
760	10^{-3}	13	1.6	2
	10^{-2}	17	1.9	2
	10^{-4}	18	1.9	2
780	10^{-3}	10	3.9	2
	10^{-2}	7.2	1.9	2

a Lüders band but without PLC. The homogeneous deformation after the passage of the Lüders band in this sample makes it ideal to test how the behavior is affected by the presence of a Lüders effect. If the hardening laws for each phase are held constant and only the Olson-Cohen parameters are modified according to the fitted values in Table 6.5, the mechanical behavior for this sample requires 100MPa to be added to the macroscopic stress of the mixture in order for the model to fit the experimental data. The ability to fit the data in this case by simply shifting the stress-strain curve upwards supports the idea of static strain aging as the culprit for the Lüders band, as static strain aging would increase the stress needed for the onset of plasticity by inhibiting dislocation motion.

When the same approach is used for samples that deform heterogeneously–for anneals at 760°C and 740°C at all strain rates except for the sample annealed at 760°C and strained at $10^{-2}s^{-1}$–the additional stress needed to fit experimental data increased. In the samples annealed at 740°C, the additional stress needed was 300MPa and for samples annealed at 760°C 400MPa was needed. Comparing the Olson-Cohen parameters for these samples with those that deformed homogeneously, the strain hardening from TRIP was reduced. The difference in the additional stress needed to account for static strain aging is perhaps due to the presence of dynamic strain aging, so a solute effect that pins dislocations and results in PLC bands.

Thus, in the case where Lüders bands are present it seems that the work hardening does not change, but a static strain aging effect is present that artificially increases the yield stress before returning to the normal behavior. The stress needed to fit experimental data when there is PLC is higher than when no PLC occurs. The fits for intercritical anneals at 740°C and 760°C are presented in Figures 6.10 and 6.11.

Up to this point, it seems to be clear that a relatively high work hardening rate is needed if the length of the Lüders plateau is to be reduced. If the steel hardens more quickly, the unpinning stress can be attained for a smaller strain increment and the Lüders strain is reduced. Results obtained by [96] and [25] show that a second intercritical anneal can also greatly reduce the Lüders strain through the modification of grain morphology. Han proposed that a larger ferrite grain size increased the propagation velocity of the Lüders band and limited dynamic recovery in grain

TABLE 6.6: Voce Parameters for $T_{IA} = 740°C$

	σ_y **(MPa)**	σ_s **(MPa)**	m **(-)**
Ferrite	122.0	250	10
Austenite	334.5	500	10
Martensite	1006.3	5000	20

TABLE 6.7: Voce Parameters for $T_{IA} = 760°C$

	σ_y **(MPa)**	σ_s **(MPa)**	m **(-)**
Ferrite	140.4	250	10
Austenite	316.4	500	10
Martensite	967.8	5000	20

boundaries that is observed in UFG microstructures. Thus, work hardening is increased in the ferrite which could reduce the Lüders strain. In Steineder's work, the second anneal results in a modification of the grain morphology of both phases in forming a more lamellar than globular microstructure. Steineder suggested that this change in morphology allows dislocation cells to form and thus permits more work hardening than is possible with UFG globular microstructures. Thus, the explanations for the reduction of the Lüders strain after a second anneal are also based on work hardening, reinforcing the assertion that control of the work hardening rate at the onset of plasticity plays an important role in controlling the Lüders strain.

6.3.2 Portevin-Le Châtelier Bands

Once the Lüders band has completely traversed the sample's tensile length, plasticity continued through the nucleation and propagation of a series of subsequent strain bands that were either propagative or random depending on the intercritical annealing temperature and strain rate. In general, the samples annealed at 740°C and 760°C showed a PLC effect, while the sample annealed at 780°C showed no PLC effect with the only exception being the sample annealed at 760°C and strained at $10^{-2}s^{-1}$ which did not have PLC. Several other authors have shown that PLC is present in Medium Mn TRIP steels within a certain range of intercritical annealing temperatures [13, 23, 24, 105], however no consensus on the origin of the effect has been established.

To demonstrate that the strain instabilities that occur over the course of plastic deformation are indeed a PLC effect, the characteristics of the band were compared to those measured on PLC bands in TWIP steels and solution-strengthened aluminum alloys. Notably, the previous chapter provided measurements of the band width, propagation velocity, strain increment in the band, and the strain rate within the band. This characterization will utilize primarily the results obtained for an anneal at 740°C as the bands in this case were purely propagative and were able to be reliably characterized. The PLC bands in samples annealed at 760°C were much more random, making it difficult to measure the propagation velocity accurately.

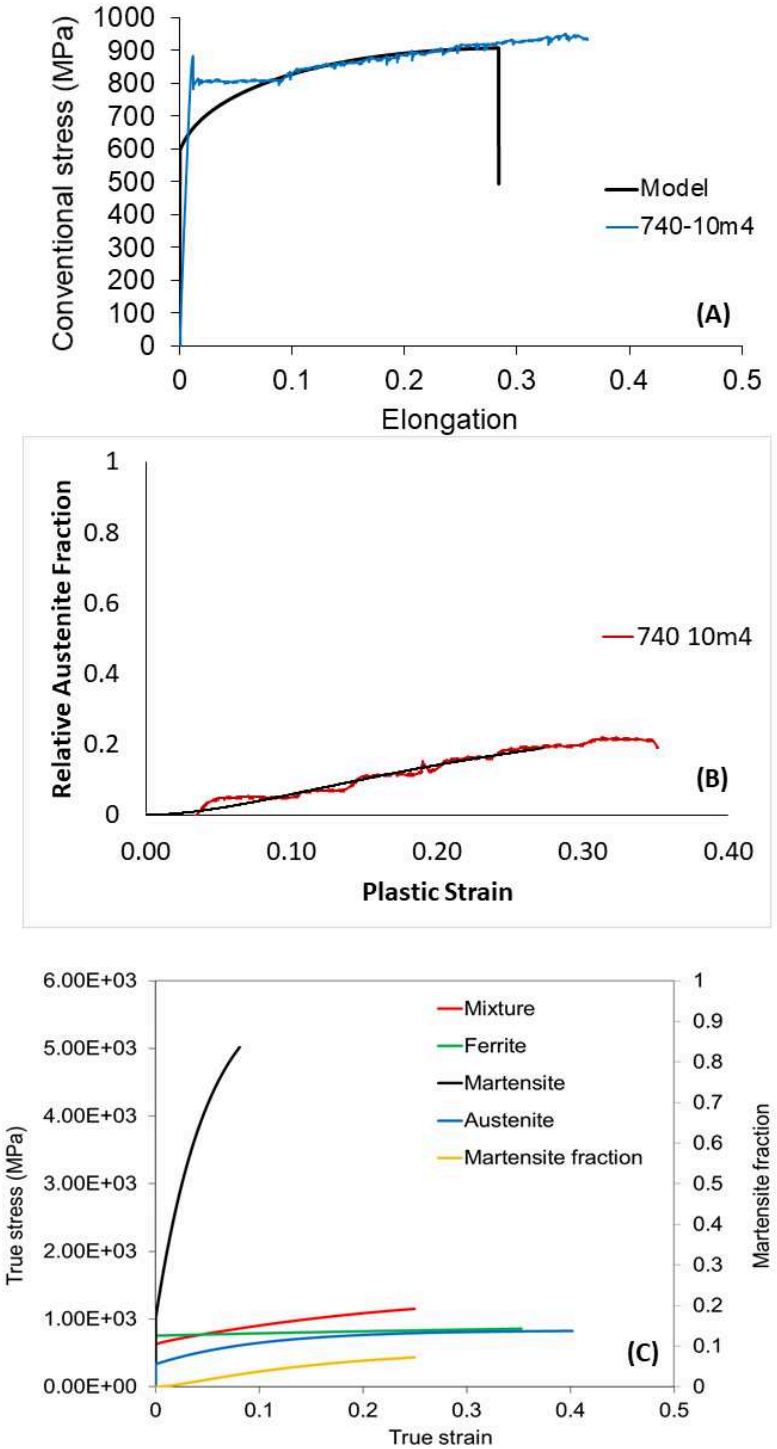

FIGURE 6.10: Comaprison of the model to experimental data for a sample annealed at 740°C and strained at $10^{-4}s^{-1}$ (A) with the Olson-Cohen data fitted to magnetic measurement data (B) and the mechanical behavior of each phase (C).

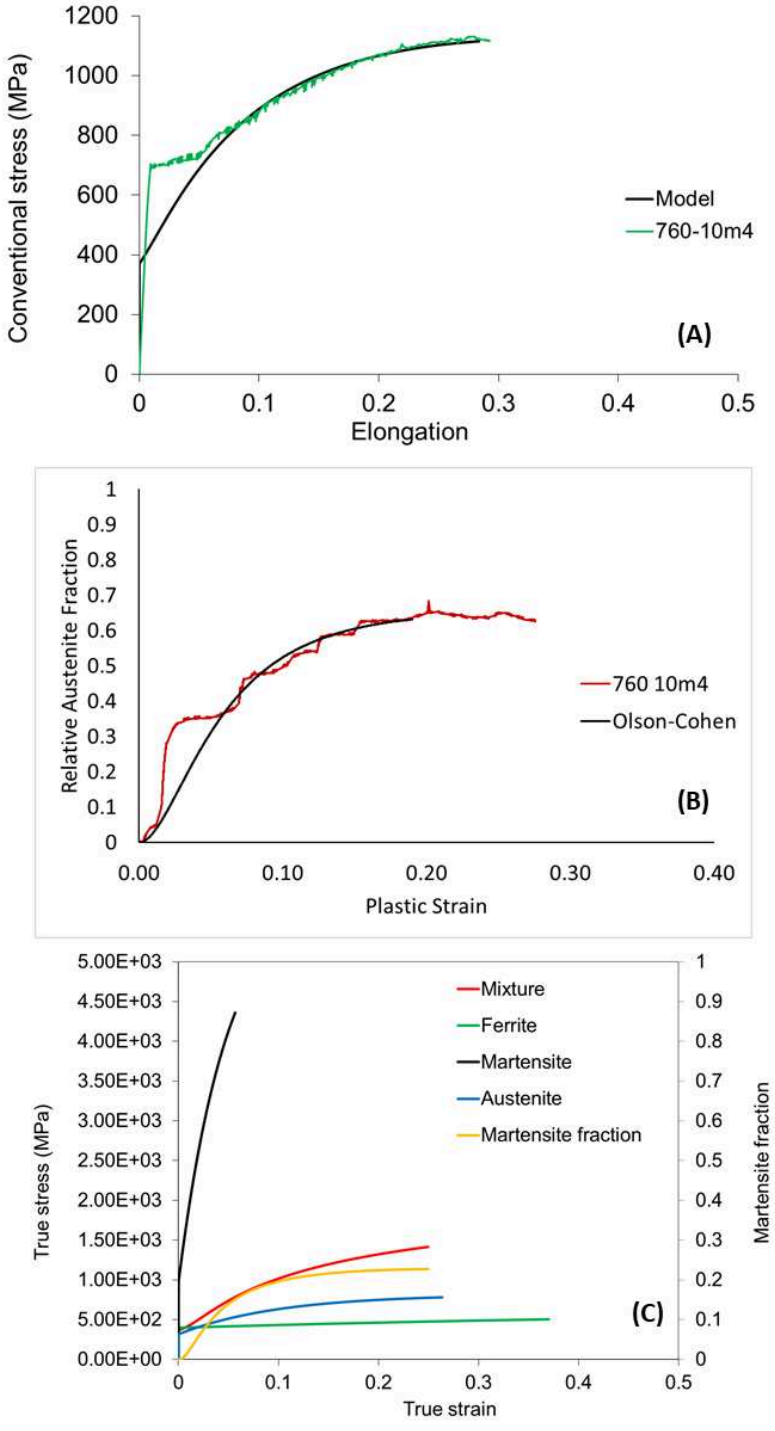

FIGURE 6.11: Comparison of the model to experimental data for a sample annealed at 760°C and strained at $10^{-4}s^{-1}$ (A) with the Olson-Cohen data fitted to magnetic measurement data (B) and the mechanical behavior of each phase (C).

The propagation velocity is also needed to calculate the band width because the displacement of the band between images needs to be taken into account. As such, the PLC bands in the sample annealed at 760°C are used only for the measured strain increment in the band and strain rate in the band since these do not require knowledge of the propagation velocity. They will also be discussed later when the difference in PLC character (propagative versus random) and effects of strain rate on PLC are analyzed.

The average band width of the PLC bands in samples annealed at 740°C was 0.77mm, which was about 27% larger than the Lüders band which was 0.605mm in width. Moreover, the average propagation velocity of PLC bands of 0.583mm/s was 53% larger than the 0.381mm/s measured for the Lüders band. The strain increment in the PLC bands was more or less constant for both 740°C and 760°C at about 0.015, perhaps increasing very slightly as the macroscopic strain increased. The strain in the Lüders bands were significantly higher–about 0.04 for $T_{IA} = 760^\circ\ C$ and 0.07 for $T_{IA} = 740^\circ\ C$–suggesting that the Lüders bands and PLC bands are indeed two different phenomena.

In the literature [34, 35, 89], the band propagation velocity and strain rate in the band are typically normalized by the imposed displacement rate and strain rate, respectively. If this methodology is applied to the results presented in Figure 4.5c in the previous chapter, they can be compared to published data for TWIP steels and aluminum alloys. The band propagation has thus been normalized by the imposed crosshead displacement speed and the strain rate in the band is normalized by the initial imposed strain rate. These results are presented in Figure 6.12.

The same measurement of the normalized band propagation velocity was made by both Zavattieri *et al.* [34] and Bian *et al.* [35], as presented in Figure 6.13. Using their data, it can be seen that in the two studies the normalized propagation velocity decreased with strain at rates of about -1.25mm/s/% and -1.4mm/m/%, respectively. Ait-Amokhtar [89] observed the same trend with a slope of about -1.2mm/s/% for the transition zone between type A and type B PLC in an Al-Mg alloy. This decreasing trend is observed in the current data as well, though the rate of decrease of -0.82mm/s/% is quite a bit smaller. However, the studies to which the current results are compared were performed on, respectively, a 0.6C-17Mn TWIP steel, a 0.6C-23Mn TWIP steel, and an aluminum alloy. The chemical composition and plastic deformation mechanism are significantly different in the current case, so to find that the rate of decrease is within an order of magnitude of the published values for such starkly different materials strongly suggests that the same type of effect is being observed. At the same time, that TWIP steel and Al have almost exactly the same slope while the current TRIP steel has a smaller slope suggests that perhaps either TRIP or the multi-phase microstructure has an effect on the propagation velocity.

If the strain rate within the band is now considered, the average value of about 12 times the applied macroscopic strain rate is in good agreement with the values

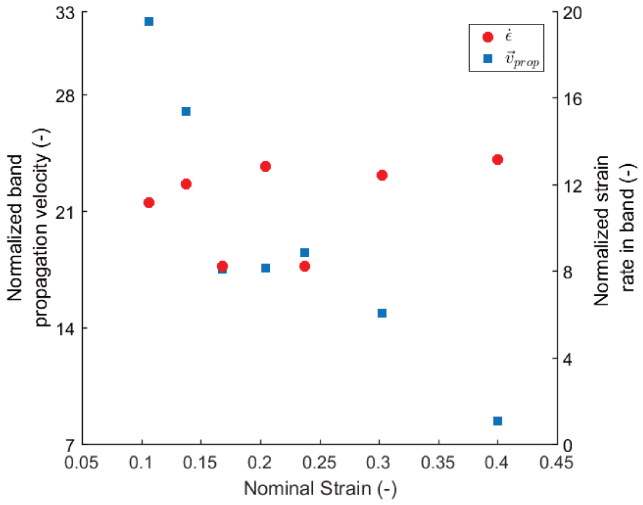

FIGURE 6.12: Band propagation velocity normalized by the crosshead speed and strain rate in the band normalized by the applied strain rate, both plotted as a function of the macroscopic strain. Data was obtained from DIC experiments on a sample annealed at 740°C and strained at $5 \cdot 10^{-4} s^{-1}$. The points corresponding to the Lüders band are removed in this figure.

obtained by Zavattieri *et al.* [34] for a TWIP steel deformed with two different applied displacement rates. Zavattieri's results are presented in Figure 6.14. In the case of the TWIP steel, it was seen that the normalized strain rate increased with applied strain. In the TRIP steel studied here, it is unclear if this same trend occurred. Fewer data points were obtained, so there are arguments to be made for the assertions that the strain rate in the band is constant or that it increases very slightly from about 10-11 to about 13. More data is required to determine definitively if this same trend is observed, but the fact that the values obtained are very close to Zavattieri's further suggests that these instabilities are indeed a type of PLC.

Ait-Amokhtar *et al.* [106] also described PLC bands as having a large longitudinal component, relatively weak transverse component, and no shear component. This was true of the PLC bands observed in the steel studied here, as can be seen in Figure 6.15.

In Chapter 5 it was suggested that the type of PLC present varied depending on the strain rate for a given intercritical annealing temperature. In fact, as can be seen in Figure 6.16, for samples annealed at 740°C PLC types A and B were observed, while types A, B, and C were each observed for the samples annealed at 760°C. To quickly reiterate the difference between types as described in [89], Type C PLC bands are purely stationary and random. Type B bands are random but propagative–that is, they will propagate, but not over the whole length of the sample. The band's propagation will abruptly stop and another will appear elsewhere in the sample. Finally type A PLC bands are purely propagative and will traverse the entire gauge length before a new band nucleates.

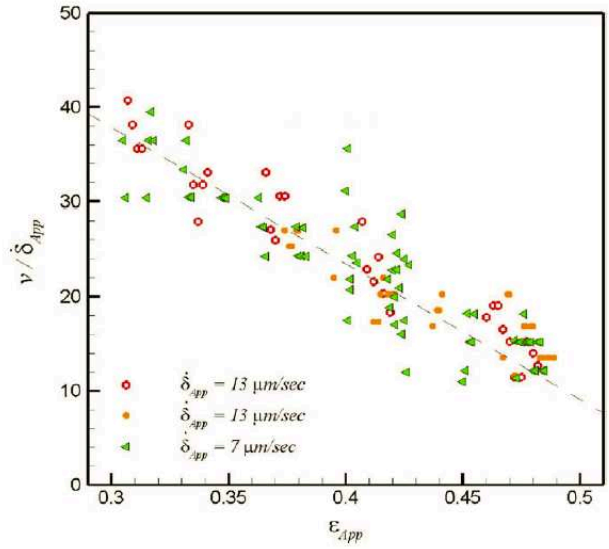

(A)

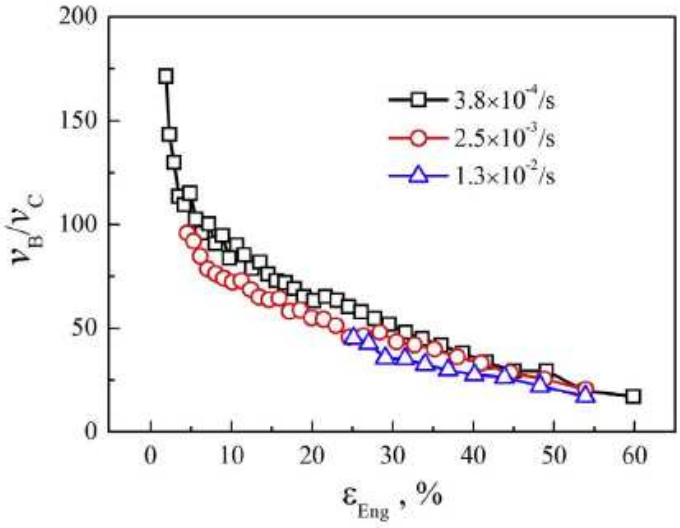

(B)

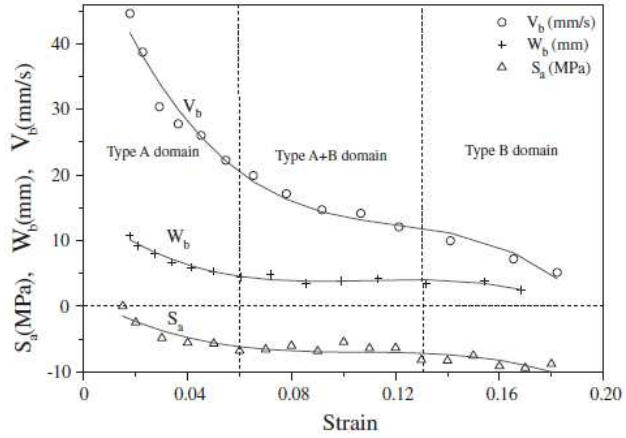

(C)

FIGURE 6.13: Published data by Zavattieri *et al.* [34] for a 0.6C-17Mn TWIP steel (A), Bian *et al.* [35] for a 0.6-23Mn TWIP steel (B), and Ait-Amokhtar *et al.* [89] for an Al-Mg alloy (C) showing a linearly decreasing trend when the band propagation velocity in normalized by the imposed displacement rate. Studies were performed on high-Mn TWIP steels exhibiting PLC instabilities.

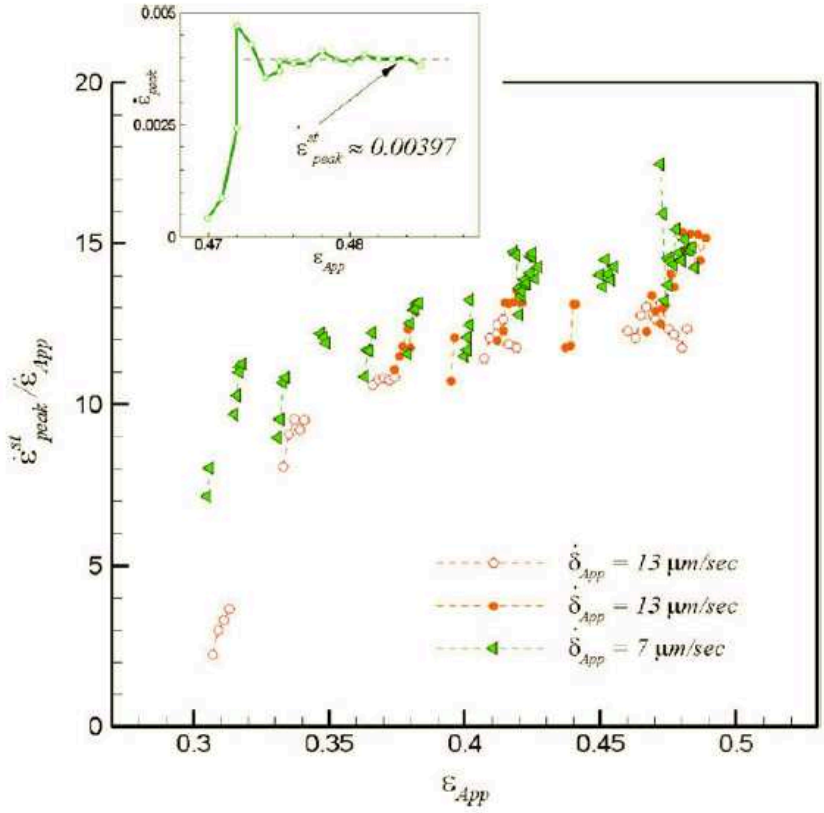

FIGURE 6.14: The strain rate in PLC bands normalized by the applied macroscopic strain rate and plotted as a function of the macroscopic strain in a 0.6C-17Mn TWIP steel from [34].

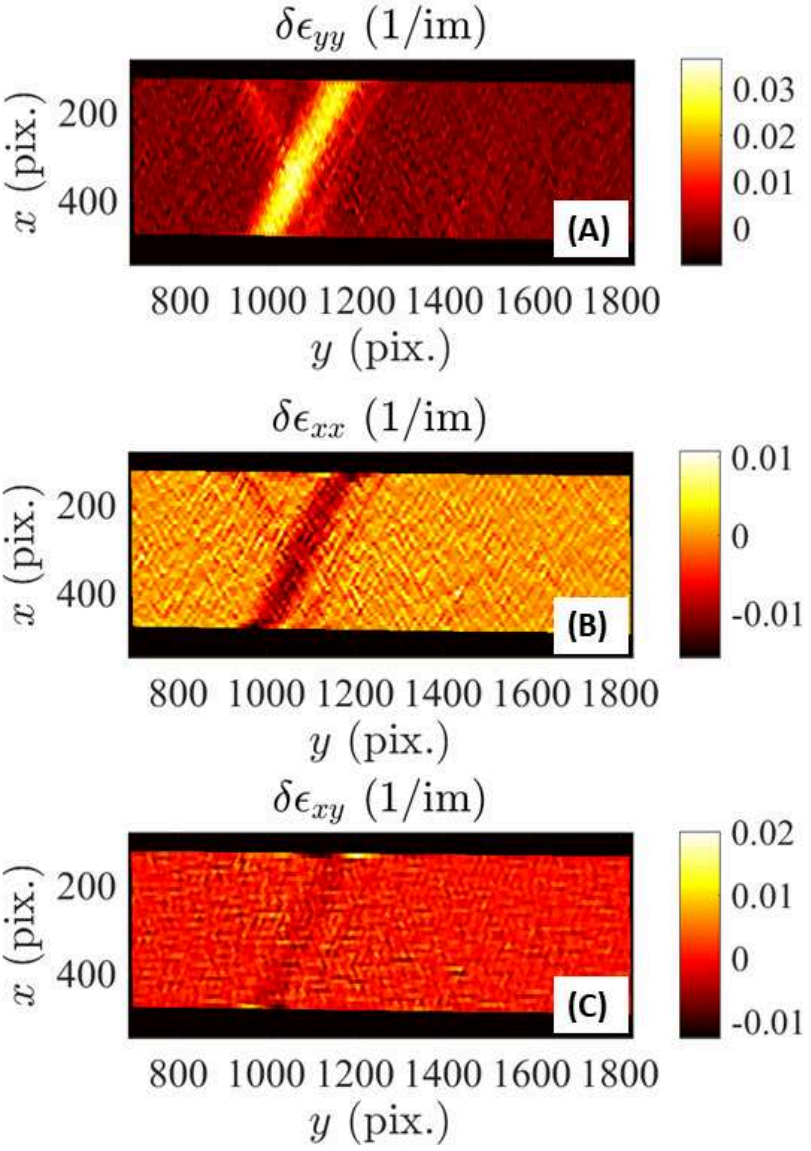

FIGURE 6.15: The strain components along the longitudinal (A), transverse (B), and shear (C) components of a PLC band in a sample annealed at 740°C and strained at $5 \cdot 10^{-4} s^{-1}$ from the current study.

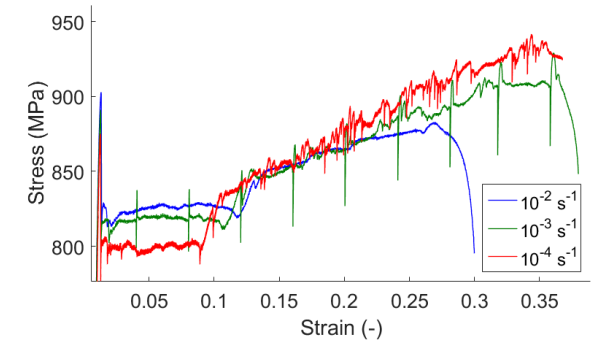

(A)

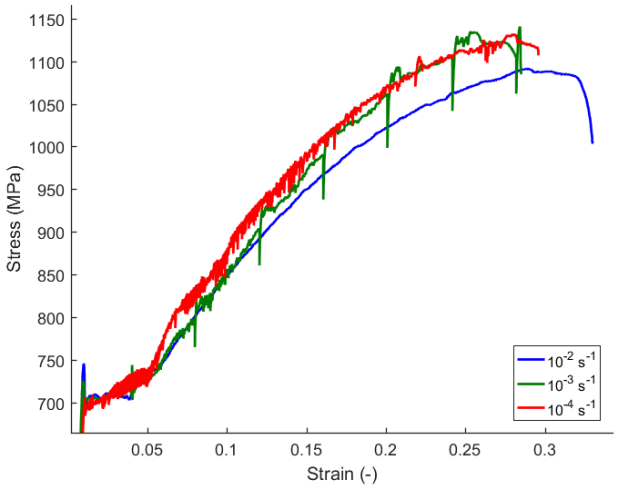

(B)

FIGURE 6.16: Changes in type of PLC behavior observed in samples annealed at 740°C (A) and 760°C (B) for different strain rates.

The samples annealed at 740°C and strained at $5 \cdot 10^{-4}s^{-1}$, $10^{-3}s^{-1}$, and $10^{-2}s^{-1}$ showed clear "steps" in the tensile curves with relatively little serrations. However in the sample strained at $10^{-4}s^{-1}$, high frequency serrations are observed in between points where significant stress relaxations occur. This is more indicative of type B PLC, much like in the samples annealed at 760°C and strained at $5 \cdot 10^{-4}s^{-1}$ or $10^{-3}s^{-1}$. The sample annealed at 760°C and strained at $10^{-4}s^{-1}$ showed very intense serrations throughout the tensile test, with the amplitude of the serrations decreasing with strain. No steps were observed in this sample. It is very interesting that the stress amplitude of the serrations decreased with strain, as typically the opposite is observed in PLC [41]. This could be explained by the decrease in retained austenite volume fraction resulting in fewer interactions between solutes and dislocations in the austenite. Finally, the sample annealed at 760°C and strained at $10^{-2}s^{-1}$ did not exhibit any PLC.

It is of interest to understand in what case PLC bands are expected to be observed in Medium Mn TRIP steels. To that end, Figure 6.17 provides a map of the combinations of macroscopic strain rate and martensite start temperature (M_s) as estimated

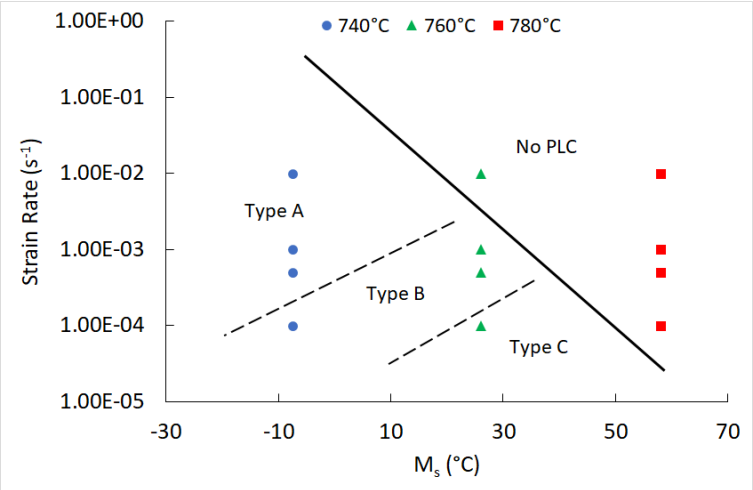

FIGURE 6.17: Map of tensile tests performed at different macroscopic applied strain rates for different intercritical annealing temperatures, indicating the type of PLC bands observed, if any.

by ThermoCalc. Interestingly, as M_s increases for a given strain rate, it seems possible to transition from type A to B to C and finally to the disappearance of PLC. If the intercritical annealing temperature is assumed to change the Mn content of the austenite, then it could be reasoned that at low T_{IA} there is relatively less manganese in austenite and thus fewer C-Mn clusters to pin dislocation motion, making type C PLC very difficult to obtain due to limited solute-dislocation interaction. With increasing strain rate, the propagation of type A PLC bands is increasingly favored over types B or C.

6.4 Strain Rate Effects on Tensile Behavior

6.4.1 Effect of Strain Rate on TRIP

Results of *in-situ* saturated magnetization measurements showed that there is a significantly different rate of martensite transformation during TRIP for the three different intercritical annealing temperatures studied. This is often explained in the literature as an effect of the stability of retained austenite [14, 15, 18]. However, it is of interest to understand exactly how this difference in transformation kinetics manifests itself, as austenite stability is not the only factor influencing it. It has been shown that there is a correlation between the stability of retained austenite and its stacking fault energy (SFE) [15], but there are also other micromechanical effects such as stress/strain partitioning and the generation of martensite nucleation sites.

Beginning with the samples annealed at 780°C since these samples did not exhibit any sort of strain bands, it can be seen in Table 6.5 that α decreases with increasing strain rate. The martensite transformation thus slows down when the strain rate is increased as the probability of transformation decreases. The decrease in work

hardening in these samples with increasing strain rate is thus a result of slower transformation kinetics and seemingly not a strain rate sensitivity of the austenite. The mechanism for the decrease in transformation probability is possibly by the increase in sample temperature due to increased adiabatic heating as the strain rate increases. This is supported by Figure 6.1 wherein the tensile data for strain rates of $10^{-4}s^{-1}$ and $10^{-2}s^{-1}$ are able to be reproduced by only changing the Olson-Cohen parameters for the transformation kinetics.

If the austenite did soften with higher strain rate, plastic strain would become more concentrated in the austenite and the transformation should speed up due to an increase in the number of nucleation sites. If this were to occur, the hardening provided by TRIP could likely compensate for the softening contributed by the austenite.

In the samples annealed at 740°C and 760°C, the trend is less clear. In these samples, strain bands form and it was demonstrated in the previous chapter that the strain rate in the band is significantly different from the applied strain rate. The concentration of strain in a band could also concentrate the adiabatic heat in the band as there is less volume deforming and less surface available for heat dissipation while a given point in the sample is being deformed. Nonetheless, it is interesting to note that for both intercritical annealing temperatures, α shows a minimum for a strain rate of $10^{-3}s^{-1}$ and β shows a maximum. So for intermediate strain rates, it seems that the probability of transformation decreases while the number of nucleation sites increases.

Interestingly, the transformation rate curves for anneals at 760°C and 780°C for a strain rate of $10^{-2}s^{-1}$ are superimposed as can be seen in Figure 6.19c. This points out a limitation in the use of a pre-strain factor in the Olson-Cohen model in that because the beginning of the curves do not superimpose with this addition, it is difficult to assert that the transformation rates are truly the same. At the same time, the fact that the transformation is partially completed must be taken into account, so this limitation will have to be accepted unless a model that can better account for the difference in initial nucleation sites is used.

Perhaps the most important result of this study was shown in Figure 5.10 in the previous chapter. In this figure it can be seen that the same steps that appear in the tensile curves for samples annealed at 740°C and 760°C appear in the retained austenite volume fraction data as well. The presence of these bands in both data sets strongly suggests that the martensite transformation and passage of Lüders or PLC bands are in fact coincident. This confirms the results of Sun *et al.* [105] who used ferritescope data to demonstrate that the TRIP effect occurs with the passage of strain bands. The current study improves upon the accuracy of the austenite fraction measurements by the correction of localization and magnetoelastic effects, but sacrifices a local strain measurement to do so.

The coincidence of the two phenomena raises the question of whether the TRIP effect is induced by the strain increment associated with PLC bands, or whether the

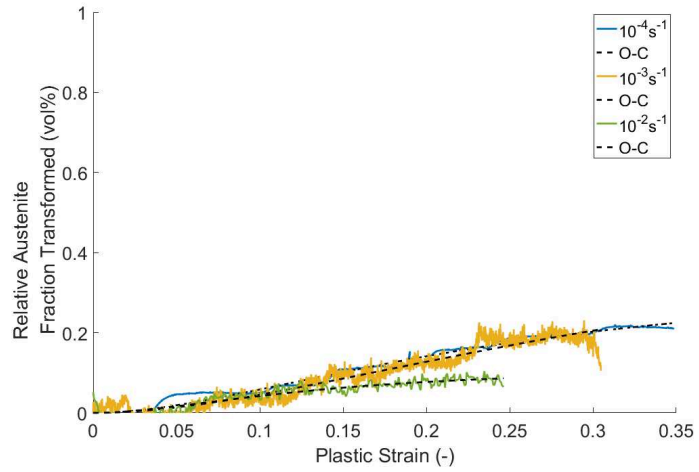

(A)

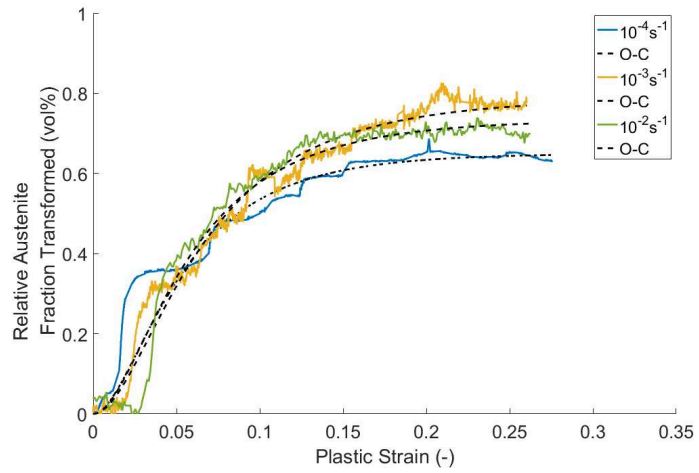

(B)

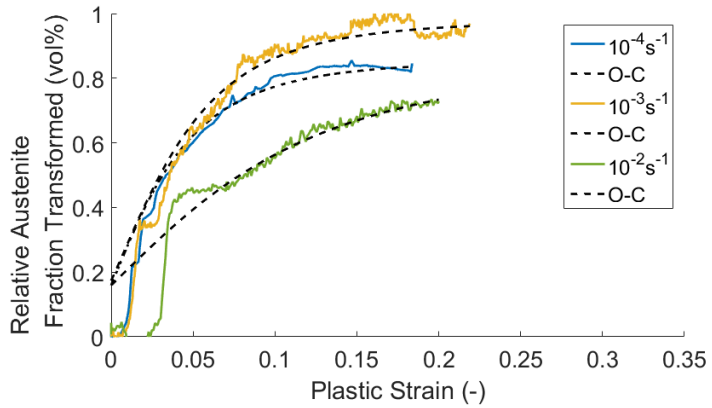

(C)

FIGURE 6.18: Comparison of experimental data and the Olson-Cohen model for each strain rate in samples annealed at 740°C (A), 760°C (B), and 780°C (C).

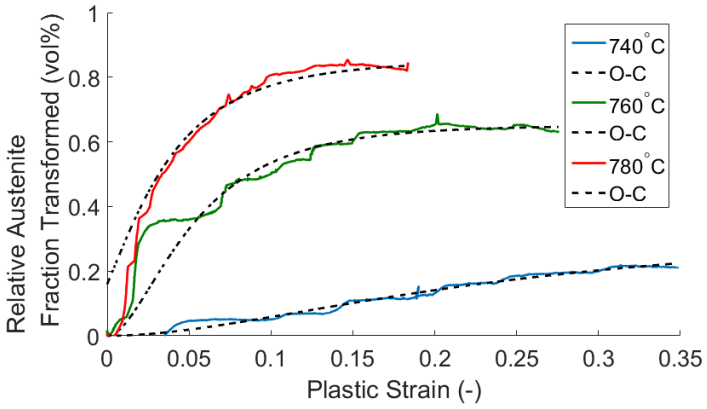

(A)

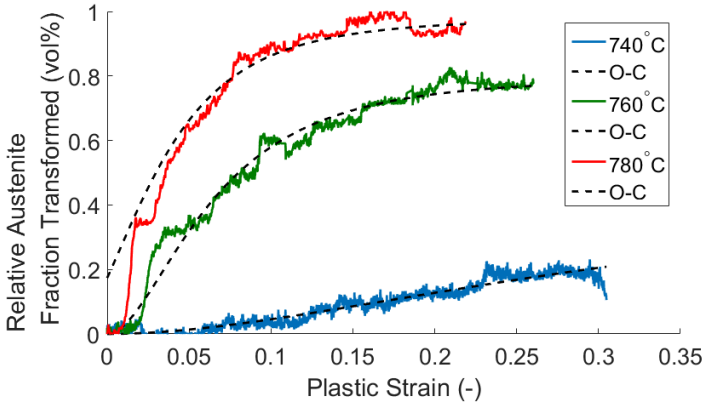

(B)

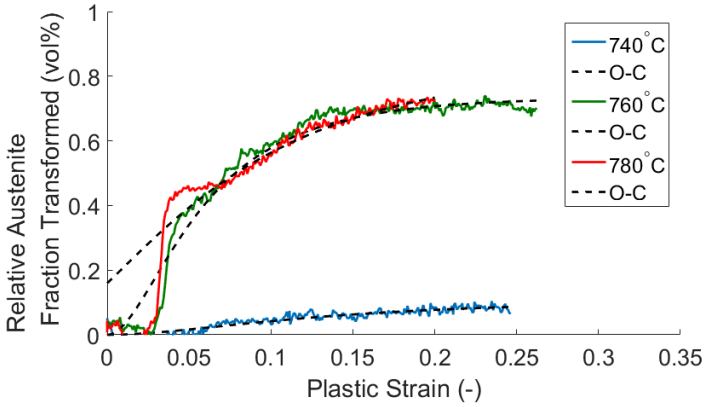

(C)

FIGURE 6.19: Comparison of experimental data and the Olson-Cohen model for each annealing temperature in samples strained at $10^{-4}s^{-1}$ (A), $10^{-3}s^{-1}$ (B), and $10^{-2}s^{-1}$ (C).

local stress/strain incompatibilities generated during TRIP can lead to the nucleation of a strain band. In reality, it is likely a combination of both. There seems to be either a solute or grain size effect given the behavior of the sample annealed at 740°C and strained at $10^{-2}s^{-1}$ wherein clear propagative PLC bands are observed over the course of the tensile test, but very little martensite transformation occurs aside from a small burst during the passage of the Lüders plateau. At the same time, the PLC bands are observable over the entire course of tensile tests even in samples annealed at 760°C which transform relatively quickly and contain less than 10 vol% austenite by the time 10-15% strain is attained. Perhaps, then, the stress relaxation that occurs when the martensite transformation occurs allows neighboring grains to soften as well, resulting in a sort of chain reaction where neighboring austenite grains can be made to transform due to localizations around a freshly-transformed martensite block. If the retained austenite transformed in small blocks rather than entire grains with each passage of a band–that is, if grains are partially transformed and thus grain size reduced–the stabilizing effect resulting from decreased grain size would increase the stress needed to transform the rest of the grain. Once that stress is attained, a relaxation would occur as the transformation happens similarly to the increase in stress and subsequent relaxation that occurs with dislocation unpinning in traditional dynamic strain aging. This is exceedingly difficult to prove definitively given the fact that the transformation is instantaneous, but could be possible using a combination of EBSD and micro-DIC to determine whether the transformation occurs grain-by-grain or in blocks and how the austenite grain size distribution evolves with increasing strain.

A study by Steineder *et al.* [25] showed that the single-parameter Ludwigson-Berger model for TRIP kinetics can be used to demonstrate that Lüders bands are observed only beyond a critical parameter value. This method was applied here to determine if PLC bands also occurred for a certain critical transformation rate. The Ludwigson-Berger model is written as

$$\frac{1}{V_\gamma} - \frac{1}{V_{\gamma,0}} = \frac{K}{p}\varepsilon \tag{6.8}$$

where V_γ is the retained austenite volume fraction and K and p are fitted parameters. For TRIP steels, p is taken as 1, so that K becomes the only parameter needed to fit the transformation kinetics. This model was applied to all of the samples to which the Olson-Cohen model was applied previously. In Figure 6.20 it can be seen that while there is not a distinct value of K that provides a limit between samples with and without PLC, there is seemingly a transition zone between $K = 40$ and $K = 50$. Between these values, the samples annealed at 760°C and 780°C strained at $10^{-2}s^{-1}$ (which did not exhibit PLC) appear as well as the sample annealed at 760°C strained at $10^{-3}s^{-1}$ (which showed type B PLC). Otherwise, samples with $K < 40$ exhibited PLC while those with $K > 50$ did not. It is unclear if a critical value of K

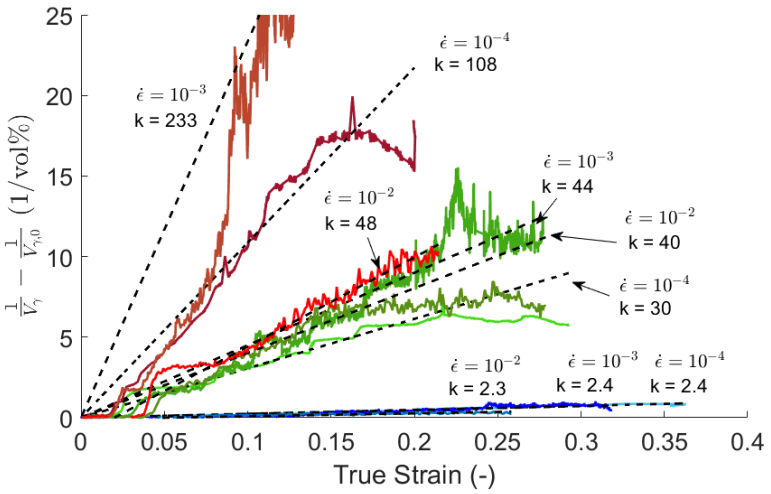

FIGURE 6.20: Comparison of experimental data and the Ludwigson-Berger model for each intercritical annealing temperature and strain rate. Only the parameter K is fitted to experimental data. Annealing temperatures of 740°C, 760°C, and 780°C are represented by blue, green, and red curves respectively.

exists for the presence of Lüders bands as was the case in [25] because the sample annealed at 780°C and strained at $10^{-2}s^{-1}$ overlaps with the sample annealed at 760°C and strained at $10^{-3}s^{-1}$ due to its reduced transformation rate at higher strain rate. Nonetheless, there is a definitive transition where above a certain value of K there is no longer any PLC. This transition seems to occur between $K = 40$ and $K = 44$.

6.5 Strain Rate Sensitivity

The strain rate sensitivity (SRS) of the steel was assessed at three different points after strain rate jumps from $10^{-4}s^{-1}$ to $10^{-2}s^{-1}$: 0.002 strain after the acceleration, 0.005 strain after the acceleration, and at the midpoint of the high strain rate period about 0.02 strain after acceleration. These three methods gave results on the same order of magnitude, but different enough to demonstrate that the point at which SRS is measured is critically important. Notably, the measurements made 0.002 strain after the strain rate jump gave positive values, while those made 0.005 strain after the jump were centered around 0 and finally the measurements at the midpoint of the high strain rate period were negative. The results were compared to [35] for SRS measurements on TWIP steel exhibiting PLC, whose results are presented in Figure 6.21.

In the figure it can be seen that the steady state SRS m_{ss} was about -0.005 and remained negative and approximately constant throughout the experiments. The values reported do not agree with the values obtained here at 0.002 or 0.005 strain after the strain rate jump. However when m_{ss} is calculated at the midpoint of the highs train rate period, the initial value of about -0.005 is very close to the measurements made by Bian *et al.* Moreover, for m_{ss}^{mid} the SRS increased towards 0 with

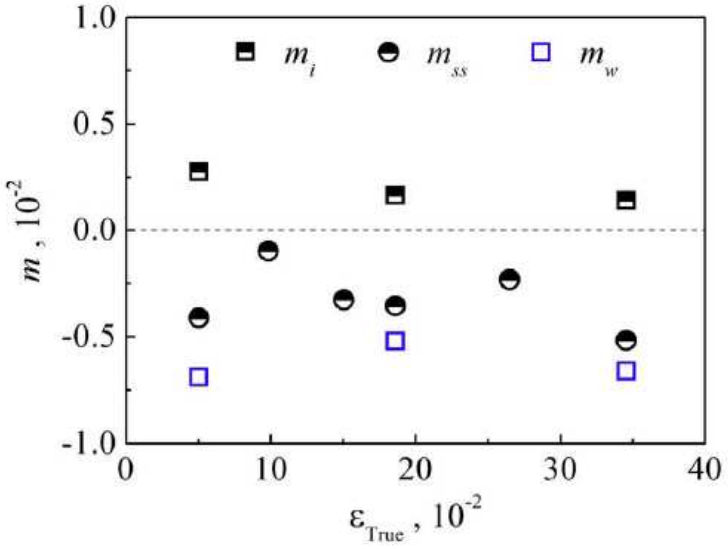

FIGURE 6.21: Strain rate sensitivity measurements made by Bian *et al.* on a 0.6C-23Mn TWIP steel exhibiting PLC. The steady state strain rate sensitivity was around 0.005. [35]

increasing strain. This would be logical if the negative SRS were due to the austenite because the retained austenite is gradually consumed by TRIP with increasing strain. It would seem then that m_{ss}^{mid} is the most appropriate measurement of the strain rate sensitivity made in this study. It should be noted that because the work hardening rate changes when the strain rate is accelerated, this method is dependent on the duration of the period at high speed (in this case, 2mm of displacement or roughly 4% strain).

The strain rate sensitivity started off negative for low strain in all samples. As the strain increased and austenite transformed to martensite, the strain rate sensitivity gradually increased towards 0, as was shown in Figure 5.26 in the previous chapter. Moreover, it was seen that if a single intercritical annealing temperature is considered, the SRS increased with decreasing retained austenite volume fraction (except for the sample annealed at 780°C, for which the two points obtained gave very similar values of m_{ss}). This seems to suggest that the retained austenite is at least partially responsible for the negative strain rate sensitivity seen in this alloy. That is, if the negative SRS were purely the result of reduced work hardening from TRIP, then the SRS as a function of V_γ should be constant. The fact that m increases as V_γ decreases suggests that the austenite itself has a negative SRS and that stabilization via adiabatic heat is not the only reason for the macroscopic negative SRS.

This explanation of the interaction between strain rate, adiabatic heat, and initial microstructure is important when considering the evolution of the microstructure during experiments in which strain rate jumps were performed. The samples upon which strain rate jumps were performed showed significantly more work hardening than either sample deformed at constant rates of $10^{-4}s^{-1}$ or $10^{-2}s^{-1}$. The same

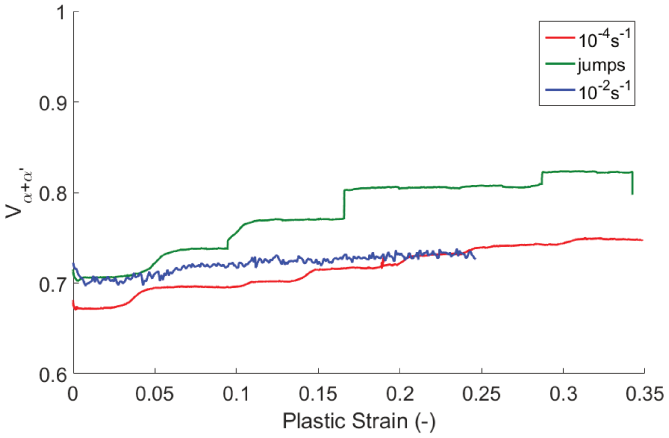

(A)

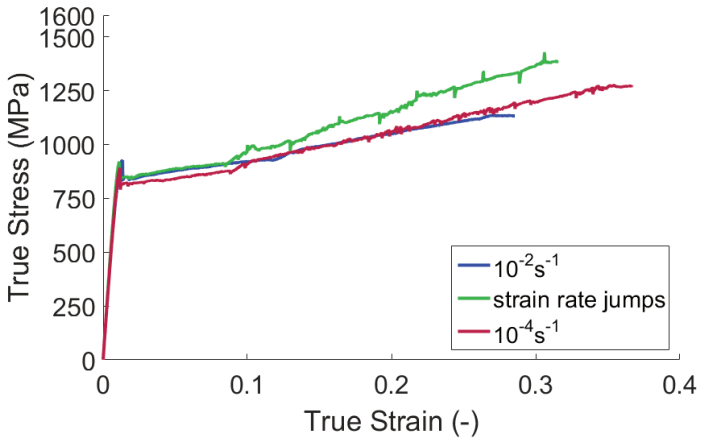

(B)

FIGURE 6.22: The ferromagnetic volume fraction ($\alpha+\alpha'$) as a function of strain for constant strain rates of $10^{-4}s^{-1}$ and $10^{-2}s^{-1}$ as well as jumps between the two. The stress peak upon accelerating the strain rate results in a burst of transformation.

explanation for the difference in mechanical behavior when the test is paused periodically can thus explain the increased work hardening when strain rate jumps are performed. A sudden increase in stress upon the strain rate acceleration results in a burst of martensite transformation. Figure 6.22 provides an example of this for samples annealed at 740°C.

It was seen in the previous chapter that in samples annealed at 740°C and 780°C, a burst of transformation occurred when the strain rate was accelerated. The sample annealed at 760°C, however, showed a burst of transformation upon decelerating. This is more difficult to explain. The samples annealed at 740°C and 780°C had the same plastic deformation mechanism at both strain rates. The samples annealed at 740°C both deformed by PLC, while both samples annealed at 780°C deformed homogeneously. The samples annealed at 760°C however, showed a transition from PLC to homogeneous deformation when the strain rate is increased from $10^{-4}s^{-1}$ to $10^{-2}s^{-1}$. This could have something to do with the fact that the martensite burst

occurs upon deceleration.

If the strain is initially proceeding in the form of a PLC band and then the strain rate is increased, if the sample remains in a PLC regime as for a 740°C anneal, the propagation speed of the band should increase [106], but otherwise the mechanical behavior remains the same. Any dislocations are generated within the band still, so a sudden increase in strain rate could generate a large quantity of dislocations which then provide nucleation sites for martensite transformation. Likewise in the case of the sample annealed at 780°C, the deformation remains homogeneous as does the evolution of the dislocation density. Thus, the transformation can occur upon accelerating.

If the strain begins localized in a band but then suddenly the strain rate is increased to one at which PLC no longer exists, it is unsure how the sample reacts. The fact that there is no work hardening during the high strain rate periods, then suddenly a burst of martensite transformation occurs upon deceleration implies that nucleation sites are generated at $10^{-2}s^{-1}$ and then activated upon decelerating to $10^{-4}s^{-1}$. This should not be a result of adiabatic heat stabilizing the austenite at $10^{-2}s^{-1}$ because if this were the case, the same behavior should be observed in samples annealed at 740°C which have even more stable austenite than those annealed at 760°C. DIC experiments on samples annealed at 760°C upon which strain rate jumps are performed are needed to attempt to determine what happens to the PLC bands when the strain rate jump occurs. These experiments have been performed for anneals at 740°C and 760°C but the DIC calculations, however, did not handle the strain rate jumps well and did not converge. They are currently being post-treated piecewise (excluding the moments at which the strain rate jumps are performed) and initially it seems that after the first jump, no strain bands are present. This would mean that the speed of the strain band, if it exists, would need to be lower than about 10mm/s based on the relative lengths of the sample and the region of interest used for DIC. This speed is well above the measured band propagation speeds, so it is possible that the band did not pass into the region of interest (ROI). The continued analysis of these experiments will hopefully show how the band characteristics are affected by the strain rate jump and how any such changes might relate to the observed trends in magnetic measurements at the time of the jump.

Conclusions and Persectives

This thesis provided an in-depth analysis of the kinetics of martensite transformation in a 0.2C-5Mn-2.5Al Medium Manganese TRIP steel, as well as a characterization of the strain instabilities that occur for certain intercritical annealing temperatures. The primary conclusions made in the study are summarized below.

An experimental setup for measuring the saturated magnetization of a tensile sample *in-situ* was developed. This system permitted measurements of the saturated magnetization–from which the retained austenite volume fraction is then deduced–to be made between 2 and 10 times per second here, though the system is capable of even higher frequencies as noted in Chapter 4. It was possible to thus measure the evolution of the microstructure during TRIP over a full tensile test without any need to interrupt the test, resulting in significant gains in time. Additionally, new corrections not used in similar experiments using ferritescopes are proposed to account for the heterogeneous magnetic field in the microstructure and the effect of an applied stress on the magnetization of the sample.

The measurements of the retained austenite fraction obtained with this system on samples annealed at 740°C, 760°C, or 780°C made it possible to demonstrate that there is a stark difference in transformation kinetics with respect to the intercritical annealing temperature when the retained austenite fraction is plotted as a function of the macroscopic plastic strain. It was seen that the Olson-Cohen model for martensite transformation kinetics is able to reproduce the experimental measurements fairly well for samples that deform homogeneously. Using this model, it was concluded that both the rate of generation of nucleations sites and the probability of their activation increase with the intercritical annealing temperature. There is, however, a complication in that no local measurement of the strain is available, so it is unsure what role the heterogeneous deformation in some samples played in these differences in transformation rate.

The appearance of steps in the plots of the retained austenite fraction as a function of plastic strain suggested a coincidence of the passage of strain bands and the martensite transformation. This was confirmed using digital image correlation (DIC) characterizations of the strain bands, showing that they are responsible for steps in the stress-strain curves for certain samples. The presence of the same kind of heterogeneous behavior in both stress-strain data and austenite fraction-strain data strongly suggests that the two phenomena are coincident.

Moreover, these same DIC characterizations of the strain bands demonstrated that there were significant differences in the width, propagation speed, and strain

rate between the first strain band and all of the subsequent bands. It was concluded that the first strain band is a Lüders band likely occurring in the ferrite, while the subsequent bands are a type of PLC though the underlying mechanism is uncertain.

The hypothesis that the strain bands that appear after yielding are a type of PLC was tested by measuring the strain rate sensitivity (SRS) of the steels at each temperature. It was seen that the SRS was negative and seemed to increase as the retained austenite fraction decreased. This suggests that the retained austenite has a negative SRS, which in turn seems to suggest that there is perhaps a solute effect in which dislocations become pinned or that the transformation itself is responsible for the mechanical instability. In the samples annealed at 780°C for which no PLC occurred, a negative SRS was nonetheless observed and is likely a result of the stabilization of the retained austenite by adiabatic heating at higher strain rates.

A map was constructed that approximates for which strain rate and martensite start temperatures (M_s) PLC bands were observed or not and, if they were observed, whether they were type A, B, or C. Such data has, to the author's knowledge, not been reported in the literature on Medium Mn steels. Additionally, using the Ludwigson-Berger model for transformation kinetics it was shown that there seems to be a critical transformation rate of about $K = 40$ to $K = 44$ below which PLC occurs.

Perspectives

While the magnetic system employed here marks an improvement over ferritescope methods, the one missing component is access to the local strain in the same area in which the saturated magnetization is measured. Were this to be done, a more direct measurement of the transformation kinetics could be made in cases where the strain is heterogeneous. It is suspected that the transformation kinetics in the strain band are the same or at least very similar to the kinetics when strain is homogeneous, but this cannot be confirmed without access to the local strain. Moreover, this would permit a correlation between the strain increment induced by the band and the amount of martensite transformed during its passage.

It was seen that when strain rate jumps are performed, there was no work hardening during the high strain rate period and there were peculiar bursts of transformation either upon accelerating or decelerating the strain rate. It is of interest to understand if and how the strain bands are modified when a strain rate jump is performed, as these changes could help explain why for $T_{IA} = 740$°C or 780°C the burst occurred upon accelerating, but for an anneal at 760°C the burst occurs upon decelerating. Experiments with strain rate jumps and DIC measurements were performed, but are still being post-treated to hopefully provide some insight into these changes. It is possible that the fact that the strain rate jumps for samples annealed at 760°C show a different behavior due to the switch from heterogeneous to homogeneous strain, but this is uncertain at this time.

To truly understand micro-mechanically what happens as plasticity occurs heterogeneously via PLC or Lüders bands, a more precise model is needed. Such a model should include a dynamic Hall-Petch effect that is accurate for grain sizes below $1\mu m$. This model would need to be a finite element crystal plasticity model in order to simulate the strain bands. This would permit the analysis of the precise microstructural conditions that lead to strain band nucleation, for example. Additionally, it could allow one to determine whether the transformation rate in the band truly corresponds to the observed macroscopic transformation rate.

Bibliography

[1] F. Roters, P. Eisenlohr, L. Hantcherli, D.D. Tjahjanto, T.R. Bieler, and D. Raabe. Overview of constitutive laws, kinematics, homogenization and multiscale methods in crystal plasticity finite-element modeling: Theory, experiments, applications. Acta Materialia, 58(4):1152–1211, feb 2010. ISSN 13596454. doi: 10.1016/j.actamat.2009.10.058.

[2] Stuart Keeler. The Science of Forming: Automotive Steels - Online Technical Resources. Metal Forming Magazine, 2012.

[3] Toshiro Kobayashi, Wataru Yagi, Toshihiko Kazino, and Yoshisada Ueda. Effect of heat treatment on toughness of high manganese cast steel. Tetsu-to-Hagane, 70(8):861–868, 1984. doi: 10.2355/tetsutohagane1955.70.8_861.

[4] Toshihiro Hanamura, Shiro Torizuka, Akira Sunahara, Masana Imagumbai, and Hiroshi Takechi. Excellent Total Mechanical-Properties-Balance of 5% Mn, 30000 MPa% Steel. ISIJ International, 51(4):685–687, 2011. doi: 10.2355/isijinternational.51.685.

[5] Jie Shi, Xinjun Sun, Maoqiu Wang, Weijun Hui, Han Dong, and Wenquan Cao. Enhanced work-hardening behavior and mechanical properties in ultrafine-grained steels with large-fractioned metastable austenite. Scripta Materialia, 63(8):815–818, 2010. ISSN 13596462. doi: 10.1016/j.scriptamat.2010.06.023.

[6] G. Dini, a. Najafizadeh, S. M. Monir-Vaghefi, and R. Ueji. Grain size effect on the martensite formation in a high-manganese TWIP steel by the Rietveld method. Journal of Materials Science and Technology, 26(2):181–186, 2010. ISSN 10050302. doi: 10.1016/S1005-0302(10)60030-8.

[7] J-H Kang, T Ingendahl, and W Bleck. A constitutive model for the tensile behaviour of TWIP steels: composition and temperature dependencies. Materials Design, pages 1–52, 2015. ISSN 0014-4886. doi: 10.1016/j.expneurol.2009.07.013.

[8] S. Allain, J.-P. Chateau, and O. Bouaziz. A physical model of the twinning-induced plasticity effect in a high manganese austenitic steel. Materials Science and Engineering: A, 387-389:143–147, 2004. ISSN 09215093. doi: 10.1016/j.msea.2004.01.060.

[9] Haiwen Luo, Jie Shi, Chang Wang, Wenquan Cao, Xinjun Sun, and Han Dong. Experimental and numerical analysis on formation of stable austenite during the intercritical annealing of 5mn steel. Acta Materialia, 59(10):4002 – 4014, 2011.

[10] T. Y. Hsu and Xuejun Jin. The 3rd Generation Automobile Sheet Steels Presenting with Ultrahigh Strength and High Ductility. The recent Scenario in Steel Science and Technology, pages 67–73, 2011. doi: 10.1007/978-3-642-17665-4.

[11] X.D. Wang, N. Zhong, Y.H. Rong, T.Y. Hsu (Z.Y. Xu), and L. Wang. Novel ultrahigh-strength nanolath martensitic steel by quenching–partitioning–tempering process. Journal of Materials Research, 24 (01):260–267, 2009. ISSN 0884-2914. doi: 10.1557/JMR.2009.0029.

[12] G. Mishra, A.K. Chandan, and S. Kundu. Hot rolled and cold rolled medium manganese steel: Mechanical properties and microstructure. Materials Science and Engineering: A, 701(April):319–327, 2017. doi: 10.1016/j.msea.2017.06.088.

[13] Z. C. Li, H. Ding, R. D.K. Misra, and Z. H. Cai. Deformation behavior in cold-rolled medium-manganese TRIP steel and effect of pre-strain on the Lüders bands. Materials Science and Engineering A, 679(September 2016):230–239, 2017. ISSN 09215093. doi: 10.1016/j.msea.2016.10.042.

[14] P. J. Gibbs, E. De Moor, M. J. Merwin, B. Clausen, J. G. Speer, and D. K. Matlock. Austenite stability effects on tensile behavior of manganese-enriched-austenite transformation-induced plasticity steel. Metallurgical and Materials Transactions A: Physical Metallurgy and Materials Science, 42(12):3691–3702, 2011. ISSN 1073-5623. doi: 10.1007/s11661-011-0687-y.

[15] Sangwon Lee and Bruno C. De Cooman. Annealing Temperature Dependence of the Tensile Behavior of 10pct Mn Multi-phase TWIP-TRIP Steel. Metallurgical and Materials Transactions A, 45(13):6039–6052, 2014. ISSN 1073-5623. doi: 10.1007/s11661-014-2540-6.

[16] Z. H. Cai, H. Ding, H. Kamoutsi, G. N. Haidemenopoulos, and R. D K Misra. Interplay between deformation behavior and mechanical properties of intercritically annealed and tempered medium-manganese transformation-induced plasticity steel. Materials Science and Engineering A, 654:359–367, 2016. ISSN 09215093. doi: 10.1016/j.msea.2015.12.057.

[17] Seawoong Lee, Seok-Jae Lee, S. Santhosh Kumar, Kyooyoung Lee, and B. C. De Cooman. Localized Deformation in Multiphase, Ultra-Fine-Grained 6 Pct Mn Transformation-Induced Plasticity Steel. Metallurgical and Materials Transactions A, 42(12):3638–3651, 2011. ISSN 1073-5623. doi: 10.1007/s11661-011-0636-9.

[18] A. Arlazarov, M. Gouné, O. Bouaziz, A. Hazotte, G. Petitgand, and P. Barges. Evolution of microstructure and mechanical properties of medium Mn steels during double annealing. Materials Science and Engineering A, 542:31–39, 2012. ISSN 09215093. doi: 10.1016/j.msea.2012.02.024.

[19] A. Marais, M. Mazière, S. Forest, A. Parrot, and P. Le Delliou. Influence of static strain aging on the cleavage fracture of a C-Mn steel. Engineering Fracture Mechanics, 141:95–110, 2015. ISSN 00137944. doi: 10.1016/j.engfracmech.2015.04.035.

[20] D. W. Beardsmore, J. Quinta da Fonseca, J. Romero, C. A. English, S. R. Ortner, J. Sharples, A. H. Sherry, and M. A. Wilkes. Study of Lüders phenomena in reactor pressure vessel steels. Materials Science and Engineering A, 588:151–166, 2013. doi: 10.1016/j.msea.2013.05.021.

[21] Ajit K. Roy, Pankaj Kumar, and Debajyoti Maitra. Dynamic strain ageing of P91 grade steels of varied silicon content. Materials Science and Engineering A, 499(1-2):379–386, 2009. ISSN 09215093. doi: 10.1016/j.msea.2008.08.027.

[22] Herdawandi Halim, David S. Wilkinson, and Marek Niewczas. The Portevin-Le Chatelier (PLC) effect and shear band formation in an AA5754 alloy. Acta Materialia, 55(12):4151–4160, 2007. doi: 10.1016/j.actamat.2007.03.007.

[23] X. G. Wang, L. Wang, and M. X. Huang. Kinematic and thermal characteristics of Luders and Portevin-Le Chatelier bands in a medium Mn transformation-induced plasticity steel. Acta Materialia, 124(November):17–29, 2017. ISSN 13596454. doi: 10.1016/j.actamat.2016.10.069.

[24] Minghui Cai, Zhun Li, Qi Chao, and Peter D. Hodgson. A Novel Mo and Nb Microalloyed Medium Mn TRIP Steel with Maximal Ultimate Strength and Moderate Ductility. Metallurgical and Materials Transactions A, 45(12):5624–5634, 2014. ISSN 1073-5623. doi: 10.1007/s11661-014-2504-x.

[25] Katharina Steineder, Daniel Krizan, Reinhold Schneider, Coline Béal, and Christof Sommitsch. On the microstructural characteristics influencing the yielding behavior of ultra-fine grained medium-Mn steels. Acta Materialia, 2017. ISSN 13596454. doi: 10.1016/j.actamat.2017.07.056.

[26] Rainer Schwab and Volker Ruff. On the nature of the yield point phenomenon. Acta Materialia, 61(5):1798–1808, 2013. ISSN 13596454. doi: 10.1016/j.actamat.2012.12.003.

[27] N. Tsuchida, Y. Tomota, K. Nagai, and K. Fukaura. A simple relationship between lüders elongation and work-hardening rate at lower yield stress. Scripta Materialia, 54(1):57 – 60, 2006. ISSN 1359-6462.

[28] D. H. Johnson, M. R. Edwards, and P. Chard-Tuckey. Microstructural effects on the magnitude of Lüders strains in a low alloy steel. Materials Science and Engineering A, 625:36–45, 2015. ISSN 09215093. doi: 10.1016/j.msea.2014.11.084.

[29] R. Song, D. Ponge, and D. Raabe. Improvement of the work hardening rate of ultrafine grained steels through second phase particles. Scripta Materialia, 52 (11):1075–1080, 2005. ISSN 13596462. doi: 10.1016/j.scriptamat.2005.02.016.

[30] H. Neuhäuser, F. B. Klose, F. Hagemann, J. Weidenmüller, H. Dierke, and P. Hähner. On the PLC effect in strain-rate and stress-rate controlled tests-studies by laser scanning extensometry. Journal of Alloys and Compounds, 378(1-2):13–18, 2004. ISSN 09258388. doi: 10.1016/j.jallcom.2003.10.064.

[31] B. Swaminathan, W. Abuzaid, H. Sehitoglu, and J. Lambros. Investigation using digital image correlation of Portevin-Le Chatelier Effect in Hastelloy X under thermo-mechanical loading. International Journal of Plasticity, 64:177–192, 2014. ISSN 07496419. doi: 10.1016/j.ijplas.2014.09.001.

[32] M. Komarasamy and R. S. Mishra. Serration behavior and shear band characteristics during tensile deformation of an ultrafine-grained 5024 Al alloy. Materials Science and Engineering A, 616:189–195, 2014. ISSN 09215093. doi: 10.1016/j.msea.2014.08.027.

[33] Zhenyu Jiang, Qingchuan Zhang, Huifeng Jiang, Zhongjia Chen, and Xiaoping Wu. Spatial characteristics of the Portevin-Le Chatelier deformation bands in Al-4 at%Cu polycrystals. Materials Science and Engineering A, 403(1-2): 154–164, 2005. ISSN 09215093.

[34] P.D. Zavattieri, V. Savic, L.G. Hector Jr., J.R. Fekere, W. Tong, and Y. Xuan. Spatio-temporal characteristics of the Portevin-Le Chatelier effect in austenitic steel with twinning induced plasticity. International Journal of Plasticity, 25 (12):2298–2330, 2009.

[35] Xiangde Bian, Fuping Yuan, and Xiaolei Wu. Correlation between strain rate sensitivity and characteristics of Portevin-LeChátelier bands in a twinning-induced plasticity steel. Materials Science and Engineering A, 696(15):220–227, 2017. ISSN 09215093. doi: 10.1016/j.msea.2017.04.078.

[36] Rajashekhar Shabadi, Subodh Kumar, Hans J. Roven, and E. S. Dwarakadasa. Effect of specimen condition, orientation and alloy composition on PLC band parameters. Materials Science and Engineering A, 382(1-2):203–208, 2004. ISSN 09215093. doi: 10.1016/j.msea.2004.04.079.

[37] R C Picu, G Vincze, F Ozturk, J J Gracio, F Barlat, and A M Maniatty. Strain rate sensitivity of the commercial aluminum alloy AA5182-O. Materials Science & Engineering A, 390:334–343, 2005. doi: 10.1016/j.msea.2004.08.029.

[38] C. Kahloun, G. Monnet, S. Queyreau, L. T. Le, and P. Franciosi. A comparison of collective dislocation motion from single slip quantitative topographic analysis during in-situ AFM room temperature tensile tests on Cu and Feα crystals. International Journal of Plasticity, 84:277–298, 2016. ISSN 07496419.

[39] Jifeng Wang and H Sehitoglu. Dislocation slip and twinning in ni-based l12 type alloys. Intermetallics, 52:20–31, 09 2014.

[40] K.M. Rahman, V.a. Vorontsov, and D. Dye. The effect of grain size on the twin initiation stress in a TWIP steel. Acta Materialia, 89:247–257, 2015. ISSN 13596454. doi: 10.1016/j.actamat.2015.02.008.

[41] K. Renard, S. Ryelandt, and P. J. Jacques. Characterisation of the Portevin-Le Châtelier effect affecting an austenitic TWIP steel based on digital image correlation. Materials Science and Engineering A, 527(12):2969–2977, 2010. ISSN 09215093. doi: 10.1016/j.msea.2010.01.037.

[42] Douglas Adams. The Hitchhiker's Guide to the Galaxy. New York : Harmony Books, 1980.

[43] A Vinogradov, A Lazarev, M Linderov, A Weidner, and H Biermann. Kinetics of deformation processes in high-alloyed cast transformation-induced plasticity/twinning-induced plasticity steels determined by acoustic emission and scanning electron microscopy: Influence of austenite stability on deformation mechanisms. Acta Materialia, 61(7):2434–2449, 2013. ISSN 1359-6454. doi: 10.1016/j.actamat.2013.01.016.

[44] D. Barbier, N. Gey, S. Allain, N. Bozzolo, and M. Humbert. Analysis of the tensile behavior of a TWIP steel based on the texture and microstructure evolutions. Materials Science and Engineering A, 500(1-2):196–206, 2009. doi: 10.1016/j.msea.2008.09.031.

[45] R. Ueji, N. Tsuchida, D. Terada, N. Tsuji, Y. Tanaka, A. Takemura, and K. Kunishige. Tensile properties and twinning behavior of high manganese austenitic steel with fine-grained structure. Scripta Materialia, 59(9):963–966, 2008. doi: 10.1016/j.scriptamat.2008.06.050.

[46] I. Gutierrez-Urrutia and D. Raabe. Dislocation and twin substructure evolution during strain hardening of an Fe-22 wt.% Mn-0.6 wt.% C TWIP steel observed by electron channeling contrast imaging. Acta Materialia, 59(16): 6449–6462, 2011. doi: 10.1016/j.actamat.2011.07.009.

[47] Bruno C. De Cooman, Yuri Estrin, and Sung Kyu Kim. Twinning-induced plasticity (TWIP) steels. Acta Materialia, 2017. ISSN 1359-6454. doi: https://dx-doi-org.bibliopam.ecp.fr/10.1016/j.actamat.2017.06.046.

[48] Christian Haase, Luis A. Barrales-Mora, Franz Roters, Dmitri A. Molodov, and Günter Gottstein. Applying the texture analysis for optimizing thermomechanical treatment of high manganese twinning-induced plasticity steel. Acta Materialia, 80:327–340, 2014.

[49] A. Soulami, K.S. Choi, Y.F. Shen, W.N. Liu, X. Sun, and M.A. Khaleel. On deformation twinning in a 17.5based phenomenological model. Materials Science and Engineering: A, 528(3):1402 – 1408, 2011. ISSN 0921-5093. doi: https://dx-doi-org.bibliopam.ecp.fr/10.1016/j.msea.2010.10.031.

[50] M. Cherkaoui, M. Berveiller, and X. Lemoine. Couplings between plasticity and martensitic phase transformation: overall behavior of polycrystalline TRIP steels. International journal of plasticity, 16(10):1215–1241, 2000.

[51] G.B. Olson and Morris Cohen. Kinetics of Strain-Induced Martensitic Nucleation. Metallurgical Transactions A, 6(April):791–795, 1975.

[52] T. Angel. Formation of martensite in austenitic stainless steels. J. Iron Steel Inst., 177:165–174, 1954.

[53] H. Ghassemi-Armaki, R. Maaß, S.P. Bhat, S. Sriram, J.R. Greer, and K.S. Kumar. Deformation response of ferrite and martensite in a dual-phase steel. Acta Materialia, 62:197–211, 2014.

[54] K. Spencer, J. D. Embury, K. T. Conlon, M. Véron, and Y. Bréchet. Strengthening via the formation of strain-induced martensite in stainless steels. Materials Science and Engineering A, 387-389(1-2 SPEC. ISS.):873–881, 2004. ISSN 09215093. doi: 10.1016/j.msea.2003.11.084.

[55] A. Benallal, T. Berstad, T. Børvik, O. S. Hopperstad, I. Koutiri, and R. Nogueira de Codes. An experimental and numerical investigation of the behaviour of AA5083 aluminium alloy in presence of the Portevin-Le Chatelier effect. International Journal of Plasticity, 24(10):1916–1945, 2008. ISSN 07496419. doi: 10.1016/j.ijplas.2008.03.008.

[56] Zbigniew Gronostajski, Adam Niechajowicz, Roman Kuziak, Jakub Krawczyk, and Slawomir Polak. The effect of the strain rate on the stress- strain curve and microstructure of AHSS. Journal of Materials Processing Technology, 242:246–259, 2017. ISSN 09240136. doi: 10.1016/j.jmatprotec.2016.11.023.

[57] M. Bach, N. Broll, A. Cornet, and L. Gaide. Diffraction X en traitements thermiques: dosage de l'austénite résiduelle par diffraction des rayons X. Journal de Physique IV Colloque, 06(C4):887–895, 1996.

[58] Mingda Zhang, Wenquan Cao, Han Dong, and Jing Zhu. Element partitioning effect on microstructure and mechanical property of the micro-laminated Fe-Mn-Al-C dual phase steel. Materials Science and Engineering A, 654:193–202, 2016. ISSN 09215093. doi: 10.1016/j.msea.2015.12.029.

[59] Chengwei Shao, Weijun Hui, Yongjian Zhang, Xiaoli Zhao, and Yuqing Weng. Microstructure and mechanical properties of hot-rolled medium-Mn steel containing 3% aluminum. Materials Science and Engineering A, 682(November 2016):45–53, 2017. ISSN 09215093. doi: 10.1016/j.msea.2016.11.036.

[60] Z.C. C. Li, H. Ding, R.D.K. D K Misra, Z.H. H. Cai, and H.X. X. Li. Microstructural evolution and deformation behavior in the Fe-(6, 8.5)Mn-3Al-0.2C TRIP steels. Materials Science and Engineering: A, 672:161–169, 2016. ISSN 09215093. doi: 10.1016/j.msea.2016.06.078.

[61] Z.H. Cai, H. Ding, R.D.K. Misra, and Z.Y. Ying. Austenite stability and deformation behavior in a cold-rolled transformation-induced plasticity steel with medium manganese content. Acta Materialia, 84:229–236, 2015. ISSN 13596454. doi: 10.1016/j.actamat.2014.10.052.

[62] Benjamin Klusemann, Gottfried Fischer, Thomas Böhlke, and Bob Svendsen. Thermomechanical characterization of Portevin-Le Châtelier bands in AlMg3 (AA5754) and modeling based on a modified Estrin-McCormick approach. International Journal of Plasticity, 67:192–216, 2014. ISSN 07496419. doi: 10.1016/j.ijplas.2014.10.011.

[63] Sangwon Lee and Bruno Charles De Cooman. Effect of the Intercritical Annealing Temperature on the Mechanical Properties of 10Pct Mn Multi-phase Steel. Metallurgical and Materials Transactions A, 45(11):5009–5016, 2014. ISSN 1073-5623. doi: 10.1007/s11661-014-2449-0.

[64] G. Besnard, F. Hild, and S. Roux. "Finite-Element" Displacement Fields Analysis from Digital Images: Application to Portevin–Le Chatelier Bands. Experimental Mechanics, 46(6):789–803, 2006.

[65] J. Réthoré, S. Roux, and F. Hild. An extended and integrated digital image correlation technique applied to the analysis fractured samples. Eur. J. Comput. Mech., 18:285–306, 2009.

[66] Zvonimir Tomicevc, Francois Hild, and Stephane Roux. Mechanics-aided digital image correlation. The Journal of Strain Analysis for Engineering Design, 48(5):330–343, 2013. doi: 10.1177/0309324713482457.

[67] M.A. Sutton. Computer vision-based, noncontacting deformation measurements in mechanics: A generational transformation. Appl. Mech. Rev., 65 (AMR-13-1009):050802, 2013.

[68] F. Hild and S. Roux. Correli T3R. IDDN.FR.001.520007.000.S.P.2015.000.31500, Agence pour la Protection des Programmes, Paris (France), 2015.

[69] D. Claire, F. Hild, and S. Roux. A finite element formulation to identify damage fields: The equilibrium gap method. Int. J. Num. Meth. Engng., 61(2): 189–208, 2004.

[70] F. Hild, A. Bouterf, and S. Roux. Damage measurements via dic. Int. J. Fract., 191(1):77–105, 2015.

[71] M.D. Abramoff, P.J. Magalhaes, and S.J. Ram. Image processing with ImageJ. Biophotonics International, 11(7):36–42, 2004.

[72] B. Reznik, A. Kontny, M. Uehara, J. Gattacceca, P. Solheid, and M. Jackson. Magnetic domains and magnetic stability of cohenite from the Morasko iron meteorite. Journal of Magnetism and Magnetic Materials, 426(October 2016): 594–603, 2017. ISSN 03048853. doi: 10.1016/j.jmmm.2016.10.161.

[73] P. Czaja, M. J. Szczerba, R. Chulist, M. Bałanda, J. Przewoźnik, Y. I. Chumlyakov, N. Schell, Cz Kapusta, and W. Maziarz. Martensitic transition, structure and magnetic anisotropy of martensite in Ni-Mn-Sn single crystal. Acta Materialia, 118:213–220, 2016. ISSN 13596454. doi: 10.1016/j.actamat.2016.07.059.

[74] Hui Zhang, Dechang Zeng, and Zhongwu Liu. The law of approach to saturation in ferromagnets originating from the magnetocrystalline anisotropy. Journal of Magnetism and Magnetic Materials, 322(16):2375–2380, 2010. doi: 10.1016/j.jmmm.2010.02.040.

[75] O. Hubert, L. Daniel, and R. Billardon. Experimental analysis of the magnetoelastic anisotropy of a non-oriented silicon iron alloy. Journal of Magnetism and Magnetic Materials, 254-255:352–354, 2003. doi: 10.1016/S0304-8853(02)00850-8.

[76] Laurent Daniel, Olivier Hubert, Nicolas Buiron, and René Billardon. Reversible magneto-elastic behavior: A multiscale approach. Journal of the Mechanics and Physics of Solids, 56(3):1018–1042, 2008. ISSN 00225096. doi: 10.1016/j.jmps.2007.06.003.

[77] Olivier Hubert and Said Lazreg. Two phase modeling of the influence of plastic strain on the magnetic and magnetostrictive behaviors of ferromagnetic materials. Journal of Magnetism and Magnetic Materials, 424(June 2016):421–442, 2017. ISSN 0304-8853. doi: 10.1016/j.jmmm.2016.10.092.

[78] Adam Bienkowski. Magnetoelastic Villari effect in Mn–Zn ferrites. Journal of Magnetism and Magnetic Materials, 215–216(1):231–233, 2000.

[79] A. M. Beese and D. Mohr. Identification of the Direction-Dependency of the Martensitic Transformation in Stainless Steel Using In Situ Magnetic Permeability Measurements. Experimental Mechanics, 51(5):667–676, 2011. ISSN 00144851. doi: 10.1007/s11340-010-9374-y.

[80] Kim, Hwigeon and Lee, Jinwoo and Barlat, Frédéric and Kim, Daeyong and Lee, Myoung Gyu. Experiment and modeling to investigate the effect of stress state, strain and temperature on martensitic phase transformation in TRIP-assisted steel. Acta Materialia, 97:435–444, 2015. ISSN 13596454. doi: 10.1016/j.actamat.2015.06.023.

[81] P. J. Jacques, S. Allain, O. Bouaziz, A. De, A.-F. Gourgues, B. M. Hance, Y. Houbaert, J. Huang, A. Iza-Mendia, S. E. Kruger, M. Radu, L. Samek, J. Speer, L. Zhao, and S. van der Zwaag. On measurement of retained austenite in multiphase TRIP steels — results of blind round robin test involving six different techniques. Materials Science and Technology, 25(5):567–574, 2009. doi: 10.1179/174328408X353723.

[82] S. Lazreg and O. Hubert. A multidomain modeling of the magnetoelastic behavior for nondestructive evaluation. Journal of Applied Physics, 109(7): 07E508, 2011. doi: 10.1063/1.3540416.

[83] X. J. Hao, W. Yin, M. Strangwood, A. J. Peyton, P. F. Morris, and C. L. Davis. Modelling the electromagnetic response of two-phase steel microstructures. NDT and E International, 43(4):305–315, 2010. ISSN 09638695. doi: 10.1016/j.ndteint.2010.01.006.

[84] Cristina Bormio-Nunes and Olivier Hubert. Piezomagnetic behavior of Fe–Al–B alloys. Journal of Magnetism and Magnetic Materials, 393:404–418, 2015. ISSN 03048853. doi: 10.1016/j.jmmm.2015.05.091.

[85] O. Hubert and L. Daniel. Energetical and multiscale approaches for the definition of an equivalent stress for magneto-elastic couplings. Journal of Magnetism and Magnetic Materials, 323:1766–1781, 2011.

[86] Michael Callahan, Olivier Hubert, François Hild, Astrid Perlade, and Jean Hubert Schmitt. Coincidence of strain-induced TRIP and propagative PLC bands in Medium Mn steels. Materials Science and Engineering A, 704:391–400, 2017. ISSN 09215093. doi: 10.1016/j.msea.2017.08.042.

[87] J.D. Eshelby. The determination of the elastic field of an ellipsoidal inclusion, and related problems. Proceedings of the Royal Society, 1957.

[88] D. Vanoost, S. Steentjes, J. Peuteman, G. Gielen, H. De Gersem, and D. Pissoort. Magnetic hysteresis at the domain scale of a multi-scale material model for magneto-elastic behaviour. Journal of Magnetism and Magnetic Materials, 414:168–179, 2016.

[89] H. Ait-Amokhtar and C. Fressengeas. Crossover from continuous to discontinuous propagation in the Portevin-Le Chatelier effect. Acta Materialia, 58(4): 1342–1349, 2010. ISSN 13596454. doi: 10.1016/j.actamat.2009.10.038.

[90] L. Samek, E. De Moor, J. Penning, and B. C. De Cooman. Influence of alloying elements on the kinetics of strain-induced martensitic nucleation in low-alloy, multiphase high-strength steels. Metallurgical and Materials Transactions A, 37(1):109–124, Jan 2006. ISSN 1543-1940. doi: 10.1007/s11661-006-0157-0.

[91] Z. H. Cai, H. Ding, H. Kamoutsi, G. N. Haidemenopoulos, and R. D K Misra. Interplay between deformation behavior and mechanical properties of intercritically annealed and tempered medium-manganese transformation-induced plasticity steel. Materials Science and Engineering A, 654:359–367, 2016. ISSN 09215093. doi: 10.1016/j.msea.2015.12.057.

[92] W. J. Dan, W. G. Zhang, S. H. Li, and Z. Q. Lin. A model for strain-induced martensitic transformation of TRIP steel with pre-strain. Computational Materials Science, 40(2):292–299, 2007. ISSN 09270256. doi: 10.1016/j.commatsci.2006.12.011.

[93] Seong-Won Yoo, Chi-Seung Lee, Woong-Sup Park, Myung-Hyun Kim, and Jae-Myung Lee. Temperature and strain rate dependent constitutive model of TRIP steels for low-temperature applications. Computational Materials Science, 50(7):2014–2027, 2011. ISSN 09270256. doi: 10.1016/j.commatsci.2011.02.002.

[94] Rong Tian, Lin Li, Bc De Cooman, Xi-chen Wei, and Peng Sun. Effect of Temperature and Strain Rate on Dynamic Properties of Low Silicon TRIP Steel. Journal of Iron and Steel Research, International, 13(3):51–56, 2006. ISSN 1006706X. doi: 10.1016/S1006-706X(06)60061-7.

[95] Jeom Yong Choi, Jaeeun Lee, Keunho Lee, Ji-Yeon Koh, Jae-Hyung Cho, Heung Nam Han, and Kyung-Tae Park. Effects of the strain rate on the tensile properties of a TRIP-aided duplex stainless steel. Materials Science and Engineering: A, 666:280–287, 2016. ISSN 09215093. doi: 10.1016/j.msea.2016.04.047.

[96] Jeongho Han, Seok Hyeon Kang, Seung Joon Lee, and Young Kook Lee. Fabrication of bimodal-grained Al-free medium Mn steel by double intercritical annealing and its tensile properties. Journal of Alloys and Compounds, 681: 580–588, 2016. ISSN 09258388. doi: 10.1016/j.jallcom.2016.04.014.

[97] S.Y.P. Allain, O. Bouaziz, I. Pushkareva, and C.P. Scott. Towards the microstructure design of DP steels: a generic size-sensitive mean-field mechanical model. Materials Science and Engineering: A, 2015. ISSN 09215093. doi: 10.1016/j.msea.2015.04.017.

[98] A. Arlazarov, O. Bouaziz, J. P. Masse, and F. Kegel. Characterization and modeling of mechanical behavior of quenching and partitioning steels. Materials Science and Engineering A, 620:293–300, 2014. ISSN 09215093. doi: 10.1016/j.msea.2014.10.034.

[99] Artem Arlazarov, Olivier Bouaziz, Alain Hazotte, Mohamed Gouné, and Sébastien Allain. Characterization and Modeling of Manganese Effect on Strength and Strain Hardening of Martensitic Carbon Steels. ISIJ International, 53(6):1076–1080, 2013. ISSN 0915-1559. doi: 10.2355/isijinternational.53.1076.

[100] X. Liang, J.R. McDermid, O. Bouaziz, X. Wang, J.D. Embury, and H.S. Zurob. Microstructural evolution and strain hardening of Fe–24Mn and Fe–30Mn alloys during tensile deformation. Acta Materialia, 57(13):3978–3988, aug 2009. ISSN 13596454. doi: 10.1016/j.actamat.2009.05.003.

[101] Haiwen Luo, Han Dong, and Mingxin Huang. Effect of intercritical annealing on the Lüders strains of medium Mn transformation-induced plasticity steels. Materials and Design, 83, 2015. ISSN 18734197. doi: 10.1016/j.matdes.2015.05.085.

[102] H. B. Sun, F. Yoshida, M. Ohmori, and X. Ma. Effect of strain rate on Lüders band propagating velocity and Lüders strain for annealed mild steel under uniaxial tension. Materials Letters, 57(29):4535–4539, 2003. ISSN 0167577X. doi: 10.1016/S0167-577X(03)00358-6.

[103] Joo Hyun Ryu, Jeong In Kim, Hyoung Seop Kim, Chang-Seok Oh, H.K.D.H. Bhadeshia, and Dong-Woo Suh. Austenite stability and heterogeneous deformation in fine-grained transformation-induced plasticity-assisted steel. Scripta Materialia, 68(12):933–936, 2013. ISSN 13596462. doi: 10.1016/j.scriptamat.2013.02.026.

[104] P. J. Gibbs, B. C. De Cooman, D. W. Brown, B. Clausen, J. G. Schroth, M. J. Merwin, and D. K. Matlock. Strain partitioning in ultra-fine grained medium-manganese transformation induced plasticity steel. Materials Science and Engineering A, 609:323–333, 2014. ISSN 09215093. doi: 10.1016/j.msea.2014.03.120.

[105] Binhan Sun, Nicolas Vanderesse, Fateh Fazeli, Colin Scott, Jianqiang Chen, Philippe Bocher, Mohammad Jahazi, and Stephen Yue. Discontinuous strain-induced martensite transformation related to the Portevin-Le Chatelier effect in a medium manganese steel. Scripta Materialia, 133:9–13, 2017. ISSN 13596462. doi: 10.1016/j.scriptamat.2017.01.022.

[106] H. Ait-Amokhtar, P. Vacher, and S. Boudrahem. Kinematics fields and spatial activity of Portevin-Le Chatelier bands using the digital image correlation method. Acta Materialia, 54(16):4365–4371, 2006. ISSN 13596454. doi: 10.1016/j.actamat.2006.05.028.

Titre : Analyse de la cinétique de transformation et des instabilités de déformation dans des aciers TRIP « Moyen Manganèse » de 3eme génération

Mots clés : bandes de Lüders, bandes de Portévin le-Châtelier, corrélation d'images, aimantation saturée, plasticité induite par la transformation (TRIP)

Abstract : Cette thèse caractérise un acier Moyen Mn à 0.2C-5Mn-2.5Al qui montre un écrouissage très fort au cours de la déformation plastique dû à l'effet TRIP. Pendant TRIP, l'austénite résiduelle paramagnétique se transforme en martensite ferromagnétique sous déformation plastique, ce qui conduit à un fort écrouissage. Le taux de cet écrouissage dépend des paramètres de fabrication et surtout la température de recuit intercritique. Ces aciers ont aussi des fois le tendance de se déformer de façon hétérogène par des bandes de Lüders ou PLC.

Dans cette thèse, une méthode de caractérisation de la cinétique de transformation de phase est développée sur la base des mesures de l'aimantation saturée de l'acier. La méthode magnétique est unique dans son implémentation in-situ sans aucun effet sur l'essai de traction. Une correction pour les effets de la contrainte appliquée sur l'aimantation est aussi introduite pour la première fois avec une base physique. Les résultats des mesures magnétiques ont été comparés contre des caractérisations des bandes de déformation pour montrer que la transformation de phase coïncide avec le passage des bandes de déformation. La sensibilité à la vitesse de déformation est analysée et une caractérisation de la présence et type de bande PLC est présentée en fonction de la cinétique de transformation de phase.

Title: Analysis of Transformation Kinetics and Strain Instabilities in 3rd Generation Medium Manganese TRIP Steels

Keywords: Lüders bands, Portévin le-Châtelier bands, digital image correlation, saturated magnetization, transformation-induced plasticity (TRIP)

Abstract: This thesis studies the mechanical behavior of a 0.2C-5Mn-2.5Al Medium Mn steel that exhibits a very high degree of work hardening due to transformation-induced plasticity (TRIP) during plastic deformation. During TRIP, paramagnetic retained austenite is transformed to ferromagnetic martensite with the application of plastic strain and generates a significant amount of work hardening. The rate of work hardening is seen to vary greatly depending on processing parameters—notably the intercritical annealing temperature. These steels also often deform heterogeneously through the propagation of Lüders or PLC strain bands.

This research develops a method to characterize the kinetics of the TRIP effect through measurements of the samples magnetic properties. The method is novel in that it is performed in-situ with no effect on the tensile test and is able to correct for the effects of the applied stress on the magnetic properties. The results of these experiments were compared to characterizations of the strain bands to demonstrate that TRIP coincides with the passage of a Lüders or PLC band. The strain rate sensitivity of the steels is analyzed and the presence and type of PLC bands are characterized with respect to the transformation kinetics.